U.S. Department of Transportation
Federal Railroad Administration

Office of Research, Development and Technology
Washington, DC 20590

Validation of Scaling Laws for Fully-Developed Passenger Rail Car Fires

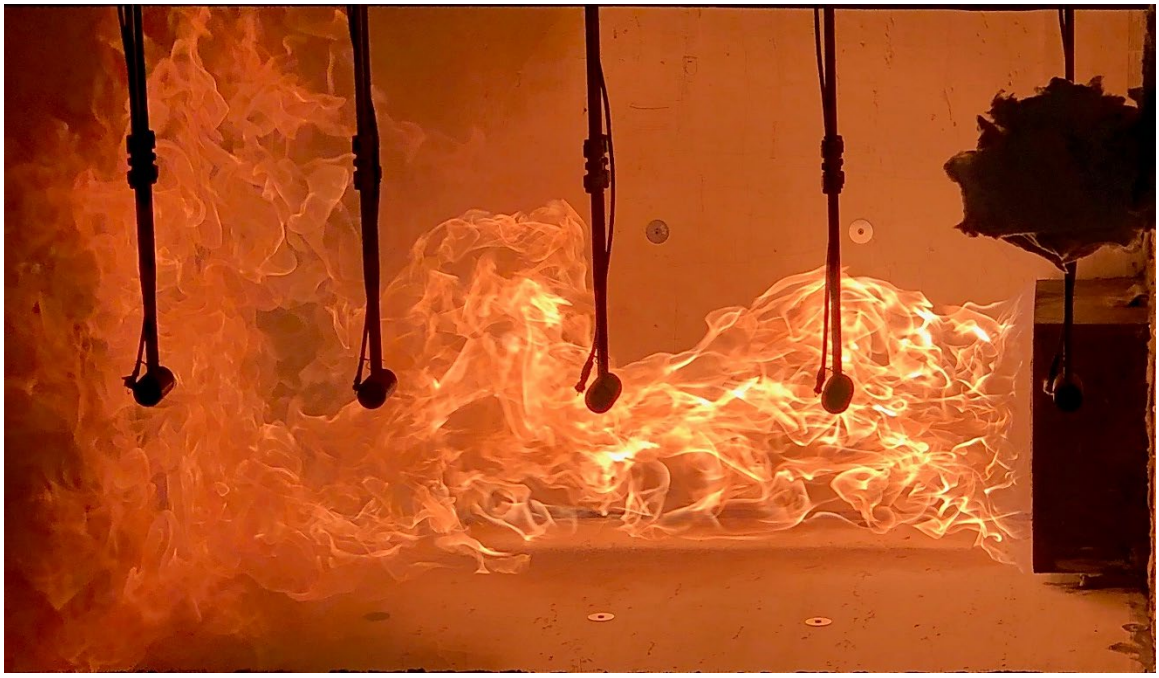

REPORT DOCUMENTATION PAGE

Form Approved
OMB No. 0704-0188

1. REPORT DATE *(DD-MM-YYYY)*	**2. REPORT TYPE**	**3. DATES COVERED** *(From - To)*
June 2022	Technical Report	October 2019–June 2021

4. TITLE AND SUBTITLE
Validation of Scaling Laws for Fully Developed Passenger Rail Car Fires

5a. CONTRACT NUMBER
693JJ618C000022

5b. GRANT NUMBER

5c. PROGRAM ELEMENT NUMBER

6. AUTHOR(S)
Jonathan L. Hodges 0000-0001-6830-0622
Matt DiDomizio 0000-0002-0472-4722
Anil Kapahi 0000-0001-9279-7544
Brian Y. Lattimer 0000-0002-4743-6122

5d. PROJECT NUMBER

5e. TASK NUMBER

5f. WORK UNIT NUMBER

7. PERFORMING ORGANIZATION NAME(S) AND ADDRESS(ES)
Jensen Hughes, Inc.
3610 Commerce Drive, Suite 817
Baltimore, MD 21227-7164

8. PERFORMING ORGANIZATION REPORT NUMBER

9. SPONSORING/MONITORING AGENCY NAME(S) AND ADDRESS(ES)
U.S. Department of Transportation
Federal Railroad Administration
Office of Railroad Policy and Development
Office of Research, Development and Technology
Washington, DC 20590

10. SPONSOR/MONITOR'S ACRONYM(S)

11. SPONSOR/MONITOR'S REPORT NUMBER(S)
DOT/FRA/ORD-22/23

12. DISTRIBUTION/AVAILABILITY STATEMENT
This document is available to the public through the FRA website.

13. SUPPLEMENTARY NOTES
COR: Melissa Shurland

14. ABSTRACT
The focus of this effort was to confirm the capability of the scaling laws to predict full-scale fully-developed compartment fire heat release rates (HRR) based on reduced-scale experiments. A total of 17 compartment fire tests were conducted in this effort consisting of 14 unique configurations and three repeated tests. Tests were conducted at three scales including full-scale, half-scale, and quarter-scale. A total of five permutations of the compartment design were evaluated to demonstrate the capability with complex ventilation, combustible linings, and liquid fuels. The results indicated that the scaling approach presents a cost-effective alternative to full-scale testing of combustible linings.

15. SUBJECT TERMS
Rail car, fire scaling, fire testing, heat release rate, HRR, heat rate release per unit area, HRRPUA rolling stock, test, compartment fire

16. SECURITY CLASSIFICATION OF:			**17. LIMITATION OF ABSTRACT**	**18. NUMBER OF PAGES**	**19a. NAME OF RESPONSIBLE PERSON**
a. REPORT	**b. ABSTRACT**	**c. THIS PAGE**			Anil Kapahi
				140	**19b. TELEPHONE NUMBER** *(Include area code)* 443-313-9795

Standard Form 298 (Rev. 8/98)
Prescribed by ANSI Std. Z39.18

METRIC/ENGLISH CONVERSION FACTORS

ENGLISH TO METRIC	METRIC TO ENGLISH
LENGTH (APPROXIMATE)	**LENGTH (APPROXIMATE)**
1 inch (in) = 2.5 centimeters (cm)	1 millimeter (mm) = 0.04 inch (in)
1 foot (ft) = 30 centimeters (cm)	1 centimeter (cm) = 0.4 inch (in)
1 yard (yd) = 0.9 meter (m)	1 meter (m) = 3.3 feet (ft)
1 mile (mi) = 1.6 kilometers (km)	1 meter (m) = 1.1 yards (yd)
	1 kilometer (km) = 0.6 mile (mi)
AREA (APPROXIMATE)	**AREA (APPROXIMATE)**
1 square inch (sq in, in^2) = 6.5 square centimeters (cm^2)	1 square centimeter (cm^2) = 0.16 square inch (sq in, in^2)
1 square foot (sq ft, ft^2) = 0.09 square meter (m^2)	1 square meter (m^2) = 1.2 square yards (sq yd, yd^2)
1 square yard (sq yd, yd^2) = 0.8 square meter (m^2)	1 square kilometer (km^2) = 0.4 square mile (sq mi, mi^2)
1 square mile (sq mi, mi^2) = 2.6 square kilometers (km^2)	10,000 square meters (m^2) = 1 hectare (ha) = 2.5 acres
1 acre = 0.4 hectare (he) = 4,000 square meters (m^2)	
MASS - WEIGHT (APPROXIMATE)	**MASS - WEIGHT (APPROXIMATE)**
1 ounce (oz) = 28 grams (gm)	1 gram (gm) = 0.036 ounce (oz)
1 pound (lb) = 0.45 kilogram (kg)	1 kilogram (kg) = 2.2 pounds (lb)
1 short ton = 2,000 pounds (lb) = 0.9 tonne (t)	1 tonne (t) = 1,000 kilograms (kg) = 1.1 short tons
VOLUME (APPROXIMATE)	**VOLUME (APPROXIMATE)**
1 teaspoon (tsp) = 5 milliliters (ml)	1 milliliter (ml) = 0.03 fluid ounce (fl oz)
1 tablespoon (tbsp) = 15 milliliters (ml)	1 liter (l) = 2.1 pints (pt)
1 fluid ounce (fl oz) = 30 milliliters (ml)	1 liter (l) = 1.06 quarts (qt)
1 cup (c) = 0.24 liter (l)	1 liter (l) = 0.26 gallon (gal)
1 pint (pt) = 0.47 liter (l)	
1 quart (qt) = 0.96 liter (l)	
1 gallon (gal) = 3.8 liters (l)	
1 cubic foot (cu ft, ft^3) = 0.03 cubic meter (m^3)	1 cubic meter (m^3) = 36 cubic feet (cu ft, ft^3)
1 cubic yard (cu yd, yd^3) = 0.76 cubic meter (m^3)	1 cubic meter (m^3) = 1.3 cubic yards (cu yd, yd^3)
TEMPERATURE (EXACT)	**TEMPERATURE (EXACT)**
[(x-32)(5/9)] °F = y °C	[(9/5) y + 32] °C = x °F

QUICK INCH - CENTIMETER LENGTH CONVERSION

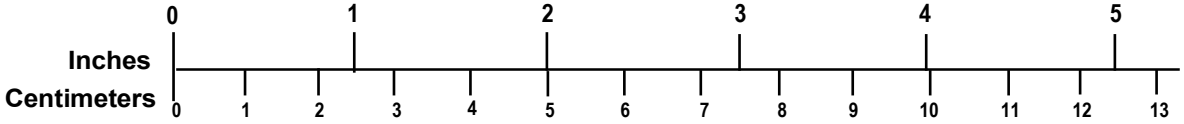

QUICK FAHRENHEIT - CELSIUS TEMPERATURE CONVERSIO

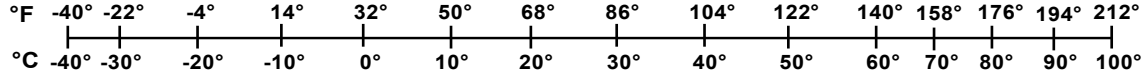

For more exact and or other conversion factors, see NIST Miscellaneous Publication 286, Units of Weights and Measures. Price $2.50 SD Catalog No. C13 10286

Updated 6/17/98

Acknowledgements

The authors appreciate the input from and discussions with the Federal Railroad Administration's Melissa Shurland, and Check Kam. We would also like to acknowledge the Volpe National Transportation Systems Center's Suzanne Horton, Matthew Lyons, Daniel Mannheim, and Bernard J. Kennedy IV for their inputs and discussion on this research topic. We would also like to thank the Naval Research Laboratory for allowing us to use their facilities for the full-scale testing.

Contents

Illustrations

Tables

Executive Summary

The Federal Railroad Administration funded research to conduct a series of compartment fire experiments to validate the scaling laws developed during a previous research effort. From October 1, 2019, to June 30, 2021, Jensen Hughes, Inc. (JH) conducted this work. The focus of this effort was to confirm the capability of the scaling laws to predict full-scale fully-developed compartment fire heat release rates (HRR) based on reduced-scale experiments. Blind simulations of the test series prior to running the experiments were conducted to assist in experiment design, validate the scaling approach, and provide detailed predictions of measured quantities.

JH conducted a total of 17 compartment fire tests in this effort consisting of 14 unique configurations and three repeated tests. Tests were conducted at three scales including full-scale, half-scale, and quarter-scale. The baseline full-scale compartment design was based on a standard size National Fire Protection Agency (NFPA) 286 fire room, which is 8.0 ft. wide (2.44 m), 8.0 ft. tall (2.44 m), and 12.0 ft. (3.66 m) deep with a single door opening which is 3.0 ft. (0.9 m) wide, and 6.6 ft. (2.0 m) tall. The initiating fire was a propane burner in the back-left corner of the compartment. The reduced-scale compartment designs were geometrically scaled except for the ventilation, which was non-linearly scaled to maintain the equivalence ratio, or availability of oxygen, of the compartment. In addition, the lining material thickness was kept the same as the full-scale to preserve the burning duration. The repeated tests were used to better understand the test-to-test variability in fire behavior.

A total of five permutations of the compartment design were evaluated. The first two scenarios were focused on validating the scaling laws with a specified HRR. Two HRR stages were included in the baseline configuration (i.e., non-combustible door configuration), including 5 minutes at a pre-flashover level (i.e., full-scale 320 kW) and 5 minutes at a post-flashover level (i.e., full-scale 640 kW). The second scenario, the non-combustible door-window configuration, added a window at the center of the east wall to evaluate the impact of additional ventilation on the scaling approach. The post-flashover level was increased to ensure flashover with the additional air flow (i.e., full-scale 720 kW).

The other three scenarios were focused on validating the scaling laws with a HRR based on thermal feedback with the fire environment. One scenario used a kerosene-type jet fuel, JP-5, in the same geometric configuration as the non-combustible door configuration but replaced the propane burner with a liquid pool fire. These tests were used to evaluate the capability of the scaling approach to model the growth of liquid fuels across scales. The last two tests replaced parts of the inert wall and ceiling material in the non-combustible door configuration with combustible linings. Two different combustible materials were used: plywood and a fiber-reinforced plastic (FRP). These scenarios were performed to evaluate the scaling approach in predicting the overall HRR for growing fires where flames are spreading across the surface of the interior finish with time.

This research determined that the scaling approach can sufficiently reproduce the thermal environment of the compartment across all scales. This included compartments lined with inert material as well as combustible linings. The plywood tests had nearly identical full-scale equivalent HRR profiles across scales with a 3.8 percent average deviation in HRR and 3.7 percent difference in total heat released while the quarter-scale FRP case under-predicted the

equivalent full-scale HRR by an average of 10.6 percent and the total heat released by 17.6 percent. These results indicate that materials with the addition of fire retardants may not scale as well. While the time-resolved HRRs from the scaling approach may not be perfect with combustible linings, the observed differences are in line with experimental (8 percent) and numerical uncertainty (34 percent) in HRRs (Mcgrattan, K., Hostikka, S., Mcdermott, R. J., Floyd, J., Vanella, M., Weinschenk, C. G., & Overholt, K., J., 2019), and the repeatability of enclosure fire tests conducted at the full-scale with 8–12 percent from (Sundström, B., 1996). These results indicate that the scaling approach presents a cost-effective alternative to full-scale testing. Tests with the liquid pool fire were not easily reproduced from across scales due to not scaling the pool fire effects, which will require additional scaling laws.

The fundamental research presented in this report has been used by the rail and fire science communities. The results were used as a basis to add a scale model testing to determine the HRR of rail cars as an alternative in NFPA 130. In addition, the pre-test simulations conducted in this work led to the development of a new pyrolysis model and its implementation in Fire Dynamics Simulator (FDS). Historic validation of computational fluid dynamics (CFD) fire model predictions of thermal exposure to surfaces from adjacent fires have been limited to small fires (i.e., on the order of 500 kW). The fire environment measured in the larger post-flashover fire tests in this research (i.e., on the order of 5,000 kW) provide a valuable dataset to assist in future validation efforts of CFD fire models such as FDS.

1. Introduction

Mass transit such as rail will need to evolve to meet the increased transportation demand from an increasing global population while also improving energy efficiency and reducing carbon footprint. The Federal Railroad Administration (FRA) published fire safety regulations in 1999 and 2002 in Title 49 Code of Federal Regulations (CFR) Part 238 Section 103 which were intended to establish fundamental safety standards to ensure the safety of passengers and crew in passenger rail cars in the United States (Code of Federal Regulations, 2014). All rail cars ordered on or after September 8, 2000, or placed in service on or after September 9, 2002, as well as rail cars refurbished or overhauled after November 9, 1999, are required to meet this standard. FRA continues to invest in research to further improve passenger safety on rail cars and in railroad stations, and re-evaluate the burden placed on the industry through this rulemaking.

The heat release rate (HRR) time history of a rail car fire is a critical input needed to design smoke control systems for tunnels and stations. FRA previously funded Jensen Hughes, Inc. (JH) to develop a new method to quantify the overall HRR time history of passenger rail cars which includes all stages of the fire (i.e., growth, flashover, fully-developed, and decay) (Yang, F., Hodges, J., Rippe, C., Kraft, S., & Lattimer, B., 2020). In this previous study, JH developed a scaling approach which allows the key physics of the fire behavior to be preserved so that the full-scale burning behavior of a rail car can be predicted from a reduced-scale experiment. This research effort focused on validating these scaling laws using a series of compartment fire experiments at different scales. This report provides an overview of the test series, measurements from each experiment, and quantifies the capability of the reduced-scale experiments to predict the full-scale fire behavior using the scaling approach.

1.1 Background

Research in the U.S. has primarily focused on reducing the flammability and smoke production of combustible materials used on rail cars to improve the fire safety of the rail car. These requirements are included to decrease the severity of the conditions that develop inside a rail car at the early stages of a fire and reduce the likelihood that an incipient fire will cause a rail car to reach flashover conditions. In addition to limiting flammability and smoke production to reduce the likelihood of a rail car reaching untenable conditions, rail systems that include underground stations and tunnels must also include smoke control systems that allow egress of passengers to a point of safety. The design of a smoke control system is typically based on the maximum HRR of a rail car fire, which is a fully-developed fire inside of a rail car. As a result, the rail car HRR time history is a critical consideration to ensure passengers are able to egress out of the rail car and reach a point of safety.

The U.S. conducted limited research on the contribution of materials to the overall HRR of a fully-developed rail car. In addition, standards include limited guidance for railroad equipment owners and rail car manufacturers on considerations for predicting the HRR of fully-developed rail car fires to assist in making material selections. The use of the overall HRR of a rail car is not only used in the design of smoke control systems for new stations and designs, it must also be considered for refurbished or replacement rail cars to ensure that the rail car HRR is within the design limits of the existing smoke control system. In previous design projects, it has been observed that including new materials on replacement rail cars can result in increasing the

overall HRR of the rail car (i.e., despite meeting the flammability requirements) which can affect the performance of the existing smoke control system.

Changes in rail car design and material selection can have a significant impact on the overall HRR profile of a rail car fire. Unfortunately, it is often not feasible to conduct full-scale testing of rail car fires to quantify the HRR due to the high costs associated with the testing. An alternative approach is to conduct a fire test using a scaled down model of a rail car and use the measurements at the reduced-scale to predict the fire behavior at the full-scale. Unfortunately, due to competing scaling requirements, it is not possible to achieve complete similarity between the full-scale and reduced-scale models in fire applications.

Scaling laws are algebraic relationships that describe how to reduce parameters in an experiment to ensure that the full-scale physics are preserved when the test is performed at a smaller scale. Previous work was conducted to develop scaling laws to inform how the geometry and fire parameters should be changed if the physical size of the test is reduced (Yang, F., Hodges, J., Rippe, C., Kraft, S., & Lattimer, B., 2020). Froude modeling is commonly used in fire dynamics to scale fire plumes and buoyancy driven flows. However, Froude modeling does not hold for compartment fires due to the dynamics of the fire being controlled by the ventilation into the room through openings (e.g., doors, windows) and hot gas layer-fuel interactions. As a result, new scaling laws were developed to ensure these physics are being maintained. Using computational fluid dynamics (CFD) fire modeling, simulations were performed on different scaled geometries and fire details. The simulation results demonstrated that the gas temperature magnitude and distribution were well-preserved between scales with noncombustible boundaries for both pre and post-flashover fires. In simulations with combustible boundaries, there were some differences in the overall HRR between scales, possibly due to the smoke layer radiation effects.

This report documents the test series conducted to validate the scaling laws to predict the full-scale HRR time history of a compartment fire based on reduced-scale experiments. The test series utilized a standard size National Fire Protection Association (NFPA) 286 fire room (8.0 ft. wide, 8.0 ft. tall, 12.0 ft deep [2.44 m x 2.44 m x 3.66 m]) with a single door opening (3.0 ft. wide and 6.6 ft. high [0.9 m wide and 2.0 m high]) as well as two scaled compartments (1:2 and 1:4). The scaling laws were able to successfully predict the fire dynamics and material burning behavior across scales in both pre-flashover and fully-developed fires.

1.2 Scope

This research is focused on evaluating the scaling laws for reducing the size of experimental rail cars in testing to predict the HRR history of rail cars. A new set of scaling laws developed during the previous phase of this research, including new scaling for material burning and compartment ventilation, was shown through simulation to scale the HRR. This phase of the research focused on validating the scaling approach using fire experimental data. The capability of the reduced-scale experiments to predict the full-scale behavior was quantified. In addition, measurements from each experiment were documented and available for use in future model validation efforts.

1.3 Overall Approach

The fire testing experiments conducted in this phase of the research used a compartment consistent with the standard size NFPA 286 fire test room (2.44 m wide, 2.44 m high, 3.66 m deep [8.0 ft. x 8.0 ft. x 12.0 ft.]) with a single door opening (0.9 m wide and 2.0 m high [3 ft.

wide and 6.6 ft. high]) as well as two scaled compartments (1:2 and 1:4). Multiple configurations were tested at each scale, including permutations changing from non-combustible to combustible linings, the addition of a window on the east side of the compartment, and changing the initiating fire to a liquid fuel source. Each experiment configuration was simulated using a computer fire model, Fire Dynamics Simulator (FDS), prior to the experiment. These model predictions were used to better design the experiments to validate the scaling laws, provide additional details about the flow field in the compartment, and produce additional validation of the scaling laws.

1.4 Objectives

Quantifying the HRR time history of a rail car fire is a critical part of determining whether passengers can safely egress to a point of safety. Scaling laws, which are algebraic expressions that can be used to reduce the size of experiments while preserving the key physics of the problem, provide a way to reduce the cost to conduct rail car experiments and allow for cost-effective experimental investigations to understand the role of different parameters on the HRR. The objectives of this study were focused on conducting fire experiments to validate the scaling laws developed in the previous phase of this research. The specific objectives to quantify the similarity of the fire behavior across scales with different configurations, document key observations on the capability of the scaling approach observed in the study, and compare the experimental scaling to the numerical scaling.

1.5 Organization of the Report

The report includes a series of five sections. Section 2 provides an overview of the scaling approach developed in phase one of this research. Section 3 presents an overview of the test series. Section 4 presents the predictions from the computer simulations of the test series. The results of the scaling law validation are presented in Section 5 and further discussed in Section 6. Section 7 summarizes the findings from this phase of the research as well as presents the proposed future work. Appendix A provides the test matrix development. Appendix B explains how the compartment is constructed. Appendix C breaks down the processing of the data received. Appendix D presents the pre-test simulation details. Appendix E contains the development of the pyrolysis model. Appendix F provides detailed measurements from each test in the test series. Appendix G summarizes the test series measurements.

2. Scaling Laws

The following sections provide an overview of HRR scaling approaches to predict the full-scale fire behavior of passenger rail car fires presented in the literature (Section 2.1), and an overview of the approach developed in the previous study (Section 2.2).

2.1 Background and Previous Work

Fire dynamics is a complex process involving fluid flow with chemical reactions, reaction of combustible materials, and multi-mode heat transfer. Complete scaling of these processes is not practical due to competing scaling requirements; however, it is often possible to gain insight and sufficient quantitative results using partial scaling (Quintiere, J. G., 1989). The premise of partial scaling is to maintain similarity for key physics while relaxing similarity for less important aspects. Researchers have shown that the behavior of a fully-developed fire is controlled by fuel burning rate, the availability of oxygen/ventilation, and thermal losses (Drysdale, D., 2011a). Partial scaling intended to predict the HRR of fully-developed fires should maintain the similarity of these parameters.

Froude modeling-based scaling has traditionally been used in fire applications (Quintiere, J. G., 1989). Froude modeling focuses on scaling the dynamics of the fire plume (i.e., matching the gas temperature and velocity of the buoyant plume), but relaxes the similarity of the solid boundary (Quintiere, J. G., 1989). Researchers presented an extensive overview of Froude scaling for tunnel and rail car applications (Li, Y. Z., Ingason, H., & Lönnermark, A., 2013). This approach is designed to predict the growth of the initial fire; however, it is difficult to maintain the fuel burning rate and thermal losses necessary to model a fully-developed fire since the similarity of the solid boundary is relaxed. Li et al. (2013) used different materials (i.e., type and thickness) between the model scale and full scale to compensate for this limitation; however, the competing material properties make it difficult to apply this method.

Surface energy-based approaches scale the burning behavior of materials by maintaining the heat release rate per unit area (HRRPUA) of the fuel, but relaxes the similarity of the fire plume (Bullen, M. L., 1976). This scaling approach has been used to predict the pre-flashover conditions in a NFPA 286 room (Bundy, M. F., Hamins, A. P., Johnsson, E. L., Kim, S. C., Ko, G., & Lenhert, D. B., 2007) (Dingyi, H., 1987) (Lee, B. T., 1985). A key advantage of this approach in predicting fully-developed fire conditions is the fuel burning rate and thermal losses are maintained between the model scale and full scale by using the same materials. However, the availability of oxygen does not directly scale in this approach. Researchers have presented a relaxed geometric scaling on the door to maintain the availability of oxygen based on flow work through the door (Bundy, M. F., Hamins, A. P., Johnsson, E. L., Kim, S. C., Ko, G., & Lenhert, D. B., 2007). Bullen (1976) showed this scaling approach can predict gas temperatures and species concentrations from a single gas burner. Lee (1985) and Dingyi (1987) showed this scaling approach can predict the onset of flashover with combustible lining materials.

These studies have not examined the capability of these scaling approaches to predict the conditions of a post-flashover, fully-developed fire. In addition, the models examined in the literature have been limited to a single ventilation source. The scaling methodology proposed by this research would predict the conditions in a fully-developed fire under complex ventilation conditions. The results of this analysis are provided in Section 2.2.

2.2 Overview of Scaling Approach

The scaling approach developed in the previous phase of research by Yang et al. (2020) consisted of direct geometric scaling of the overall dimensions of the compartment and two new scaling laws: material burning scaling and non-linear scaling of ventilation to preserve the fully-developed compartment behavior.

The material burning scaling approach is based on the idea that the HRRPUA due to the material burning must be preserved across scales. This leads to the algebraic scaling relationship for the HRR shown in Equation 1,

$$\frac{\dot{Q}_M}{\dot{Q}_F} = \left(\frac{l_M}{l_F}\right)^2 \qquad \text{Equation 1}$$

where $\dot{Q}$ is the HRR (subscripts M and F correspond to the model scale and full-scale), l_M is the model length scale, and l_F is the full-scale length scale. In addition, the burning duration in this approach scales with the material thickness, according to Equation 2

$$\frac{t_M}{t_F} = \left(\frac{\delta_M}{\delta_F}\right) \qquad \text{Equation 2}$$

where t is the burning duration and δ is the material thickness. As a result, the material thickness must be the same between the model-scale and full-scale (i.e., as opposed to being reduced geometrically) to maintain the burning duration between scales.

The HRRPUA of the material is a function of the thermal feedback from the fire environment. For the thermal exposure to the materials to be the same, the gas temperature and layer depth of the compartment fire must be similar across scales. The gas temperature of a post-flashover compartment fire is driven by the availability of oxygen into the compartment (i.e., to what extent is the compartment over or under-ventilated). Figure 1 demonstrates the difficulty matching the post-flashover gas temperatures when the compartment dimensions and ventilation opening are geometrically scaled.

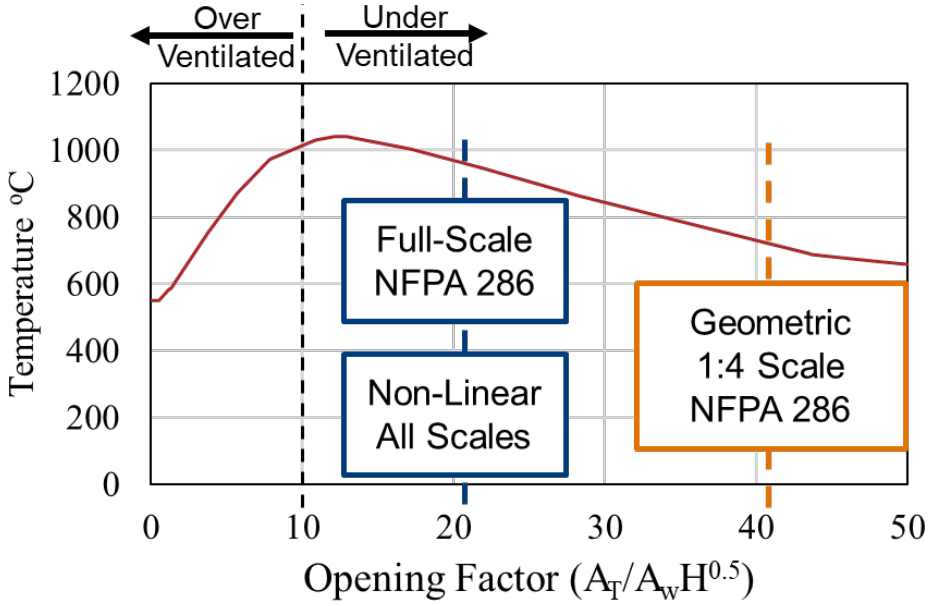

Figure 1: Comparison of post-flashover compartment temperature across scales

As shown in Figure 1, it has been experimentally determined that the gas temperature in a post-flashover fire is a function of the opening factor, which represents the ratio of the heat loss to the internal surfaces of the compartment and the HRR possible through the air entering the compartment. The opening factor scales with the compartment and ventilation geometry as:

$$\frac{l_M^2}{\left(W_M H_M^{3/2}\right)} = \frac{l_F^2}{\left(W_F H_F^{3/2}\right)} \quad \text{Equation 3}$$

Unfortunately, Equation 3 is not satisfied in direct geometric scaling. Thus, the size of the ventilation opening must be scaled differently between the full-scale and model-scale to maintain the post-flashover gas temperature. A scaling law for the ventilation height, H, can be defined as shown in Equation 4:

$$\frac{H_M}{H_F} = \left(\frac{l_M}{l_F}\right)^a \quad \text{Equation 4}$$

and for the ventilation width, W, as in Equation 5

$$\frac{W_M}{W_F} = \left(\frac{l_M}{l_F}\right)^b \quad \text{Equation 5}$$

where the coefficients a and b can be related through Equation 3 as Equation 6

$$b = 2 - \frac{3}{2}a \quad \text{Equation 6}$$

The results of the previous phase of this research showed it was preferable to increase the height of the ventilation and maintain the width to maximize the velocity at the opening. However, for large aspect ratio openings (e.g., doors) it is often not possible to scale the height enough to maintain the post-flashover behavior without also scaling the width due to the height of the ceiling. The maximum a can be calculated using Equation 7.

$$a_{max} = 1 - \frac{\ln\left(H_F/H_{F,max}\right)}{\ln\left(l_M/l_F\right)} \quad \text{Equation 7}$$

where $H_{F,\,max}$ is the ceiling height inside the compartment adjacent to the opening. Thus, the following procedure was proposed to scale each ventilation path:

- Determine a' with an assumed $b = 1$ in Equation 6
- Determine a_{max} based on Equation 7 based on the specific geometry and desired scaling ratio
- Calculate b using Equation 6 with $a = \max(a', a_{max})$
- Calculate opening height and width using Equation 4 and Equation 5

In the previous phase of this research (Yang, F., Hodges, J., Rippe, C., Kraft, S., & Lattimer, B., 2020), this scaling approach was shown through simulation to provide gas temperatures at the full and reduced scales that were within 10 percent for various flow conditions.

3. Experiment Configuration

A series of compartment fire tests were conducted for the purpose of developing a set of data to validate scaling laws to predict full-scale fire behavior from small-scale experiments. The baseline geometry of the full-scale compartment is consistent with the standard fire test compartment used in ISO 9705-1 (International Organizations for Standarization, 1993), NFPA 286 (National Fire Protection Association, 2015), UL 1715 (American National Standards Institute, 2017), ASTM E2257 (ASTM International, 2017), and others. The overall dimensions of the full-scale fire room are 8.0 ft x 8.0 ft x 12.0 ft (2.44 m x 2.44 m x 3.66 m) with a single door opening which is 3.0 ft wide x 6.6 ft high (i.e., 0.9 m wide x 2.0 m high). The initiating fire was placed in the back-left corner with respect to the door for each configuration. Similar experiments were conducted using two scaled compartments (i.e., 1:2 and 1:4) which were scaled according to the scaling laws described in Section 2.2. The research team performed the reduced-scale experiments at the JH fire laboratory in Baltimore, MD, and conducted the full-scale experiments at the Chesapeake Bay Detachment (CBD) facility in Chesapeake Bay, MD.

The following subsections describe the specific tests conducted in this study as well as provide an overview of the compartment design, instrumentation, and test procedure. In addition, the data quantifying the fire environment at each scale are also presented.

3.1 Overview of Test Series

Five configurations were tested at three length scales to evaluate the capability of the scaling approach to model the fire behavior under different configurations. Table 1 provides an overview of the test series. The following discussion highlights the motivation behind each test in the series.

Two of the configurations focused on validating the scaling laws were able to capture the fire behavior of the compartment with a prescribed HRR using a propane gas burner. These scenarios were performed with a non-combustible lining with a single door opening (e.g., Tests 1, 6, and 11) and with a single door and a window opening on one side wall (e.g., Tests 2, 7, and 12). The addition of the window was performed to assess the scaling approach to predict the fire behavior with a ventilation configuration more representative of a rail car. In both configurations, the pre-flashover HRR was maintained for 5 minutes, then the HRR was increased to the post-flashover HRR for an additional 5 minutes. In a subsect of tests (e.g., Tests 2 and 7) a third, higher HRR stage was added to evaluate the impact of a more ventilation limited fire on the results. The additional third stage was added to account for uncertainties in the empirical relationship used to determine the HRR required for post-flashover with multiple ventilation paths. The HRR for the post-flashover fires were 640 kW for the non-combustible door configuration and 720 kW for the door-window configuration. The pre-flashover HRR was selected to be 320 kW for both the door and door-window configuration to allow comparison of this stage across configurations. Appendix A provides details regarding the selection of the HRR for each stage.

The propane initiating fires used square propane sand burners. The size of the burner (i.e., side length) for the full-scale, half-scale, and quarter-scale tests was 24 in. (0.61 m), 12 in. (0.30 m), and 6 in. (0.15 m), respectively. The fire was fixed at the lower, pre-flashover HRR for 5 minutes and then increased to the higher, flashover causing HRR for an additional 5 minutes for a total test duration of 10 minutes.

Table 1. Test matrix

Test No.	Scale	Lining Material	Target Fire (kW)	Actual Fire (kW)	Ventilation	Fuel Type
1[a]	Quarter	NC	20/40[b]	20/40	Door	Propane
2	Quarter	NC	20/45/50[b]	20/45/50	Door + Window	Propane
3	Quarter	NC	21/38[c]	20/60 [c]	Door	JP-5
4	Quarter	Plywood	40/125[d]	40/113	Door	Propane
5	Quarter	FRP	40/125[d]	40/87[d]	Door	Propane
6	Half	NC	80/160[b]	80/160	Door	Propane
7[a]	Half	NC	80/180/360[b]	80/180/200	Door + Window	Propane
8	Half	NC	106/163[c]	60/110[c]	Door	JP-5
9	Half	Plywood	160/500[d]	160/466	Door	Propane
10	Half	FRP	160/500[d]	160/400	Door	Propane
11	Full	NC	320/640[b]	720/1430	Door	Propane
12[a]	Full	NC	320/720[b]	720/1610	Door + Window	Propane
13	Full	NC	505/697[c]	-[e]	Door	JP-5
14	Full	Plywood	640/2,000[d]	1,430/5,500[f]	Door	Propane
15	Full	FRP	640/2,000[d]	1,430/4,500[f]	Door	Propane

[a] The test was conducted twice.

[b] The propane burner fires were held at each HRR for 5 minutes and then increased to the next HRR stage. Most of the tests used two stages designed to capture pre-flashover and post-flashover conditions. Tests 2 and 7 used three stages to evaluate the impact of higher ventilation limitation on the results.

[c] The JP-5 pool fire HRR was time-varying; the value provided is the estimated HRR during the pre and post-flashover portion of the fire. The amount of fuel in the pan was calculated to provide a fire duration of approximately 10 minutes with a 5-minute post-flashover fire.

[d] The tests with combustible lining used a steady propane burner as a fuel source. The first number corresponds to the burner HRR and the second corresponds to the peak HRR (e.g., burner and linings).

[e] Due to difficulties achieving the desired HRR from the liquid JP-5 fires, Test 13 was replaced with a repeat of Test 12.

[f] HHR was higher than target due to an issue with calibration scaling and the mass flow meter.

The other three configurations focused on validating the scaling laws when the overall HRR was dependent on the feedback between combustibles and the fire environment. The first of these configurations was similar to the non-combustible door configuration but replaced the propane gas burner with a liquid pool fire (e.g., Tests 3 and 8). The focus of this scenario was two-fold:

1. To evaluate the impact of feedback between the room environment and the liquid pool on the scaling approach.
2. To evaluate the impact of higher soot yield (smoke generation) on the scaling approach.

The size and depth of the liquid pool was designed to provide a similar peak HRR and burning duration to the gas burner experiments. The size of the burner and depth of liquid at each scale is summarized in Table 2. The burner side length at each scale was: 1:4 scale 6.5 in (0.17 m), 1:2 scale 12 in (0.30 m), 1:1 scale 22 in (0.56 m). The predicted HRR at each scale was: 1:4 scale pre-flashover 21 kW post-flashover 38 kW, 1:2 scale pre-flashover 106 kW post-flashover 163 kW, and 1:1 scale pre-flashover 505 kW post-flashover 697 kW. The depth of the liquid pool at each scale was 1:4 scale 0.75 in (18.8 mm), 1:2 scale 0.98 in (25.0 mm), 1:1 scale 1.31 in (33.2 mm). Additional details regarding the selection of the pan size and liquid depth are provided in

Appendix A. Due to difficulties achieving the desired HRR from the liquid JP-5 fires, the full-scale liquid pool experiment (Test 13) was replaced with a repeat of the door-window configuration (Test 12).

Table 2: Liquid pool summary

Scale	Side Length, in (m)	Liquid Depth, in (mm)	Pre-flashover HRR, kW	Post-flashover HRR, kW
1:1	22 (0.56)	1.31 (33.2)	505	697
1:2	12 (0.30)	0.98 (25.0)	106	163
1:4	6.5 (0.17)	0.75 (18.8)	21	38

The last two configurations used the propane burner at its second stage HRR as an initiating fire, but replaced the non-combustible lining with combustible linings. The focus of these two scenarios was to assess the effect of combustible boundaries on the overall HRR across scales. The two materials were selected to have different ignition properties. The plywood case (i.e., Tests 4, 9, and 14) represented a combustible material without fire retardants, while the FRP case (i.e., Tests 5, 10, and 15) represented a less combustible material containing fire retardants resulting in a lower HRRPUA compared with plywood. Material and fire property data were measured for each combustible material in the previous phase of this research (Luo, C., et al., 2019).

The total area covered by each lining material was calculated to limit the maximum HRR in the test so that post-flashover conditions could be maintained without requiring suppression. The coverage of the combustible lining test series is shown in Figure 2 and Figure 3. The FRP composite material tests lined the complete back wall, the back 8.0 ft (2.4 m) of the left wall (i.e., not containing the window), and the back 8.0 ft (2.4 m) of the ceiling. This is also consistent with the methodology of UL 1715 (American National Standards Institute, 2017). The plywood material tests lined the left 4.0 ft (1.2 m) of the back wall, the back 4.0 ft (1.2 m) of the left wall, and the back 4.0 ft (1.2 m) of the ceiling. Note, these dimensions are for the full-scale experiments and were reduced geometrically for the reduced-scale experiments. The plywood lining material was 0.25 in. (6.4 mm) thick, while the FRP composite material was 0.125 in. (3.2 mm) thick.

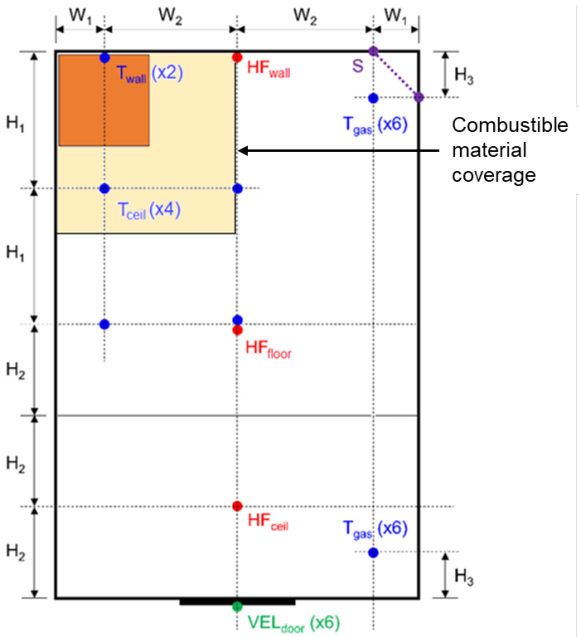

Figure 2: Plywood combustible lining coverage

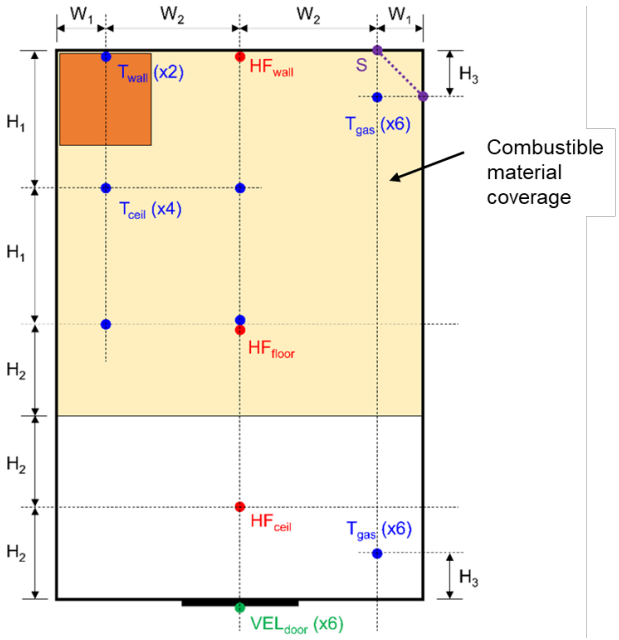

Figure 3: FRP combustible lining coverage

3.2 Compartment Construction

3.2.1 Full-Scale Tests

Figure 4 shows diagrams showing compartment dimensions and construction used in the full-scale testing. Note that these dimensions refer to the interior dimensions of the compartment with the lining materials in place.

The compartment was constructed on a wood framed support system using 2 x 4 SPF lumber as shown in Figure 5. The figure shows the frame being supported on posts; however, in this test series the compartment was constructed on a subfloor of 2 x 6 SPF lumber. The top of the subfloor (i.e., the inside of the compartment) was covered by layers of 0.72 in. (18.3 mm) thick plywood (fastened to the studs using wood screws), 0.63 in. (15.9 mm) thick United States Gypsum Corporation (USG) Firecode (Type X) gypsum wallboard, and 0.5 in. (12.7 mm) thick USG Durock cement board. The propane gas burner was built into the subfloor such that the top of the burner was located 12 in. (0.30 m) above the compartment floor.

Sheet materials were affixed to the inside walls and ceiling of the framing in the following order (i.e., from outside-to-inside): 0.72 in. (18.3 mm) thick plywood, 0.63 in. (15.9 mm) thick USG Firecode (Type X) gypsum wallboard, and 0.5 in. (12.7 mm) thick USG Durock cement board. In the combustible lining test series, the lining materials were directly affixed to the cement board lining of the compartment interior. Additional detail on the compartment construction is provided in Appendix B.

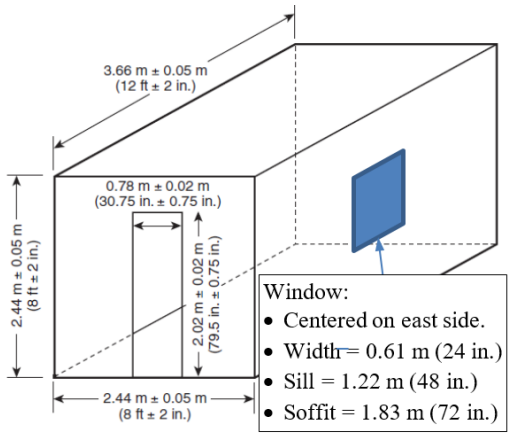

Figure 4: Interior dimensions of the compartment (full-scale)
(National Fire Protection Association, 2015)

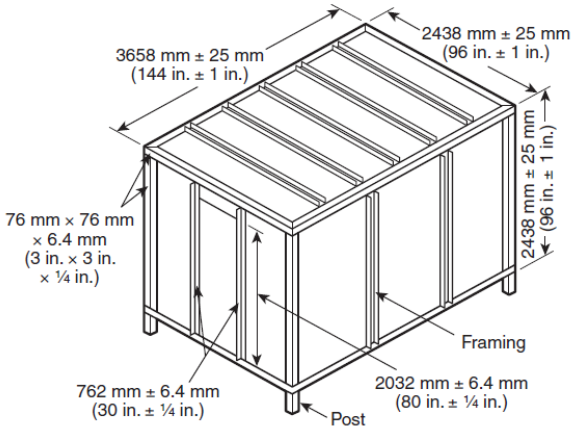

Figure 5: Frame support system (full-scale)
(National Fire Protection Association, 2015)

The condition of non-combustible lining materials was assessed after each test. Failing noncombustible materials (i.e., cracking and/or falling apart) were replaced as needed prior to additional testing. The remains of combustible lining materials were removed after the test once the compartment had adequately cooled.

3.2.2 Half-Scale and Quarter-Scale Tests

The compartment geometry for half-scale and quarter-scale tests was scaled down from the full-scale test using the scaling approach described in Section 2.2; refer to Table 3 (SI units) and Table 4 (USC units) for dimensions and tolerances. The door and window widths were scaled non-linearly to maintain the opening factor between the full and model scales based on the scaling laws described in Section 2.2. Note that the sill and soffit of the window were scaled geometrically and only the width non-linearly scaled to maintain airflow. This slight modification of the scaling approach presented in Section 2.2 was used so that the door and window would be using the same scaling approach.

While the overall compartment size was reduced, the thickness of framing and lining materials was unchanged at these scales. Lining materials were affixed using the same methods; however, the size and spacing of wood screws and diameter of fender washers were scaled down, accordingly. The location of the top surface of the burners above the floor was scaled geometrically, corresponding to 6.0 in. (0.15 m) and 3.0 in. (0.08 m) in the half-scale and quarter-scale tests, respectively.

Two images showing the general compartment configuration of the quarter-scale compartment prior to the start of the non-combustible door experiment are provided in Figure 6. Two images of the half-scale compartment during the non-combustible door-window experiment are provided in Figure 7.

Table 3: Interior dimensions of compartment and openings at all test scales (SI units)

	Compartment			Door		Window		
Scale	Length (m)	Width (m)	Height (m)	Width (m)	Height (m)	Width (m)	Sill (m)	Soffit (m)
Full	3.66 (±0.05)	2.44 (±0.05)	2.44 (±0.05)	0.78 (±0.02)	2.02 (±0.02)	0.61 (±0.02)	1.22 (±0.02)	1.83 (±0.02)
Half	1.83 (±0.02)	1.22 (±0.02)	1.22 (±0.02)	0.55 (±0.01)	1.01 (±0.01)	0.42 (±0.01)	0.61 (±0.01)	0.91 (±0.01)
Quarter	0.91 (±0.01)	0.61 (±0.01)	0.61 (±0.01)	0.39 (±0.01)	0.50 (±0.01)	0.30 (±0.01)	0.30 (±0.01)	0.46 (±0.01)

Table 4: Interior dimensions of compartment and openings at all test scales (USC units)

	Compartment			Door		Window		
Scale	Length (m)	Width (m)	Height (m)	Width (m)	Height (m)	Width (m)	Sill (m)	Soffit (m)
Full	144 (±2)	96 (±2)	96 (±2)	30-3/4 (±3/4)	79-1/2 (±3/4)	23-5/8 (±3/4)	48 (±3/4)	72 (±3/4)
Half	72 (±1)	48 (±1)	48 (±1)	21-3/4 (±3/8)	39-3/4 (±3/8)	16-3/4 (±3/8)	24 (±3/8)	36 (±3/8)
Quarter	36 (±1/2)	24 (±1/2)	24 (±1/2)	15-3/8 (±3/16)	19-7/8 (±3/16)	11-7/8 (±3/16)	12 (±3/16)	18 (±3/16)

(a) Exterior of compartment **(b) Interior of compartment**

Figure 6: Quarter-scale compartment prior to start of non-combustible door configuration (before installation of bi-directional velocity probe [BDVP])

(a) Front-view **(b) Side-view**

Figure 7: Half-scale compartment during testing of non-combustible door-window configuration

These details of the compartment setup beneath the exhaust hood are depicted in Figure 8 through Figure 10. The compartments were supported on an identical subfloor as that of the full-scale tests. Each compartment was elevated 8 in. (0.20 m) above the subfloor by placing the compartment on top of concrete masonry units (CMUs). The reduced-scale compartments were placed on to a steel scaffold located under the 10 ft by 10 ft exhaust hood. A small extension constructed of non-combustible cement board, 24 in. (0.61 m) long for half-scale and 12 in. (0.30 m) long for quarter-scale, was installed at the front of the compartment to simulate the presence of the floor in front of the door and window in the full-scale compartment. Each compartment

was elevated such that the top of the compartment was approximately 6 in. (0.15 m) below the bottom of the skirts of the hood, and the doorway was aligned with the center of the hood duct. Additional skirt extensions were installed on all four sides of the hood to ensure that all combustion gases were captured by the calorimetry system. Noncombustible welding blanket was used as hood skirt extensions and were extended to be even with the bottom of the window.

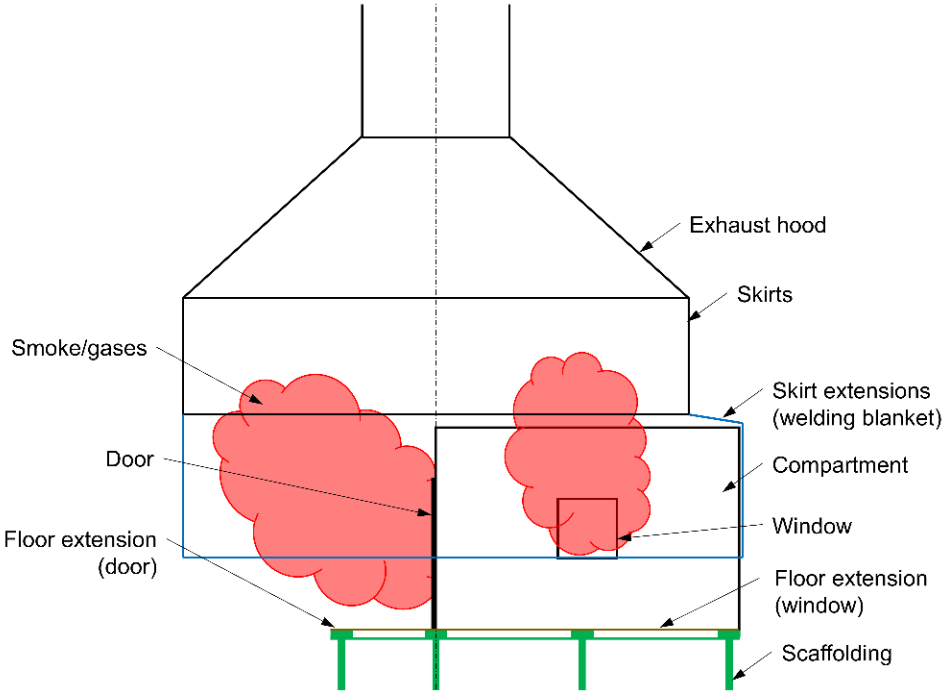

Figure 8: Orientation of compartment under hood for half-scale tests at JH lab (front view)

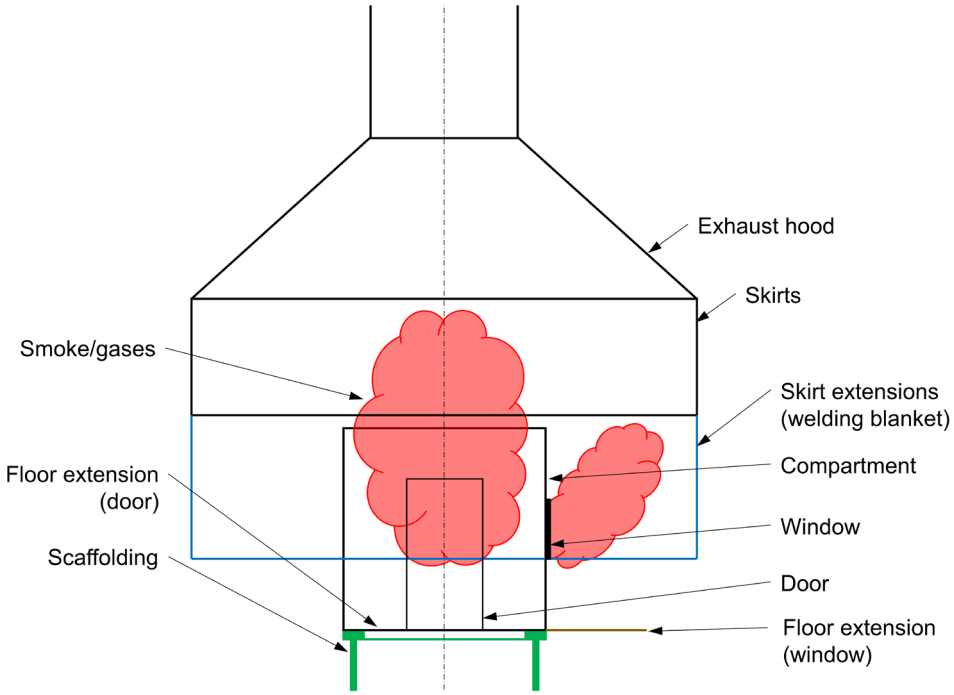

Figure 9: Orientation of compartment under hood for half-scale tests at JH lab (side view)

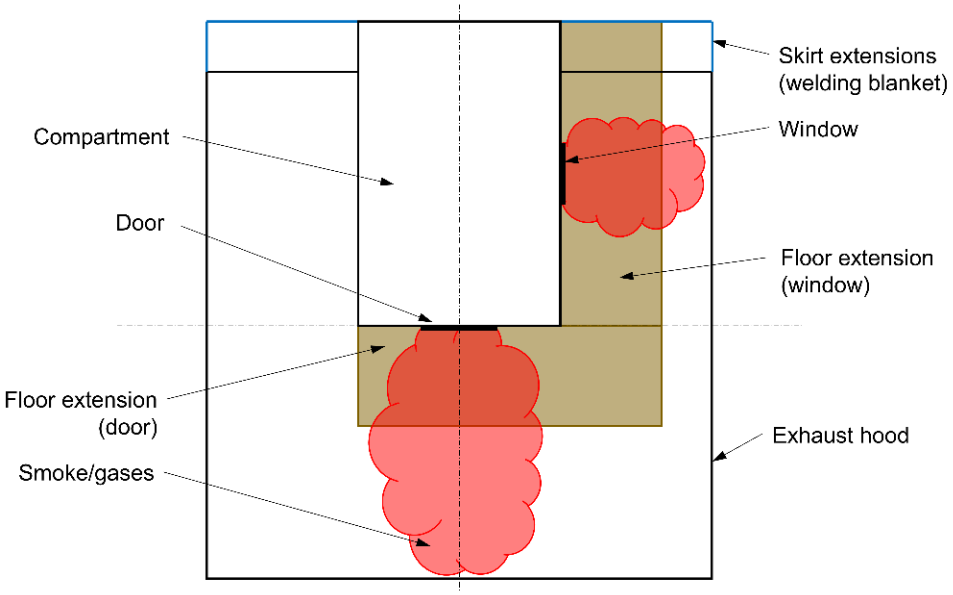

Figure 10: Orientation of compartment under hood for half-scale tests at JH lab (top view)

3.3 Instrumentation

Each compartment was instrumented to measure gas temperatures, heat flux, velocity, and optical density. A top-view schematic indicating the position of each instrument is shown in Figure 11. Detailed measurements of the variables in Figure 11 at each scale are provided in Table 5. A front-view schematic indicating the height of each instrument is shown in Figure 12. Detailed heights of the thermocouple trees shown in Figure 12 are provided in Table 6.

Additionally, instrumentation for oxygen consumption calorimetry was present in the exhaust duct. Additional details are provided in the following sections.

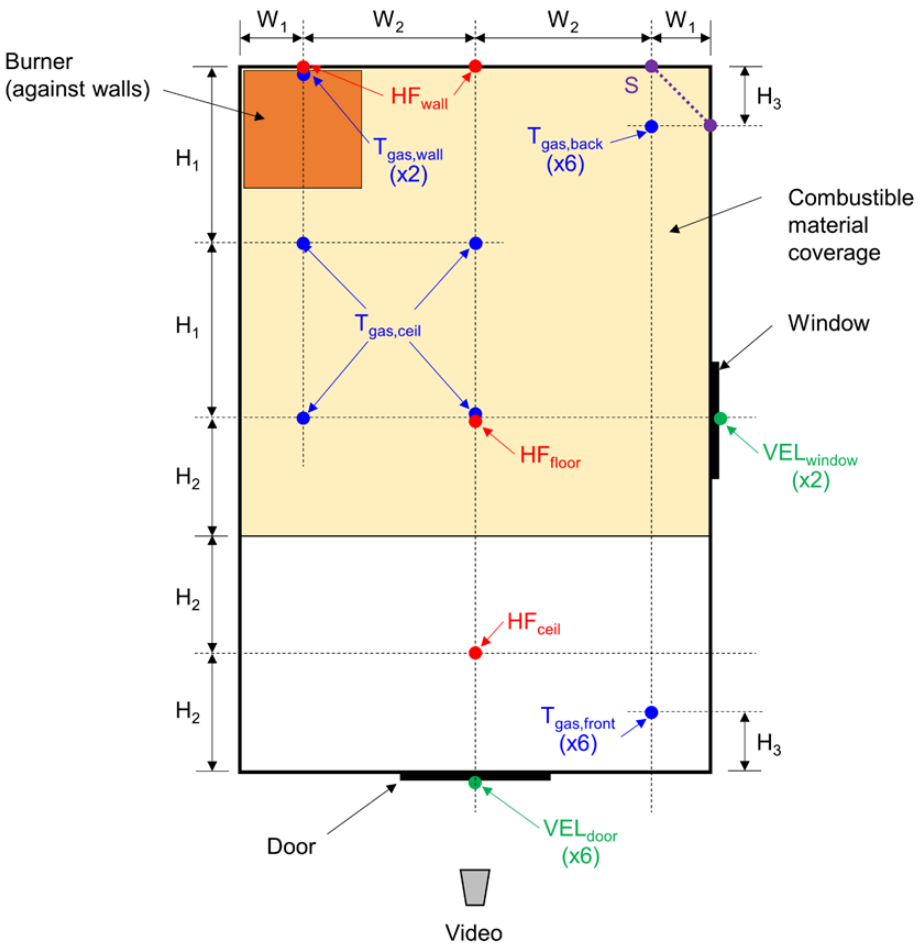

Figure 11: Overall compartment instrumentation plan

Table 5: Dimensions for overall instrumentation schematic

		W_1		W_2		H_1		H_2		H_3
Scale	(m)	(in.)	(m)	(in.)	(m)	(in.)	(m)	(in.)	(m)	(in.)
Full	0.30	12	0.91	24	0.91	36	0.61	24	0.30	12
Half	0.15	6	0.46	12	0.46	18	0.30	12	0.15	6
Quarter	0.08	3	0.23	6	0.23	9	0.15	6	0.08	3

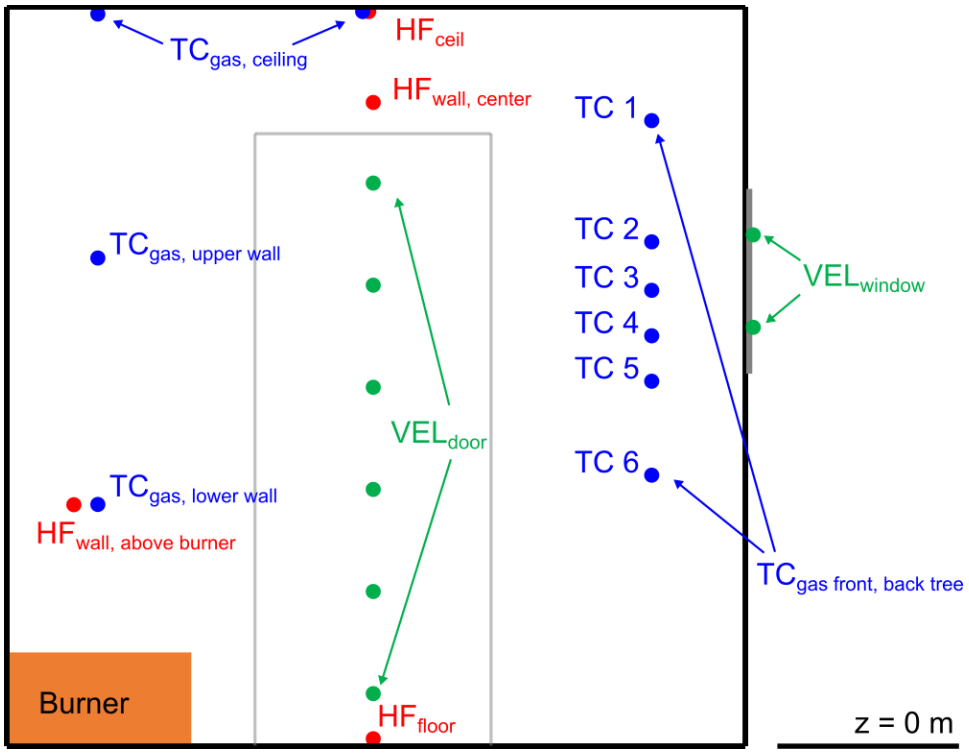

Figure 12: Front-view of compartment showing vertical location of sensors

Table 6: Thermocouple tree height positions to be used in this test series

		TC 1		TC 2		TC 3		TC 4		TC 5		TC 6
Scale	(m)	(in.)	(m)	(in.)	(m)	(in.)	(m)	(in.)	(m)	(in.)	(m)	(in.)
Full	2.08	82	1.68	66	1.52	60	1.37	54	1.22	48	0.91	36
Half	1.04	41	0.84	33	0.76	30	0.69	27	0.61	24	0.46	18
Quarter	0.52	20 1/2	0.42	16 1/2	0.38	15	0.34	13 1/2	0.30	12	0.23	9

3.3.1 Heat Release Rate Measurements

The propane mass flow rate to the sand burner was regulated using an Alicat MCR-500SLPM-D/5M mass flow controller calibrated for propane. The HRR of the propane from the sand burner was recorded throughout testing.

In addition, the overall HRR for the test (i.e., source fire and combustibles) was quantified using oxygen consumption calorimetry from measurements in the exhaust duct. Duct mass flow rate was determined from measurements of velocity and gas temperature (i.e., via bidirectional probe, differential pressure transducer, and thermocouple) in the exhaust duct. A gas sampling pump was used to draw gases from a probe located in the duct through particulate filters, desiccant, and a cold trap, and into O_2 (Servomex MultiExact 4100) and CO/CO_2 (Servomex Multigas 4900) gas analyzers. The flow of CO and CO_2 were set to 0.5 L/min via rotameter, and flow of O_2 was set to 0.5 L/min via mass flow controller. The HRR was calculated using oxygen consumption calorimetry in accordance with ISO 9705.

3.3.2 Gas Temperature Measurements

Gas temperatures were measured in two corners of the compartment at six different elevations. The heights of the thermocouples (TC) above the floor of the compartment were selected to quantify the upper layer temperature and resolve the interface height. The vertical position of each sensor was geometrically scaled, with the positions at each scale provided in Figure 12. Each of these "thermocouple trees" consisted of six TCs attached to steel chains using steel tie wire. TCs were fabricated from Inconel over-braided, K-type, ceramic fiber sheathed, 24 gauge thermocouple wire.

In addition to the two corner thermocouple trees, six additional TCs were located at key points of interest in the compartment. A total of four TCs were located at ceiling-level as shown in Figure 11. These TCs protruded through the ceiling into the compartment no more than 1 in. (25.4 mm) for full-scale tests, 0.5 in. (12.7 mm) for half-scale tests, and 0.25 in. (6.4 mm) for quarter-scale tests. These TCs were also K-type, 3.2 mm (0.125 in.) Inconel-sheathed, 24 gauge, with an exposed bead hot junction. Two TCs were located on the back wall of the compartment, centered with the burner, protruding from the wall by the same amounts as those protruding from the ceiling. These two TCs were positioned at 1/3 and 2/3 of the compartment height.

3.3.3 Heat Flux Measurements

Heat flux was measured at four locations, as indicated in Figure 11. The heat flux gauge at the center of the back wall was positioned below the ceiling by 0.61 m (12 in.) for full-scale tests, 0.30 m (6 in.) for half-scale tests, and 0.15 m (3 in.) for quarter-scale tests. The heat flux gauge above the burner was positioned at 1/3 height. The heat flux gauges used in this testing were Schmidt-Boelter type (Medtherm Series 64). These gauges measure total heat flux and are water cooled. Water cooling was achieved by connecting the inlet and outlet sides of all gauges into respective inlet and outlet brass manifolds. The inlet manifold was supplied by warm water, and the outlet manifold was drained outside or to a nearby drain. The water temperature to each gauge was controlled for consistent measurements and the outlet water temperature was monitored for each gauge to verify in accordance with instrument calibration.

The uncertainty in heat flux measurements increases as the total operating range of the heat flux gauge increases. Thus, the highest accuracy measurements will be achieved by using the lowest rated gauge which is not exceeded during testing. The two gauges on the back wall and ceiling were expected to be flame-impinged in some scenarios and 200 kW/m^2 rated gauges were used in those locations. A 100 kW/m^2 rated gauge was used for the ceiling heat flux gauge since direct flame-impingement was not expected, but the high temperatures in the gas layer were expected to exceed 50 kW/m^2. A 50 kW/m^2 gauge was used at the floor since the heat fluxes were not expected to exceed this threshold.

3.3.4 Velocity Measurements at Compartment Door and Window

Velocity profiles were measured at each ventilation opening of the compartment using BDVP, differential pressure transducers (DPTs), and gas TCs. BDVPs were manufactured to the size recommended by Tanaka (Tanaka, T., 2016), as shown in Figure 13, using 316L stainless steel. Probes were manufactured using the direct metal laser sintering process. The flow coefficient for this probe, generally taken to be 1.08, was verified by a test conducted in a flow-straightened duct relative to a hot-wire anemometer.

BDVPs were distributed vertically along the compartment as shown below in Figure 14 (door) and Figure 15 (window). Detailed heights of positions shown in Figure 14 (door) and Figure 15 (window) are provided in Table 7 and Table 8, respectively. Six probes were at the door, and two probes were at the window. Probes were centered along the vertical centerline of the openings. A thermocouple was co-located at each BDVP location, with the hot junction positioned approximately 6 mm (0.25 in.) above the BDVP probe. BDVP probe tubes were extended along the side of the compartment using additional lengths of stainless steel tubing and compression fittings. The probes and tube extensions were supported using metal brackets along the side of the compartment. These brackets fixed the probe orientation, ensuring each probe remained parallel to the direction of flow, and minimized shifting of the probes and tubing during testing.

DPTs were positioned at the same elevation as each BDVP and connected to the stainless steel tubing using flexible silicone tubing and barb fittings. DPTs were covered by ceramic fiber insulation to avoid heat exposure during tests. The pressure transducers used in this testing were MKS Baratron 223BD models, which have a range of +/- 25 Pa, accuracy of +/- 0.5 percent FS, resolution of 0.01 percent FS, a temperature coefficient of 0.10 percent of FS per °C on zero, and a temperature coefficient of 0.04 percent of reading per °C on span. Transducers were re-calibrated prior to testing.

TCs were co-located at the BDVP location and were K-type, 3.2 mm (0.125 in.) Inconel-sheathed, 24 ga, exposed bead, with a 24-inch length terminating in a quick-connect. At the termination point TCs were connected to glass fiber sheathed TC extensions. The quick-connect junction was protected by a ceramic fiber blanket.

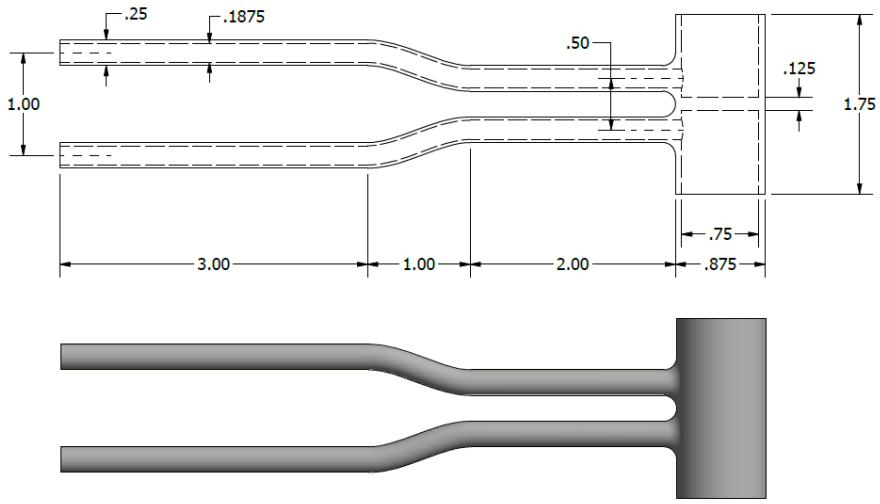

Figure 13: Bidirectional velocity probe schematic (dimensions in inches, 1 in. = 25.4 mm)

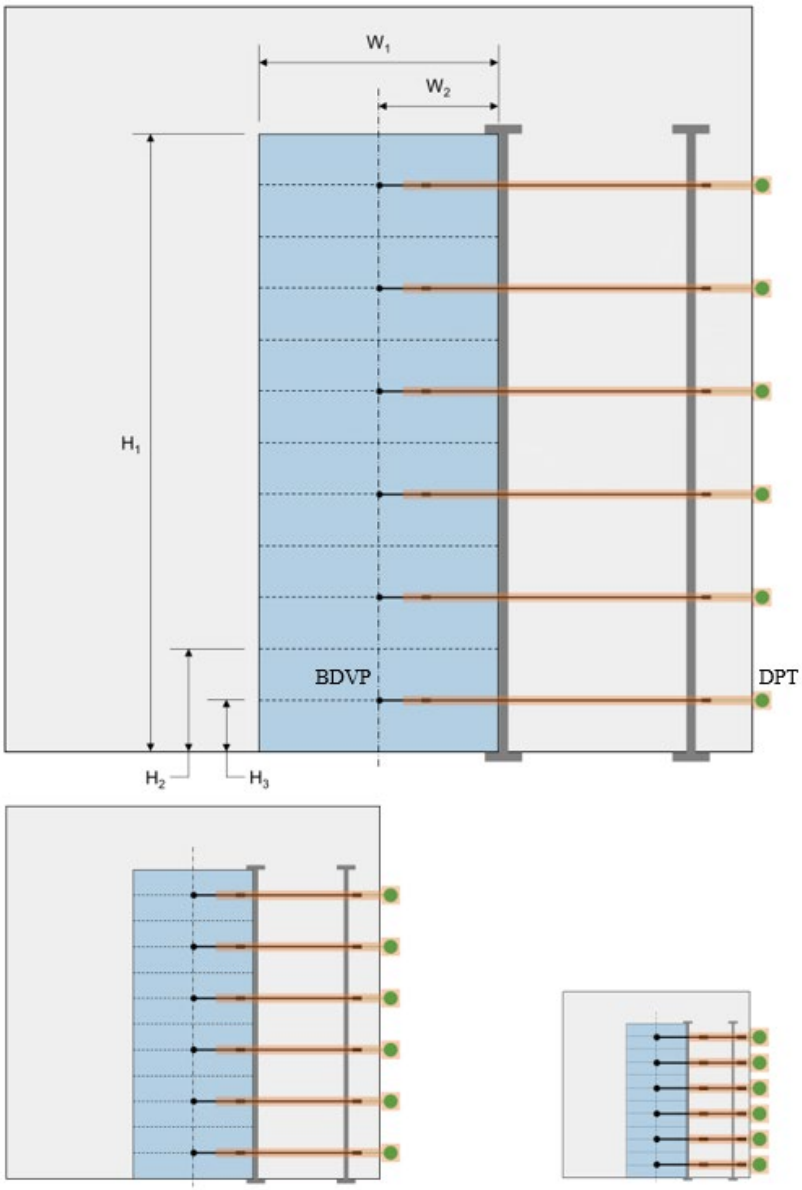

Figure 14: Door BDVP and DPT configuration for full-scale, half-scale, and quarter-scale tests

Table 7: Dimensions for door BDVP spacing

		W_1		W_2		H_1		H_2		H_3
Scale	(mm)	(in.)	(mm)	(in.)	(mm)	(in.)	(mm)	(in.)	(mm)	(in.)
Full	781	30 3/4	391	15 3/8	2019	79 1/2	337	13 1/4	168	6 5/8
Half	391	15 3/8	195	7 11/16	1010	39 3/4	168	6 5/8	84	3 5/16
Quarter	195	7 11/16	98	3 27/32	505	19 7/8	84	3 5/16	42	1 21/32

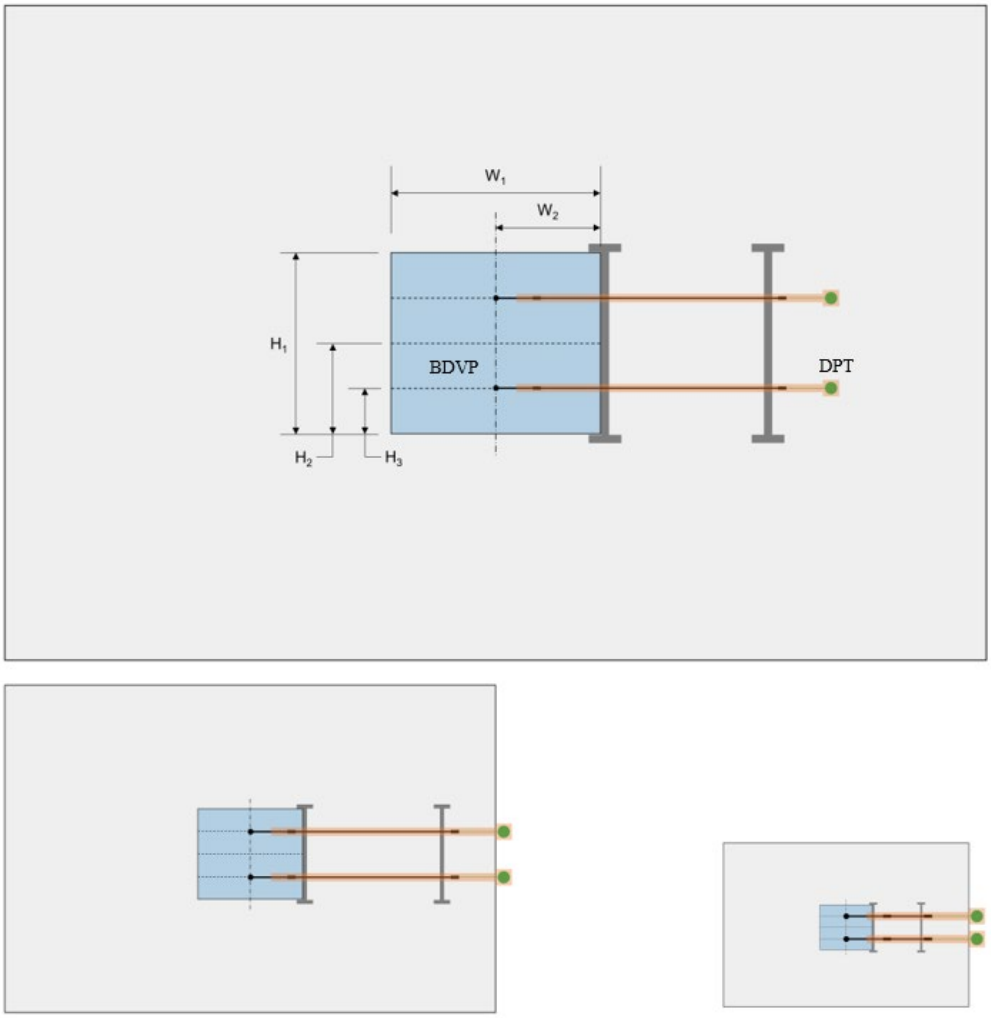

Figure 15: Window BDVP and DPT configuration for full-scale, half-scale, and quarter-scale tests

Table 8: Dimensions for window BDVP spacing

		W_1		W_2		H_1		H_2		H_3
Scale	(mm)	(in.)	(mm)	(in.)	(mm)	(in.)	(mm)	(in.)	(mm)	(in.)
Full	610	24	305	12	610	24	305	12	152	6
Half	305	12	152	6	305	12	152	6	76	3
Quarter	152	6	76	3	152	6	76	3	38	1 1/2

3.3.5 Optical Density Measurements

Optical transmission was measured across a path length in the exhaust duct to quantify the concentration of soot. A Thorlabs HNLS008R Helium-Neon laser (i.e., 632.8 nm, 0.8 mW, randomly polarized) and PDA36A2 photodetector (i.e., 350–1,100 nm, 12 MHz bandwidth, 13 mm^2 active area) were used. An external tube was installed on both sides of the laser path and included holes and a tap for a Nitrogen purge. Nitrogen was connected to each tube using Tygon tubing.

3.4 Data Processing

Additional processing of raw measurements was required to calculate the gas velocities, duct mass flow rates, remove the transport time between sensors and changes in the physical system, and calculate the HRR from calorimetry.

Gas velocities through the door and window were calculated based on the measured temperatures and differential pressure at each bidirectional probe location using the ideal gas properties of air. Duct mass flow rates in the exhaust hood at JH were calculated using measured temperatures and differential pressure within the exhaust hood as well as the duct flow coefficient determined for a range of flow rates. Duct mass flow rates in the exhaust hood at CBD were calculated based on ASTM E2067 recommendations for bidirectional probe measurements (ASTM International, 2016). The flow C-factor was determined through calorimetry with a calibrated propane flow.

A propane burner test using the "apparent response" methodology determined the transport time for each sensor (i.e., duct temperatures and bidirectional velocity probes and gas analyzers). HHR, total heat release, smoke production rate, total smoke production, and CO, CO_2, and soot yields were calculated from duct measurements (e.g., gas composition, light obscuration, duct temperature, duct BDVP differential pressure) in accordance with the methodology laid out in ISO 9705, Annex E (International Organizations for Standarization, 1993). Additional details on the post-processing of sensor data are provided in Appendix C.

During a compartment fire, hot combustion gases collect in the upper space of the enclosure due to the high temperatures of the smoke resulting in a buoyantly stable smoke layer. Ambient air enters the lower space of the room through ventilation, leading to a lower layer which is generally cooler and less dense than the smoke layer. The interface between these two layers is often called the interface height. An example of this phenomena from a CFD model of a compartment fire is shown in Figure 16. The thermocouple tree measurements in the north-east and south-east corners of the compartment were used to evaluate the upper- and lower-layer temperatures and interface height for comparison across scales. Additional details on this calculation are provided in Appendix C.

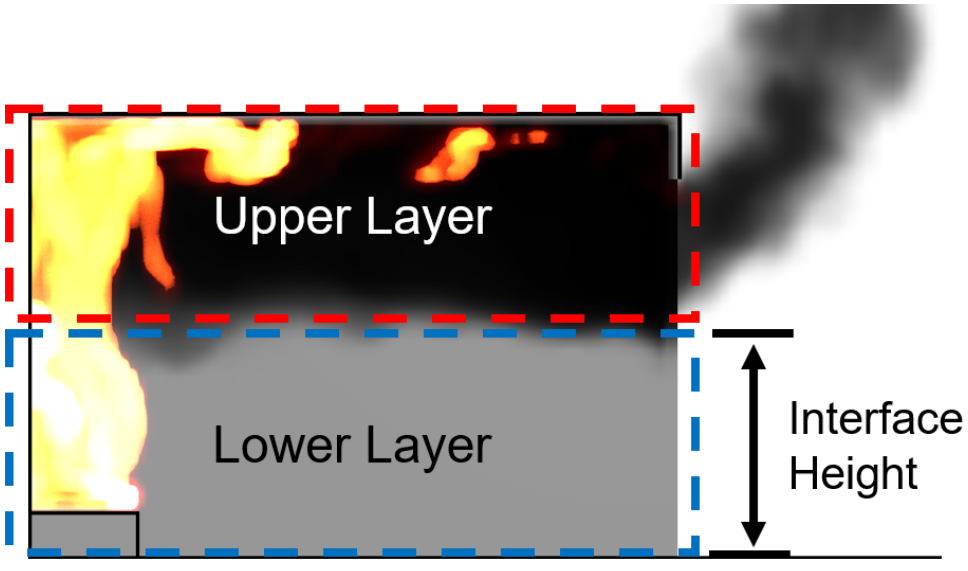

Figure 16: Example two-layer environment in compartment fire

3.5 Test Procedure

3.5.1 Daily HRR Calibration

Prior to each day of testing a calibration burn was conducted to verify the HRR and duct mass flow calibration. A HRR profile was established for each hood by control of the propane gas input to the burner, per Table 9. The propane was at least 95 percent purity, and its net heat of combustion was taken to be 46.4 kJ/g. HRR C-factor calibration tests were conducted using a propane burner (i.e., centered under the hood, outside of the compartment). The overall C-factor was 6.1–6.9 $(kg\text{-}m\text{-}K)^{1/2}$ and 18.4 $(kg\text{-}m\text{-}K)^{1/2}$ at JH and CBD, respectively.

Table 9: Propane burner HRR output for calibration tests

		Heat release rate (kW)	
Step #	Time (min)	JH	CBD
1	0 to 2	0	0
2	2 to 7	100	250
3	7 to 12	300	750
4	12 to 17	100	250
5	17 to 19	0	0

3.5.2 Test Protocol

At the start of each test day, daily checks and calibrations were carried out: analyzers zero/span, HRR calibration, and instrumentation check of all sensors. Afterward, the correct operation of the data acquisition system was verified. The exhaust flow rate was set according to the expected rate of heat release.

The test was then initiated by starting the data acquisition system (DAQ) and video camera, and collecting 2 minutes of baseline data. Next, the burner (i.e., or pool fire, depending on the test) was ignited using a remote ignition device (e.g., electric match).

During the test, data was monitored, and the burner HRR set via mass flow controller as outlined in the test matrix. The test operators noted any observations during the test, including the transition to flashover, if it occurred. Once the burner completed the test duration of 10 or 15 minutes, the burner gas supply was shut off. The HRR and other measurements were recorded for an additional 5 minutes (i.e., non-combustible lining tests and combustible lining tests) as the fire decayed. After this time, for tests with combustible linings, the test firefighter applied a light water mist using a hose from the doorway to any burning materials that remained.

After each test was completed, a portable fan was placed at the doorway and activated, allowing the compartment to return to ambient conditions. Once it was safe, the condition of the lining materials was assessed. Instruments were gently removed and set aside, as needed. Remnants of combustible lining materials were removed, and any sufficiently damaged noncombustible lining materials were identified and replaced. The compartment was then prepared for the next test, which included installing new lining materials (as needed) and reinstalling any instruments that were removed.

4. Pre-Test Simulations

Prior to conducting the experiments, the research team used FDS version 6.5.2 to develop and simulate detailed computational models of key scenarios. The primary objective of the pre-test simulations was to demonstrate the scaling approach to represent the full-scale simulations based on reduced-scale simulations for each configuration to be tested even though the experimental configuration slightly varied across scales (e.g., full-scale compartment resting on a solid slab, but reduced-scale compartments elevated in the lab).

The following subsections provide an overview of the models and present the results of the simulations.

4.1 Fire Dynamics Simulator

FDS is a general-purpose low-speed (Mach number < 0.3) CFD software developed by the National Institute of Standards and Technology which is primarily designed to model buoyantly driven flows typical of diffusion flames (McGrattan, K., Hostikka, S., Mcdermott, R. J., Vanella, M., Weinschenk, C. G., & Overhold, K., 2019; McGrattan, K., Mcdermott, R. J., Hostikka, S., Floyd, J., Weinschenk, C., & Overholt, K., 2019). In an FDS simulation, the computational domain is divided into small (on the order of 10 s of cm) control volumes, often called grid cells. By solving a set of partial differential equations asserting conservation of mass, momentum, and energy in each grid cell as well as a radiation transport equation, the software predicts the time-evolution of the gas temperature, velocities, and species concentrations in each grid cell as well as heat transfer to solid surfaces. FDS has an extensive validation basis in fire safety applications (Mcgrattan, K., Hostikka, S., Mcdermott, R. J., Floyd, J., Vanella, M., Weinschenk, C. G., & Overholt, K., J., 2019) and is considered the state-of-the-art in fire modeling for diffusion flames. An overview of the sub-models in FDS used in this analysis and the results of the grid sensitivity study are summarized in Appendix D.

4.2 Model Configuration

The compartment geometry in the simulations was developed to represent the geometry of the experimental test series described in Section 3. The exhaust hood was included in the model along with skirt extensions dropping below the sill height of the window. The reduced-scale compartments were elevated on the false floor, while the full-scale compartment was resting on the lab floor. A grid size of 5.0 cm/10.0 cm inside/outside the compartment was used for the full-scale simulations, 2.5 cm/5.0 cm inside/outside was used for the half-scale simulations, and 1.25/5.0 cm inside/outside were used for the quarter-scale simulations. A section view of the full-scale and half-scale non-combustible door configuration models is provided in Figure 17.

The floor, ceiling, and wall linings in the computational models were gypsum board with a thickness of 5/8 in. (15.9 mm). The exhaust hood was modeled as steel with a thickness of 3/8 in. (10 mm). The material properties of steel and gypsum used in this work are included in Table 10. Note the specific heat capacity of the gypsum wall board used in the CFD modeling was temperature dependent, as shown in Figure 18. The durock material was assumed to have the same properties as gypsum in this analysis.

Note the material properties of the combustible linings are provided in Appendix D in the context of pyrolysis modeling.

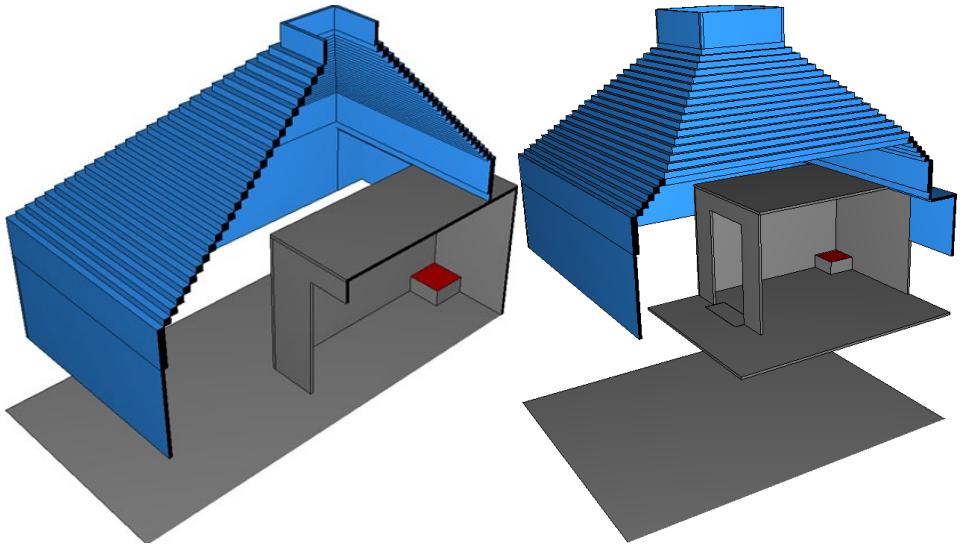

(a) Full-scale model **(b) Half-scale model**

Figure 17: Section view of non-combustible door configuration models

Table 10: Material properties of solid boundaries in CFD modeling

Material	Density (kg/m^3)	Specific Heat (kJ/kg-K)	Conductivity (W/m-K)	Emissivity -
Gypsum	711	1.0 to 12.9*	0.17	0.9
Steel	7,832	0.434	63.9	0.9

* Temperature dependent, see Figure 18.

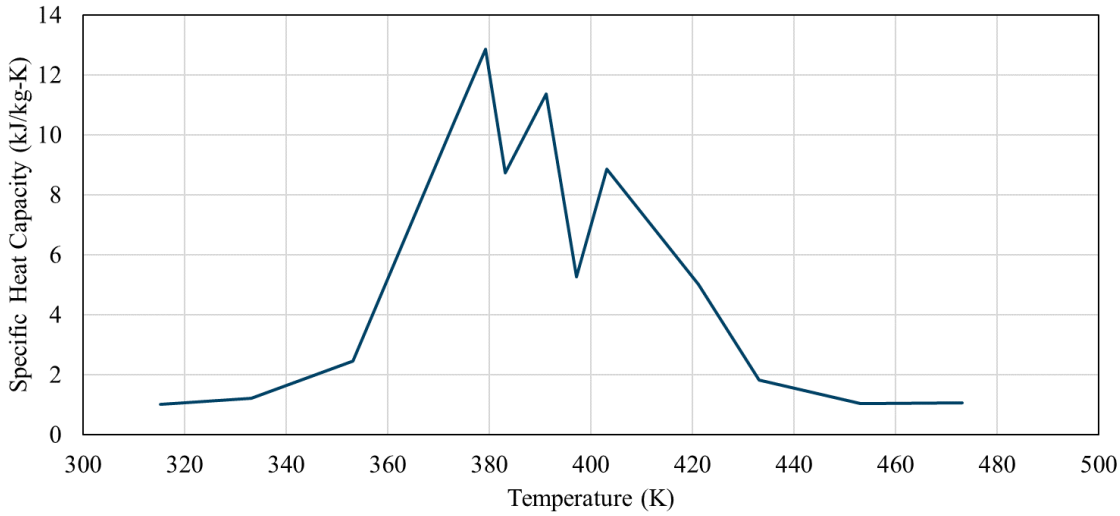

Figure 18: Specific heat capacity of gypsum wall board as a function of temperature (Gwynne, S. M. V., & Boyce, K. E., 2016)

4.3 Results

4.3.1 Demonstrating Scaling Approach on Planned Tests

The simulation result for the case with non-combustible boundaries and a single door are provided in Figure 19 through Figure 21. The lower and upper bars indicate pre- and post-flashover conditions, respectively (Figure 21). The vertical temperature profile in the south-east corner of the compartment is compared for the non-combustible door configuration in pre-flashover and post-flashover conditions in Figure 19 and Figure 20, respectively. The lower layer temperature, upper layer temperature, and interface height agreed well across all scales. The upper layer temperature had the largest variability across scales but was within 10 percent during the pre-flashover exposure and within 5 percent during the post-flashover exposure. This is in line with expected experimental uncertainty of 7 percent (Mcgrattan, K., Hostikka, S., Mcdermott, R. J., Floyd, J., Vanella, M., Weinschenk, C. G., & Overholt, K., J., 2019).

The time-averaged gauge heat flux at the wall, ceiling, and floor positions are shown for the non-combustible door configuration under pre-flashover and post-flashover conditions in Figure 21. The agreement across scales was the best at the ceiling heat flux measurement location where both the pre- and post-flashover regimes were within 1.5 kW/m^2 (8 percent). The floor heat fluxes across scales were similar in absolute magnitude with a max deviation of 1.1 kW/m^2 (41.1 percent) during pre-flashover and 2.8 kW/m^2 (24.7 percent) during post-flashover. The half-scale and full-scale wall heat fluxes agreed well in both pre- and post-flashover with a deviation of 0.7 kW/m^2 (10.7 percent) and 1.3 kW/m^2 (5.3 percent), respectively. However, the quarter-scale wall heat flux was significantly higher than the full-scale heat flux with a deviation of 8.6 kW/m^2 (35.1 percent). This was in part attributed to the flame extension and ceiling jet flow being different at this reduced scale. In addition, this may be due to the treatment of the radiative path length used in FDS, which has since been modified. In general, these results indicate that the scaling approach is robust to the small deviations in experimental configuration across scales.

Similar comparisons for the test with non-combustible boundaries having a door and window opening (door-window configuration) are provided in Figure 22 through Figure 24. The lower and upper bars indicate pre- and post-flashover conditions, respectively (Figure 24). The vertical temperature profiles and time-averaged gauge heat fluxes were similar to those observed in the non-combustible door configuration. Again, the heat flux on the north wall had the largest deviation with full-scale; however, the difference was lower in this configuration. Overall, these results further supported that the scaling approach was robust even with multiple ventilation paths.

The capability of the scaling approach to reproduce the transient flame spread along combustible linings was also assessed through simulations on the test with a single door and plywood lining the corner with the fire (plywood scenario). Figure 25 contains a comparison of the transient HRR as the predicted full-scale heat release using the scaling law in Equation 1. The reduced scale results were within 20 percent which is within the expected uncertainty of the combustible lining test HHRs. These results indicated that the scaling approach will also be appropriate for developing fires where flames are spreading over combustible surfaces.

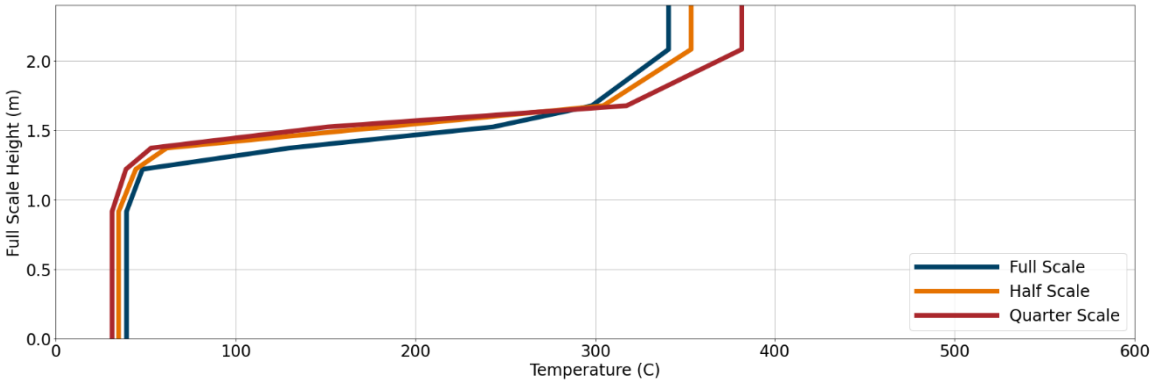

Figure 19: Pre-flashover predictions of temperature in south-east corner across scales in non-combustible door configuration

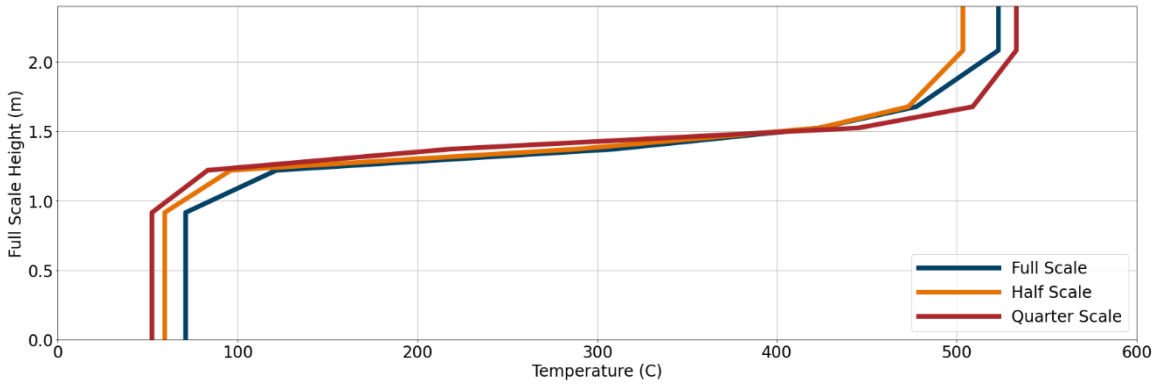

Figure 20: Post-flashover predictions of temperature in south-east corner across scales in the non-combustible door configuration

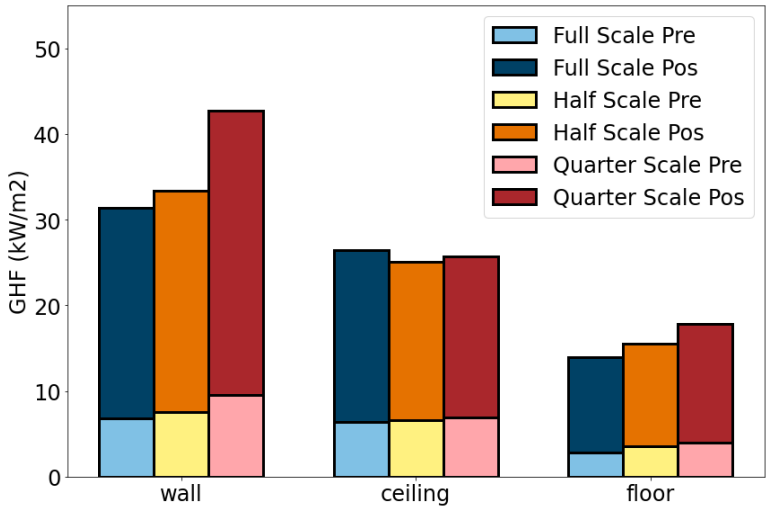

Figure 21: Comparison of gauge heat flux at each sensor location in non-combustible door configuration

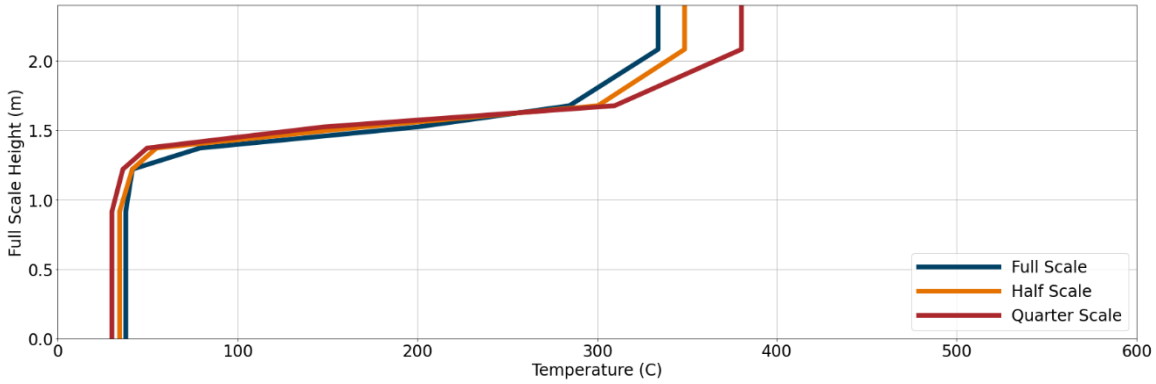

Figure 22: Pre-flashover predictions of temperature in south-east corner across scales in window configuration

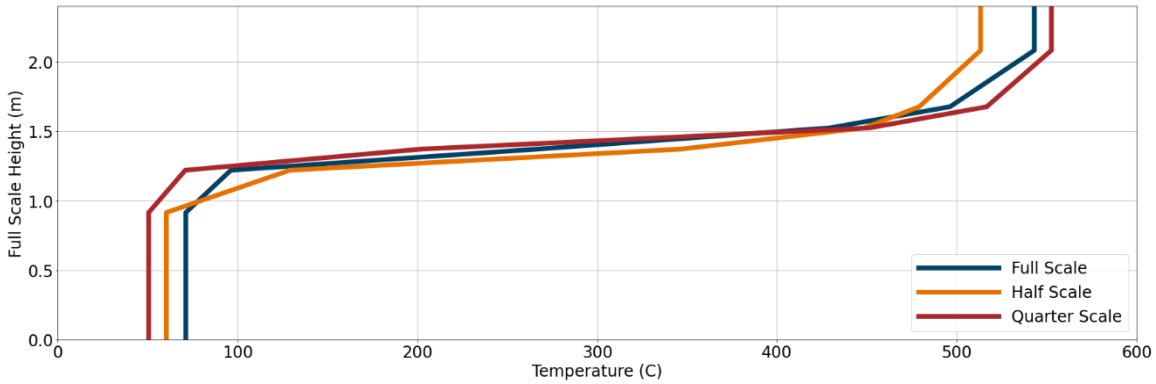

Figure 23: Post-flashover predictions of temperature in south-east corner across scales in window configuration

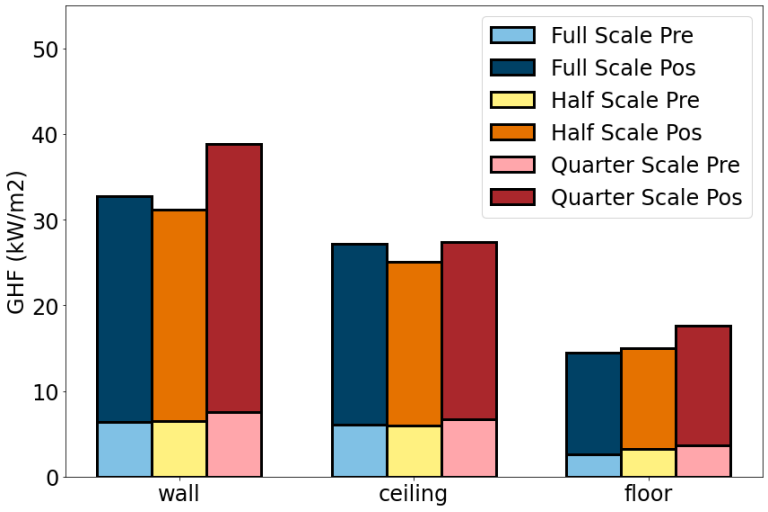

Figure 24: Comparison of gauge heat flux at each sensor location in door-window configuration

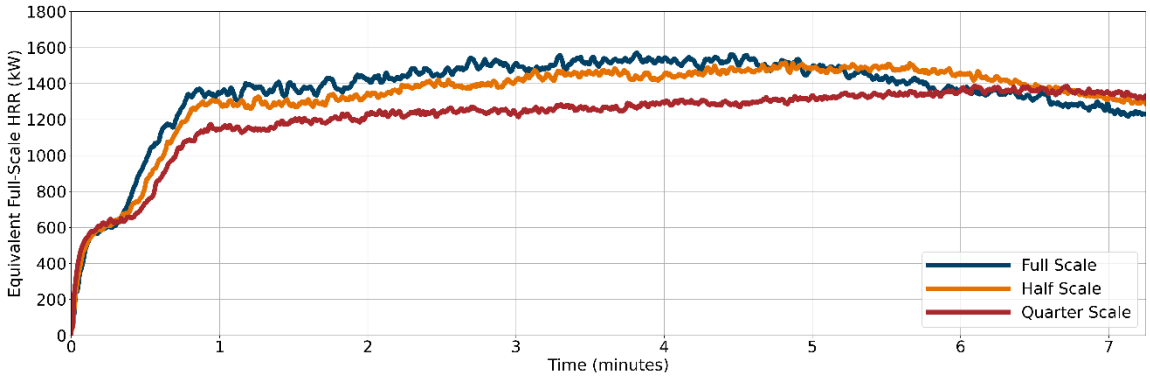

Figure 25: Comparison of predicted HRR across scales from plywood combustible lining simulations

4.3.2 Pyrolysis Model Development

An existing limitation of FDS was identified in the development of the pre-test simulations for this project. Appendix D details the two pyrolysis models which exist in the software to model fire spread. The first model is simplistic, with a specified HRR profile once a material reaches an ignition temperature. The second model is highly complex, requiring close to 50 material and reaction parameters to be quantified from experiments. While conducting the pre-test simulations, JH recognized the need for a new pyrolysis model which is less complex than the Arrhenius kinetics model which can account for different pyrolysis rates at different levels of thermal exposure. Appendix E presents the fundamental basis for this new pyrolysis model which has been implemented into FDS as a new feature.

5. Test Results

This section provides results from the testing performed at three different scales as previously described in Table 1. The initial section contains exemplar results from the testing, while the second section contains a summary of key data from the test series.

5.1 Sample Test Results (Quarter-Scale Non-Combustible Door Configuration)

Detailed measurements for the quarter-scale non-combustible door configuration (Test 1) are provided in the following subsections. Note the fractions in the legends correspond to the percentile location between the floor and the ceiling. For example, the 0.87 H TC was located near the ceiling at a height of 20.6 in. (0.52 m) above the floor where the maximum height of the quarter-scale compartment was 24 in. (0.60 m). Detailed measurements for the rest of the test series are provided in Appendix F.

5.1.1 Heat Release Rate

The target HRR profile for this test was 5 minutes at 20 kW, followed by an additional 5 minutes at 40 kW. The actual HRR during testing is shown in Figure 26.

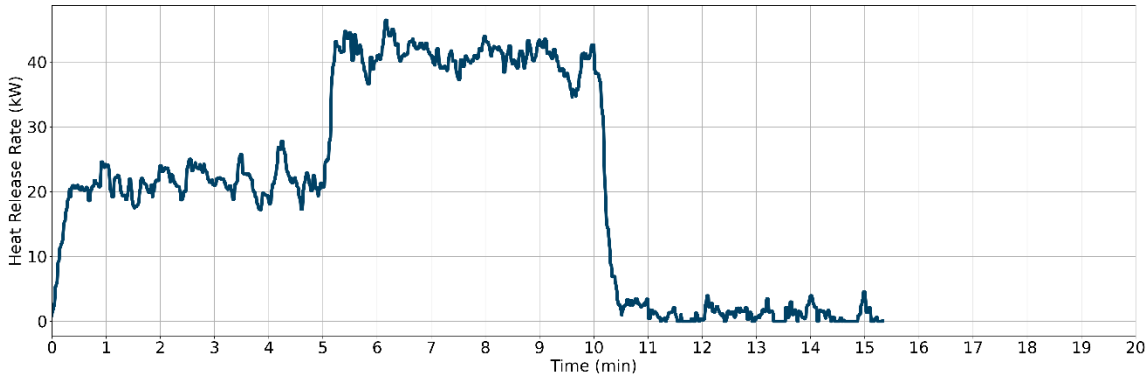

Figure 26: Test 1 HRR

5.1.2 Gas Temperatures

A total of 24 temperature measurements were obtained during testing. Twelve of these measurements were part of the thermocouple trees in the north-east and south-east quadrant of the compartment, shown in Figure 27 and Figure 28, respectively. An additional two temperature measurements were taken at two heights above the burner, shown in Figure 29. Temperatures are slightly higher in the north-east corner (e.g., back of the compartment opposite the burner) due to these TCs being closer to the burner. Based on both thermocouple tree temperatures, the interface height is approximately 0.57 H with the higher temperature upper layer above this and the lower temperature layer below this. The highest gas temperatures at the end of the test are 500–700 °C, which indicates the compartment fire conditions are just at flashover.

Six temperature measurements were taken at the door, shown in Figure 30. Four temperature measurements were taken at the ceiling, shown in Figure 31. The spatial locations of the TCs correspond to those shown in Figure 11.

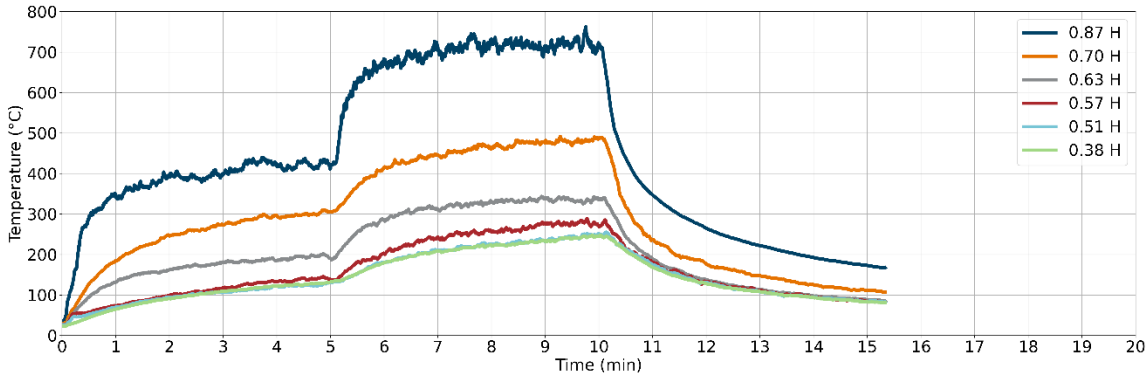

Figure 27: Test 1 gas temperatures in north-east corner

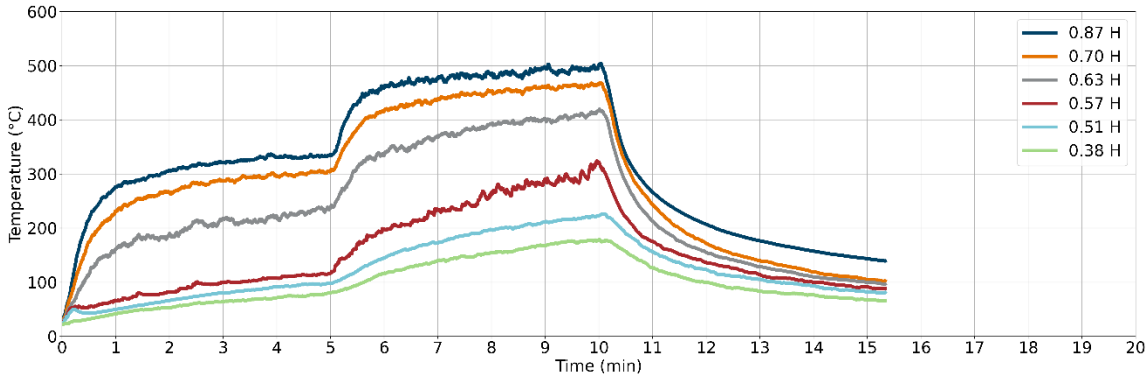

Figure 28: Test 1 gas temperatures in south-east corner

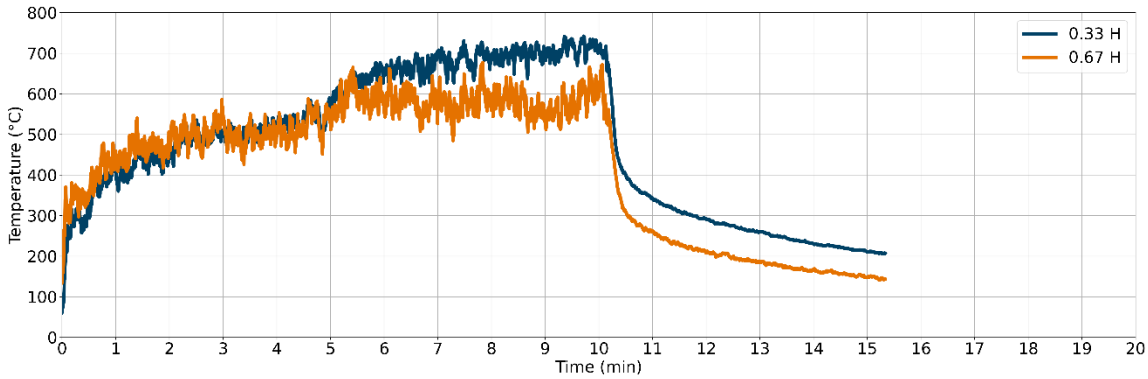

Figure 29: Test 1 gas temperatures at the burner

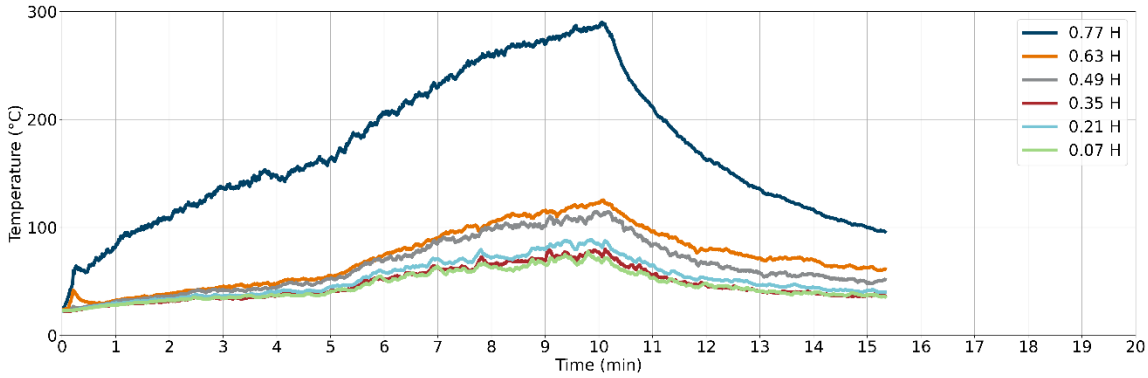

Figure 30: Test 1 gas temperatures at the door

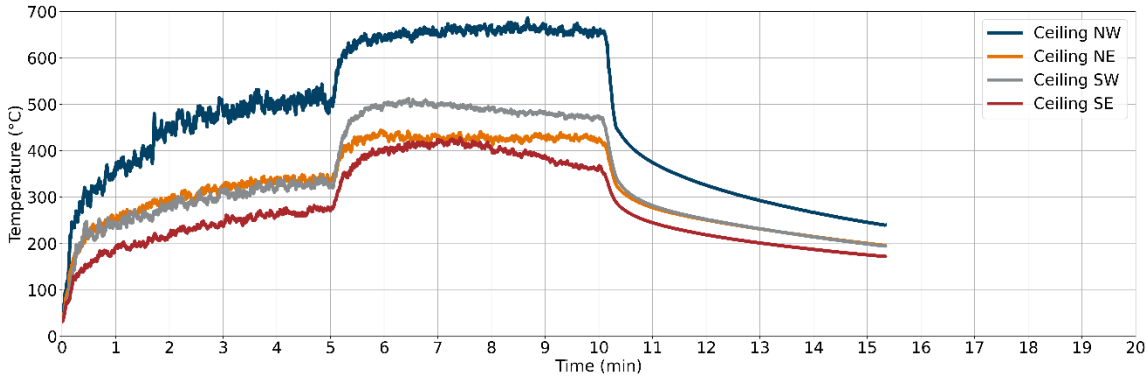

Figure 31: Test 1 gas temperatures at the ceiling

5.1.3 Gas Velocities

A total of six gas velocity measurements were obtained during testing. Each of these measurements was obtained at the centerline of the door at different heights, and are shown in Figure 32. Positive velocities represent gas flow out of the compartment while negative velocities are gas flow into the compartment. Zero velocity (i.e., close to the 0.49 H height) is where the neutral plane is located, which is where the outflow and inflow meet.

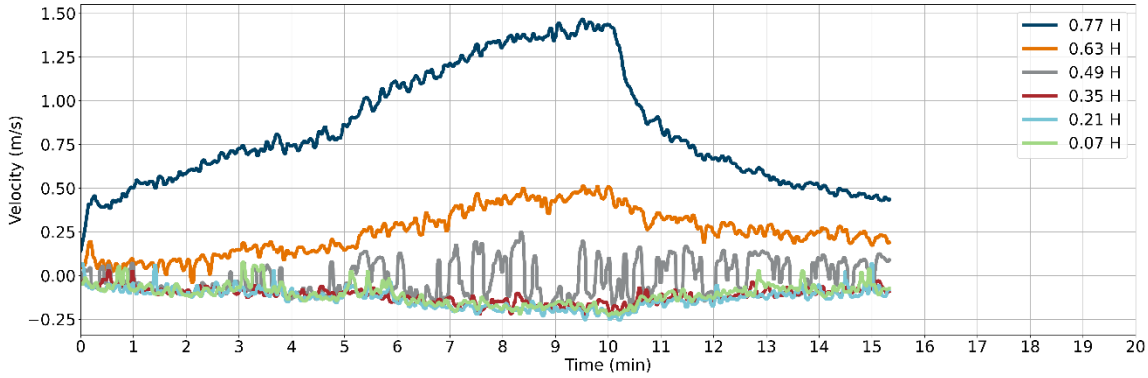

Figure 32: Test 1 gas velocities at the door

5.1.4 Heat Fluxes

A total of four gauge heat flux measurements were obtained during testing, with the measurements shown in Figure 33. The spatial location of the heat flux gauge corresponds to those shown in Figure 11. Note that the heat flux measurements shown in Figure 33 have been filtered with a 30 second median filter to reduce noise. In this test, the highest heat fluxes are in the corner where the burner is located while the heat flux at the top of the back wall due to the hot gas flow along the ceiling from the burner. Heat flux to the ceiling and the floor is 15–20 kW/m^2 indicating the compartment fire conditions are just at flashover.

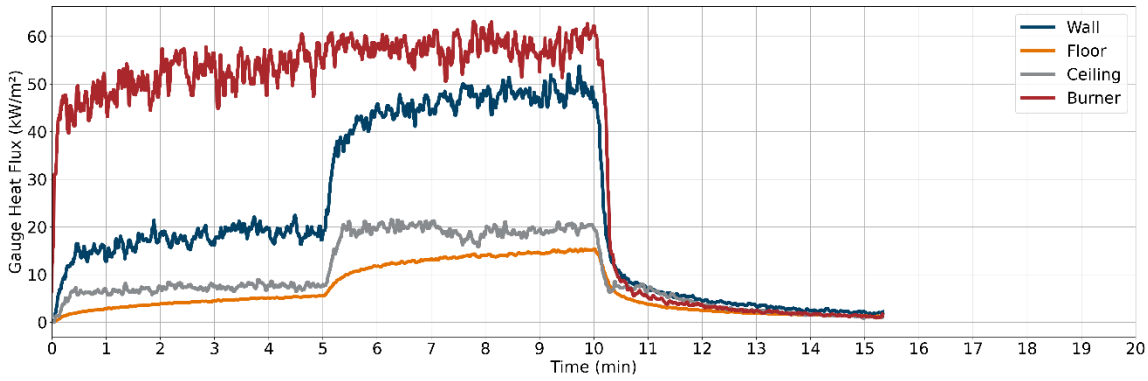

Figure 33: Test 1 heat fluxes

5.1.5 Optical Obscuration

The obscuration through the exhaust duct was measured at one location during testing, as shown in Figure 34.

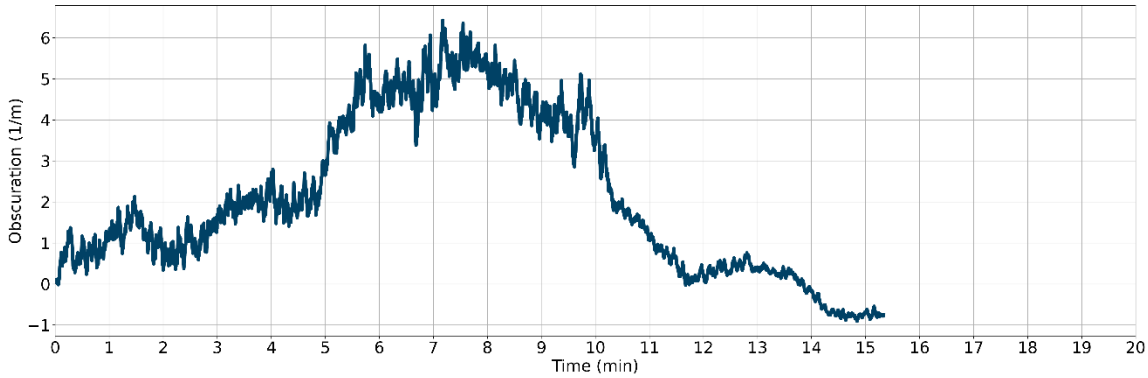

Figure 34: Test 1 optical obscuration in exhaust duct

5.2 Summary Results

The test results are summarized in Figure 35 through Figure 39. Additional summary details are provided for each test in the series in Appendix G.

Figure 35 compares the compartment environment observed in the south-east corner for each non-combustible test across scales with different full-scale equivalent (FSE) HRRs. The bottom and top of each bar indicate the lower layer and upper layer temperature, respectively. The x-axis value indicates the FSE interface height. The resulting heat fluxes at each measurement location

are shown in Figure 36 and Figure 37. All comparisons within the same FSE HRR regime are expected to have similar compartment environments.

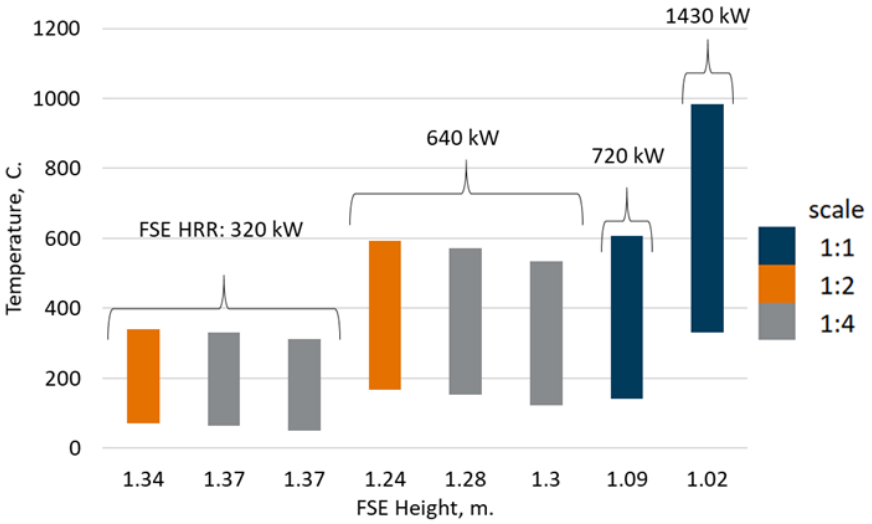

(a) Door-configuration

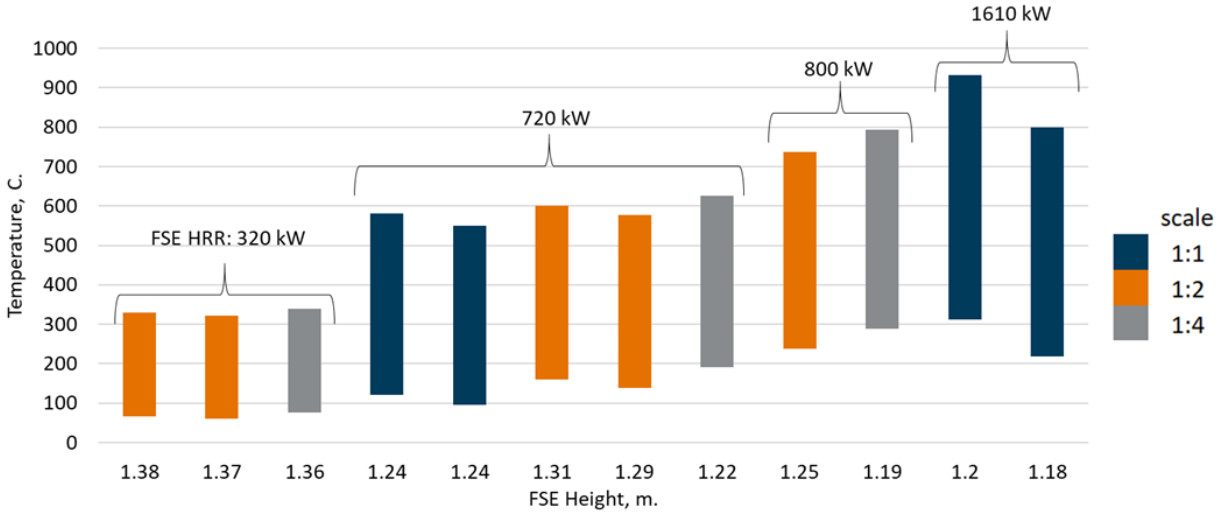

(b) Window-configuration

Figure 35: South-east thermocouple tree comparison

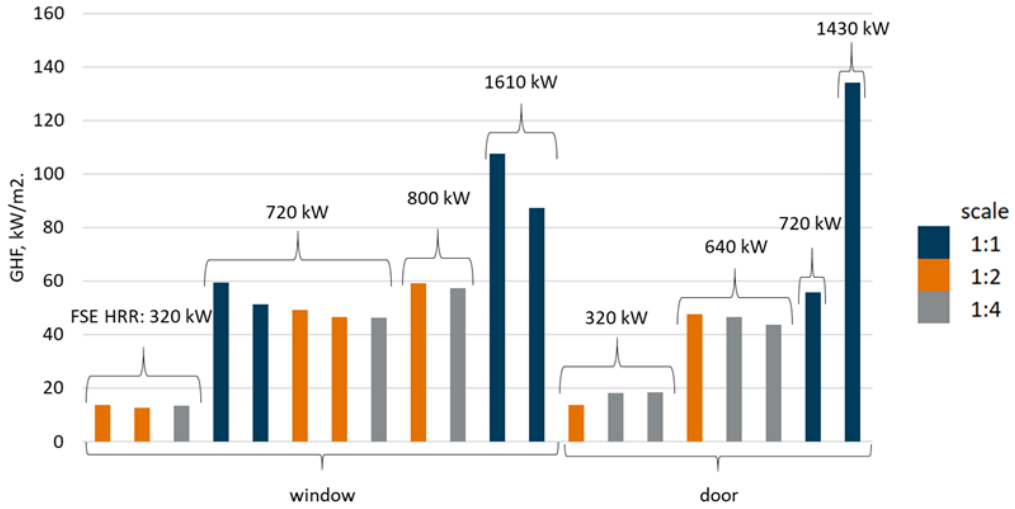

(a) Wall

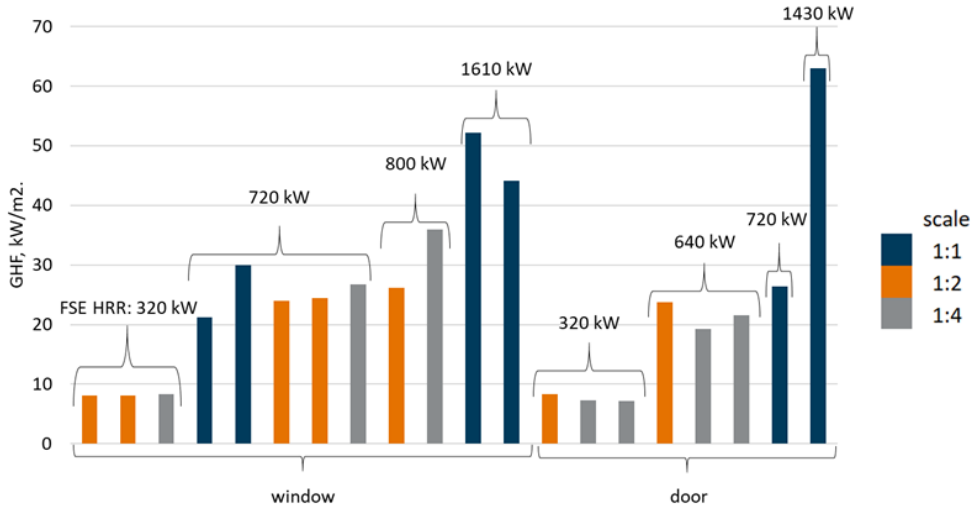

(b) Ceiling

Figure 36: Comparison of wall and ceiling heat fluxes for window and door-configuration at different FSE HRR levels

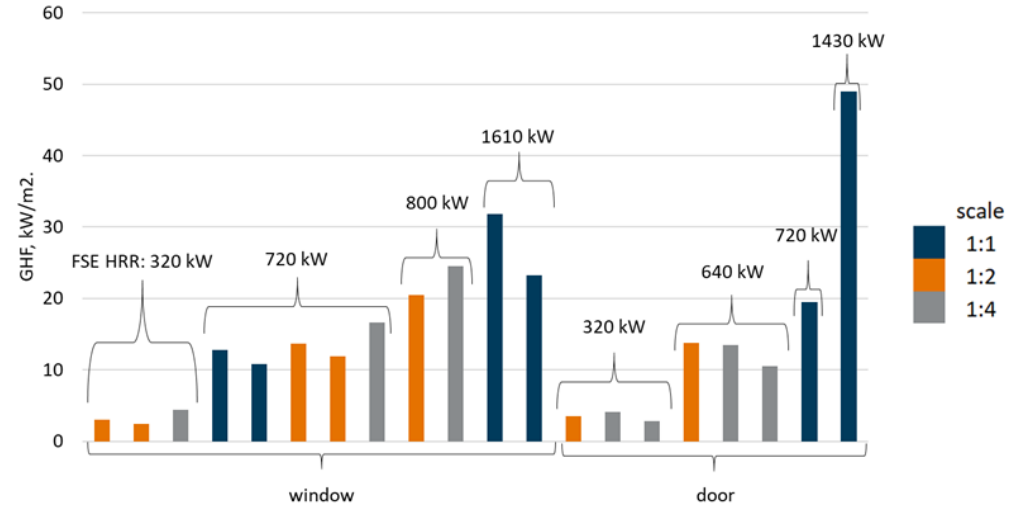

(a) Floor

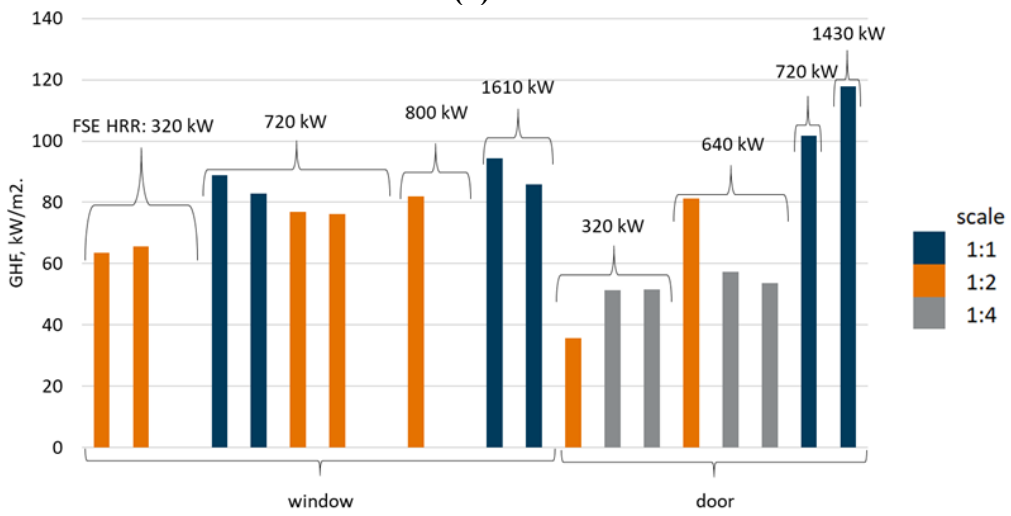

(b) Burner

Figure 37: Comparison of floor and burner heat fluxes for window and door-configuration at different FSE HRR levels

Figure 38 compares the FSE HRR observed in the variable HRR experiments. Figure 38a shows the peak 60 second average HRR, and Figure 38b shows the test average HRR. Similarly, Figure 39 compares the FSE total heat released for each experiment. All comparisons within the same fuel grouping are expected to have similar FSE HRRs and FSE total heat released.

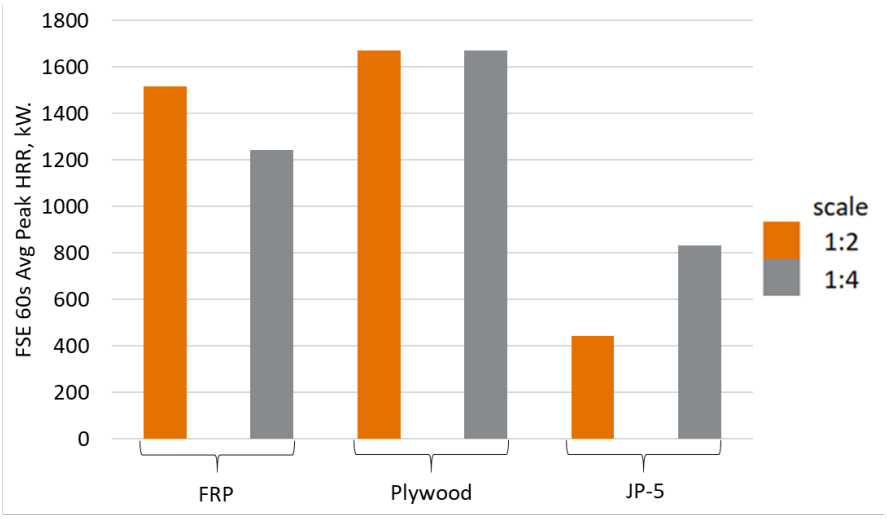

(a) 60 s Average Peak

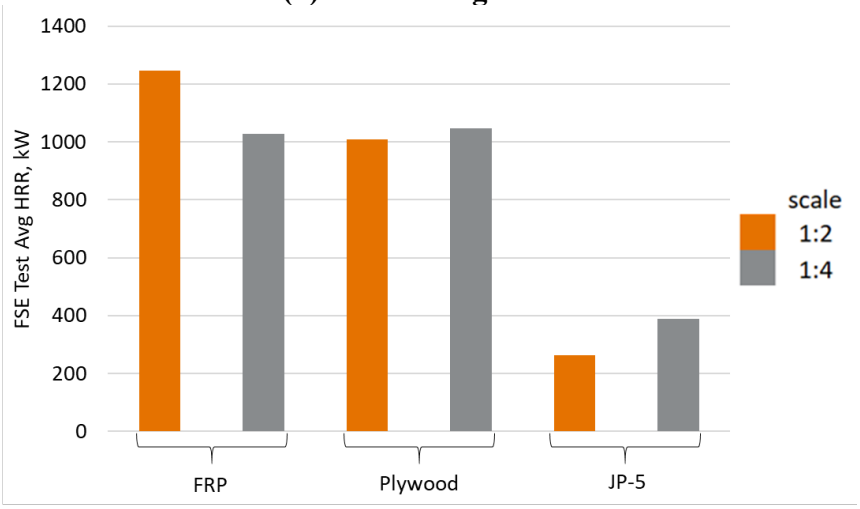

(b) Test Average Peak

Figure 38: Summary average FSE HRR from variable HRR experiments

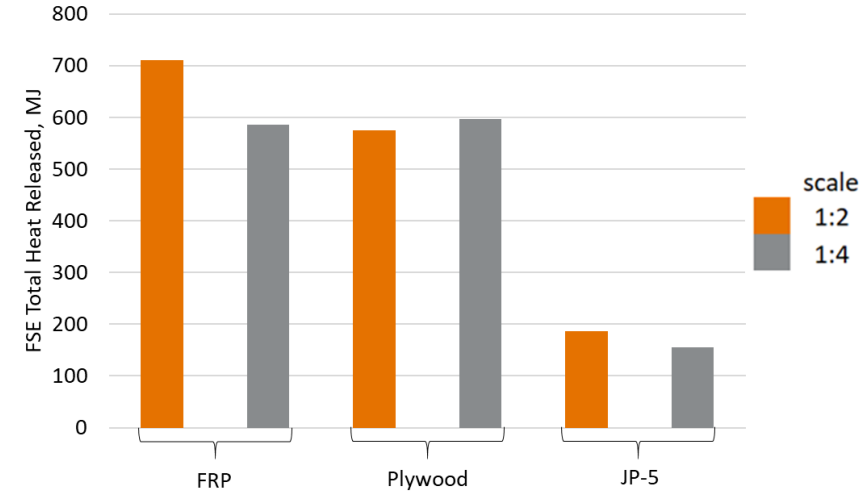

Figure 39: Summary FSE total heat released from variable HRR experiments

6. Scaling Law Evaluation

This section analyzes the results from the testing performed at three different scales as previously described in Table 1. The initial section presents scaling comparisons from gas burner tests with non-combustible lining. The next section presents similar comparisons from gas burner tests with additional fuel loading from combustible lining. The final section presents similar comparisons for tests with a liquid pool fire having non-combustible boundaries. In each section, the quality of the scaling comparisons is evaluated, and the performance of the approach discussed.

6.1 Non-combustible Boundaries

Direct comparison of quarter-scale and half-scale experiments with the full-scale experiments was not possible for all non-combustible test cases due to an issue with the gas mass flow controller. However, the initial HRR level in the full-scale corresponded to the original target values for post-flashover. Therefore, the comparison of the HRRs and exposures across all model scales was performed with the post-flashover quarter and half-scale models with the initial HRR level for the full-scale test. In addition, the conditions at both HRR levels were compared for the quarter and half-scale models. This was performed for tests with only a door opening as well as with both door and window openings.

6.1.1 Door

This section provides a comparison of results at different scales with only a door opening from Tests 1-A, 1-B, 6, and 11. The measured HRRs for the different scales are provided in Figure 40 along with the FSE values based on data at the quarter and half scales (i.e., scaling factor applied). Note that the first 5 minutes of the full-scale test is compared with conditions from 5 minutes to 10 minutes, in the quarter and half scale tests. However, the entire test duration could be compared for the quarter and half scales. As seen in the figure, the FSE HRRs match well for the quarter and half scales for the full duration, and the offset HRR at the full-scale matches the quarter and half scales during the 5–10 minute range.

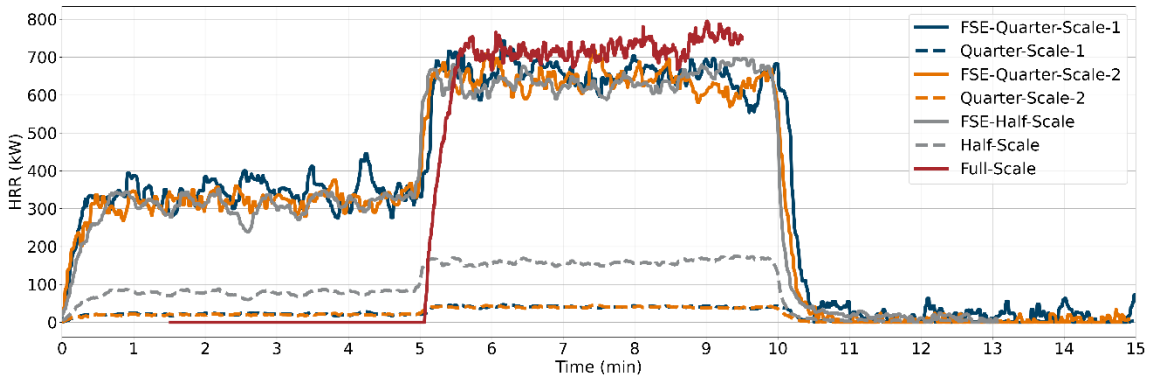

Figure 40: HRRs from non-combustible door experiments

Comparisons across scales at the pre- and post-flashover exposure for the non-combustible door scenarios (i.e., Tests 1-A, 1-B, 6, and 11) are shown in Figure 41 and Figure 42. Figure 41a shows the temperature profile away from the initiating fire in the south-east corner in the pre-flashover exposure. The compartment fire environment was similar across scales. The upper layer temperatures were generally within 3 percent and the full-scale equivalent interface heights

within 0.03 m. The lower layer temperatures had slightly less agreement with a difference of 25 percent (25 °C).

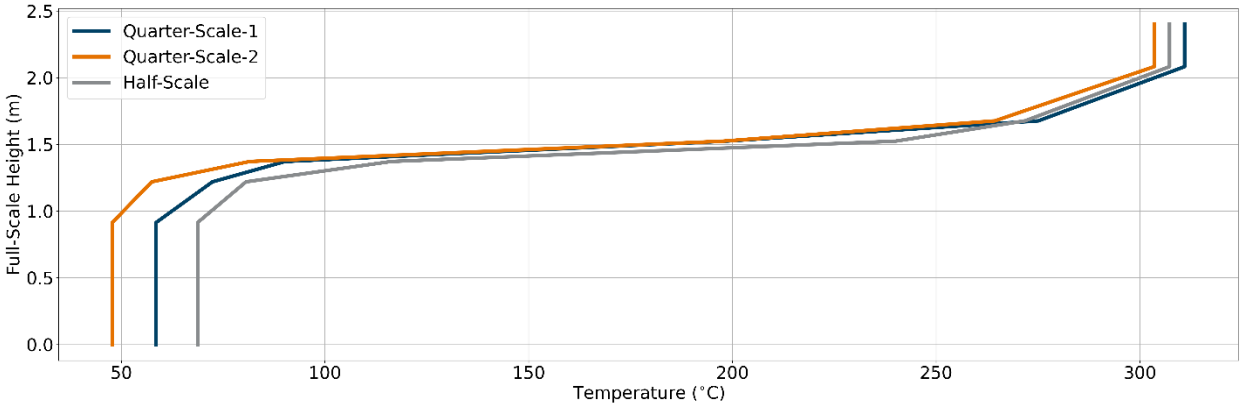

(a) Pre-flashover (quarter and half scales)

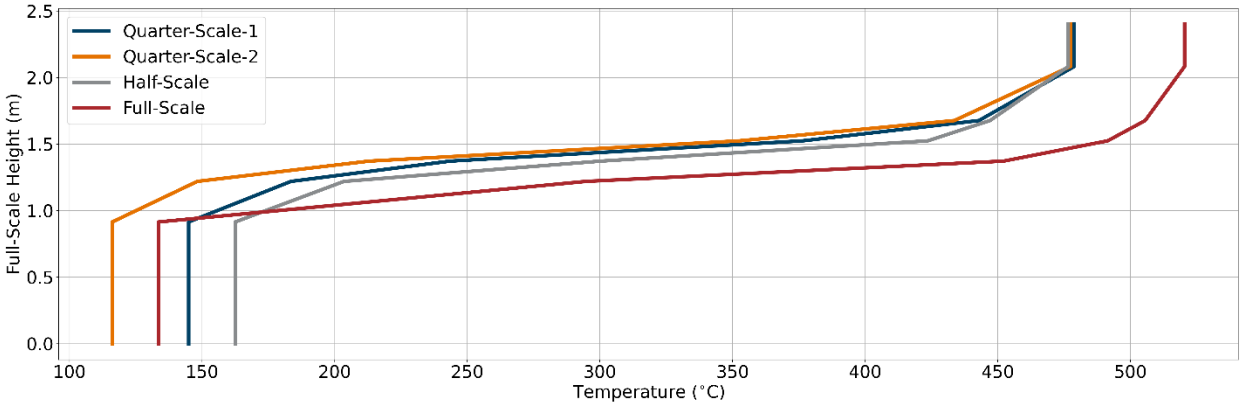

(b) Post-flashover (all scales)

Figure 41: Vertical temperature profile in south-east corner with only a door opening during pre- and post-flashover

Figure 42 compares the heat fluxes at each measurement location. The heat fluxes in the pre-flashover exposure shown in Figure 42a followed similar trends observed in the pre-test simulations. The ceiling heat fluxes were within 1.1 kW/m^2; however, the quarter-scale wall heat fluxes were 4.6 kW/m^2 higher than observed at the half-scale. The floor heat fluxes were similar across scales. Since the heat flux to the floor is often used as an indicator of flashover, these results indicate the quarter-scale and half-scale experiments would provide a similar time to flashover.

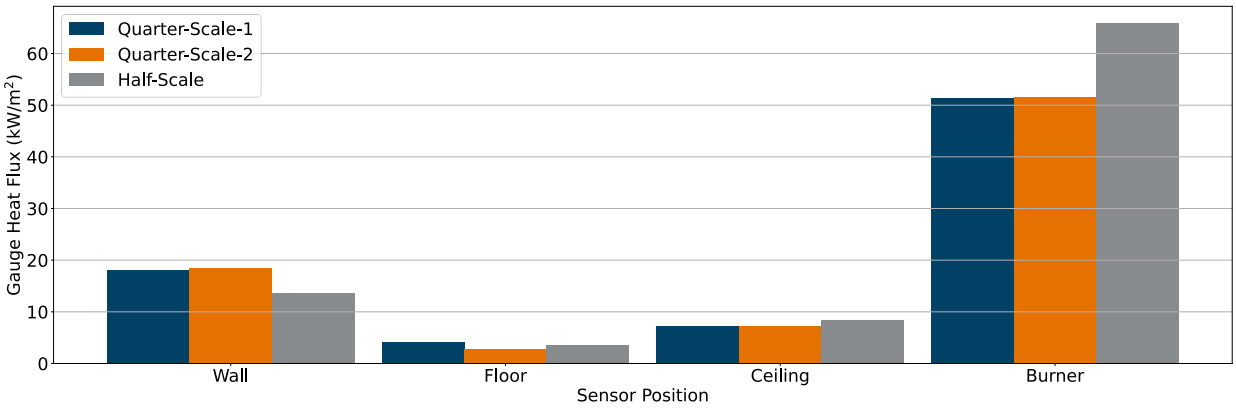

(a) Pre-flashover (quarter and half scales)

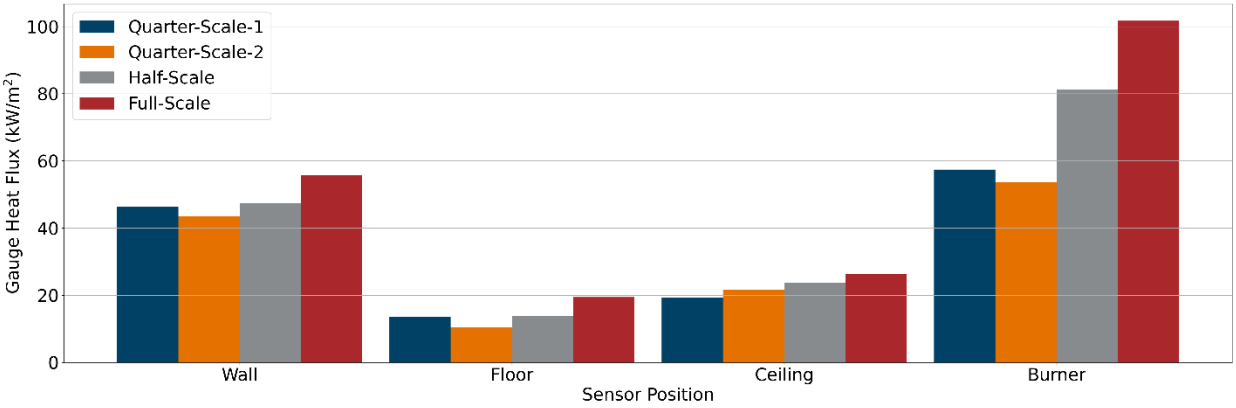

(b) Post-flashover (all scales)

Figure 42: Heat flux levels at different locations with only a door opening during pre- and post-flashover

Figure 41b shows the temperature profile away from the initiating fire in the south-east corner in the post-flashover exposure. The vertical temperature profile shows that the upper layer temperature and interface height agreed well across all scales. The upper layer temperatures of the quarter-scale and half-scale were within 3 percent of each other; however, the full-scale upper layer temperatures were approximately 10 percent higher than the other scales. The FSE interface heights of the quarter and half scales were within 0.06 m of each other; however, the full-scale interface height was approximately 0.2 m lower than the other scales. Larger disagreement was observed in the lower layer temperatures, which varied 123 °C to 168 °C with no consistent trends observed in the deviations. The differences in the upper layer temperature and interface heights were attributed to the full-scale HRR (720 kW) in this comparison being 11 percent higher than the FSE HRR of the other scales (640 kW).

Figure 42b compares the heat fluxes in the post-flashover exposure. The wall and floor heat fluxes were similar across scales with a slightly elevated measurements observed in the full-scale experiment. The ceiling and burner heat flux were inversely correlated with scale, with the trend more pronounced in the burner heat flux. In addition, the higher wall heat fluxes predicted in simulation (see Figure 21) were not measured experimentally (see Figure 42b). The elevated heat flux measurements at the full-scale were attributed to the higher upper layer gas temperatures resulting from the difference in FSE HRR.

Overall, these comparisons indicate that the reduced scale compartments were able to produce a similar compartment fire environment to the full-scale.

6.1.2 Door and Window Openings

This section provides a comparison of results at different scales with door and window openings from Tests 2, 7-A, 7-B, 12-A, and 12-B. The measured HRRs for the different scales are provided in Figure 43 along with the full-scale equivalent values based on data at the quarter and half scales (i.e., scaling factor applied). Note that the first 5 minutes of the full-scale test is compared with conditions from 5–10 minutes. in the quarter and half scale tests. However, the entire test duration could be compared for the quarter and half scales. As seen in the figure, the FSE HRRs match well for the quarter and half scales for the full duration, and the offset HRR at the full-scale matches the quarter and half scales during the 5–10 minute range.

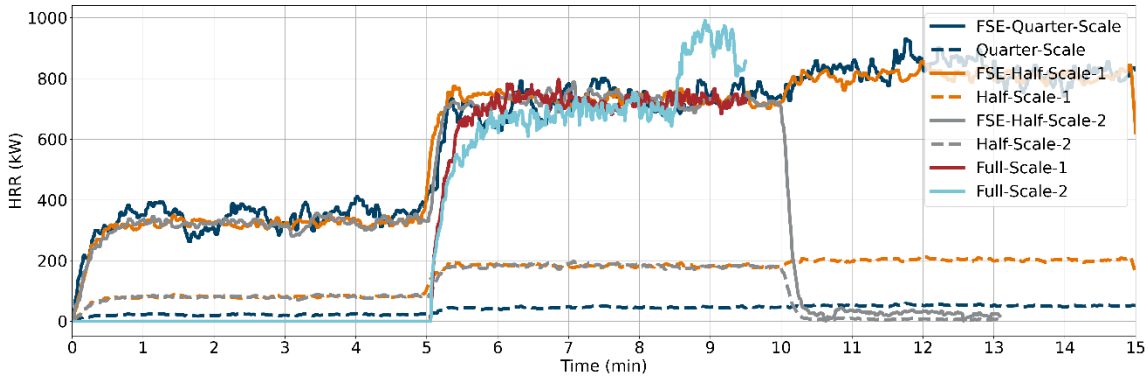

Figure 43: HRRs from non-combustible door-window experiments

Comparisons across scales at the pre- and post-flashover exposure for the non-combustible door-window scenarios (i.e., Tests 2, 7-A, and 7-B) are shown in Figure 44 and Figure 45. Figure 44a shows the temperature profile away from the initiating fire in the south-east corner in the pre-flashover exposure. The compartment fire environment was similar across scales. The upper and lower layer temperatures were generally within 5–10 percent and the full-scale equivalent interface heights were within 0.02 m.

Figure 45 compares the heat fluxes at each measurement location. The heat fluxes in the pre-flashover exposure shown in Figure 45a followed similar trends observed in the pre-test simulations. The wall and ceiling heat fluxes were within 3 percent; however, the floor heat flux was 1.4-2.0 kW/m^2 higher in the quarter-scale than the half scale (50 percent). The higher heat flux at the floor in the quarter-scale was attributed to the higher gas temperatures in the quarter-scale, particularly in the lower layer. Since the heat flux to the floor is often used as an indicator of flashover, the quarter scale is expected to provide a conservative indication of the time to flashover.

Figure 44b shows the temperature profile away from the initiating fire in the south-east corner in the post-flashover exposure. The vertical temperature profile shows that the upper layer temperature and interface height agreed well across all scales. The upper layer temperatures were within 3 percent, and the full-scale equivalent interface heights were within 6 percent. Larger disagreement was observed in the lower layer temperatures, where the lower layer temperatures were found to be inversely correlated with the scale of the model (i.e., higher in quarter scale compared with half and full scales).

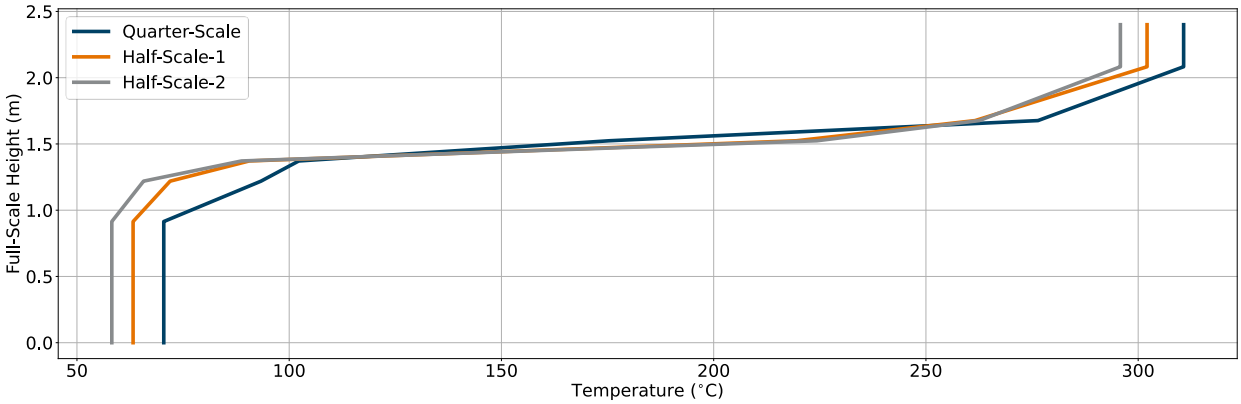

(a) Pre-flashover (quarter and half scales)

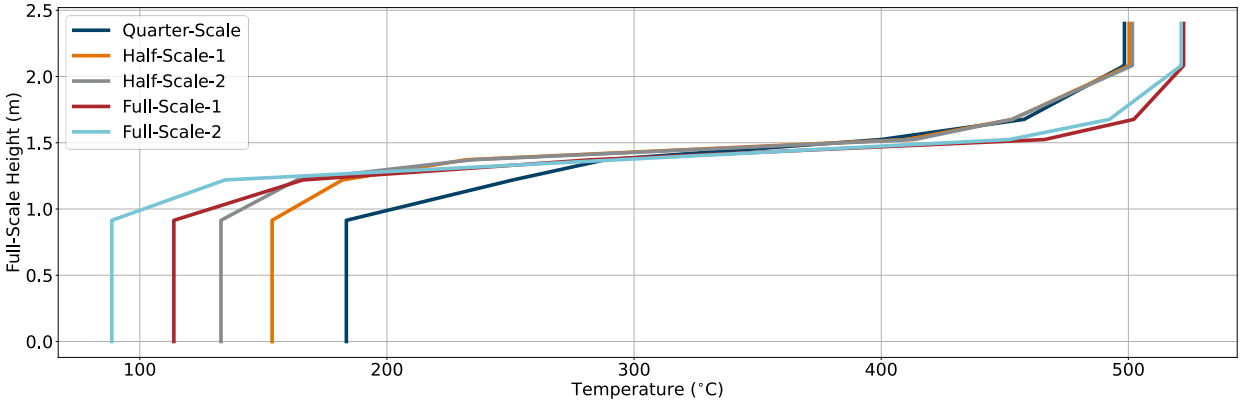

(b) Post-flashover (all scales)

Figure 44: Vertical temperature profile in south-east corner with door and window openings during pre- and post-flashover

Figure 45b compares the heat fluxes in the post-flashover exposure. A similar relationship to the numerical models and the pre-flashover behavior was observed, where the floor heat flux was inversely correlated to scale and the wall and ceiling heat fluxes agreed well. The higher heat fluxes at the floor as the scale reduces may be in part due to more convection from the higher lower layer gas temperature at the smaller scales.

Figure 45b also shows there is a slight difference between the heat fluxes in the corner directly above the burner in the full and half scales. Unfortunately, data from the burner heat flux gauge was not available for the quarter scale window configuration experiment. However, comparison of the heat fluxes from tests with a non-combustible lining and a door in the pre-flashover and post-flashover regimes shown in Figure 42a and Figure 42b show a similar trend. In addition, the higher wall heat fluxes predicted in simulation (see Figure 21) were not measured experimentally (see Figure 42b).

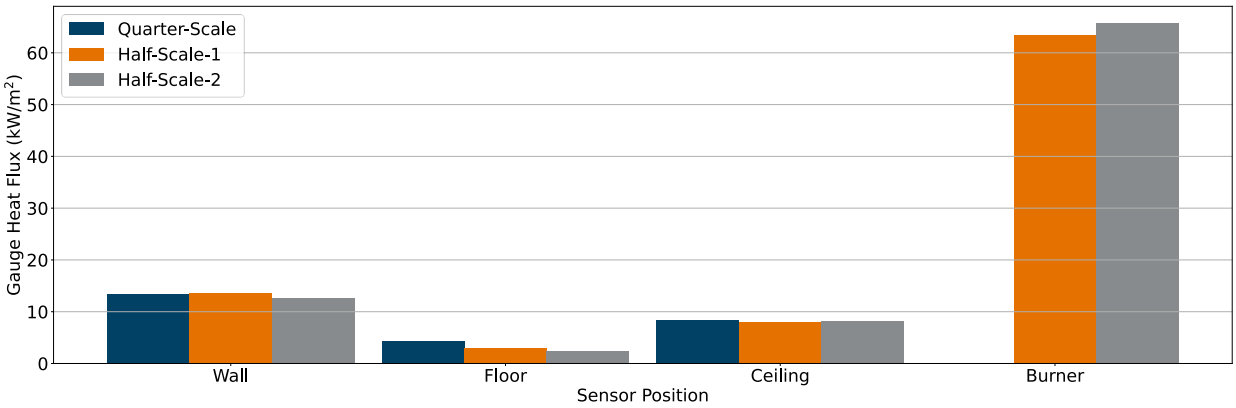

(a) Pre-flashover (quarter and half scales)

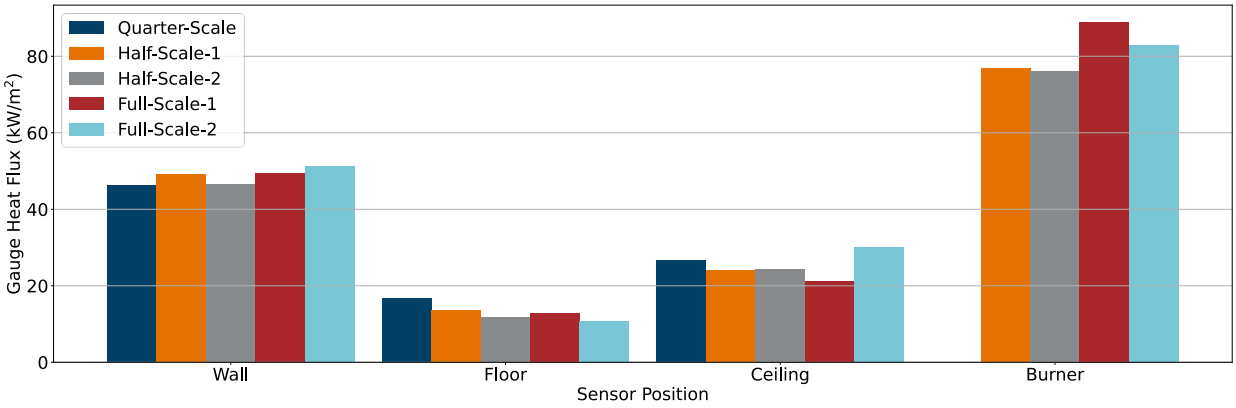

(b) Post-flashover (all scales)

Figure 45: Heat flux levels at different locations with door and window openings during pre- and post-flashover

Overall, these comparisons indicate that the reduced scale compartments were able to produce a similar compartment fire environment to the full-scale.

6.2 Combustible Lining Scaling

The focus of the combustible lining scenarios was to examine the capability of the scaling approach when the HRR was dependent on the feedback between combustibles and the room environment. The combustible lining test series (plywood and FRP) were compared directly at the quarter and half-scale.

The measured and full-scale equivalent (using Equation 1) HRR profile of the plywood experiments is provided in Figure 46. These results highlight the ability of the scaling approach to accurately predict the time-resolved profile of the HRR across scales for a growing fire that is spreading along a combustible surface. The corresponding compartment environment at the time of peak HRR (3 minutes) is provided in Figure 47 and Figure 48. The temperature profiles in both corners agreed across scales, with the upper layer temperature within 4 percent, lower layer temperatures within 4 and 7 percent (i.e., north-east and south-east, respectively), and full-scale equivalent interface heights within 17 and 12 percent (i.e., north-east and south-east, respectively). The average deviation in HRR was 3.8 percent and difference in total heat released was 3.7 percent.

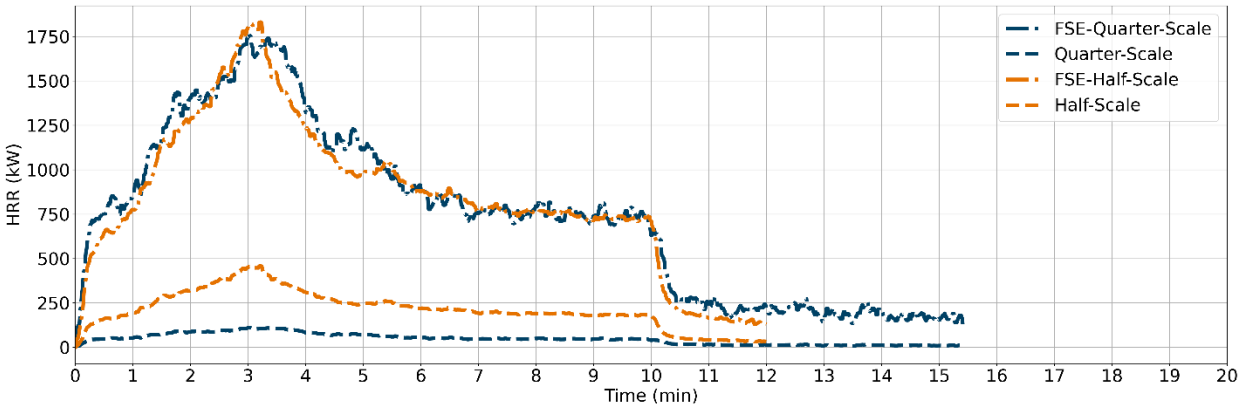

Figure 46: Comparison of full-scale equivalent HRR from plywood test configuration

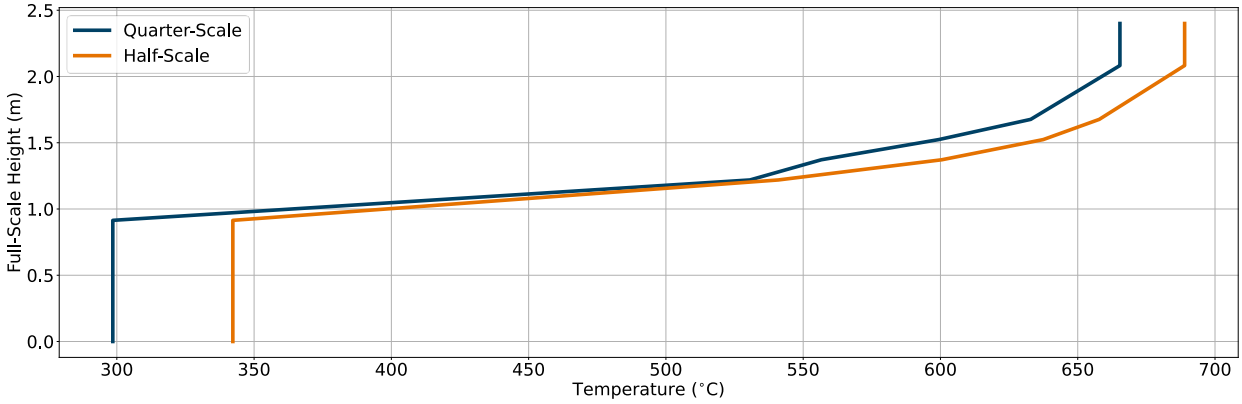

Figure 47: Comparison of temperature profile in south-east corner from plywood test configuration at a test time of 3 minutes

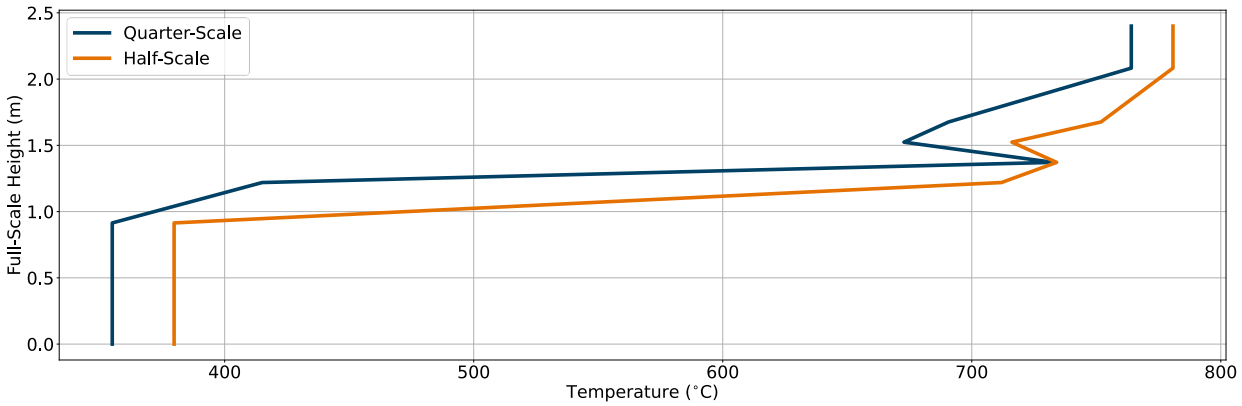

Figure 48: Comparison of temperature profile in north-east corner from plywood test configuration at a test time of 3 minutes

The measured and full-scale equivalent (using Equation 1) HRR profile of the FRP experiments is compared in Figure 49. The overall time-resolved profile of the HRR was similar across scales; however, there were a few key discrepancies observed. The quarter-scale HRR reached a higher initial peak of 800 kW during the first 2 minutes of exposure compared to the half-scale HRR at 650 kW. After 2 minutes the HRR from both scales continued to grow; however, the

half-scale grew at a faster rate reaching a peak value of 1,600 kW compared to the 1,400 kW peak in the quarter-scale.

The compartment fire environment at the transition time of 2 minutes is compared in Figure 50 and Figure 51. The temperature profiles indicate the half-scale had a higher temperature (~10 percent) in both the upper and lower layers at both locations. The increasing temperatures due to the higher HRR resulted in an increasing heat flux as well, as shown in Figure 52, with the half scale test having heat fluxes up to 38 percent higher than that in the quarter scale. These higher heat fluxes in the half scale increase the heat feedback to the surface which is in part why the fire growth increases. The test summary data provided in Appendix G shows that the full-scale equivalent 60 second average peak HRR was underpredicted by 18.0 percent, and the total heat released was 17.6 percent less. The average percent difference in full-scale equivalent HRR was 10.6 percent throughout the experiments.

Additional insight can be gained by comparing the heat fluxes from the plywood case where the HRR profile agreed well across scales. As seen in Figure 53, the heat flux to the floor was similar at both scales; however, the heat flux to the wall and ceiling was higher in the half scale (19 and 27 percent, respectively). The trends are the same in the two tests, but with larger differences in the FRP tests. These differences are possibly due to the increase in smoke production, or may be related to more material remaining on the surface for the test duration due to the lower burning rate.

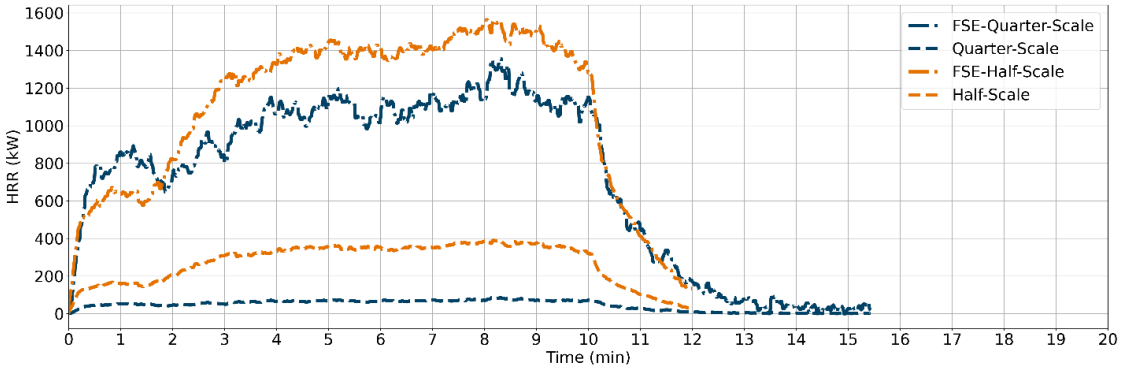

Figure 49: Comparison of full-scale equivalent HRR from FRP test configuration

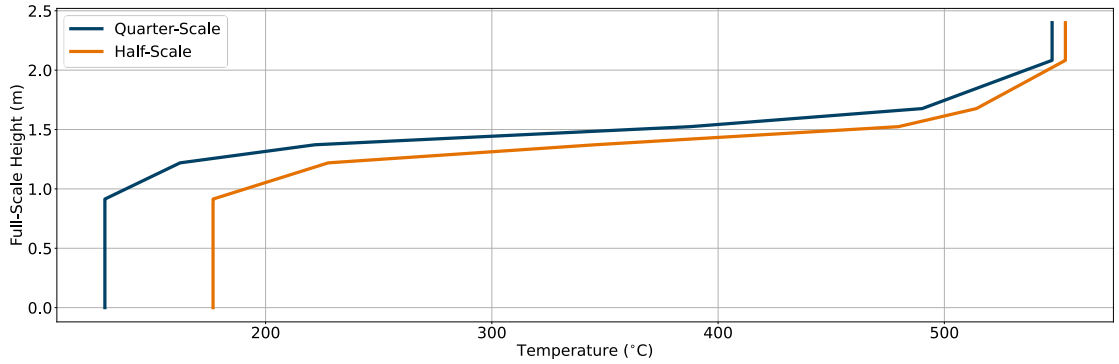

Figure 50: Comparison of temperature profile in south-east corner from FRP test configuration at a test time of 2 minutes

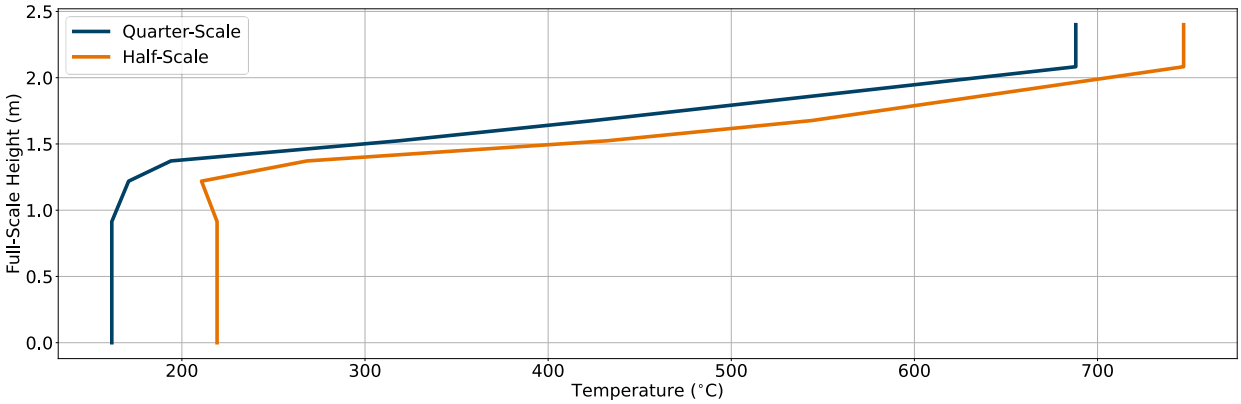

Figure 51: Comparison of temperature profile in north-east corner from FRP test configuration at a test time of 2 minutes

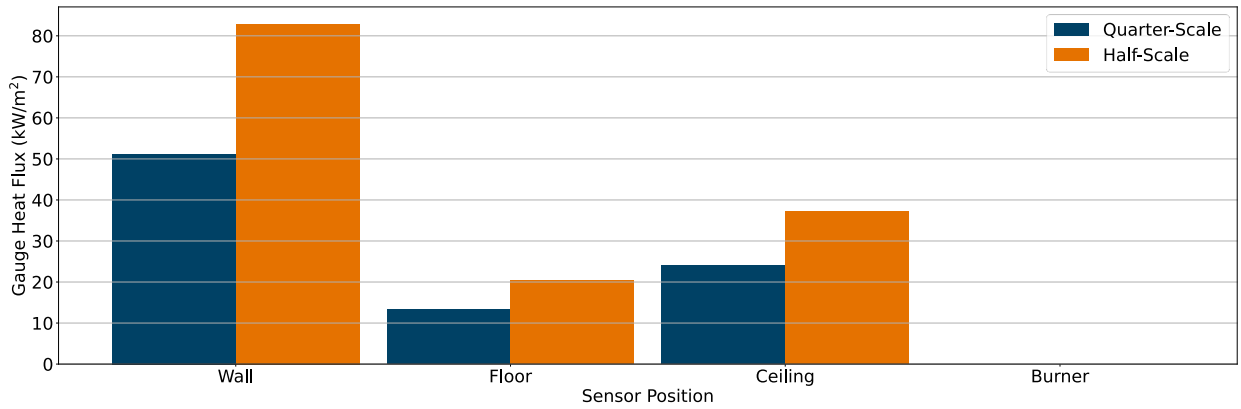

Figure 52: Comparison of heat fluxes from FRP test configuration at a test time of 2 minutes

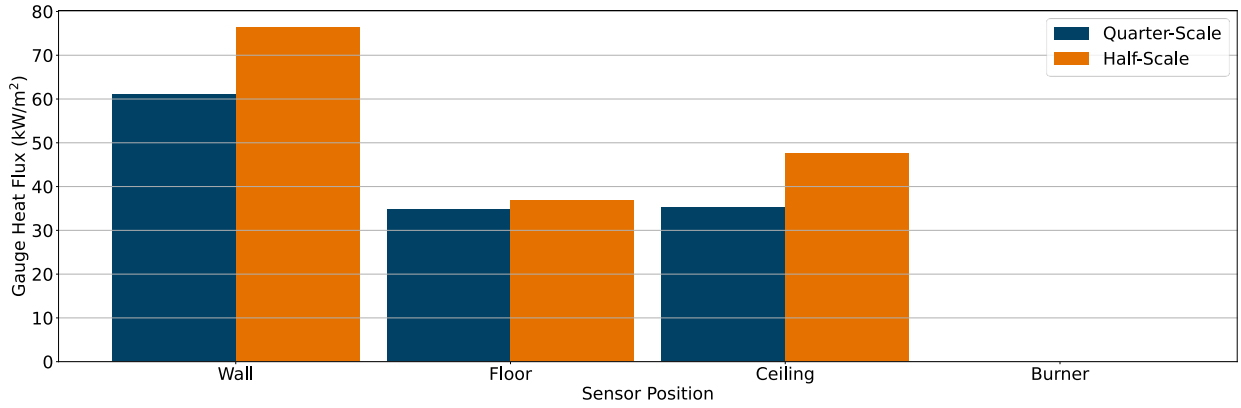

Figure 53: Comparison of heat fluxes from plywood test configuration at a test time of 3 minutes

While the time-resolved HRRs from the scaling approach may not be perfect with combustible linings, the observed differences are in line with experimental (8 percent) and numerical uncertainty (34 percent) in HRRs (Mcgrattan, K., Hostikka, S., Mcdermott, R. J., Floyd, J., Vanella, M., Weinschenk, C. G., & Overholt, K., J., 2019), and the repeatability of enclosure fire

tests conducted at the full-scale with 8–12 percent from (Sundström, B., 1996). These results indicate that the scaling approach presents a cost-effective alternative to full-scale testing.

6.3 Liquid Pool Fire Scaling

The measured and full-scale equivalent (using Equation 1) HRR profile of the JP-5 liquid pool fire experiments is compared in Figure 54. The time-resolved HRR profile with the liquid fuel source did not agree well across scales; however, there are some key observations, such as recall that the burning rate for a liquid fuel is directly related to the heat feedback from the flame back to the pool. The time-resolved heat flux measurements for the JP-5 experiments at quarter and half-scale are shown in Figure 55 and Figure 56, respectively.

The reduced-scale experiment took longer than the half-scale experiment to start its growth (6.5 minutes versus 2.5 minutes); however, it rapidly grew to a more intense fire than the half-scale, reaching a peak HRR twice as high as observed in the half-scale. Comparing the heat fluxes at a test time of 8 minutes shows that while the full-scale equivalent HRR is similar, the heat flux at each sensor was also similar. However, the heat flux to the floor in the quarter-scale continued to rise resulting in the liquid pool exceeding the peak burning behavior predicted with the analytical model in Section 2. With the scaling laws demonstrated in the non-combustible and combustible lining experiments, these results highlight that the scaling laws for the liquid pool fire were not adequate to capture all of the physics and need to be revisited.

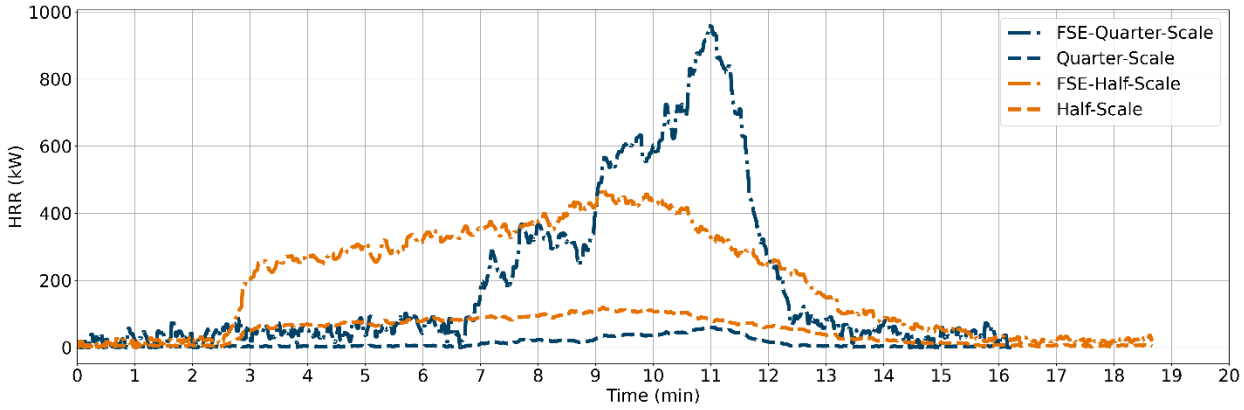

Figure 54: Comparison of full-scale equivalent HRR from JP-5 test configuration

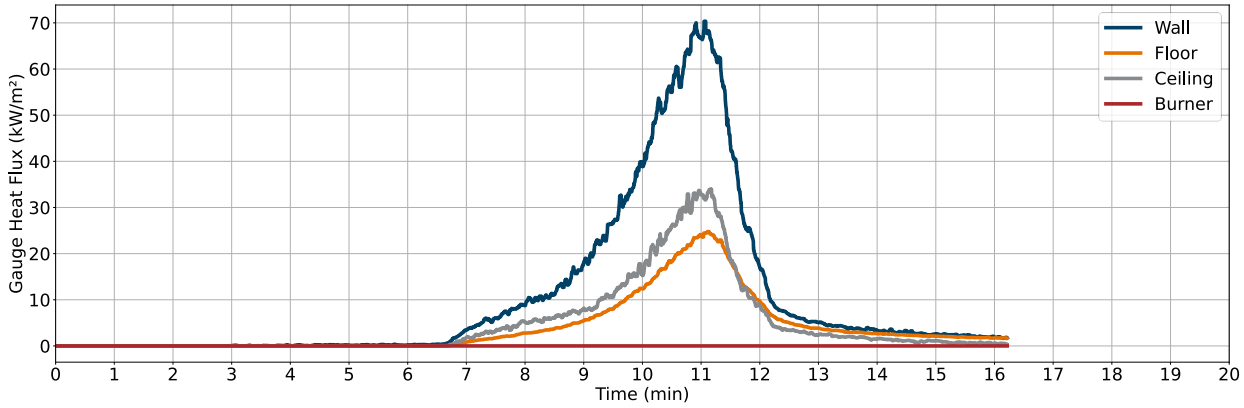

Figure 55: Comparisons of time-resolved heat flux from JP-5 test at quarter-scale

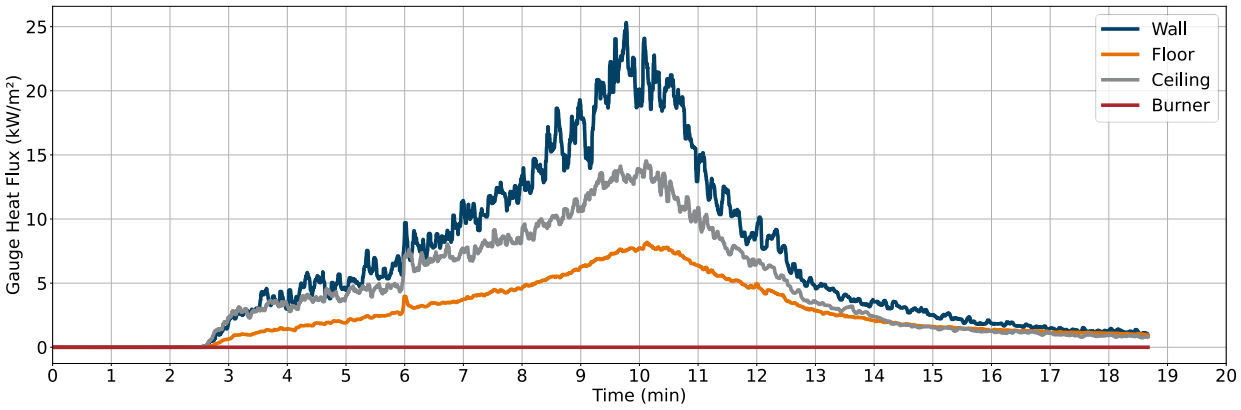

Figure 56: Comparisons of time-resolved heat flux from JP-5 test at half-scale

7. Conclusion

This research focused on evaluating scaling laws to reduce the size of experimental rail cars to predict the HRR history of rail cars. The scaling laws developed during Phase 1 of this research showed through simulation that scaling HRR based on material burning and maintaining ventilation has the potential to meet this need. This phase of the research focused on validating the capability of the scaling approach using live fire experiments. JH conducted a series of compartment fire tests at three scales (i.e., quarter, half, and full-scale) in a total of 17 tests (i.e., 14 unique configurations and 3 repeats). The measurements from these experiments were used to examine the capability of the scaling approach in each tested configuration. The repeated tests were used to better understand the test-to-test variability in fire behavior.

7.1 Findings

Pre-test simulations demonstrated that the scaling laws could provide similar fire environments across all scales, and scaling laws could be used to predict full-scale HRR within 20 percent for the planned test series. In addition, a method for predicting HRR of materials with a time varying heat exposure was created using scaling laws, and it is now implemented into the NIST FDS software as an option to predict material HRR with heat feedback from the fire environment.

The series of tests were used to evaluate the scaling laws. The following observations were made based on the test data:

1. The noncombustible lining tests demonstrated that the scaling laws can be used to produce similar upper-layer gas temperatures and heat fluxes in the upper part of the room across all scales. Lower-layer temperatures and heat flux to the floor increased with a decrease in scale.
2. The combustible lining tests had HRRs that could be related by the scaling laws to within 10.6 percent. HRRs were higher at larger scales.
3. Heat fluxes to combustible linings increased with an increase in scale, which caused the increase in HRR.
4. The liquid pool fires burned differently across the scales indicating that how the liquid pool burning was scaled in this research was not adequate and should be revisited.

7.2 Recommendation and Future Work

The scale modeling methodology and demonstration from this research was used as the basis to add scale model testing as an alternative method for predicting the HRR of rail cars to support emergency ventilation design in the upcoming revision to NFPA 130 (National Fire Protection Association, 2014). JH believes this research would benefit from an additional phase applying the validated scaling laws to predict the HRR profile in rail car geometries. The follow-up studies would include both detailed CFD simulations and experiments to quantify the impact of different geometric and material performance variations on the HRR time history of a rail car.

In this research effort, JH worked with NIST to incorporate a new method to predict material burning behavior into FDS based on cone calorimeter measurements which overcomes the difficulties of determining accurate decomposition kinetics parameters. Research needs to be

performed to validate this new material simulation approach with the room-corner test data generated in the FRA program.

The scaling laws validated in this work have previously focused on simplified compartment geometries. While a necessary first step in this analysis, rail cars include more complicated geometric and material configuration. Representative rail car geometries should be developed in the validated CFD simulation tool and used to demonstrate equivalent fire behavior across scales. In addition, the predictions should be used to quantify the impact of geometric and combustible material variations as well as show that the HRR can be measured at the test facilities. These results should be used to design a test matrix on full-scale and scale model rail cars.

Experimental validation of the scaling on rail car assemblies should then be conducted to demonstrate the effectiveness of the scaling approach on rail car geometries. This test series should include changes in ventilation conditions as well as combustible material variations. A blind pre-test simulation of each experiment should then be compared with the experimental data and analyzed to understand any differences between the model and measurements. The HRR of a full-scale rail car should then be predicted based on experimental data and FDS simulations. Statistical differences will be calculated, and analysis will be performed to understand any differences. At the conclusion of this work, a final methodology should be developed to perform scale model testing on rail cars and for recommendation into NFPA 130.

8. References

American National Standards Institute. (2017). *ANSI/UL 1715: Standard for Safety Fire Test of Interior Finish Material*. Retrieved from ANSI.

ASTM International. (2016). *ASTM E2067: Standard Practice for Full-Scale Oxygen Consumption Calorimetry Fire Tests.*

ASTM International. (2017). *E2257-17: Standard Test Method for Room Fire Test of Wall and Ceiling Materials and Assemblies*. Retrieved from ASTM.

Beyler, C. L. (2016). Flammability Limits of Premixed and Diffusion Flames. In *SFPE Handbook of Fire Protection Engineering* (pp. 529–553). New York, NY: Springer.

Bullen, M. L. (1976). A Combined Overall and Surface Energy Balance for Fully-Developed Ventilation-Controlled Liquid Fuel Fires in Compartments. *Fire Technology, 22*(3), 257–259.

Bundy, M. F., Hamins, A. P., Johnsson, E. L., Kim, S. C., Ko, G., & Lenhert, D. B. (2007). *Measurements of Heat and Combustion Products in Reduced-Scale Ventilation-Limited Compartment Fires.* Gaithersburg, MD: U.S. Department of Commerce, National Institute of Standards and Technology.

Code of Federal Regulations. (2014). *Title 49 CFR Section 238.103–Fire Safety, pp. 1–28*. Retrieved from National Archives.

Dingyi, H. (1987). Evaluation of quarter-scale compartment fire modeling for constant and stepped heat inputs. *Fire and Materials, 11*(4), 179–190.

Drysdale, D. (2011a). The Post-Flashover Compartment Fire. In *An Introduction to Fire Dynamics, Third Edition* (pp. 387–439).

Drysdale, D. (2011b). The Pre-Flashover Compartment Fire. In *An Introduction to Fire Dynamics, Third Edition* (pp. 349–386).

Grosshandler, W. L. (1993). *RADCAL: A Narrow-Band Model for Radiation Calculations in a Combustion Environment.* Report No. QC 100 U5753 #1402, Gaithersburg, MD: U.S. Department of Commerce, National Institute of Standards and Technology.

Gwynne, S. M. V., & Boyce, K. E. (2016). Engineering Data. In *SFPE Handbook of Fire Protection Engineering* (pp. 2429–2551).

International Organizations for Standarization. (1993). *Fire tests - Full-scale room test for surface products.* Report No. ISO 9705, Geneva, Switzerland: International Organizations for Standarization.

Janssens, M., & Tran, H. C. (1992). Data reduction of room tests for zone model validation. *Journal of Fire Sciences*, 528–555.

Lee, B. T. (1985). Quarter-scale room-fire tests of interior finishes. *Fire and Materials, 9*, 185–191.

Li, Y. Z., Ingason, H., & Lönnermark, A. (2013). *Correlations Between Different Scales of Metro Carriage Fire Tests.* The METRO Project. SP Report 2013:13, Sweden: SP Technical Research Institute of Sweden.

Luo, C., et al. (2019). *Heat Release Rate Requirements for Railcar Interior Finish.* Office of Research, Development and Technology. Technical Report No. DOT/FRA/ORD-19/39, Washington, DC: U.S. Department of Transportation, Federal Railroad Administration.

Mcgrattan, K., Hostikka, S., Mcdermott, R. J., Floyd, J., Vanella, M., Weinschenk, C. G., & Overholt, K., J. (2019). *Fire Dynamics Simulator Technical Reference Guide Volume 3: Validation.* NIST Special Publication 1018-1, Gaithersburg, MD: National Institute of Standards and Technology.

McGrattan, K., Hostikka, S., Mcdermott, R. J., Floyd, J., Weinschenk, C., & Overholt, K. (2019). *Fire Dynamics Simulator Technical Reference Guide Volume 3: Validation.* NIST Special Publication 1019, Gaithersburg, MD: National Institute of Standards and Technology.

McGrattan, K., Hostikka, S., Mcdermott, R. J., Vanella, M., Weinschenk, C. G., & Overhold, K. (2019). *Fire Dynamics Simulator Technical Reference Guide Volume 1: Mathematical Model.* NIST Special Publication 1018-1, Gaithersburg, MD: National Institute of Standards and Technolog.

McGrattan, K., Mcdermott, R. J., Hostikka, S., Floyd, J., Weinschenk, C., & Overholt, K. (2019). *Fire Dynamics Simulator User's Guide.* NIST Special Publication 1019-1, Gaithersbur, MD: National Institute of Standards and Technology.

National Fire Protection Association. (2014). *NFPA 130: Standard for Fixed Guideway Transit and Passenger Rail Systems.* Quincy, MA: NFPA.

National Fire Protection Association. (2015). *NFPA 286: Standard Methods of Fire Tests for Evaluating Contribution of Wall and Ceiling Interior Finish to Room Fire Growth.* Quincy, MA: NFPA.

Quintiere, J. G. (1989). Scaling applications in fire research. *Fire Safety Journal, 15*(1), 3–29.

Sundström, B. (1996). *Fire Safety of Upholstered Furniture: The Final Report on the CBUF Research Programme.* Brussels: Interscience Communication Limited.

Tanaka, T. (2016). Vent Flows. In *SFPE Handbook of Fire Protection Engineering: Fifth Edition* (pp. 459–460). Springer. doi:10.1007/978-1-4939-2565-0.

The Pre-Flashover Compartment Fire. (2011b). In T. E. An Introduction to Fire Dynamics.

Yang, F., Hodges, J., Rippe, C., Kraft, S., & Lattimer, B. (2020). *Predicting Fully-Developed Passenger Rail Car Fire Heat Release Rate.* Office of Research, Development and Technology. Technical Report No. DOT/FRA/ORD-20/32, Washington, DC: U.S. Department of Transportation, Federal Railroad Administration.

Zabetakis, M. G., & Burgess, D. S. (1961). *Research on the Hazards Associated with the Production and Handling of Liquid Hydrogen.* Washington, DC: U.S. Department of the Interior.

Appendix A.
Test Matrix Development

Inert Boundary Heat Release Rates

Two HRR levels were used in each of the non-combustible propane fire scenarios, which were designed to approximate pre-flashover and post-flashover conditions. The HRR that could cause flashover was calculated using the McCaffrey, Quintiere, and Harkleroad (MQH) relationship presented by Drysdale (2011b) in Equation A-1

$$\dot{Q}_{FO} = 610 \times \left(h_k A_T V_W V_H{}^{3/2}\right)^{1/2} \tag{A-1}$$

where $\dot{Q}_{FO}$ is the HRR required to reach flashover (defined as a temperature rise of 932 °F (500 °C) in kW, h_k is the effective heat transfer coefficient of the compartment boundaries in kW/m^2-K, A_T is the surface area of the walls and ceiling excluding the ventilation openings in m^2, V_W is the ventilation opening width in m, and V_H is the ventilation opening height in m. The effective heat transfer coefficient was calculated assuming a thermally thin boundary in Equation A-2.

$$h_k = \frac{k}{\delta} \tag{A-2}$$

where k is the thermal conductivity of the wall linings (0.17 W/m-K), and δ is the boundary thickness in m. The wall and ceiling surface area was calculated using Equation A-3.

$$A_T = 2s^2 \text{ x } (C_L C_W + C_L C_H + C_W C_H) - s^a s^b \text{ x } (D_W D_H + W_W W_H) \tag{A-3}$$

where s is the scale ratio (i.e., 0.25 for quarter scale, 0.50 for half scale, 1.0 for full-scale), C designates a compartment side length, D designates a door side length, W designates a window side length, the subscripts L, W, and H designate length, width and height, and a and b are the scaling coefficients from Equation 4 through Equation 7. The ventilation opening term in Equation A-1 was calculated using Equation A-4:

$$V_W V_H^{3/2} = D_W D_H^{3/2} + W_W W_H^{3/2} \tag{A-4}$$

The resulting HRR required to cause flashover was 640 kW and 680 kW for the full-scale with and without a window. An additional factor of 40 kW was added to the window HRR at the full-scale to account for the uncertainties in the MQH relationship with multiple ventilation openings. Thus, the HRR used for the full-scale window scenario was 720 kW. The pre-flashover HRR was selected to be half the post-flashover HRR of the non-combustible door configuration, 320 kW, for both the door and door-window configuration to allow comparison of this stage across configurations.

Liquid Fuel HRRs

The size and depth of the liquid pool was designed to provide a similar peak HRR and burning duration to the gas burner experiments. The HRR of the JP-5 fuel was calculated using Equation A-5.

$$\dot{Q}_{peak} = B_L^2 \dot{m}'' \Delta H_c \tag{A-5}$$

where B_L is the side length of the pan in m, $\dot{m}''$ is the burning rate of the liquid pool in kg/m^2-s, and ΔH_c is the heat of combustion of the liquid, 43,000 kJ/kg for JP-5. The burning rate of the liquid pool was calculated using Equation A-6.

$$\dot{m}'' = \left(q''_{free,net} + q''_{layer}\right)\Delta H_g \tag{A-6}$$

where $q''_{free,net}$ is the net heat flux from the burning volatiles in the air to the liquid surface, q''_{layer} is the gauge heat flux from the layer to the liquid surface, and ΔH_g is the heat of gasification of the liquid, 700 kJ/kg for JP-5. The heat flux from the layer to the liquid surface was assumed to be similar to the heat flux to the floor measured experimentally in the non-combustible door configuration at the quarter-scale, 4 kW/m^2 in the pre-flashover regime and 14 kW/m^2 in the post-flashover regime. The free burning net heat flux was calculated in Equation A-7 based on the steady burning rate and the heat of gasification,

$$q''_{free,net} = \frac{\dot{m}''_s}{\Delta H_g} \tag{A-7}$$

where $\dot{m}''_s$ is the steady burning rate in kg/m^2-s. The steady burning rate was calculated based on the method presented by Equation A-8 (Zabetakis, M. G., & Burgess, D. S., 1961),

$$\dot{m}''_s = \dot{m}''_\infty(1 - \exp(-k\beta D)) \tag{A-8}$$

where $k\beta$ is the extinction coefficient in m^{-1} multiplied by a unitless mean beam length corrector, 1.6 m^{-1} for JP-5, D is the equal area diameter of a circular liquid pool in m, and $\dot{m}''_\infty$ is the maximum burning rate of the liquid fuel, 0.054 kg/m^2-s for JP-5. The equal area diameter of the pool was defined as shown in Equation A-9:

$$D = \left(\frac{4}{\pi}B_L^2\right)^{1/2} \tag{A-9}$$

The burner side length to use in the experiments to achieve the peak HRR was calculated at each scale using Equation A-5 through Equation A-9. The resulting burner side length at each scale was: 1:4 scale 6.5 in (0.17 m), 1:2 scale 12 in (0.30 m), 1:1 scale 22 in (0.56 m). The predicted HRR at each scale was: 1:4 scale pre-flashover 21 kW post-flashover 38 kW, 1:2 scale pre-flashover 106 kW post-flashover 163 kW, and 1:1 scale pre-flashover 505 kW post-flashover 697 kW.

The depth of the liquid pool for each scale was calculated using Equation A-10

$$B_D = \left(\dot{Q}_{POST}\Delta t_{POST} + \dot{Q}_{PRE}\Delta t_{PRE}\right)\Delta H_c^{-1}\rho^{-1}B_L^{-2} \tag{A-10}$$

where B_D is the depth of the liquid pool in m, Δt is the target burning duration, ρ is the density of the liquid, 810 kg/m^3 for JP-5, and the subscripts PRE and POST designated the pre-flashover and post-flashover target HRRs in kW, respectively. The resulting fuel depth at each scale was: 1:4 scale 0.75 in (18.8 mm), 1:2 scale 0.98 in (25.0 mm), 1:1 scale 1.31 in (33.2 mm).

Appendix B.
Compartment Construction

The plywood backing layer was fastened directly to the wood frame using wood screws. All subsequent sheet materials were fastened to the plywood backing layer using wood screws. The lining material was fastened using wood screws and 2 in. (50.8 mm) diameter flat steel fender washers. The screw pattern nominally adhered to that shown in Figure B-1 (walls) and Figure B-2 (ceiling). Gypsum wallboard was fastened to the exterior of the compartment near the door and window to prevent damage to the structure as flames roll out of these openings. Additionally, ceramic fiber insulation was applied in cracks and near instrumentation where deemed necessary. Staggered materials were used to ensure that the edges of the compartment were well-sealed. In addition, noncombustible cement board was used at the edges of the door and window, and joints were sealed with high temperature construction caulk.

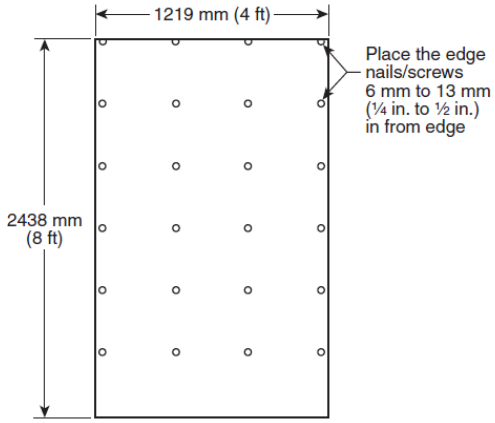

Figure B-1: Attachment details for vertical samples (walls) (National Fire Protection Association, 2015)

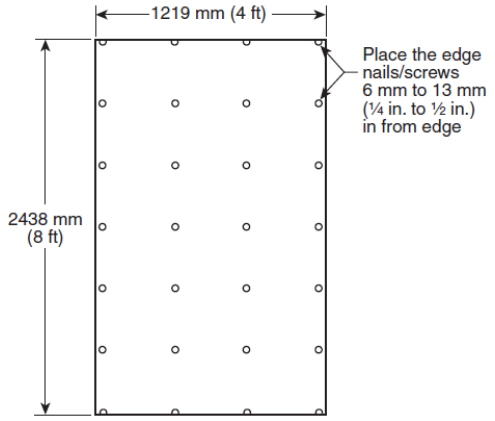

Figure B-2: Attachment details for horizontal samples (ceiling) (National Fire Protection Association, 2015)

Appendix C.
Data Processing

Gas Velocity

Gas velocities were calculated from measured temperature and differential pressure at each bidirectional probe (BDVP) location, i, according to Equation C-1 through Equation C-3:

$$\dot{m}_i'' = \frac{\rho_i}{k_i}\sqrt{\frac{2\Delta P_i}{\rho_i}} \tag{C-1}$$

$$v = \frac{\dot{m}_i''}{\rho_i} = \frac{1}{k_i}\sqrt{\frac{2\Delta P_i}{\rho_i}} \tag{C-2}$$

where

$$\rho_i = \frac{P_i M_{gas}}{RT_i} \tag{C-3}$$

The absolute pressure P_i was assumed to be equal at all BDVP locations at the compartment openings, and the gas composition was assumed to be air (M_{gas} = 28.96 g/mol). The Reynolds number correction factor, k_i, has a nominal value of 1.08; however, prior to the start of the test series, the correction factor was determined for each BDVP relative to a hot wire anemometer.

Duct Flow Calibration

In the reduced-scale testing at the JH facility, the flow profile within the exhaust duct was calibrated and the duct flow coefficient was determined over a range of flow rates. This procedure is outlined below.

At a location near the bidirectional probe pressure taps in the duct, a series of velocity measurements were taken over the width of the duct using a handheld unidirectional hot wire anemometer, and the average velocity $(\dot{v}_{\text{avg}})$ across the profile is calculated. This was repeated at several different exhaust flow rates, based on different frequency settings (f) on the variable-speed exhaust fan. During these tests, differential pressure of the bidirectional probe (ΔP_e) and temperature (T_e) in the duct were also measured. A relationship was developed between the volume flow rate of gases in the duct (based on velocity measurements) and fan frequency.

For this calibration the gas in the duct was composed of moist air, which is assumed to have the same composition as that of ambient. Density of the moist air in the duct (Equation C-4) was computed from measurements of the ambient pressure ($P°$) and relative humidity ($H°$), as well as the temperature of the moist air in the duct (T_e). Molar mass of the moist air ($M°_a$) was calculated from Equation C-5, where the molar masses of water vapor (M_{H2O}) and dry air (M_a) were taken to be 18.02 g/mol and 28.96 g/mol, respectively. The mole fraction of water vapor in the duct was computed from Equation C-6, where the Antoine equation (Equation C-7) was used to deduce the saturation vapor pressure of water ($P°_{\text{sat}}$). The value used for the universal gas constant (R) was 8.314 J/mol·K.

$$^{\circ}\rho_{a,e} = \frac{P^{\circ}M^{\circ}_{a}}{RT^{\circ}_{e}} \quad \text{(C-4)}$$

$$M^{\circ}_{a} = X^{\circ}_{H20}M_{H20} + (1 - X^{\circ}_{H20})M_{a} \quad \text{(C-5)}$$

$$X^{\circ}_{H20} = \frac{P^{\circ}_{H20}}{P^{\circ}} = \frac{P^{\circ}_{\text{sat}}H^{\circ}}{P^{\circ}} \quad \text{(C-6)}$$

$$\log_{10}\left(\frac{P^{\circ}_{\text{sat}}}{133.322}\right) = 8.07131 - \frac{1730.63}{233.426 + T^{\circ}_{e}} \quad \text{(C-7)}$$

Volume flow rate of gases in the duct was calculated from the measured average velocity and duct diameter (Equation C-8), and the mass flow rate was calculated as the product of volume flow rate and density of the moist air in the duct (Equation C-9).

$$\dot{V}_{e} = \dot{v}_{\text{avg}}\frac{\pi}{4}D^{2} \quad \text{(C-8)}$$

$$\dot{m}_{e} = \rho^{\circ}_{a,e}\dot{V}_{e} \quad \text{(C-9)}$$

The average mass flow rate of gases in the duct corresponded to the frequency setting of the variable speed drive. A total of four measurements were taken (e.g., f = 30, 40, 50, and 60 Hz). For each measurement of mass flow rate, the duct flow coefficient C_f was calculated via Equation C-10:

$$\dot{m}_{e} = C_{f}\sqrt{\frac{\Delta P_{e}}{T_{e}}} \quad \text{(C-10)}$$

where $\dot{m}_e$ was the mass flow rate of gases in the duct, T_e was the gas temperature in the duct, and ΔP_e was the bidirectional probe pressure differential. The subscript in C_f denotes its presumed dependence on the exhaust fan flow rate, thus on the frequency setting. The flow C-factor used in this testing was 4.9 (kg-m-K)$^{1/2}$ at the quarter-scale and 5.4 (kg-m-K)$^{1/2}$ at the half-scale.

The procedure used at the JH facility requires an independent measurement of the flow velocity within the exhaust ducting to determine the flow C-factor. Since this measurement was not available at the CBD facility, an alternative approach was used to determine the flow C-factor (ASTM International, 2016). A calibration burn with propane at a fixed HRR of 720 kW was used as the independent measurement. Calorimetry based on the generation of combustion gases, depletion of oxygen, and mass flow rate from an assumed flow C-factor were used to measure the HRR, see the following sections for a discussion of calorimetry. The C-factor was iteratively adjusted until the calorimetry measured HRR aligned with the specified burner HRR. This resulted in a total C-factor of 18.4. This was divided into a HRR C-factor of 1.2 which could vary from day to day and a flow C-factor of 15.3 (kg-m-K)$^{1/2}$.

Gas Sampling Delay Times

Measurements of gas composition by the analyzers lag behind the actual gas composition in the duct at a given time. This is attributed to two factors: analyzer response (i.e., a dynamic effect inherent in and unique to each analyzer) and transit time (i.e., the time taken for a gas sample to be pumped from the sampling location to the analyzer location).

For this test series the dynamic response of the analyzers was neglected, and constant values were assumed. Response times were measured via direct gas injection to the analyzers (i.e., N_2 for the oxygen analyzer, CO and CO_2 for the CO and CO_2 analyzers, respectively). This measurement was completed once for each analyzer.

Transit times were determined by conducting a propane burner test, per the "apparent response" methodology (i.e., time to first change in measured O_2). The burner was centered under the hood, outside of the compartment. The burner HRR was set to 300 kW at the JH facility and 750 kW at the CBD facility, which is consistent with the values used for daily HRR calibrations. This calibration was completed once at each facility.

The total delay time for each analyzer was then the sum of response and transit times. For all tests the measured gas concentrations have been time-shifted by these values.

Calorimetry

HRR, total heat release, smoke production rate, total smoke production, and CO, CO_2, and soot yields were calculated from duct measurements (e.g., gas composition, light obscuration, duct temperature, duct BDVP differential pressure) in accordance with the methodology laid out in ISO 9705, Annex E (International Organizations for Standarization, 1993).

The HRR was calculated using Equation C-11:

$$\dot{Q} = E\dot{V}_{298}\chi_{O_2}^{a}\left(\frac{\phi}{\phi(\alpha-1)+1}\right) - \frac{E}{E_{C_3H_8}}\dot{Q}_B \tag{C-11}$$

where $\dot{Q}$ is the HRR from calorimetry in kW, E is the heat release per volume of oxygen consumed in kJ/m^3 (i.e., 17,200 kJ/m^3 for a generic combustion product), $\chi_{O_2}^{a}$ is the ambient mole fraction of oxygen including water vapor, α is the expansion factor due to chemical reaction of the air that is depleted of its oxygen (1.105 for combustion of a tested product), $E_{C_3H_8}$ is the heat release per volume of oxygen consumed from propane (16,800 kJ/m^3), $\dot{Q}_B$ is the HRR of the burner in kW, and ϕ is the oxygen depletion factor. The oxygen depletion factor is calculated in Equation C-12:

$$\phi = \frac{\chi_{O_2}^{0}(1-\chi_{CO_2}) - \chi_{O_2}(1-\chi_{CO_2}^{0})}{\chi_{O_2}^{0}(1-\chi_{CO_2}-\chi_{O_2})} \tag{C-12}$$

where χ_{O_2} is the mole fraction of oxygen, χ_{CO_2} is the mole fraction of carbon dioxide, and the superscript ^{0} denotes the initial value of the gas analyzer reading during the test.

The calorimeter was calibrated each day before testing as described in Section 3.5.1.

Two-Layer Compartment Environment

During a compartment fire, hot combustion gases collect in the upper space of the enclosure due to the high temperatures of the smoke resulting in a buoyantly stable smoke layer. Ambient air enters the lower space of the room through ventilation, leading to a lower layer which is generally cooler and less dense than the smoke layer. One way to quantify the compartment fire dynamics is to calculate the average temperature in this upper layer, the average temperature in the lower layer (below the smoke) and identify the height at which the transition between layers occurs. Reducing the thermocouple tree data to these key parameters describing the compartment fire dynamics facilitates the comparison of experiments across scales. The method suggested by Janssens was used to calculate the layer average temperatures and interface height in this work (Janssens, M., & Tran, H. C., 1992). The interface height is calculated using Equations C-13 through C-16,

$$I_1 = (H - z_{int})T_u + z_{int}T_l \tag{C-13}$$

$$I_2 = (H - z_{int})\frac{1}{T_u} + z_{int}\frac{1}{T_l} = \int_0^H \frac{1}{T(z)}dz \tag{C-14}$$

$$z_{int} = \frac{T_l(I_1 I_2 - H^2)}{I_1 + I_2 T_l^2 - 2T_l H} \tag{C-15}$$

$$T_u = \frac{1}{(H - z_{int})}\int_{z_{int}}^H T(z)dz \tag{C-16}$$

where H is the total height in m, z_{int} is the interface height in m, T_u is the upper layer gas temperature in K, T_l is the lower layer temperature in K (taken to be equal to the lowest temperature measured in the thermocouple tree), and z is the height above the floor in m.

The upper- and lower-layer temperatures and interface heights were calculated using Equations C-13 through C-16 using the average temperatures within each fixed HRR interval, neglecting the first and last minute within each time interval (i.e., during the first 5 minute exposure, each thermocouple measurement was averaged from 1 to 4 minutes).

Appendix D.
Pre-Test Simulations Details

The following sections provide an overview of the computational fluid dynamics fire model used in the pre-test simulations as well as present the results of the grid sensitivity study for this work.

Fire Dynamics Simulator

FDS is a general-purpose low-speed (Mach number < 0.3) CFD software developed by the National Institute of Standards and Technology which is primarily designed to model buoyantly driven flows typical of diffusion flames (McGrattan, K., Hostikka, S., Mcdermott, R. J., Vanella, M., Weinschenk, C. G., & Overhold, K., 2019; McGrattan, K., Mcdermott, R. J., Hostikka, S., Floyd, J., Weinschenk, C., & Overholt, K., 2019). By solving a set of partial differential equations asserting conservation of mass, momentum, and energy in each grid cell as well as a radiation transport equation, the software predicts the time-evolution of the gas temperature, velocities, and species concentrations in each grid cell as well as heat transfer to solid surfaces. An overview of the sub-models in FDS used in this analysis are summarized in the following subsections.

Turbulence Model

Similar to other CFD software, FDS numerically solves the Navier-Stokes equations which are the set of partial differential equations for the transport of mass, momentum, and energy by a fluid acting as a continuum. In this context a continuum means that the fluid density is high enough that molecule-molecule interactions are not modeled by the equations outside of bulk physical quantities. Typically, FDS simulations are conducted using the large eddy simulation (LES) method. In this mode of operation, the grid cells are not small enough to fully resolve the diffusive fluxes of heat and mass on the grid. As a result, a subgrid model is needed to characterize the dissipation of energy from smaller eddies. The Deardorff subgrid turbulence model is the default turbulence model in FDS, which was selected for this analysis due to the agreement with full-scale experiments (Mcgrattan, K., Hostikka, S., Mcdermott, R. J., Floyd, J., Vanella, M., Weinschenk, C. G., & Overholt, K., J., 2019).

Pressure Solver

One of the equations in the Navier-Stokes system of equations under the low Mach number approximation is the pressure Poisson equation. The pressure Poisson equation in FDS is solved using a fast Fourier transform (FFT). The pressure solver operates globally in the model (the solution at an individual point depends on the solution everywhere else in the domain). However, the computational domain in FDS is often split into smaller meshes to reduce the computational time required by the model. In this configuration the global pressure solution is approximated by independently solving the pressure within each mesh. The local pressure solution is iteratively solved within each mesh until the difference in the pressure solution at the mesh boundaries is less than a pre-defined threshold. The default convergence criteria in FDS can be coarse in some applications which can lead to errors at mesh boundaries growing over time. In this work the error tolerances at the mesh boundaries were decreased to reduce this impact. A velocity error tolerance of 0.01 m/s and a maximum number of pressure iterations of 100 at each time step were used.

Radiation Transport

FDS solves an additional transport equation for gray gas radiation through an absorbing, emitting, but not scattering medium. The radiation transport equation is solved using a finite volume method similar to the convective transport equations. Each grid cell is discretized into a number of discrete radiation angles, with the total emission split among the different angles. The absorption along each angle is calculated based on the absorption coefficient in adjacent grid cells. The absorption coefficient is calculated based on species concentration, temperature, and an assumed radiative path length using an external model, RadCal (Grosshandler, W. L., 1993). At the LES grid scales, the cell-averaged gas temperatures within the flaming regions are smeared due to the flame thickness (i.e., on the order of 0.1 cm) not being resolved. The fourth power dependence on temperature in the radiation emission leads to an underprediction in the radiant emission in the flaming regions. This underprediction is corrected using a corrective factor based on the reaction rate in a specific cell and a globally defined radiative fraction which is a property of the gas phase combustion reaction.

Combustion Model

The combustion model used in this analysis was a single-step, mixing-controlled combustion. In this model, the reaction is assumed to occur infinitely fast, which means whenever gaseous fuel and oxygen are present in the same grid cell, they are assumed to react instantly until either the fuel is consumed or oxygen concentration in the cell reaches the lower flammability limit. The lower flammability limit is based on the limiting oxygen index concept discussed by (Beyler, C. L., 2016). FDS can be used to predict piloted and unpiloted ignition through the use of an autoignition temperature. Piloted ignition was used in this analysis.

FDS simulations typically limit the gas phase combustion to a single reaction to reduce the number of transport equations in the solver. When operating in this mode, combustible fuel in the air is stored as a single gas phase species specified by the gas phase reaction. The quantity of fuel that is injected into the gas phase from other reactions (such as the decomposition of the lining materials) is scaled according to the ratio of the heat of combustions of the two materials.

The gas phase reaction used for all models involving propane used a CO yield of 0.005 g/g, a soot yield of 0.024 g/g, a heat of combustion of 46,460 kJ/kg, and a radiative fraction of 0.35, yielding a chemical formula shown in Equation D-1:

$$C_3H_8 + 4.9063\ O_2 \quad 2.9048\ CO_2 + 3.9952\ H_2O + 0.0079\ CO + 0.0970\ Soot \qquad \text{(D-1)}$$

The gas phase reaction used for all models involving JP-5 used a CO yield of 0 g/g, a soot yield of 0.04 g/g, a heat of combustion of 44,100 kJ/kg, and a radiative fraction of 0.40, yielding a chemical formula shown in Equation D-2:

$$C_{12}H_{26} + 17.92\ O_2 \quad 11.44\ CO_2 + 12.97\ H_2O + 0.00\ CO + 0.62\ Soot \qquad \text{(D-2)}$$

The composition of soot was assumed to be a mixture of 90 percent carbon and 10 percent hydrogen in all models.

Solid Boundaries

Solid boundaries in FDS are handled using a simple immersed boundary method. A subgrid model is needed to predict convection heat transfer since the boundary layer near the wall is not resolved. FDS contains a number of different correlations for computing the heat transfer

coefficient to surfaces. The default approach used in FDS is to compute a natural and a forced convection heat transfer coefficient using flat plate heat transfer correlations where FDS picks the larger number of the two correlations. This model was used in this analysis.

Pyrolysis Model

FDS has two main approaches to modeling the decomposition (or pyrolysis) of solids (McGrattan, K., Mcdermott, R. J., Hostikka, S., Floyd, J., Weinschenk, C., & Overholt, K., 2019). The simplest model specifies the decomposition rate of the material directly based on bench-scale test data (i.e., HRRPUA measurements from cone calorimeter testing). Ignition is assumed to occur at any solid grid cell which exceeds its ignition temperature. Once ignition occurs, the material decomposes following the prescribed profile from test data. This model performs relatively well when the thermal exposure does relatively well in over-ventilated configurations; however, due to the large impact ventilation has on the thermal exposure in post-flashover compartments, this model is not well suited to predict these HRRs.

An alternative model available in FDS bases the rate of decomposition of the material on the surface temperature, fuel concentration, and oxygen concentration. In this model, the reaction rate is represented in an Arrhenius form shown in Equations D-3 through D-5:

$$\frac{dY_i}{dt} = -\sum_{j=1}^{N_{r,i}} r_{ij} + \sum_{i'}^{N_m} \sum_{j=1}^{N_{r,i'}} \nu_{i'j} r_{i'j} \quad (i' \neq i) \tag{D-3}$$

$$r_{ij} = A_{ij} Y_i^{n_{s,ij}} \exp\left(-\frac{E_{ij}}{RT_s}\right) X_{O_2}^{n_{O_2,ij}} \tag{D-4}$$

$$Y_i = \left(\frac{\rho_i}{\rho(0)}\right) \tag{D-5}$$

where, Y_i is the mass fraction of material i in g/g, t is time in s, j is the reaction number, Nr,i is the number of reactions for a material, r_{ij} is the reaction rate in s^{-1} of material i undergoing reaction j, N_m is the number of all reactions, $N_{r,i'}$ is the number of reactions in other materials, $v_{si'j}$ is the material i yielded from other reactions, A_{ij} is the pre-exponential factor of material i during reaction j in s^{-1}, n_s is the reaction order, E is the activation energy in J/mol, R is the universal gas constant in J/mol-K, T_s is the surface temperature, X_{O2} is the oxygen concentration at the surface, $n_{o2,ij}$ is the reaction power for material oxidation reactions, ρ_i is the density of material I, and $\rho(0)$ is the initial density of material i.

A key advantage of the Arrhenius form pyrolysis model over the simplified prescribed decomposition model is the capability to consider the impact of changes in thermal exposure and oxygen concentration on the rate of decomposition. The primary difficulty using this model is there are several material and reaction properties that must be specified. The Arrhenius pyrolysis model was used to model the decomposition of the combustible linings in this work. The simple prescribed profile model was used to model the target HRR profile of the initiating fuel source.

The following two lining materials were used in this work and were previously characterized by JH (Luo, C., et al., 2019):

1. Plywood - Composite material consisting of a layer of plywood sandwiched between layers of aluminum, nominally 0.5 in. (12.7 mm) thick. Decorative melamine facing on the exposed side. Commonly used for wall panels, ceiling panels, and closets. Note that the face sheeting was removed prior to testing to determine the material and reaction properties of the plywood (Sample 2). The plywood inner core was used in this work.
2. FRP - Fiberglass reinforced plastic (FRP) material, nominally 0.275 in. (7.0 mm) thick. The composite was composed of a chopped fiberglass mat with a polyester-type resin with fire retardant additives and a gel coat, commonly used for wall lining, window masks, and seat components (Sample 6).

Material and reaction parameters of plywood are provided in Table D-1 and Table D-2, respectively. Similarly, material and reaction parameters of FRP are provided in Table D-3 and Table D-4, respectively. Note the temperature dependence is based on the temperature in °C.

Table D-1: Material parameters of plywood

Parameter	Component 1	Component 2	Component 3	Char
$Y_{i,0}$ (-)	0.298	0.419	0.283	0.0
k_i $(W / m \cdot K)$	0.139 + 0.0128 T	0.402 + 0.0363 T	0.643 + 0.0285 T	0.001 + 0.0013 T
$c_{p,i}(J/(kg \cdot K))$	10.4 + 0.799 T	403.4 + 0.0894 T	1203.8 + 0.0014 T	85.6 + 5.1177 T
ρ (kg/m^3)	630.0	630.0	630.0	178.0
$H_{p,i}(J/(kg)$	4.72×10^6	5.81×10^6	1.01×10^4	-
κ_i $(1/m)$	8.15×10^5	2.72×10^5	5.73×10^5	1.91×10^5
ε_i (-)	0.95	0.95	0.907	0.986

Table D-2: Reaction parameters of plywood

Parameter	Reaction 1	Reaction 2	Reaction 3
A_i (1/s)	3.98×10^8	2.08×10^{12}	2.27×10^{21}
E_i (kJ/kmol)	1.36×10^5	1.48×10^5	1.51×10^5
n_i	0.374	4.067	14.515
v_i	0.241	0.001	0.566
Initial Component	Component 1	Component 2	Component 3
Final Component	Char	Char	Char
Heat of Combustion (kJ/kg)	11,660	11,660	11,660

Table D-3: Material parameters of FRP

Parameter	Component 1	Component 2	Component 3	Char
$Y_{i,0}$ (-)	0.281	0.298	0.421	0.0
k_i $(W / m \cdot K))$	0.030 + 1.2764 T	0.5072 + 3.5019 T	0.9133 + 0.0009 T	0.0583
$c_{p,i}(J/(kg \cdot K))$	10.9 + 5.776 T	2694.8 + 0.312 T	326.1 + 5.940 T	585.0 + 2.810 T
ρ (kg/m^3)	1600	1600	1600	800
$H_{p,i}(J/(kg)$	1.19×10^6	3.95×10^6	1.31×10^5	-
κ_i $(1/m)$	6.79×10^5	7.18×10^5	5.36×10^5	5.75×10^5
ε_i (-)	0.874	0.841	0.947	0.908

Table D-4: Reaction parameters of FRP

Parameter	Reaction 1	Reaction 2	Reaction 3
A_i (1/s)	2.45×10^{10}	4.90×10^{16}	9.70×10^{17}
E_i (kJ/kmol)	1.59×10^5	1.45×10^5	2.04×10^5
n_i	1.170	6.962	5.301
v_i	0.014	0.747	0.607
Initial Component	Component 1	Component 2	Component 3
Final Component	Char	Char	Char
Heat of Combustion (kJ/kg)	18,755	18,755	18,755

Grid Sensitivity

A grid sensitivity study was conducted to quantify the grid resolution needed at each scale for a grid-independent solution. In the grid sensitivity study, the fire was located in the center of the compartment and there was no window. The grid resolutions evaluated at each scale are summarized in Table D-5. For each case, a hybrid meshing strategy was used, where the compartment and a small area around the door used the inside grid resolution included in Table D-5, and the rest of the model used the outside grid resolution. The environment around the full-scale model was limited to reduce the number of grid cells in the grid sensitivity study; however, the full exhaust hood and the neighboring environment was included in the reduced-scale convergence models. The model geometries are visualized in Figure D-1.

Table D-5: Grid resolutions evaluated in sensitivity study

Scale	HRR (kW)	Inside Δx (cm)	Outside Δx (cm)	D*/ Δx
1:1	640	5.0	10.0	16.1
1:1	640	2.5	5.0	32.2
1:2	160	2.5	5.0	18.5
1:2	160	1.25	5.0	37.0
1:4	40	1.25	5.0	21.2
1:4	40	0.75	3.0	35.4

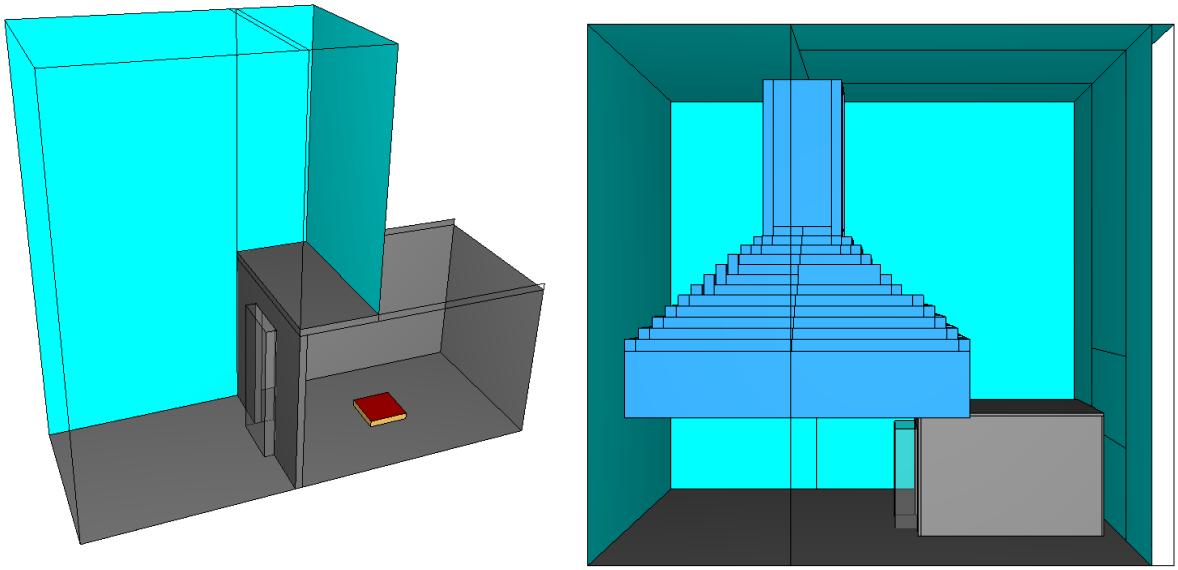

(a) Full-scale model **(b) Half-scale model**

Figure D-1: Grid sensitivity model configurations

The gauge heat flux on the west wall of the compartment at each scale at two grid resolutions is provided in Figure D-2. In these figures, the gauge heat flux was averaged from 0–240 seconds of simulation time. The general profile of the heat flux agreed across grid resolutions on the vertical walls as well as the ceiling. The time-averaged peak values on the walls were generally within 10–15 percent at the less resolved resolution, whereas the peak values on the ceilings were generally within 20 percent. This level of grid independence was judged to be sufficiently resolved for the purposes of the pre-test simulations in this work.

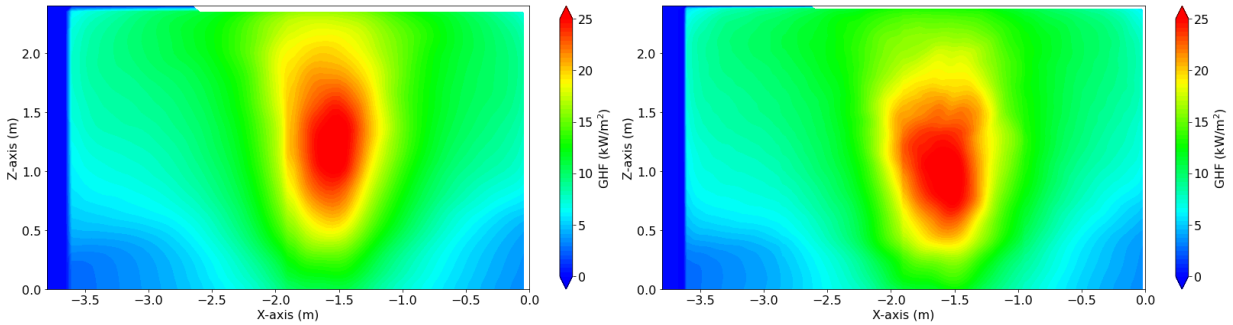

(a) Full-scale Δx = 5 cm **(b) Full-scale Δx = 2.5 cm**

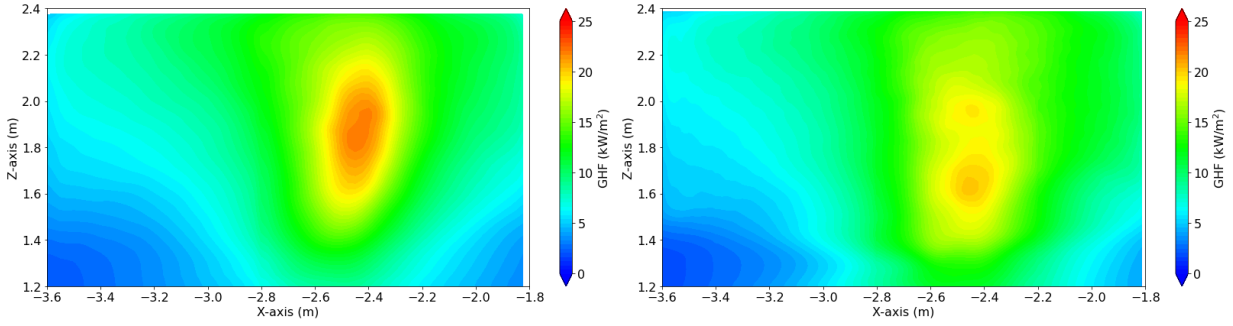

(c) Half-scale Δx = 2.5 cm **(d) Half-scale Δx = 1.25 cm**

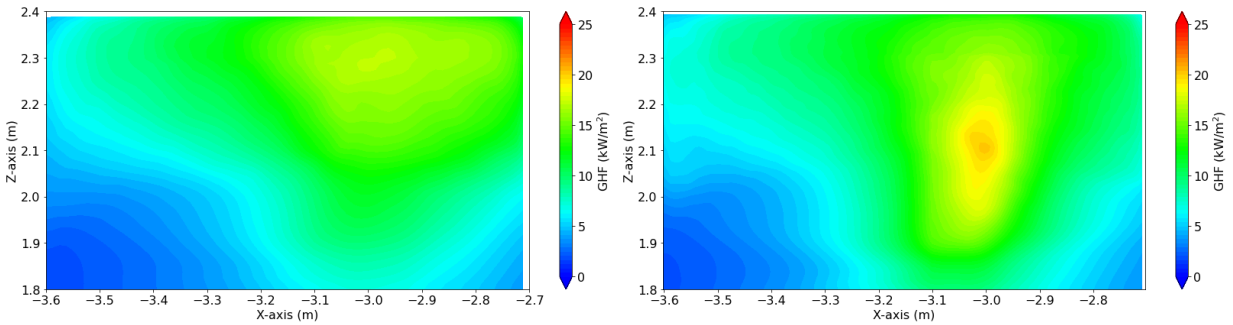

(e) Quarter-scale Δx = 1.25 cm **(f) Quarter-scale Δx = 0.75 cm**

Figure D-2: West wall time-averaged gauge heat flux from 0–240 seconds of simulation

Appendix E.
Pyrolysis Model Development

As discussed in Appendix D, FDS currently includes two pyrolysis models which can be used to model fire spread. The first model is simplistic, with a specified HRR profile once a material reaches an ignition temperature. The second model is highly complex, requiring close to 50 material and reaction parameters to be quantified from experiments. While conducting the pre-test simulations, JH recognized the need for a new pyrolysis model which is less complex than the Arrhenius kinetics model which can account for different pyrolysis rates at different levels of thermal exposure.

A new model was developed during this work which is based on the concept of an effective heat of gasification using data from a cone calorimeter and scaling laws previously developed. The model is based on the observation that both the HRRPUA and the net heat flux into the sample should scale at the same rate. The HRR can be calculated using an effective heat of gasification shown in Equation E-1,

$$\dot{Q}'' = q'' \frac{\Delta H_{c,eff}}{\Delta H_{g,eff}} \tag{E-1}$$

Where $\dot{Q}''$ is the HHRPUA in kW/m^2, q" is the net heat flux into the material in kW/m^2, $\Delta H_{C,eff}$ is the effective heat of combustion of the material in kJ/kg, and $\Delta H_{g,eff}$ is the effective heat of gasification of the material in kJ/kg.

With the effective heat of gasification and effective heat of combustion of the material being constant at all scales, this leads to the scaling law in Equation E-2, which accounts for the change in the magnitude of the HRR based on the applied heat flux onto the surface. In addition to the applied heat flux affecting the magnitude of the HRR, it also affects how long the material will burn. In all cases, the burning duration is dependent on the total energy released per unit area shown in Equation E-2,

$$E'' = \dot{m}'' \Delta H_{c,eff} t_{burn,dur} = q'' \frac{\Delta H_{c,eff}}{\Delta H_{g,eff}} t_{burn,dur} \tag{E-2}$$

where E" is the total energy released per unit area in kJ/m^2, $\dot{m}''$ is the mass burning rate per unit area in kg/s-m^2, and $t_{burn,dur}$ is the total burning duration in seconds. Since the total energy released per unit area is constant at all scales assuming the same material thickness is used, these can be equated at resulting in Equation E-3.

$$\left[q'' \frac{\Delta H_{c,eff}}{\Delta H_{g,eff}} t_{burn,dur} \right]_{hi} = \left[q'' \frac{\Delta H_{c,eff}}{\Delta H_{g,eff}} t_{burn,dur} \right]_{lo} \tag{E-3}$$

where the subscripts *hi* and *lo* indicate different scales. This equation is valid at any point in time during the burning. Since the material properties are the same, this results in the scaling law in Equation E-4 through E-5 as,

$$t_{burn,dur,lo} = \frac{q''_{lo}}{q''_{hi}} t_{burn,dur,hi} \tag{E-4}$$

$$Q''_{hi}(t) = \frac{q''_{hi}(t)}{q''_{lo}(t)} Q''_{lo}(t) \tag{E-5}$$

Where $Q''_{lo}(t)$ is the HRRPUA from a bench scale test resulting in the net heat flux $q''_{lo}(t)$, $q''_{hi}(t)$ is the resulting net heat flux from a different scaled thermal exposure, and $Q''_{hi}(t)$ is the scaled HRRPUA. In this model, the time from the reference experiment is scaled according to Equation E-4 where higher exposures than reference will reduce the duration and lower exposures than reference will expand the duration. The time-resolved HRRPUA for a specific exposure is calculated according to Equation E-5, which is used to scale the HRR from the reference experiment at each time step.

The results of this new model are compared with experimental measurements in Figure E-1 for plywood. The reference test data was from a cone calorimeter experiment with an exposure of 50 kW/m^2. The two additional solid curves show test data on the same material with exposures at 25 and 75 kW/m^2. The dashed lines show the reference experiment scaled to each of the other exposures. Overall, the results agree well, particularly at the higher exposure heat fluxes. This model was implemented as an additional option in FDS based on this work.

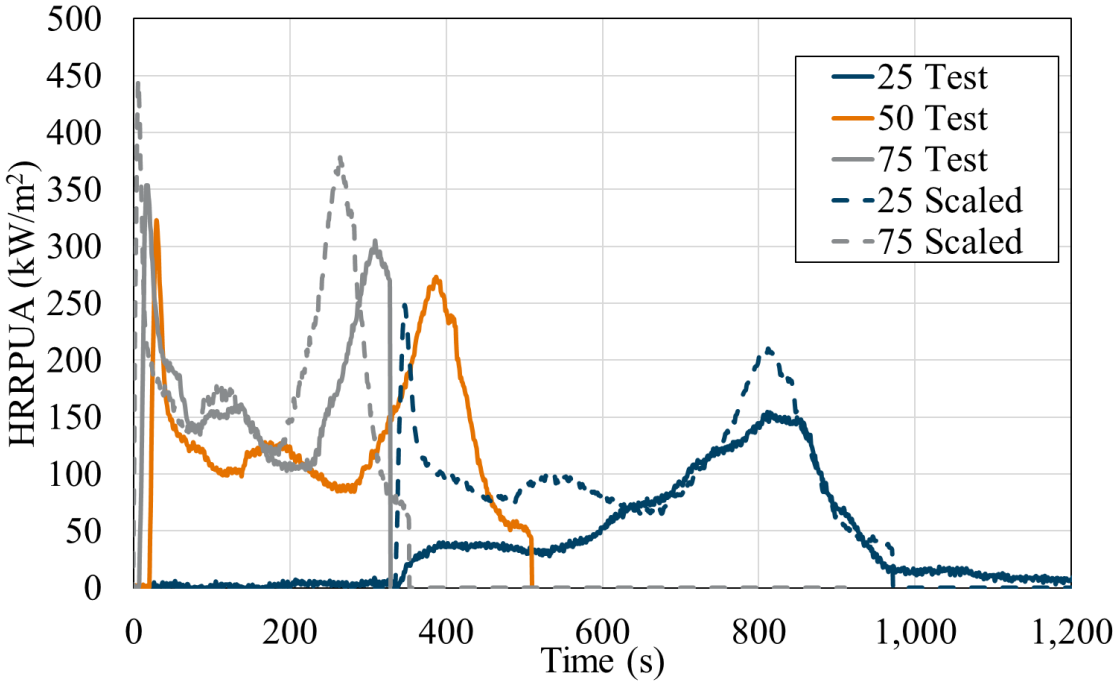

Figure E-1: Scaling-based pyrolysis model compared with experiments. Reference test data was from a 50 kW/m^2 cone calorimeter experiment

Appendix F.
Test Series Measurements

Detailed measurements are provided for each test in the following sections. The following notes apply to all test data:

Twelve TC measurements were part of the thermocouple trees in the north-east and south-east quadrant of the compartment. Note the percentages in the legends correspond to the percentile location between the floor and the ceiling. For example, at the quarter-scale the 85 percent thermocouple was located near the ceiling at a height of 20 in. (0.51 m) above the floor where the maximum height of the quarter-scale compartment was 24 in. (0.60 m). An additional two temperature measurements were taken at two heights above the burner. Six temperature measurements were taken at the door and two at the window (if present). Four temperature measurements were taken at the ceiling with the spatial locations of the TCs shown in Figure 11.

Six gas velocity measurements were taken at the door and two at the window (if present).

A total of four gauge heat flux measurements were obtained during testing, with the spatial location of heat flux gauge shown in Figure 11. Note that the heat flux measurements have been filtered with a 30 second median filter to reduce noise. The heat flux gauge located above the burner was not available for all tests due to difficulty with material blocking the sensor.

Test 1-A Results (Quarter-Scale Non-Combustible Door Configuration)

Heat Release Rate

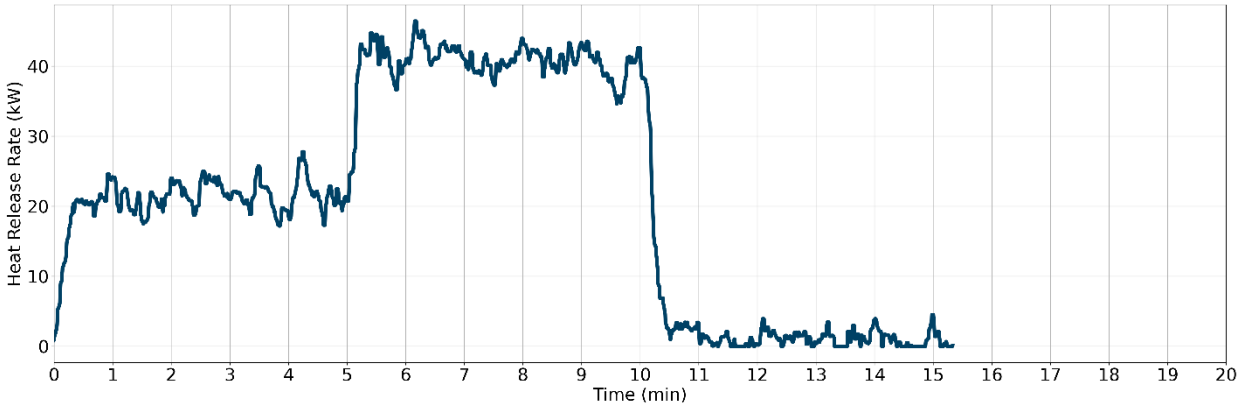

Figure F-1: Test 1-A HRR

Gas Temperatures

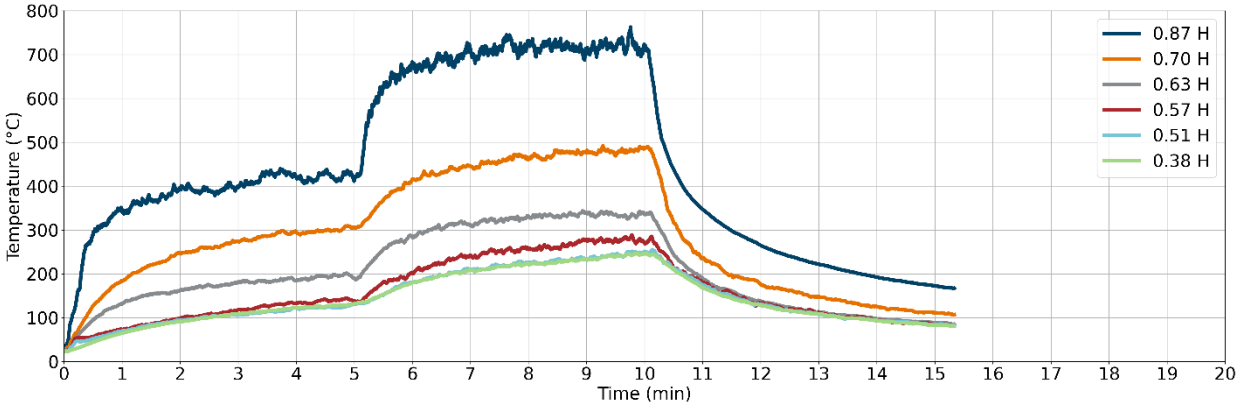

Figure F-2: Test 1-A gas temperatures in the north-east corner

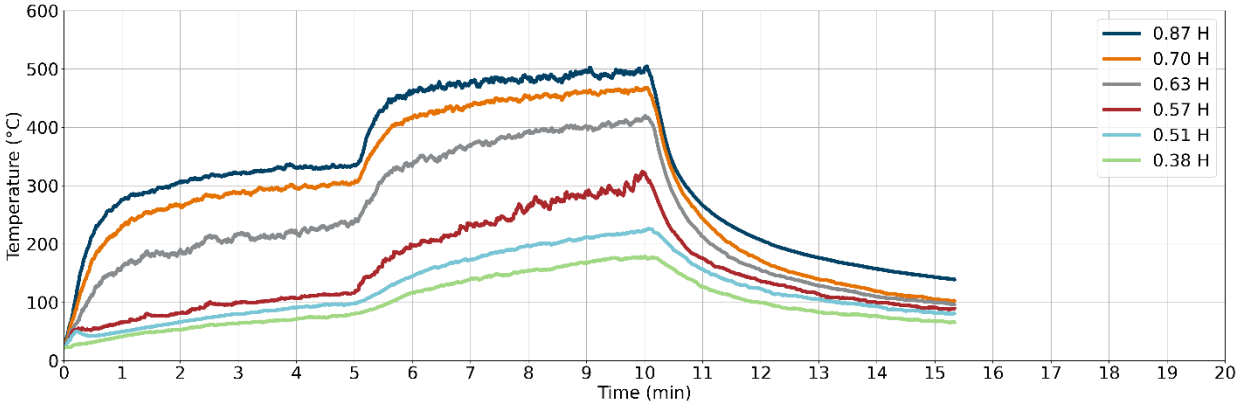

Figure F-3: Test 1-A gas temperatures in the south-east corner

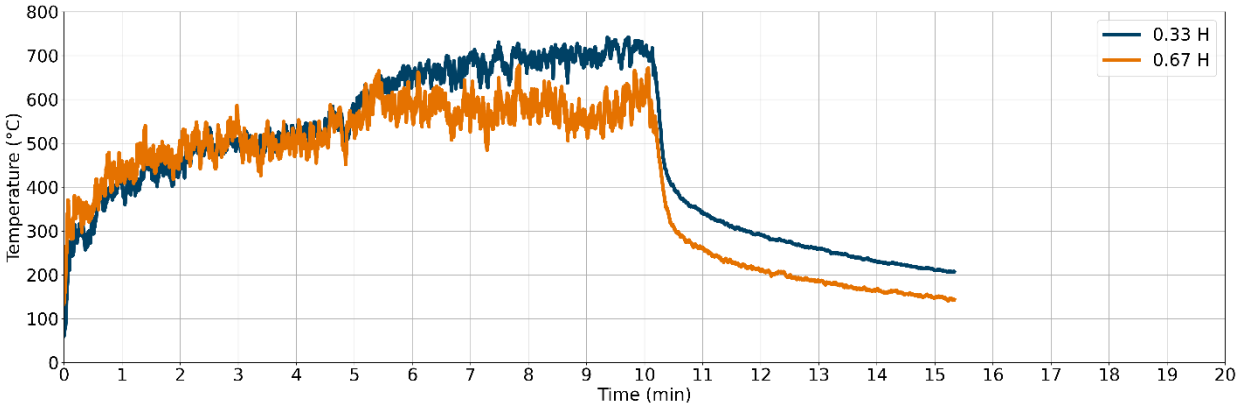

Figure F-4: Test 1-A gas temperatures at the burner

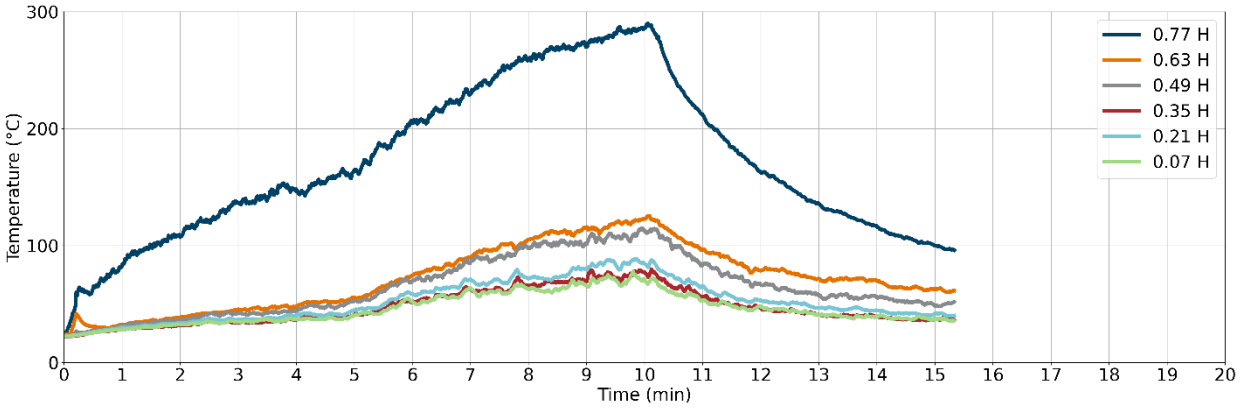

Figure F-5: Test 1-A gas temperatures at the door

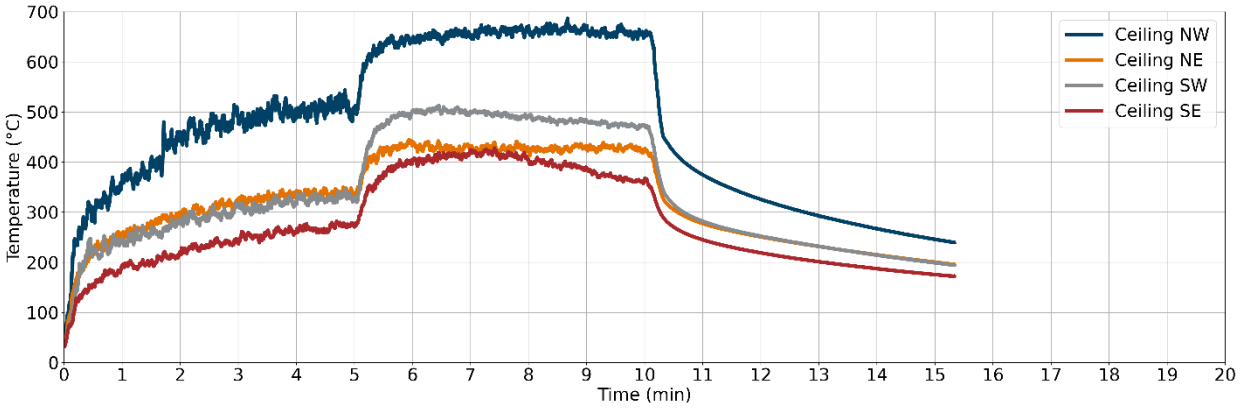

Figure F-6: Test 1-A gas temperatures at ceiling

Gas Velocities

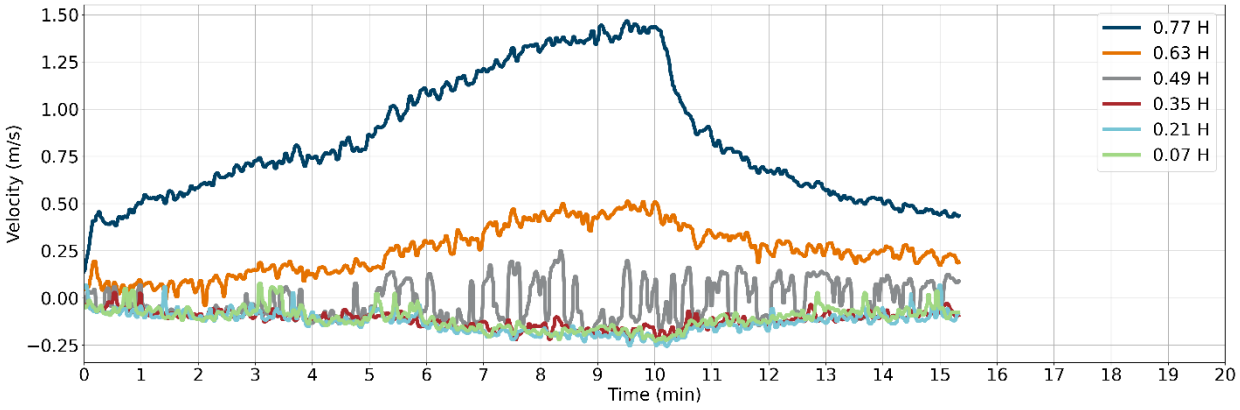

Figure F-7: Test 1-A gas velocities at the door

Heat Fluxes

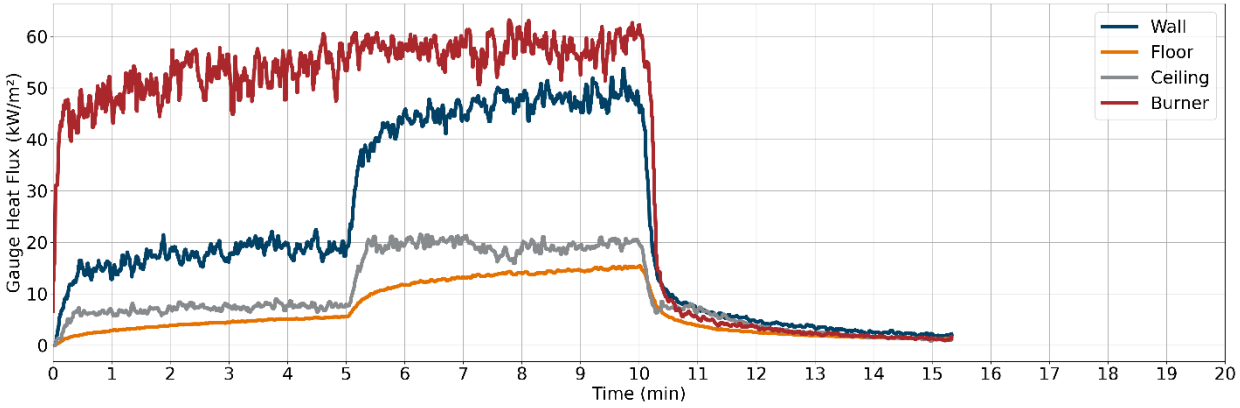

Figure F-8: Test 1-A heat fluxes

Optical Obscuration

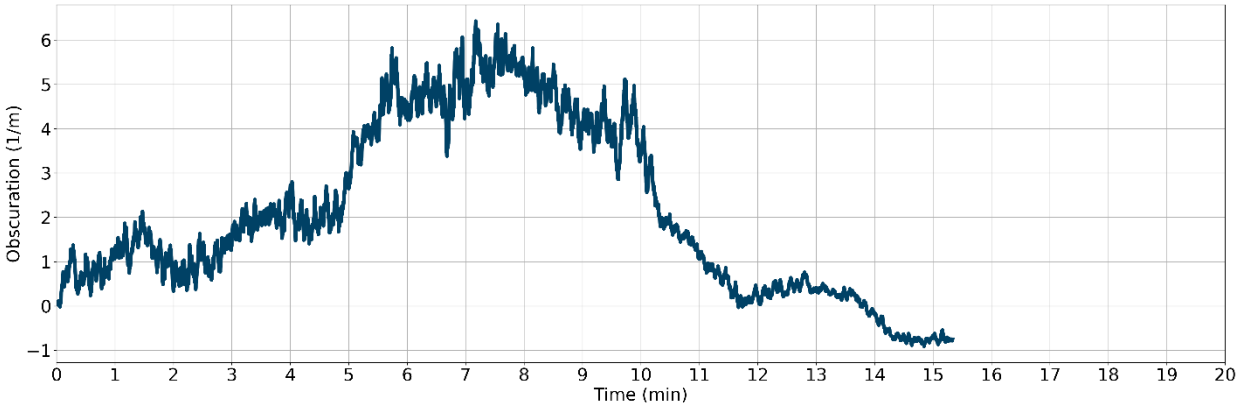

Figure F-9: Test 1-A optical obscuration in the exhaust duct

Test 1-B Results (Quarter-Scale Non-Combustible Door Configuration)

Heat Release Rate

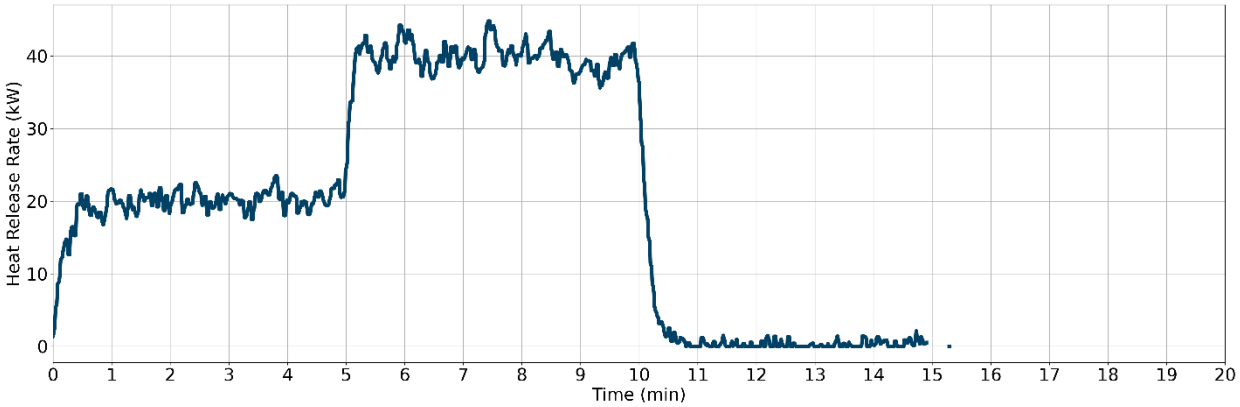

Figure F-10: Test 1-B HRR

Gas Temperatures

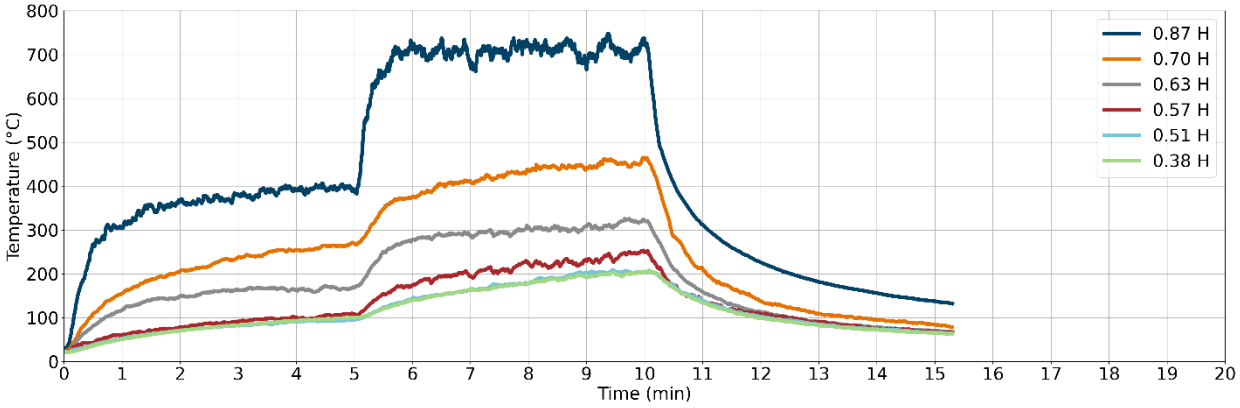

Figure F-11: Test 1-B gas temperatures in the north-east corner

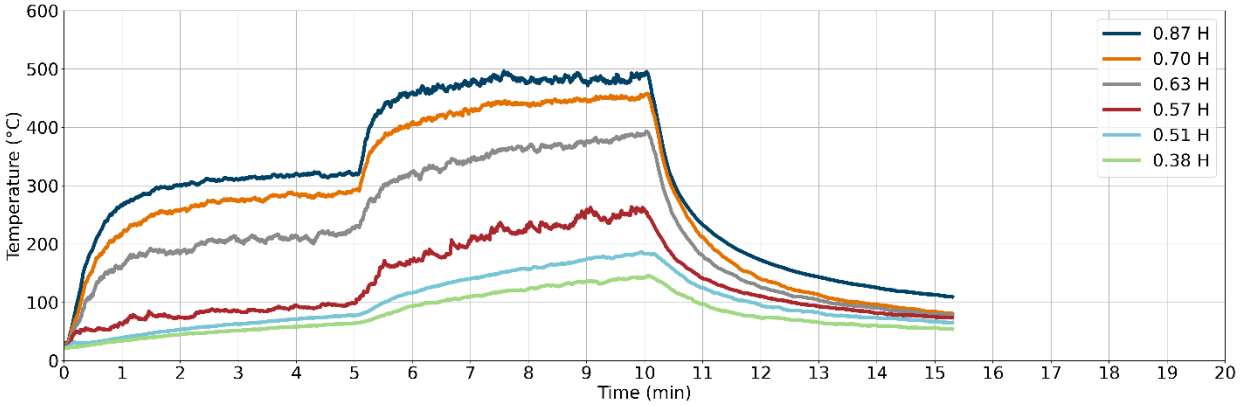

Figure F-12: Test 1-B gas temperatures in the south-east corner

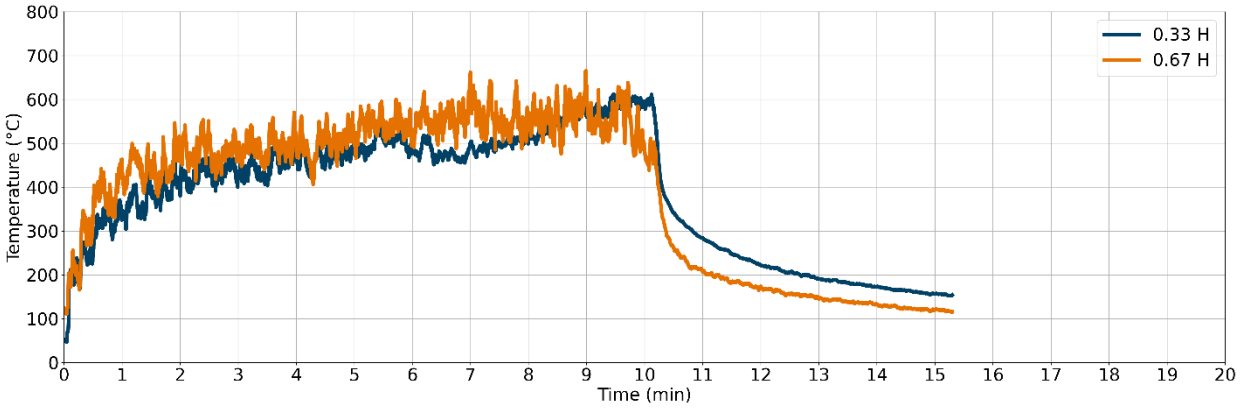

Figure F-13: Test 1-B gas temperatures at the burner

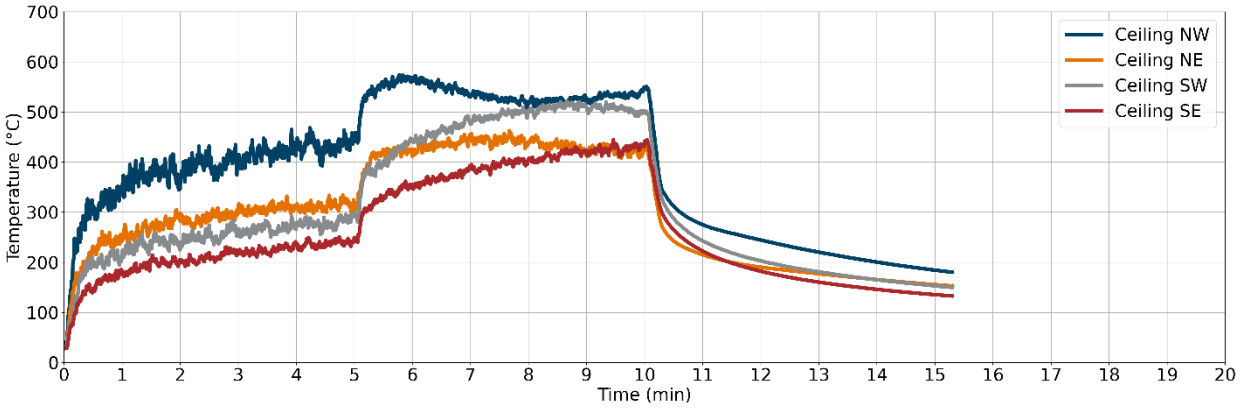

Figure F-14: Test 1-B gas temperatures at ceiling

Gas Velocities

None recorded for this test.

Heat Fluxes

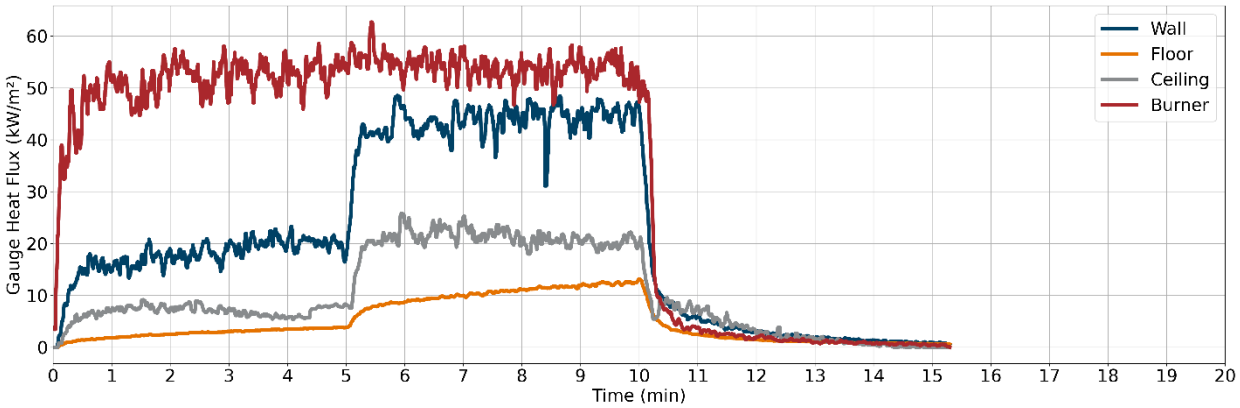

Figure F-15: Test 1-B heat fluxes

Optical Obscuration

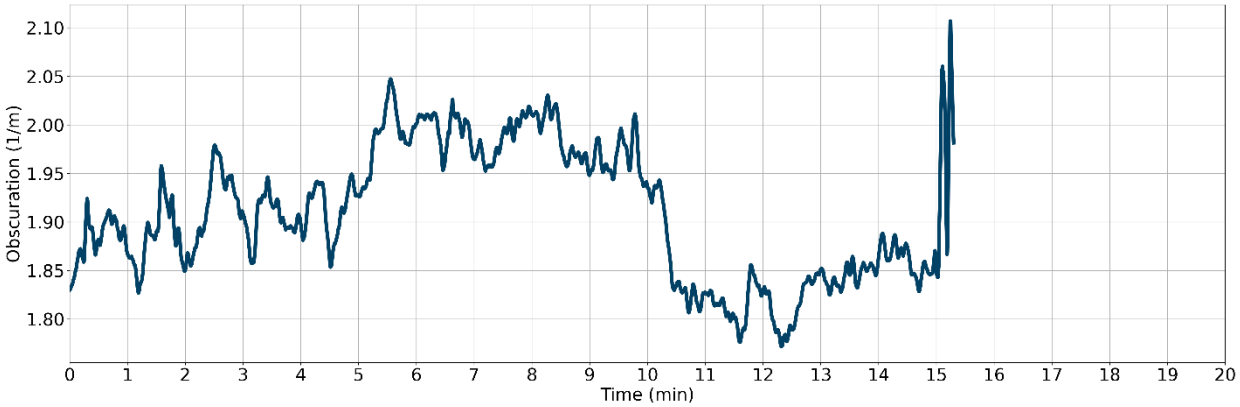

Figure F-16: Test 1-B optical obscuration in the exhaust duct

Test 2 Results (Quarter-Scale Non-Combustible Door-Window Configuration)

Heat Release Rate

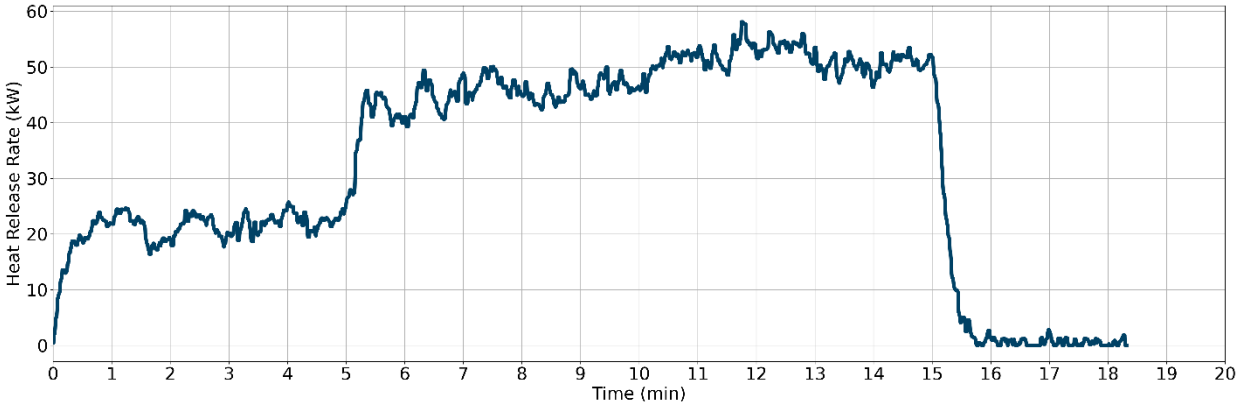

Figure F-17: Test 2 HRR

Gas Temperatures

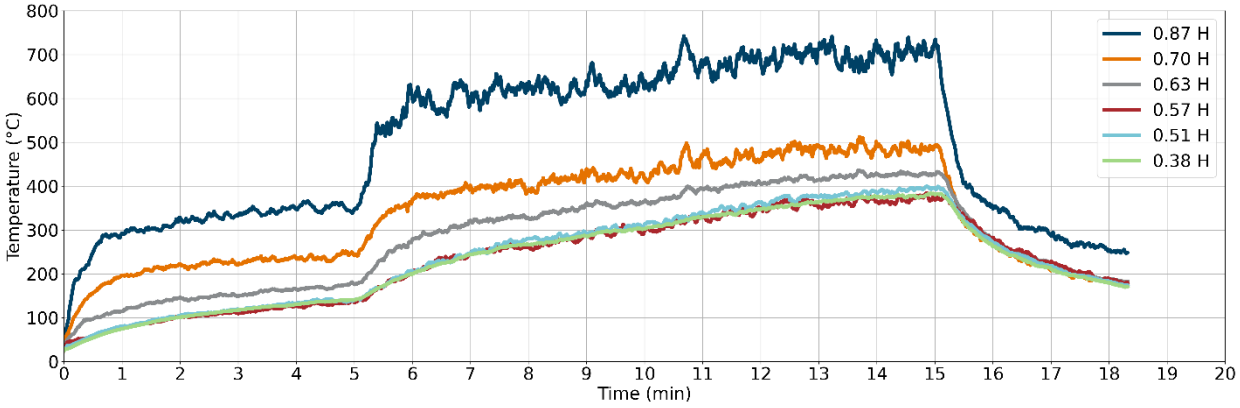

Figure F-18: Test 2 gas temperatures in the north-east corner

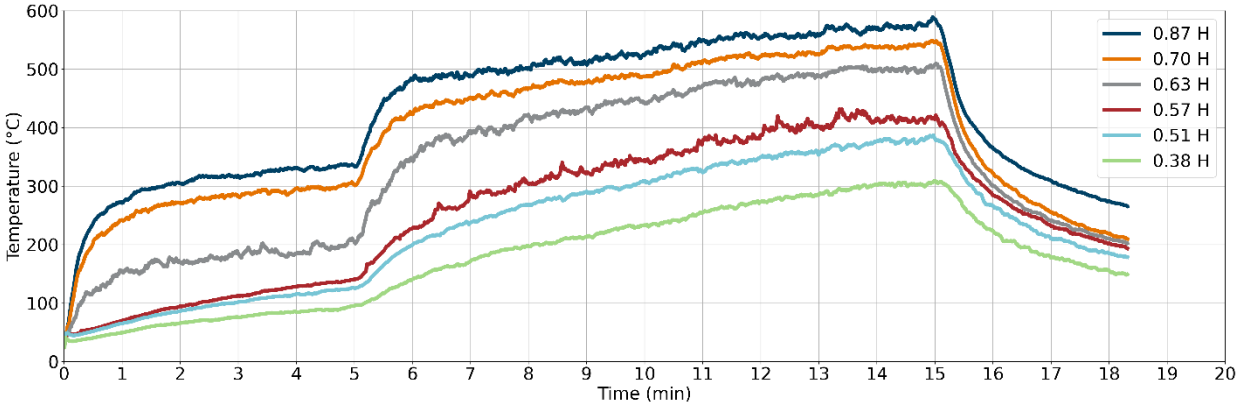

Figure F-19: Test 2 gas temperatures in the south-east corner

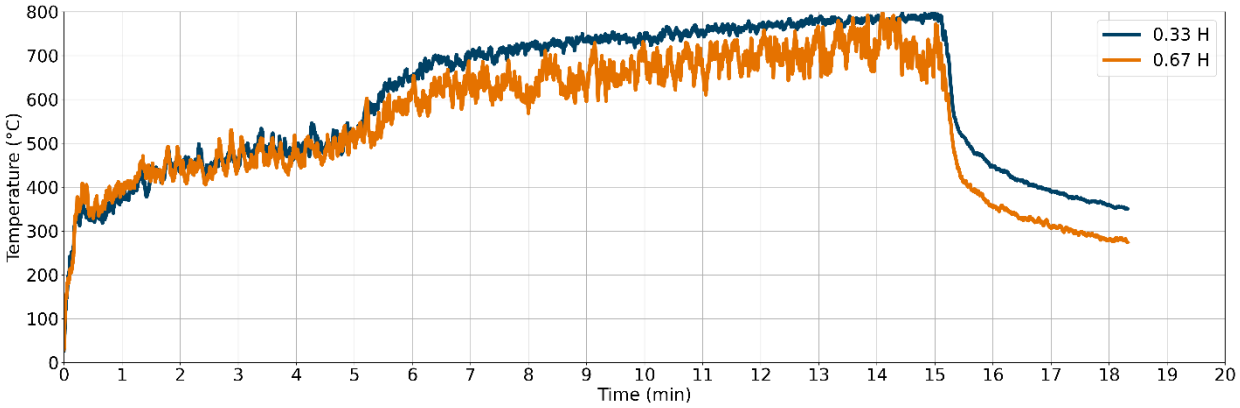

Figure F-20: Test 2 gas temperatures at the burner

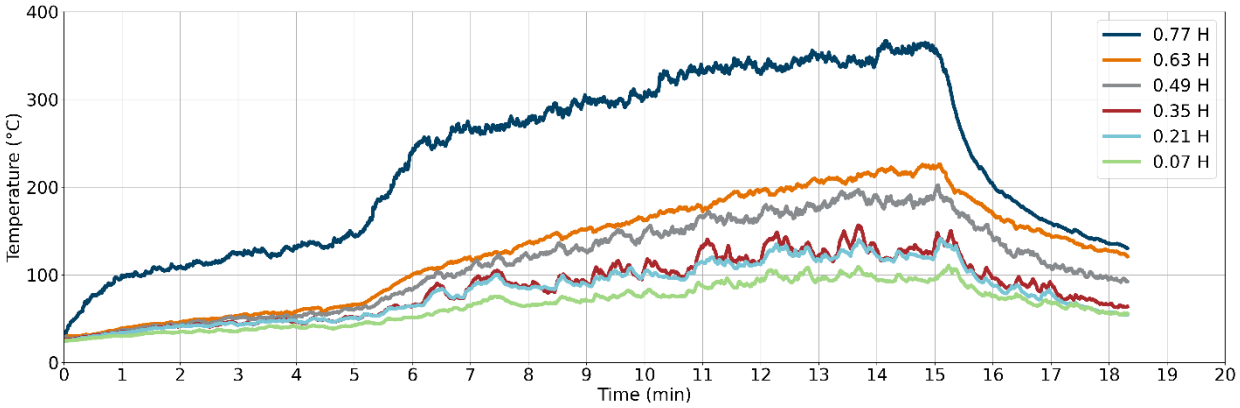

Figure F-21: Test 2 gas temperatures at the door

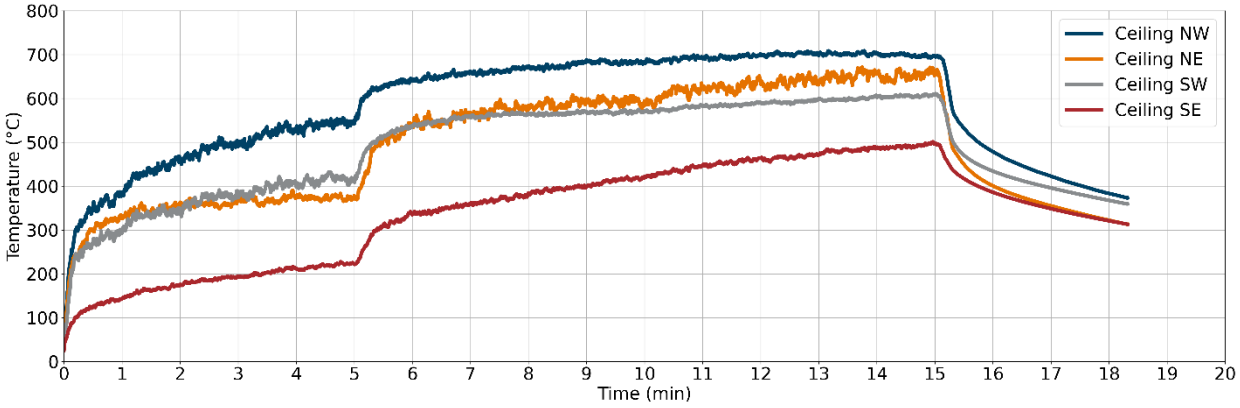

Figure F-22: Test 2 gas temperatures at ceiling

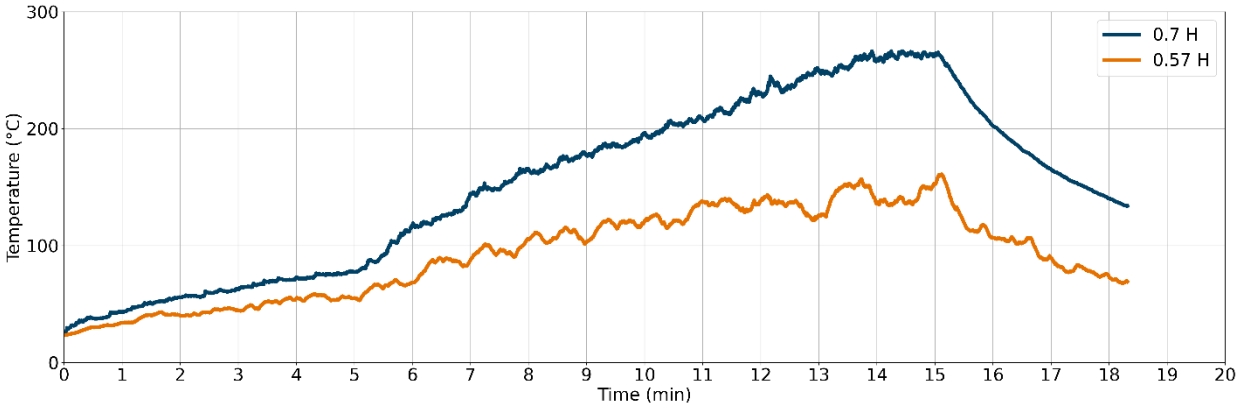

Figure F-23: Test 2 gas temperatures at the window

Gas Velocities

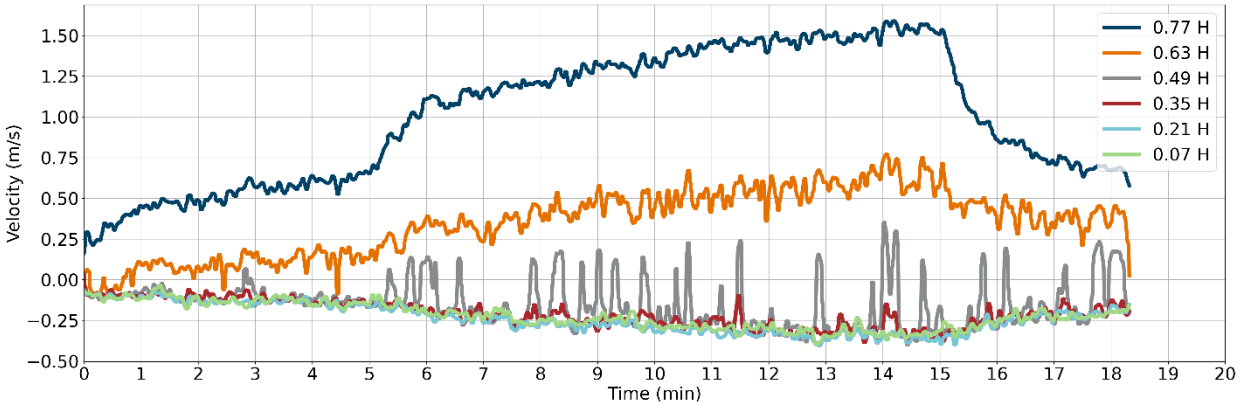

Figure F-24: Test 2 gas velocities at the door

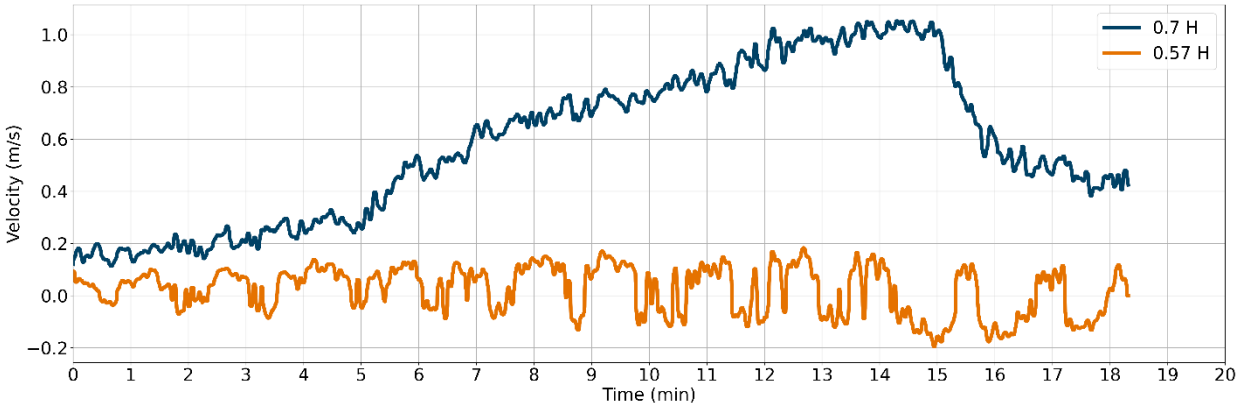

Figure F-25: Test 2 gas velocities at the window

Heat Fluxes

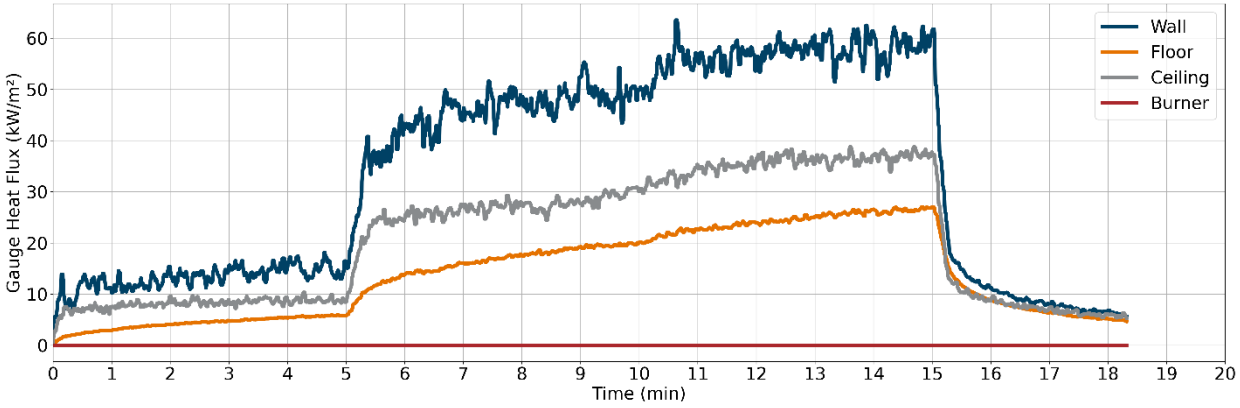

Figure F-26: Test 2 heat fluxes

Optical Obscuration

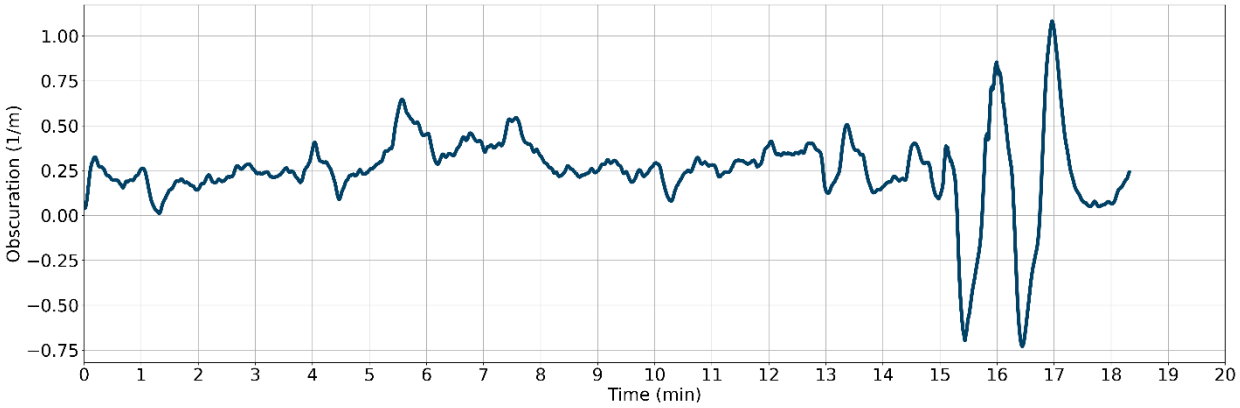

Figure F-27: Test 2 optical obscuration in the exhaust duct

Test 3 Results (Quarter-Scale Liquid Fuel / JP-5 Configuration)

Heat Release Rate

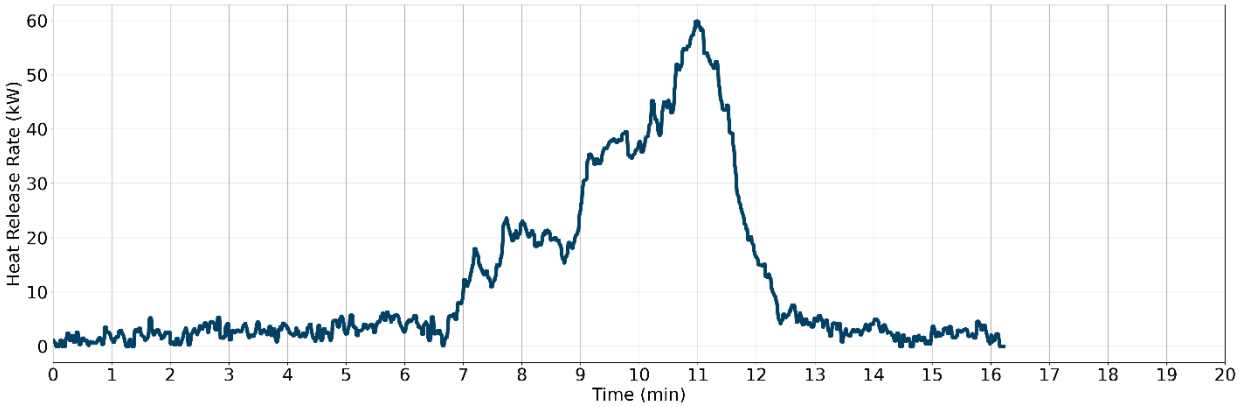

Figure F-28: Test 3 HRR

Gas Temperatures

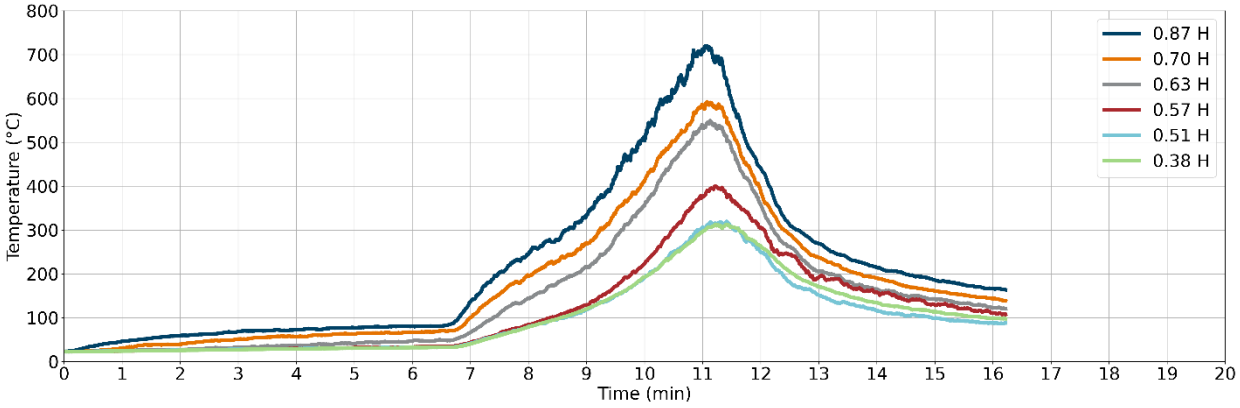

Figure F-29: Test 3 gas temperatures in the north-east corner

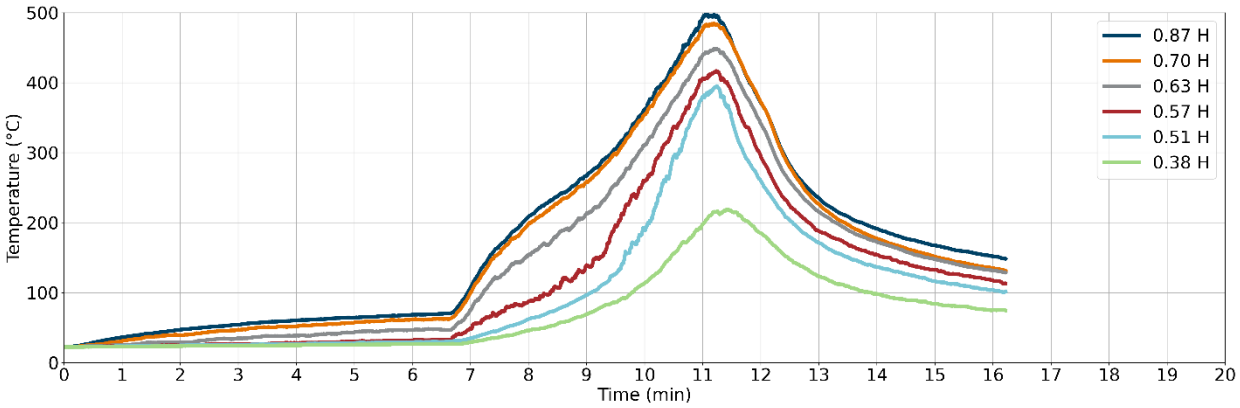

Figure F-30: Test 3 gas temperatures in the south-east corner

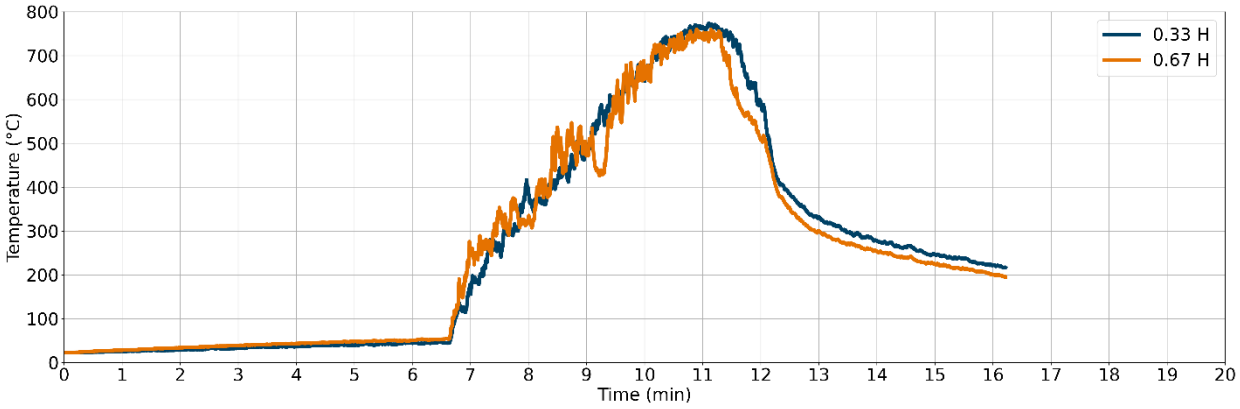

Figure F-31: Test 3 gas temperatures at the burner

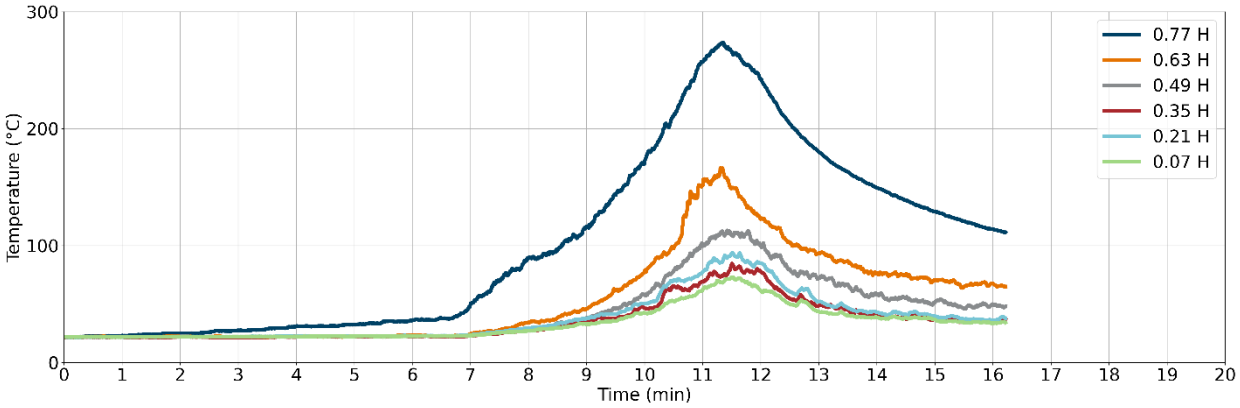

Figure F-32: Test 3 gas temperatures at the door

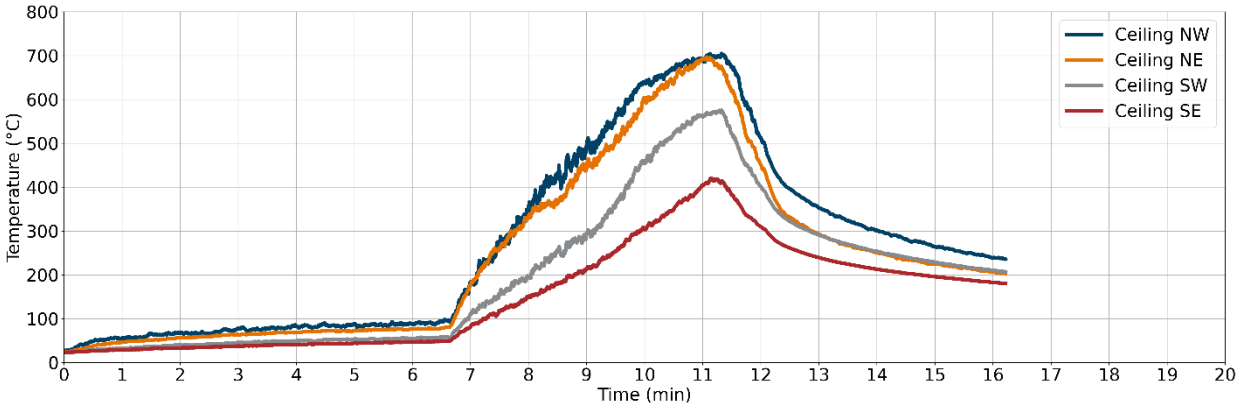

Figure F-33: Test 3 gas temperatures at ceiling

Gas Velocities

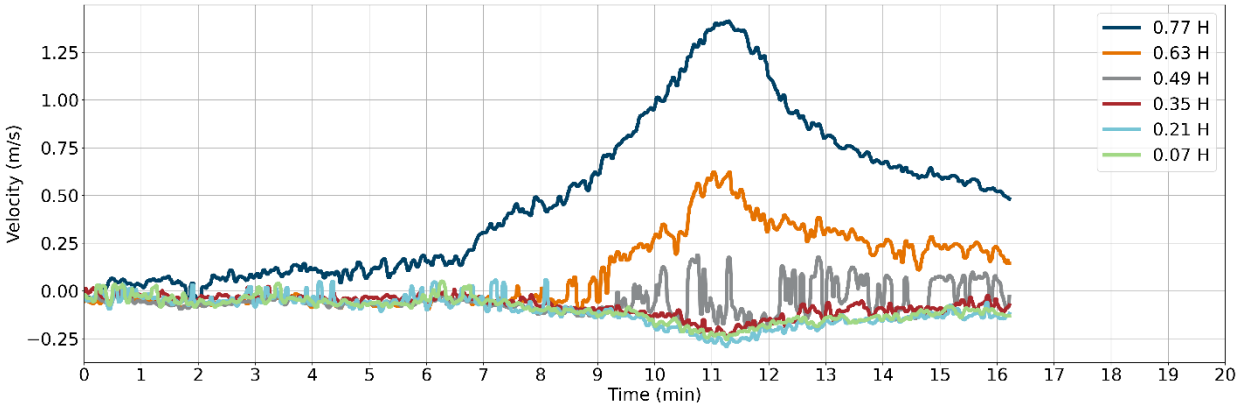

Figure F-34: Test 3 gas velocities at the door

Heat Fluxes

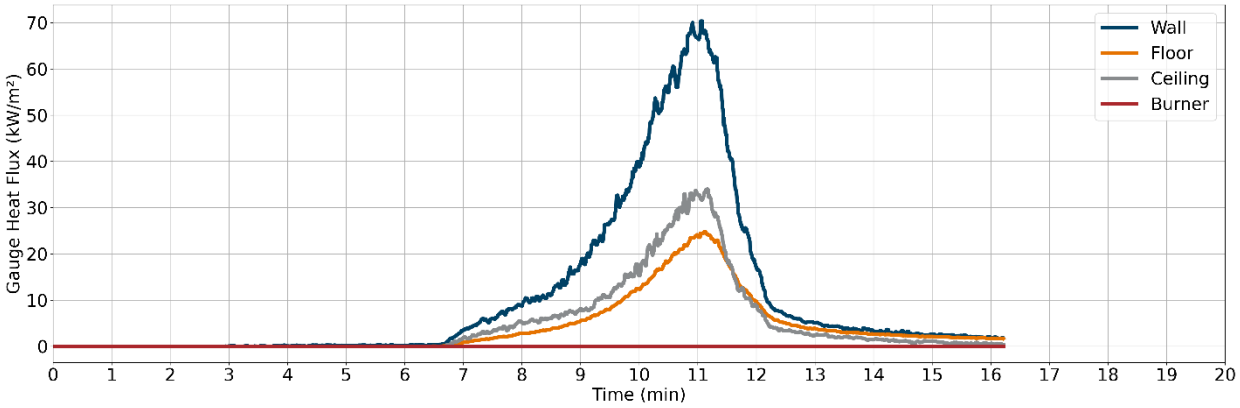

Figure F-35: Test 3 heat fluxes

Optical Obscuration

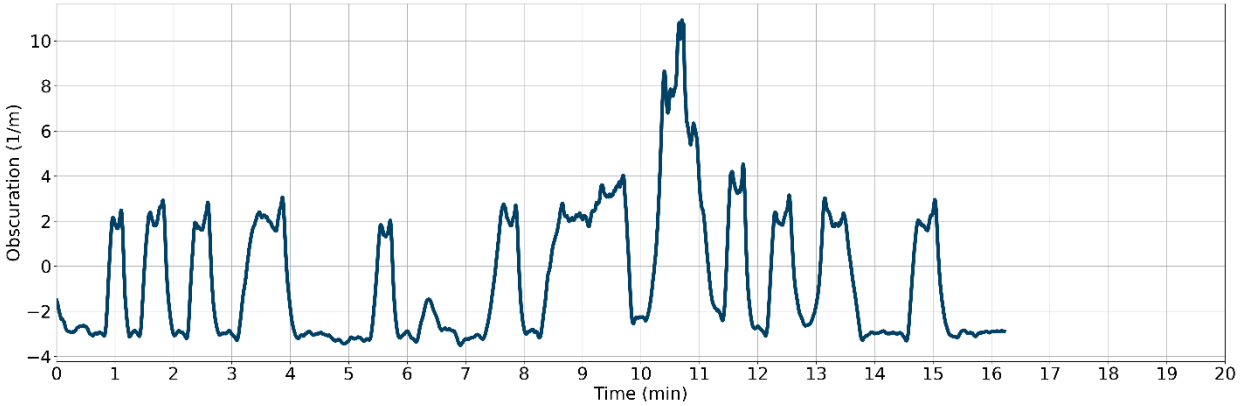

Figure F-36: Test 3 optical obscuration in the exhaust duct

Test 4 Results (Quarter-Scale Plywood Lining Configuration)

Heat Release Rate

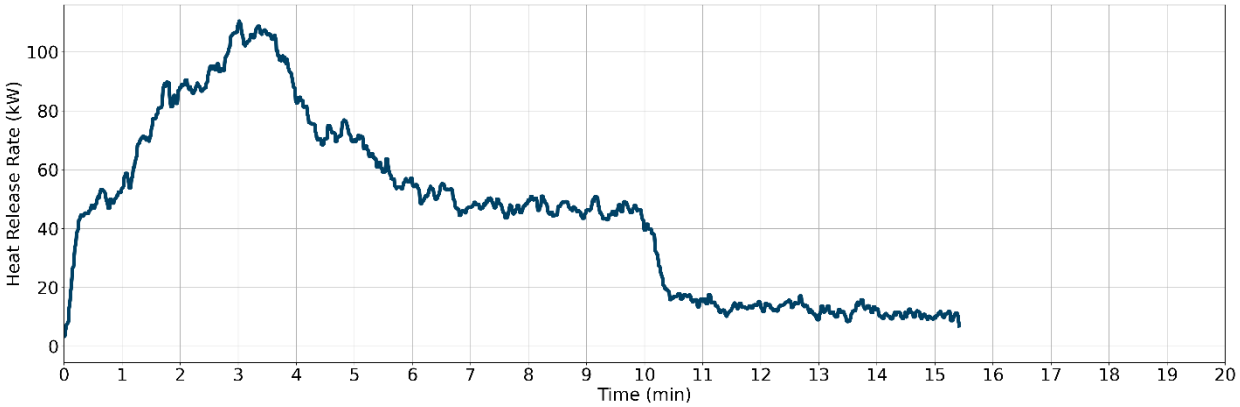

Figure F-37: Test 4 HRR

Gas Temperatures

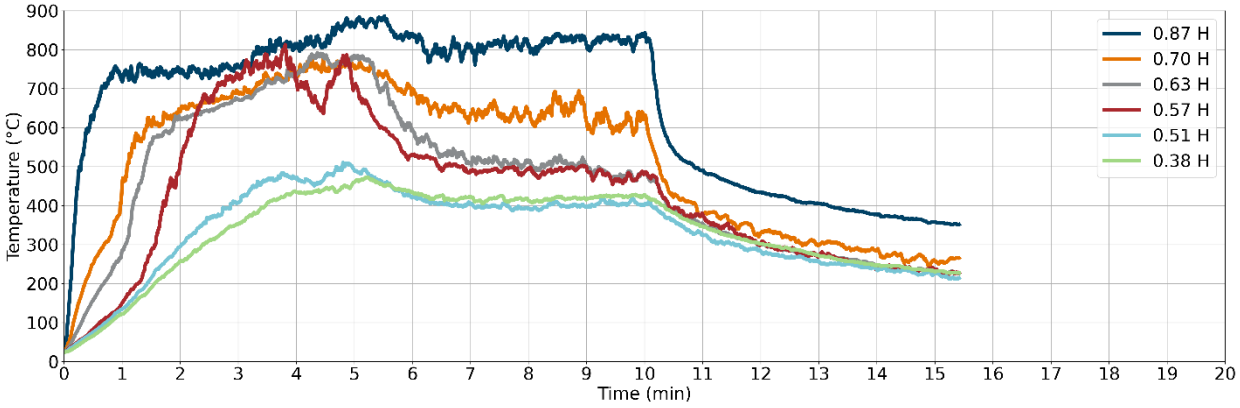

Figure F-38: Test 4 gas temperatures in the north-east corner

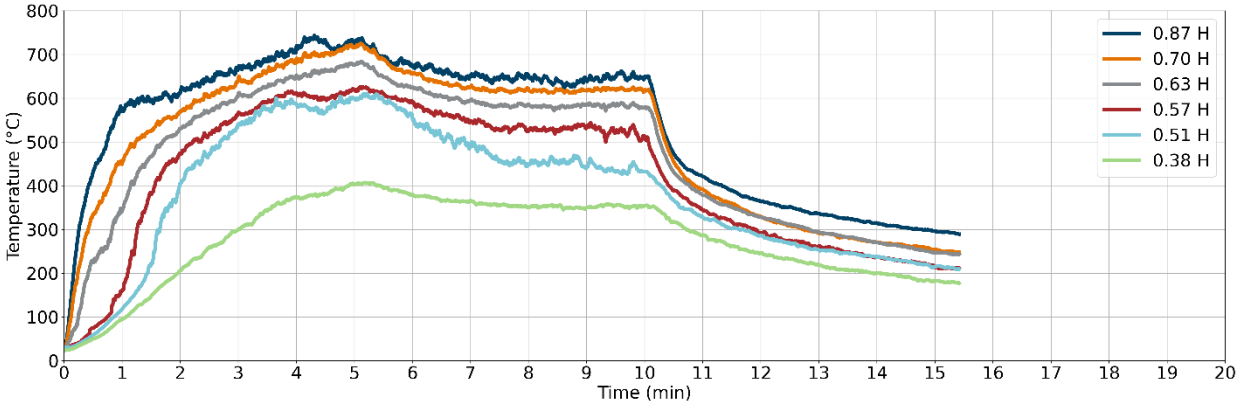

Figure F-39: Test 4 gas temperatures in the south-east corner

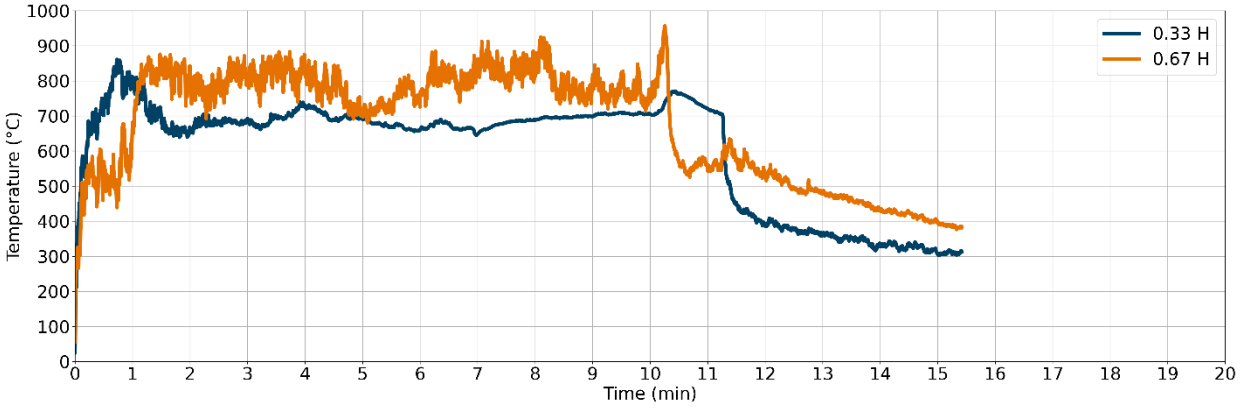

Figure F-40: Test 4 gas temperatures at the burner

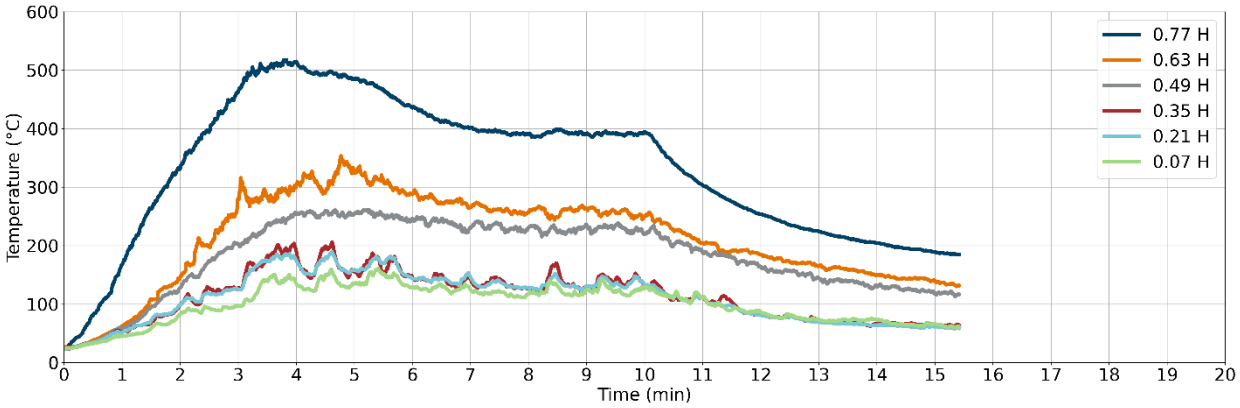

Figure F-41: Test 4 gas temperatures at the door

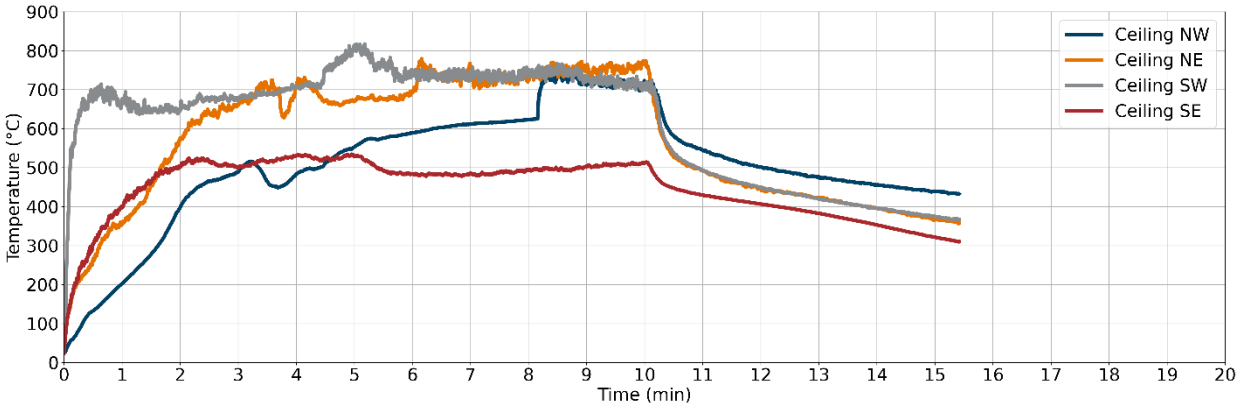

Figure F-42: Test 4 gas temperatures at ceiling

Gas Velocities

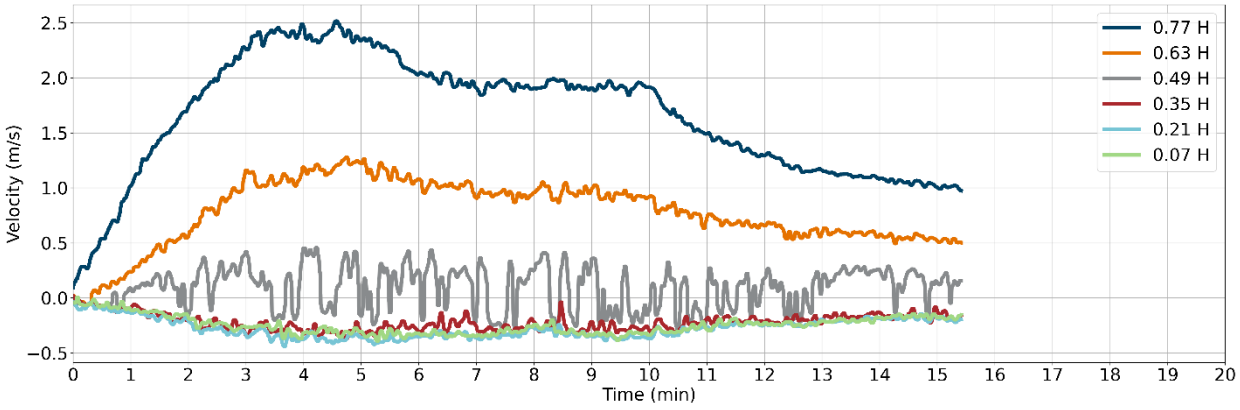

Figure F-43: Test 4 gas velocities at the door

Heat Fluxes

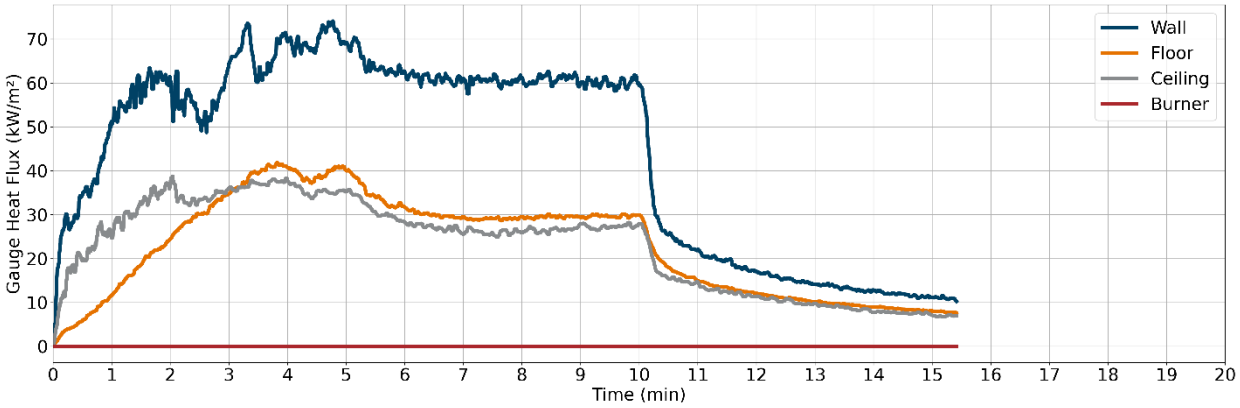

Figure F-44: Test 4 heat fluxes

Optical Obscuration

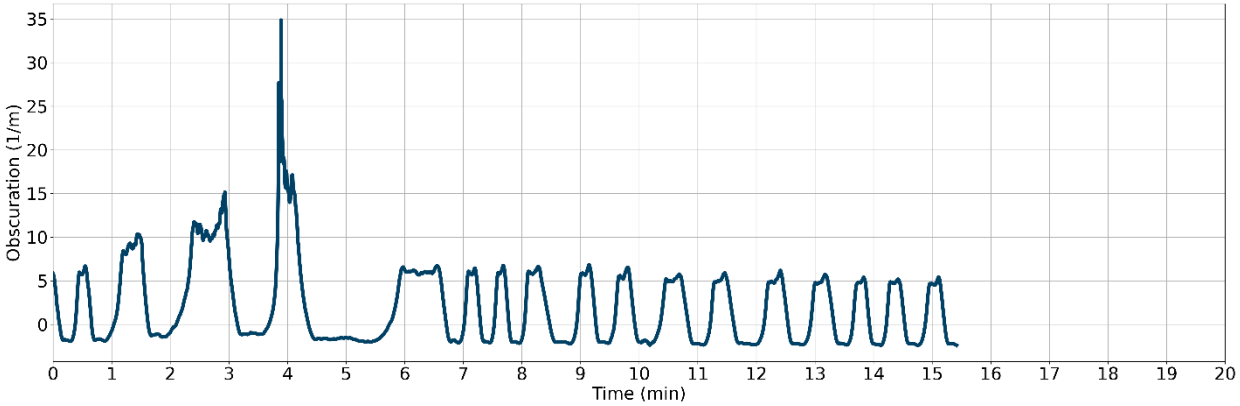

Figure F-45: Test 4 optical obscuration in the exhaust duct

Test 5 Results (Quarter-Scale FRP Lining Configuration)

Heat Release Rate

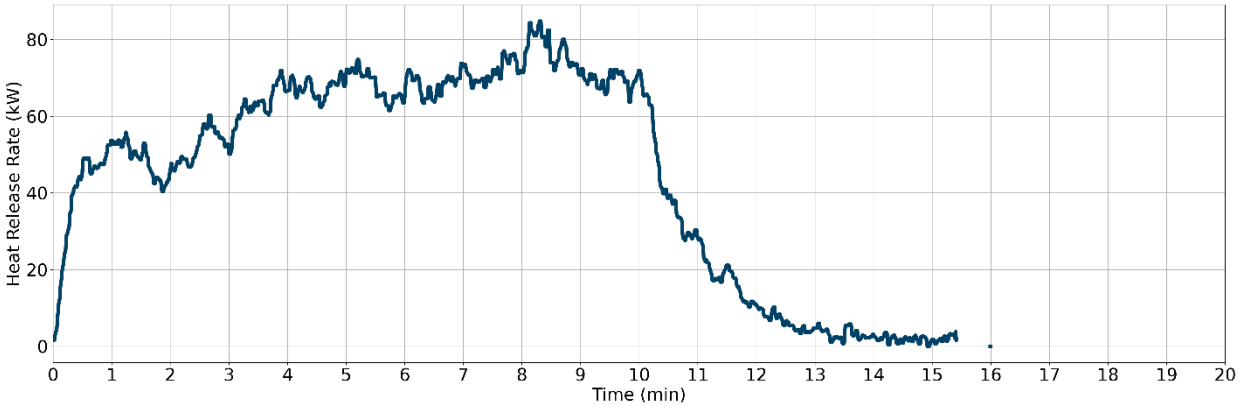

Figure F-46: Test 5 HRR

Gas Temperatures

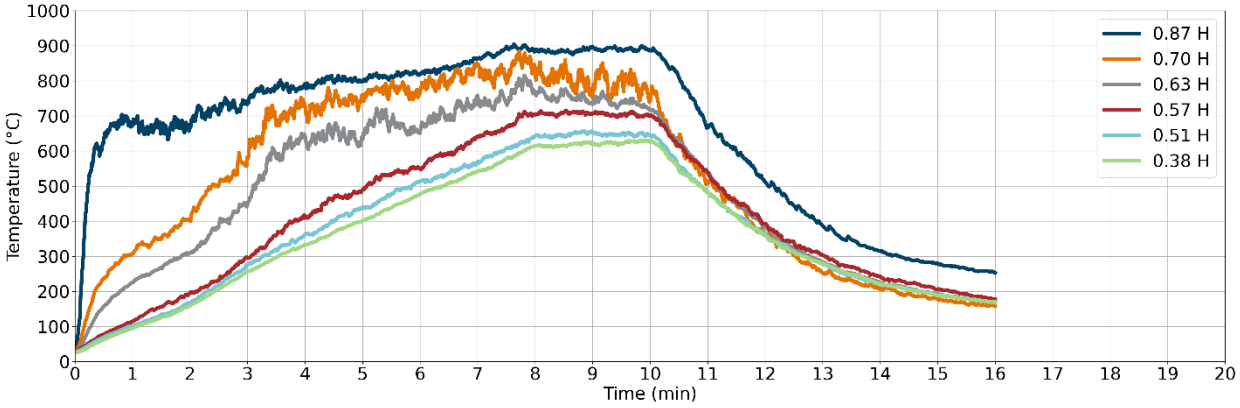

Figure F-47: Test 5 gas temperatures in the north-east corner

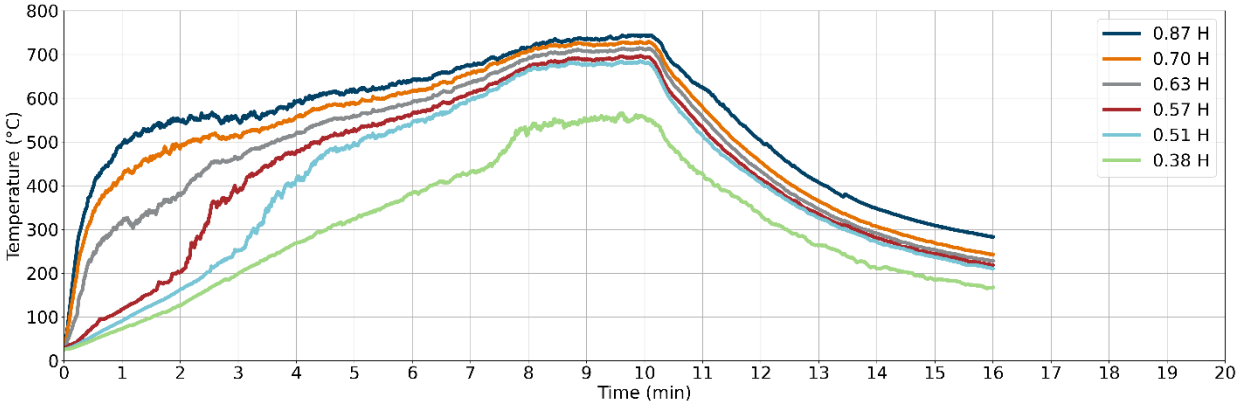

Figure F-48: Test 5 gas temperatures in the south-east corner

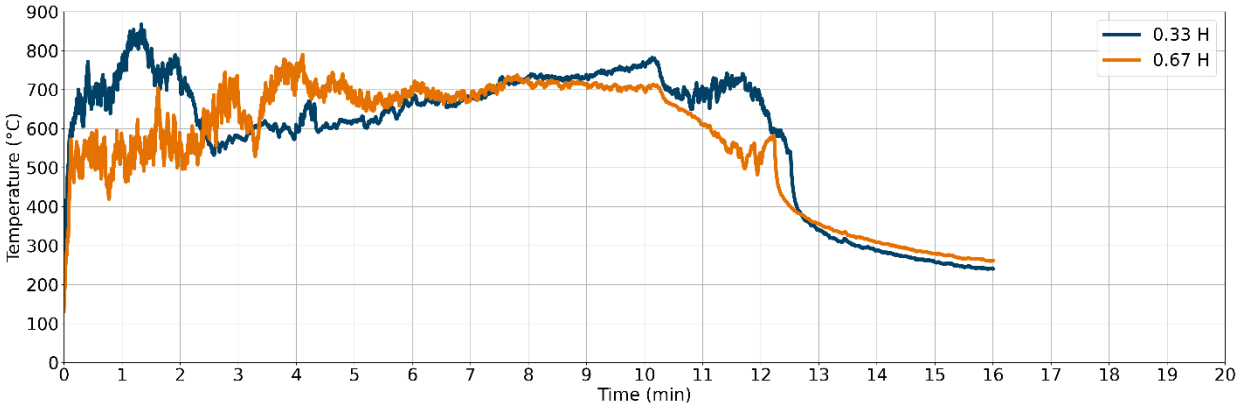

Figure F-49: Test 5 gas temperatures at the burner

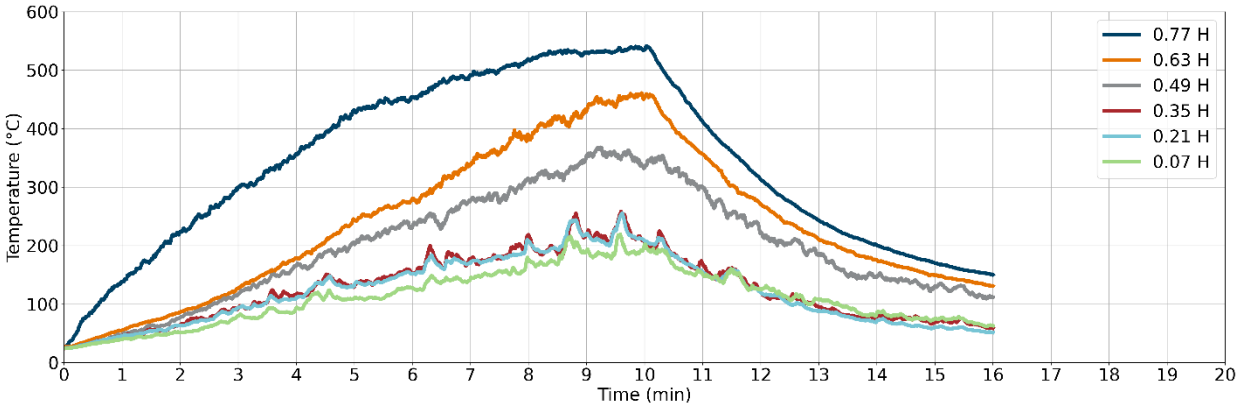

Figure F-50: Test 5 gas temperatures at the door

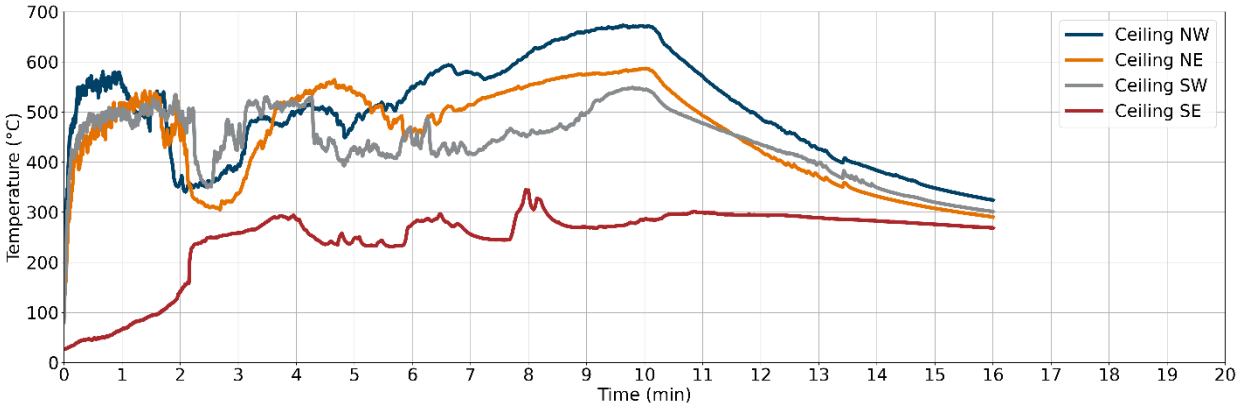

Figure F-51: Test 5 gas temperatures at ceiling

Gas Velocities

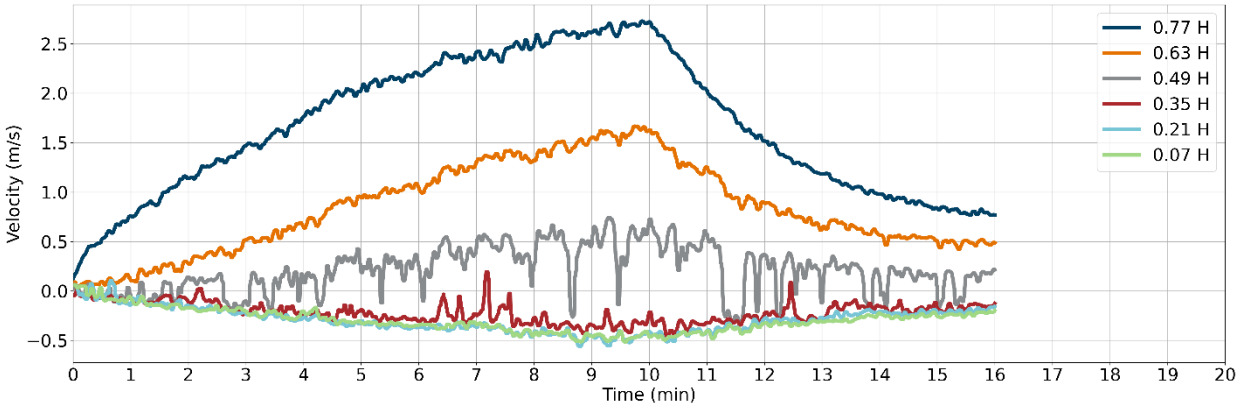

Figure F-52: Test 5 gas velocities at the door

Heat Fluxes

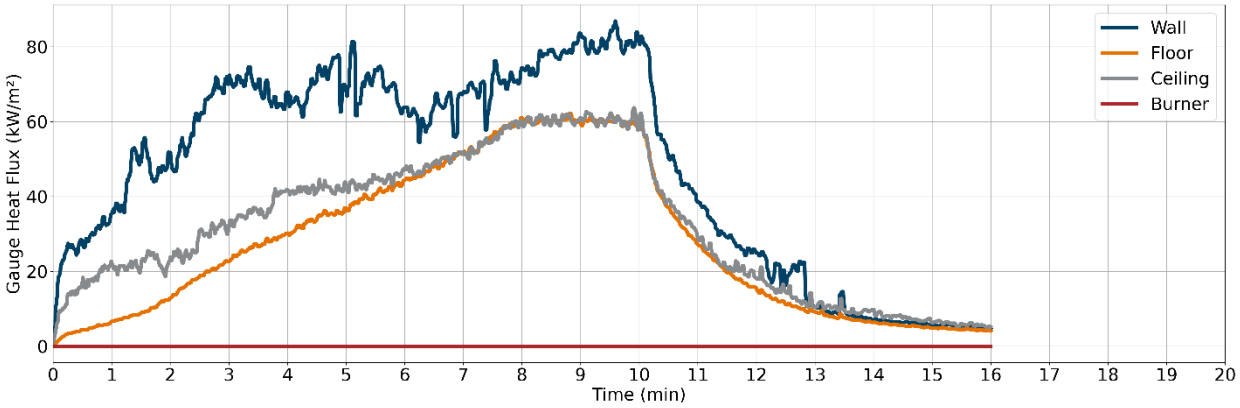

Figure F-53: Test 5 heat fluxes

Optical Obscuration

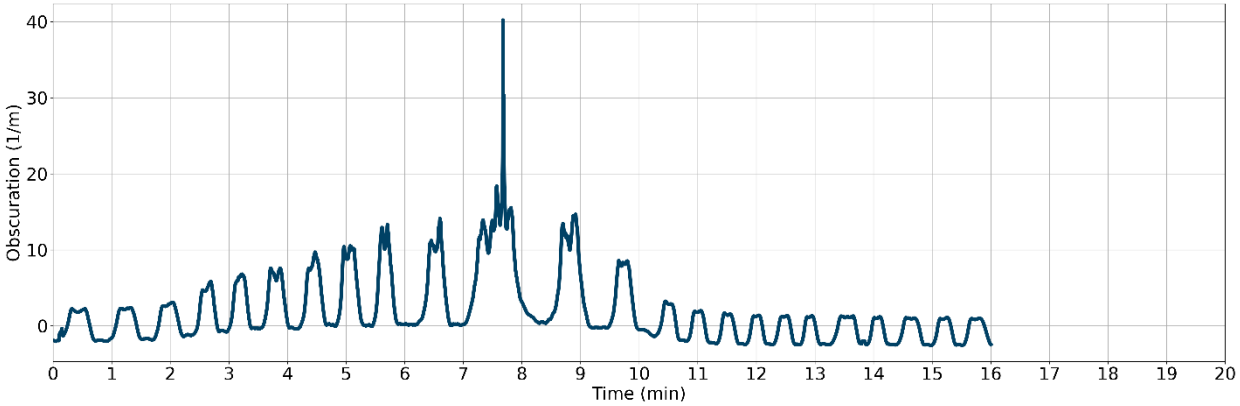

Figure F-54: Test 5 optical obscuration in the exhaust duct

Test 6 Results (Half-Scale Non-Combustible Door Configuration)

Heat Release Rate

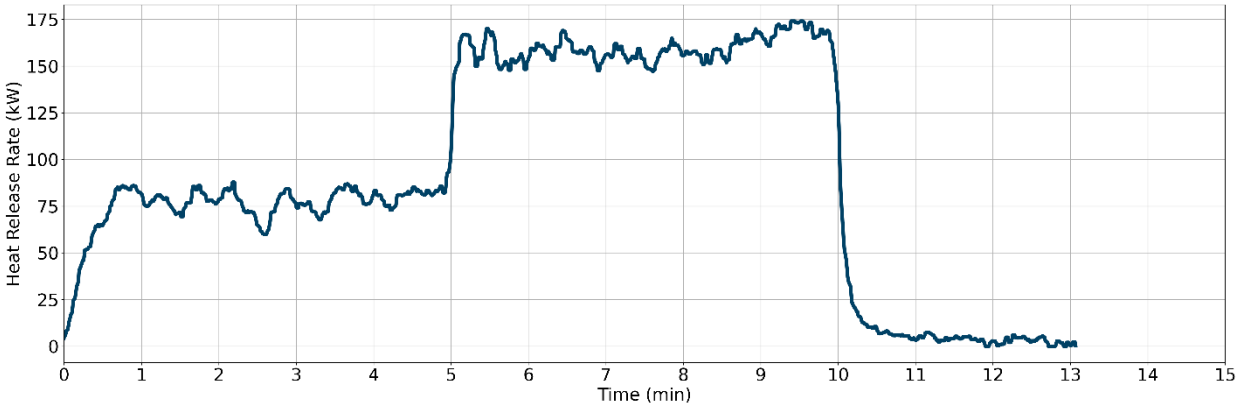

Figure F-55: Test 6 HRR

Gas Temperatures

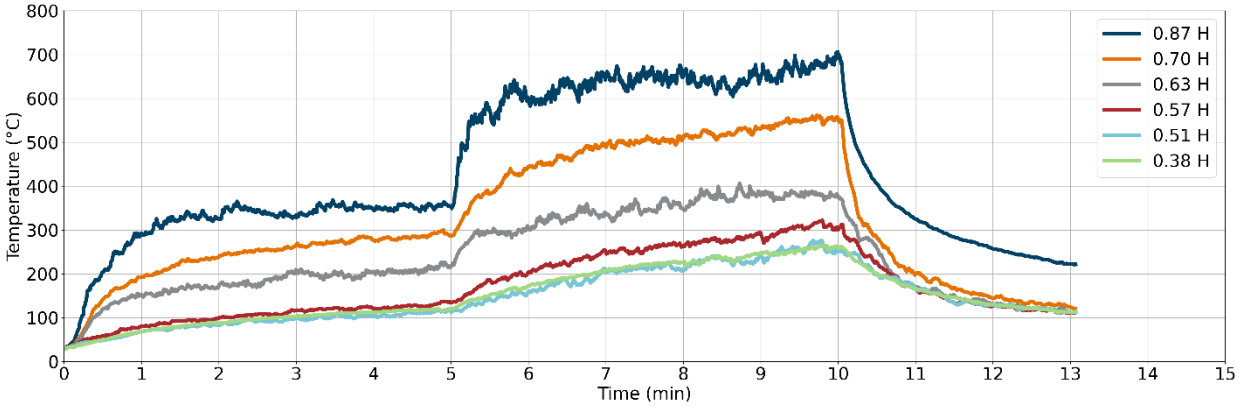

Figure F-56: Test 6 gas temperatures in the north-east corner

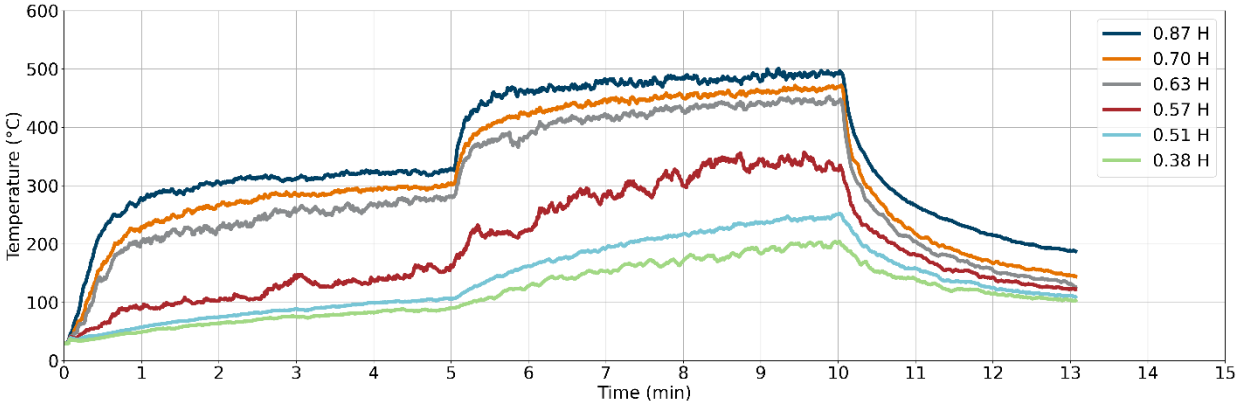

Figure F-57: Test 6 gas temperatures in the south-east corner

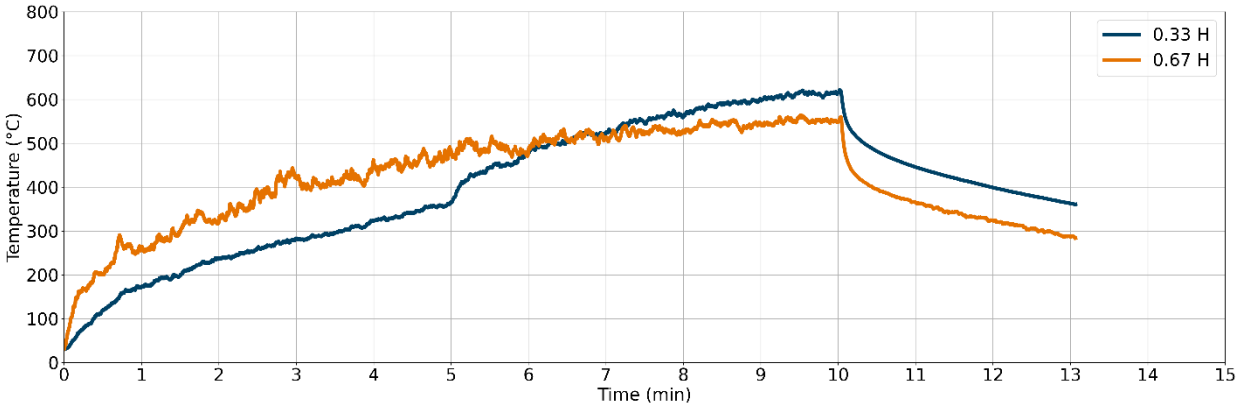

Figure F-58: Test 6 gas temperatures at the burner

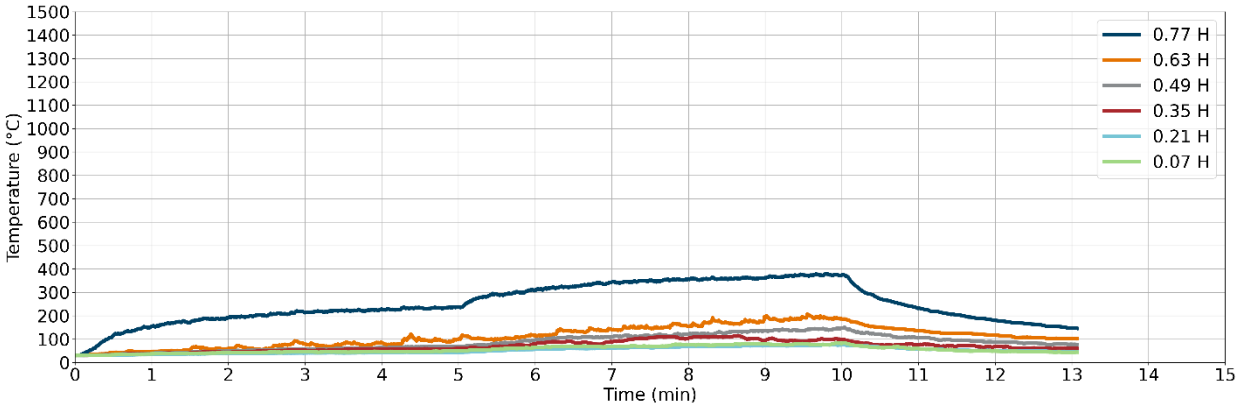

Figure F-59: Test 6 gas temperatures at the door

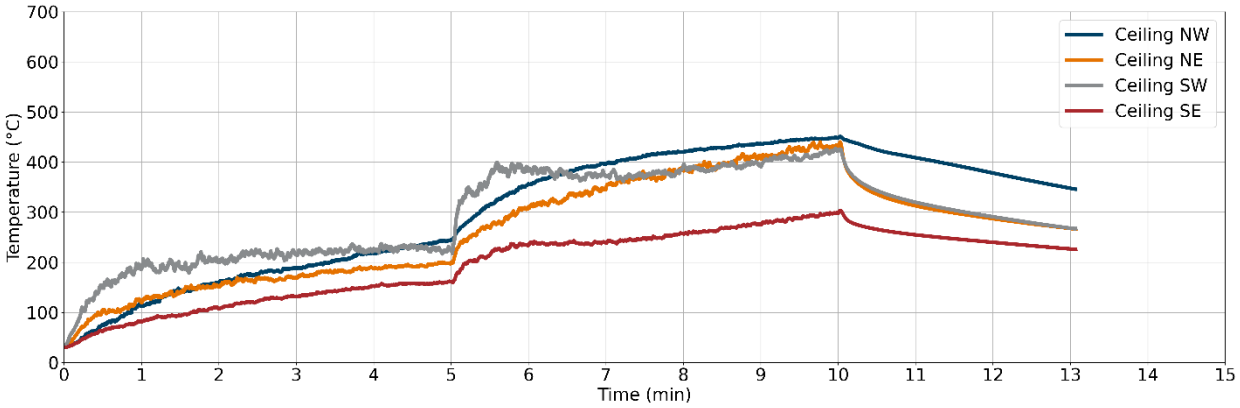

Figure F-60: Test 6 gas temperatures at ceiling

Gas Velocities

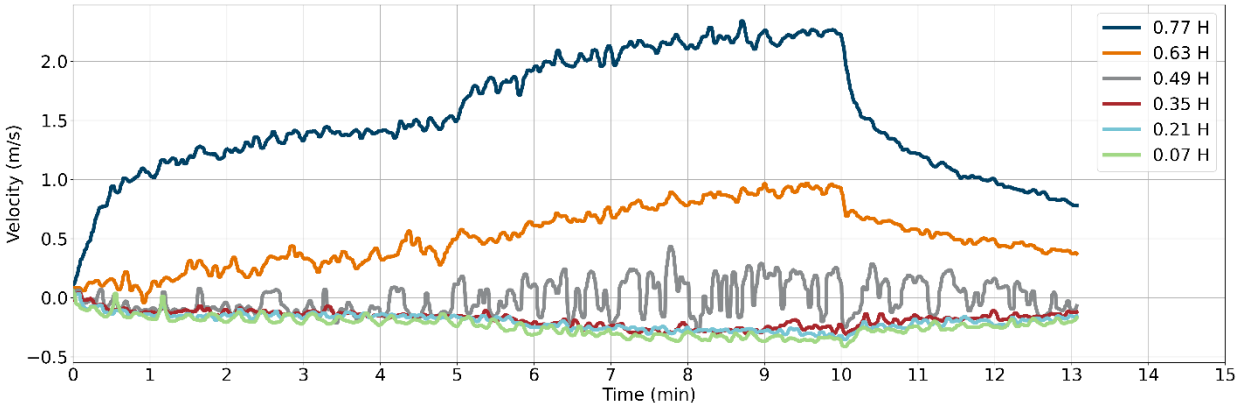

Figure F-61: Test 6 gas velocities at the door

Heat Fluxes

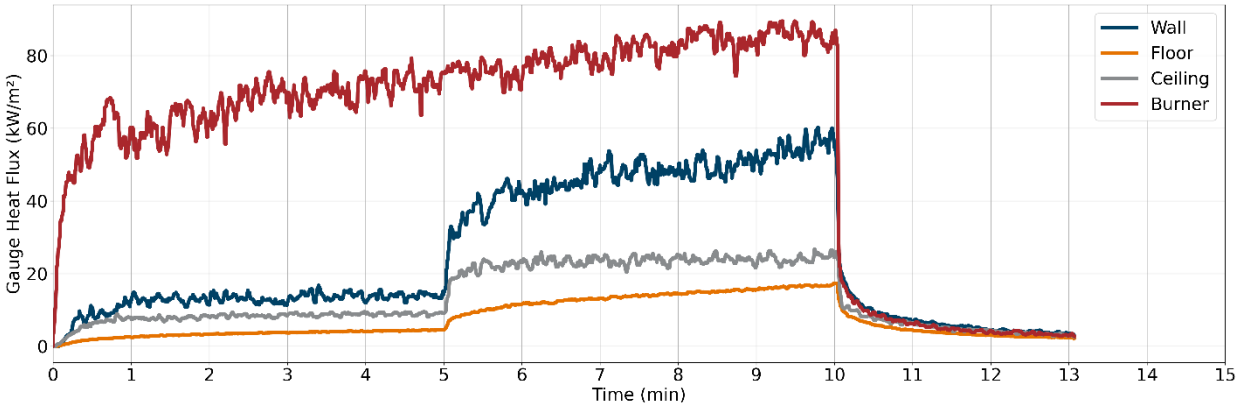

Figure F-62: Test 6 heat fluxes

Optical Obscuration

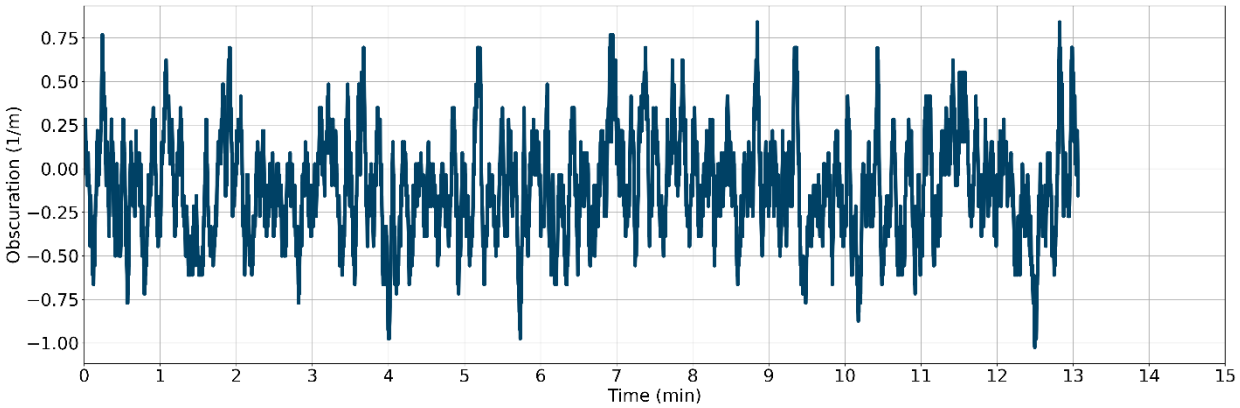

Figure F-63: Test 6 optical obscuration in the exhaust duct.

Test 7-A Results (Half-Scale Non-Combustible Door-Window Configuration)

Heat Release Rate

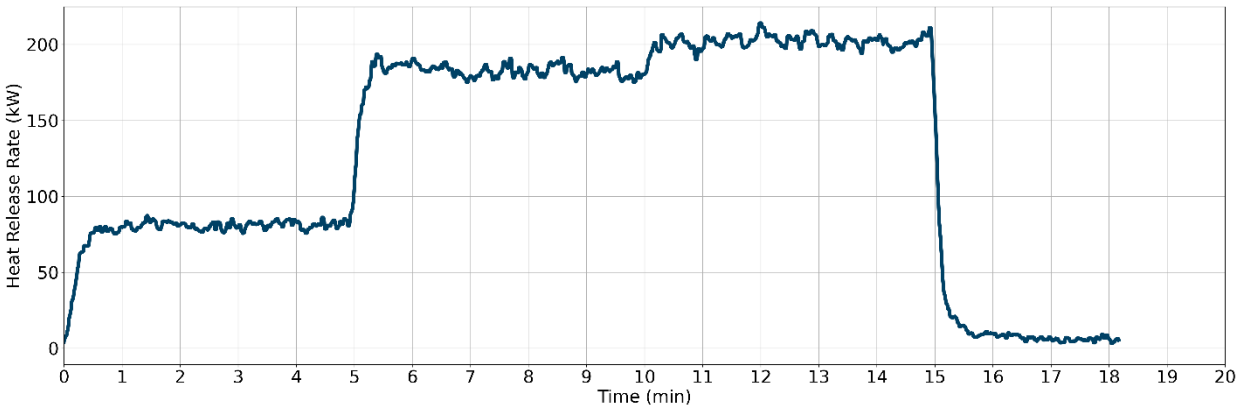

Figure F-64: Test 7-A HRR

Gas Temperatures

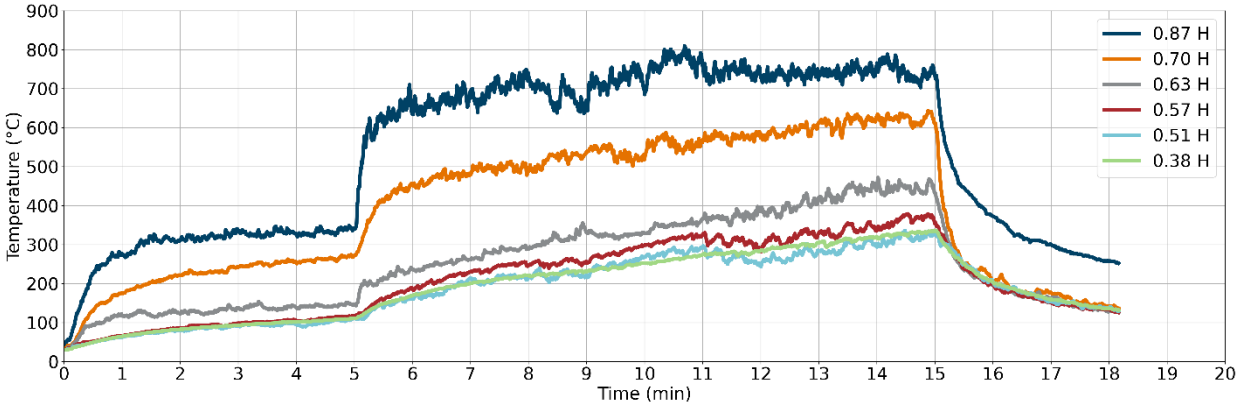

Figure F-65: Test 7-A gas temperatures in the north-east corner

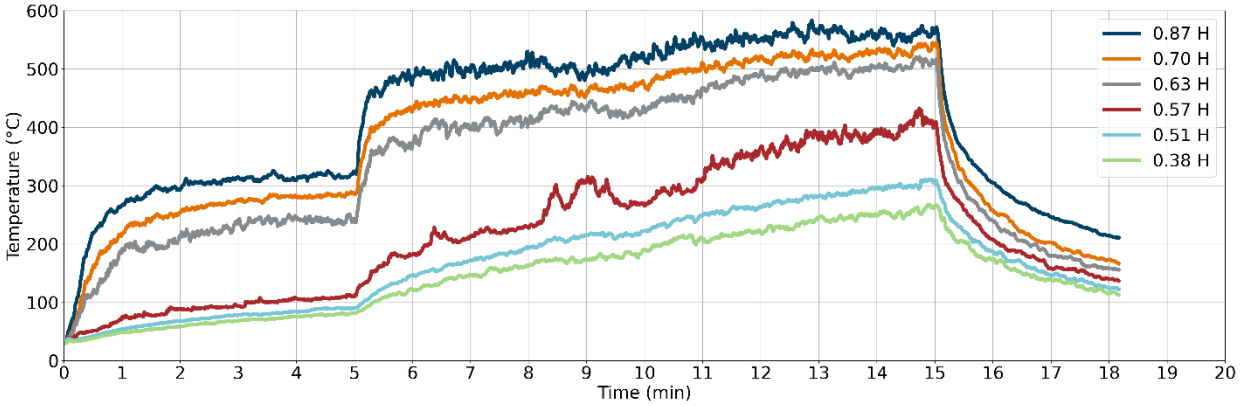

Figure F-66: Test 7-A gas temperatures in the south-east corner

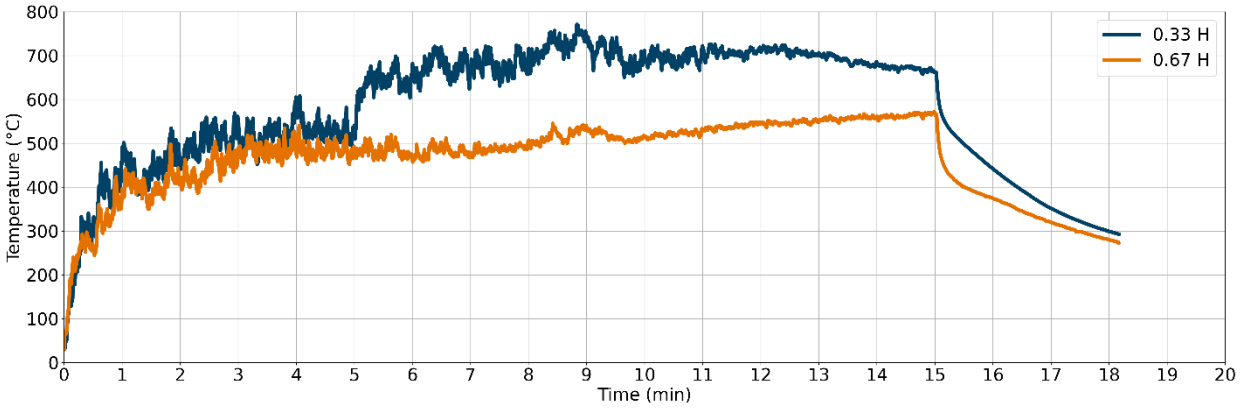

Figure F-67: Test 7-A gas temperatures at the burner

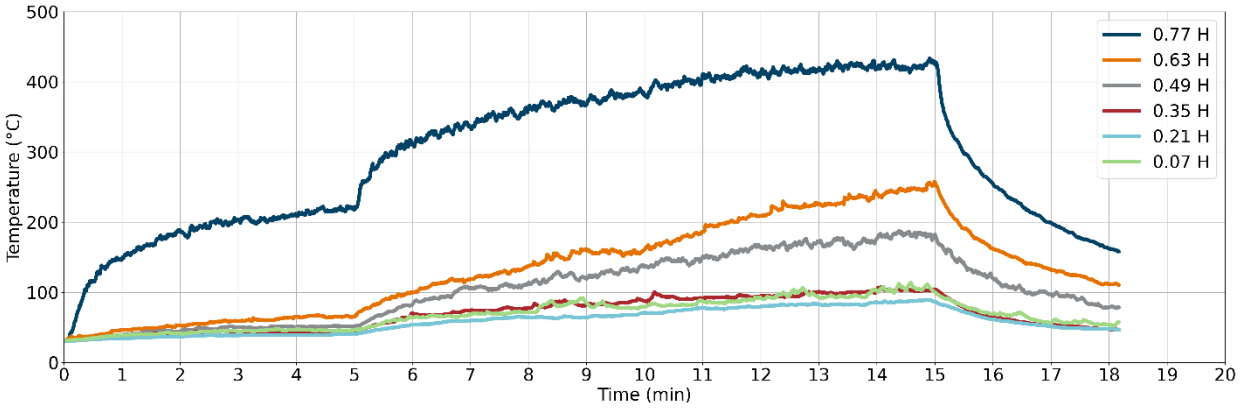

Figure F-68: Test 7-A gas temperatures at the door

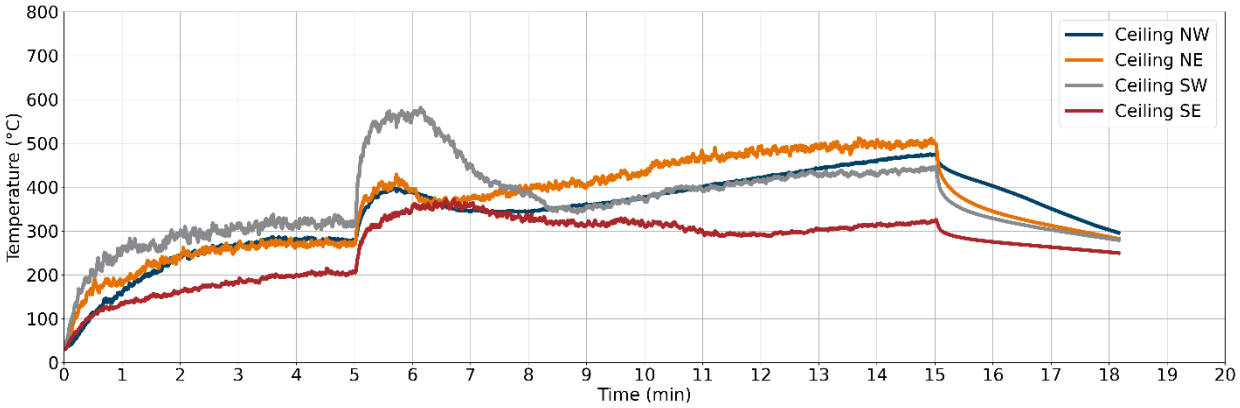

Figure F-69: Test 7-A gas temperatures at ceiling

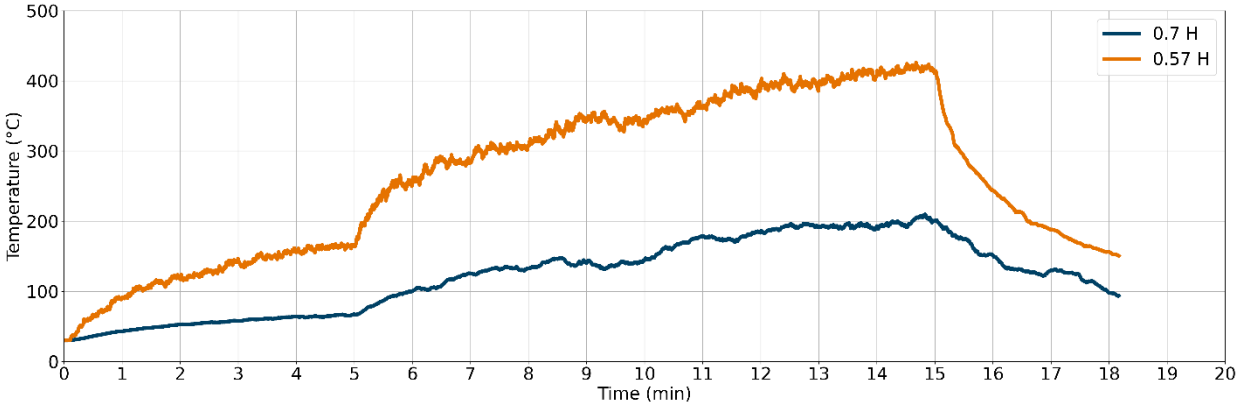

Figure F-70: Test 7-A gas temperatures at the window

Gas Velocities

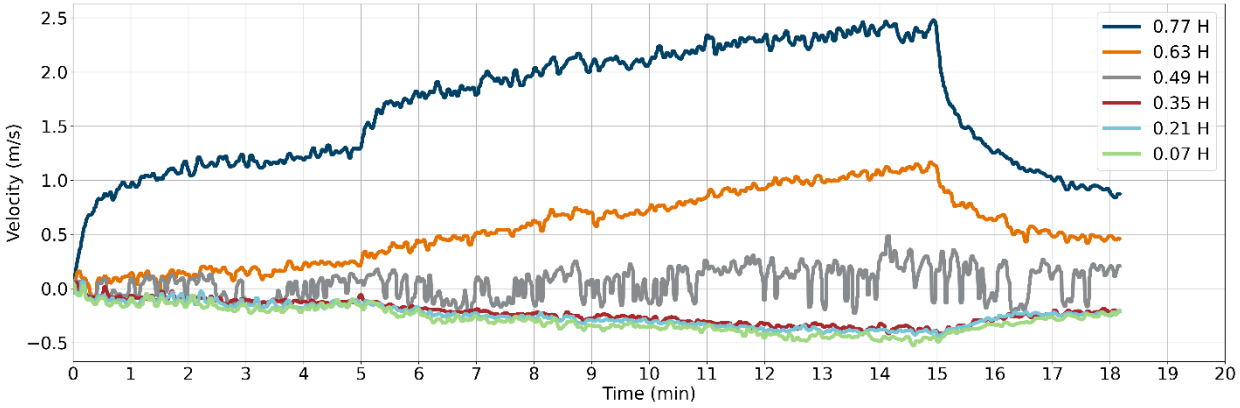

Figure F-71: Test 7-A gas velocities at the door

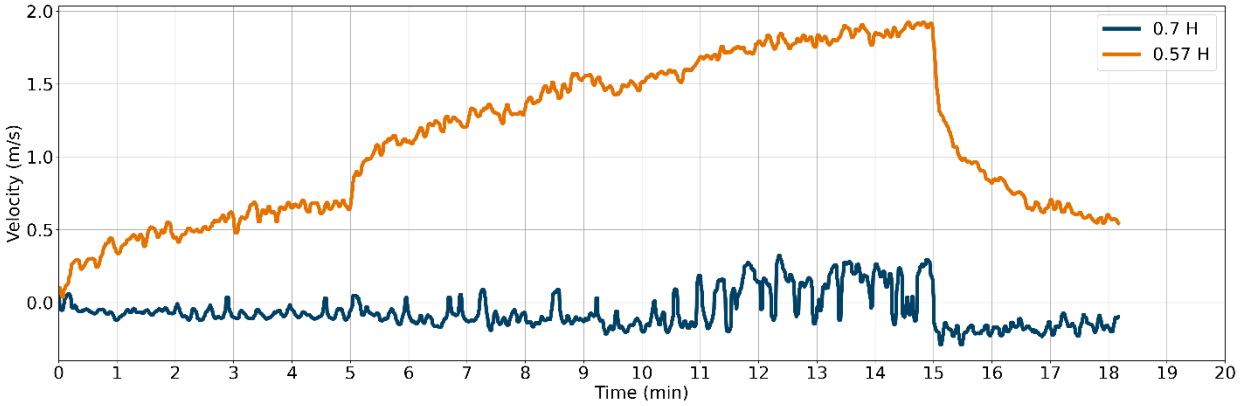

Figure F-72: Test 7-A gas velocities at the window

Heat Fluxes

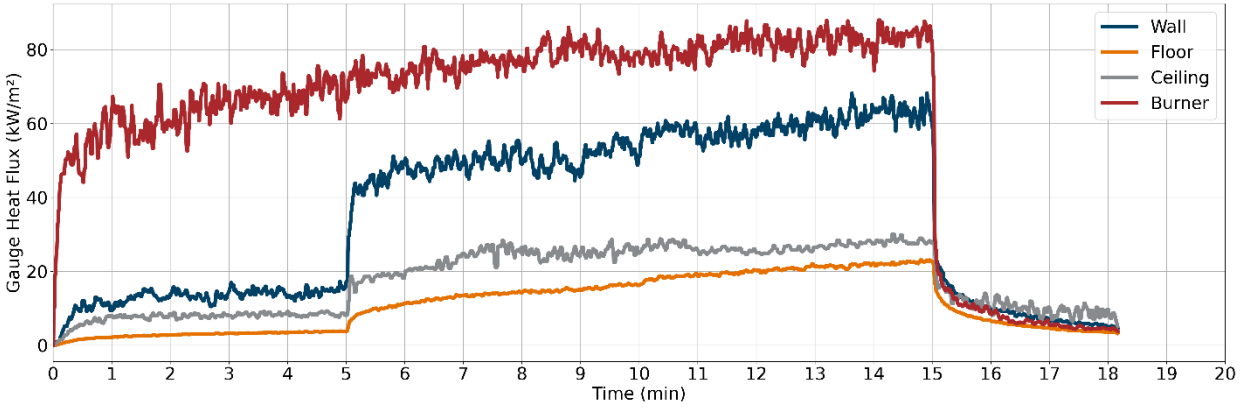

Figure F-73: Test 7-A heat fluxes

Optical Obscuration

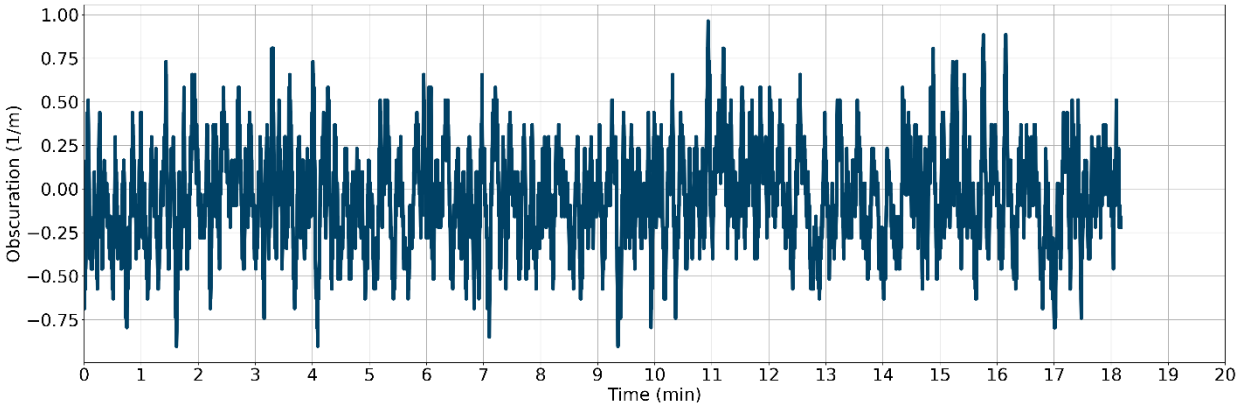

Figure F-74: Test 7-A optical obscuration in the exhaust duct

Test 7-B Results (Half-Scale Non-Combustible Door-Window Configuration)

Heat Release Rate

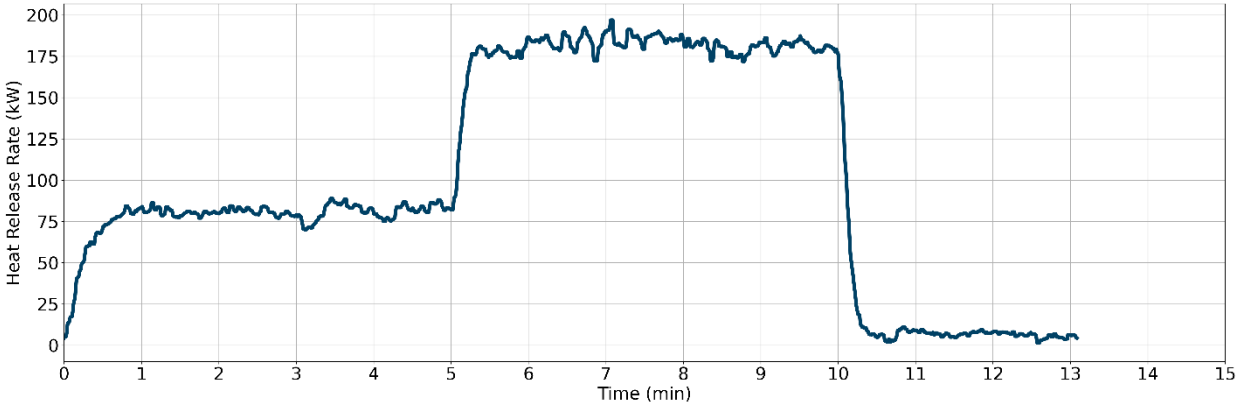

Figure F-75: Test 7-B HRR

Gas Temperatures

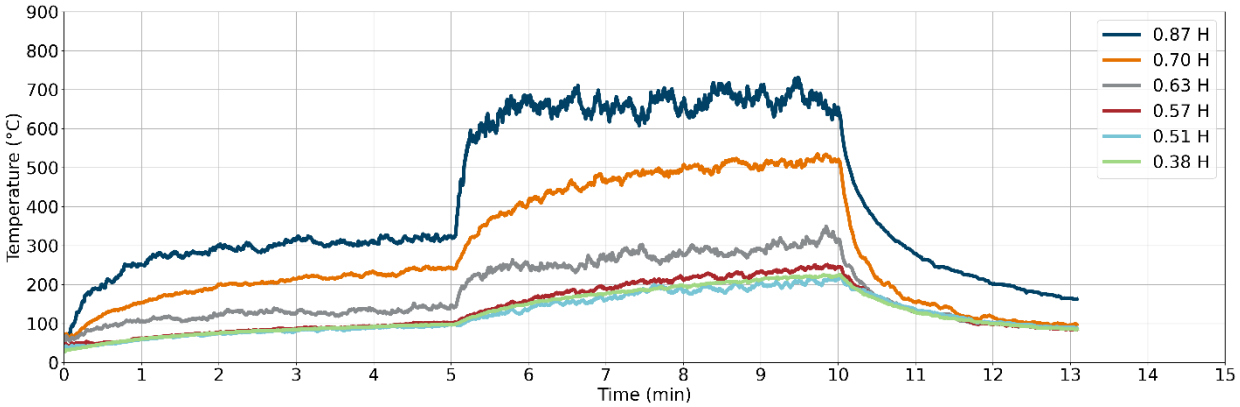

Figure F-76: Test 7-B gas temperatures in the north-east corner

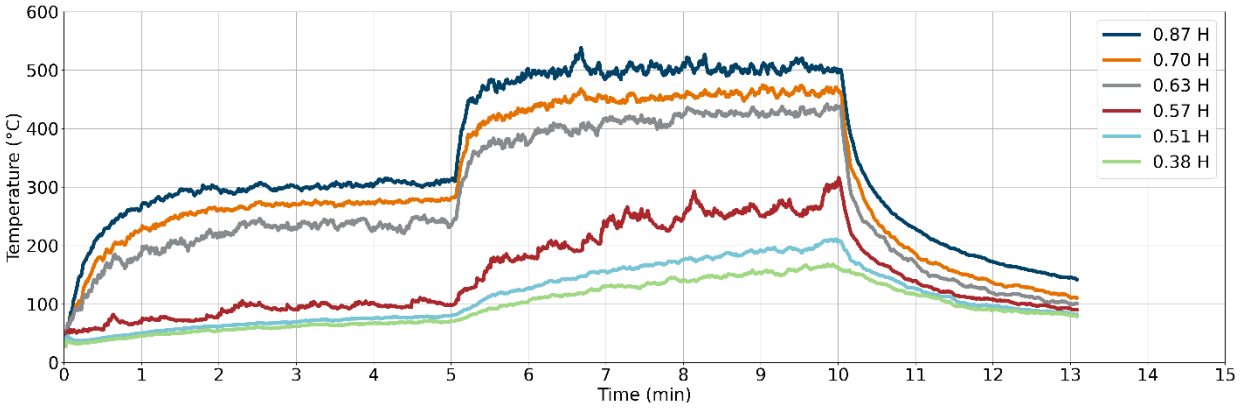

Figure F-77: Test 7-B gas temperatures in the south-east corner

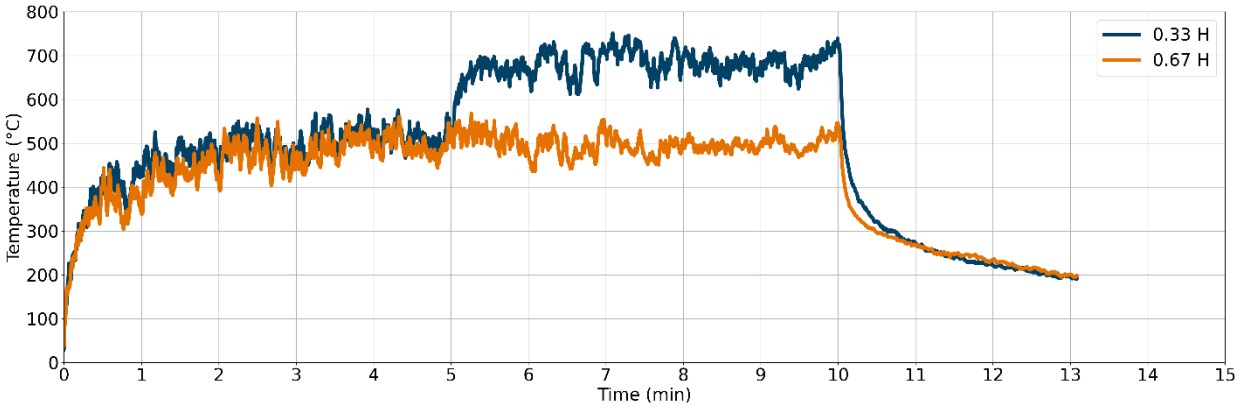

Figure F-78: Test 7-B gas temperatures at the burner

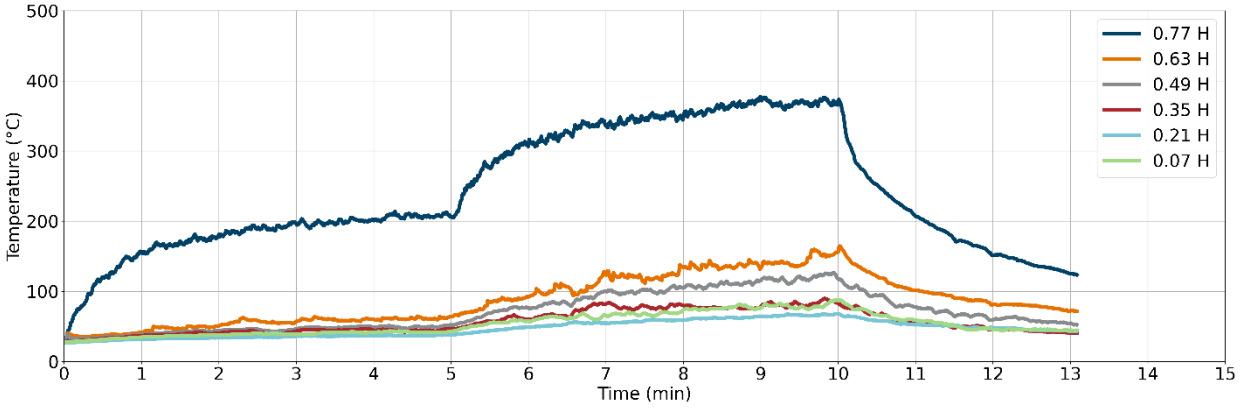

Figure F-79: Test 7-B gas temperatures at the door

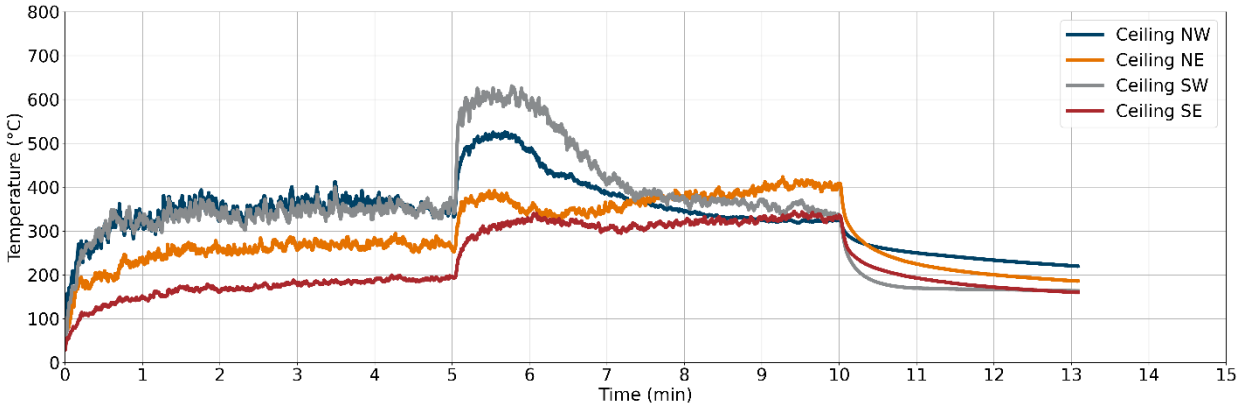

Figure F-80: Test 7-B gas temperatures at ceiling

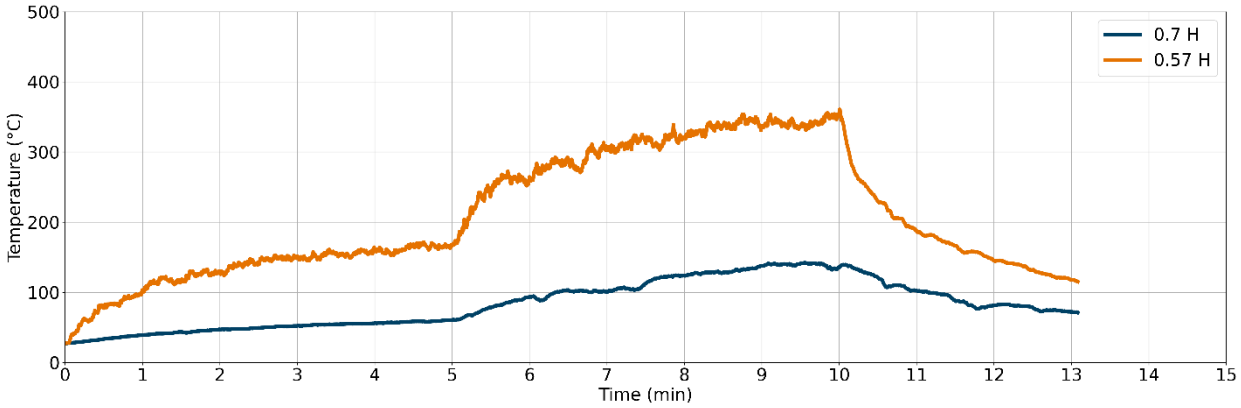

Figure F-81: Test 7-B gas temperatures at the window

Gas Velocities

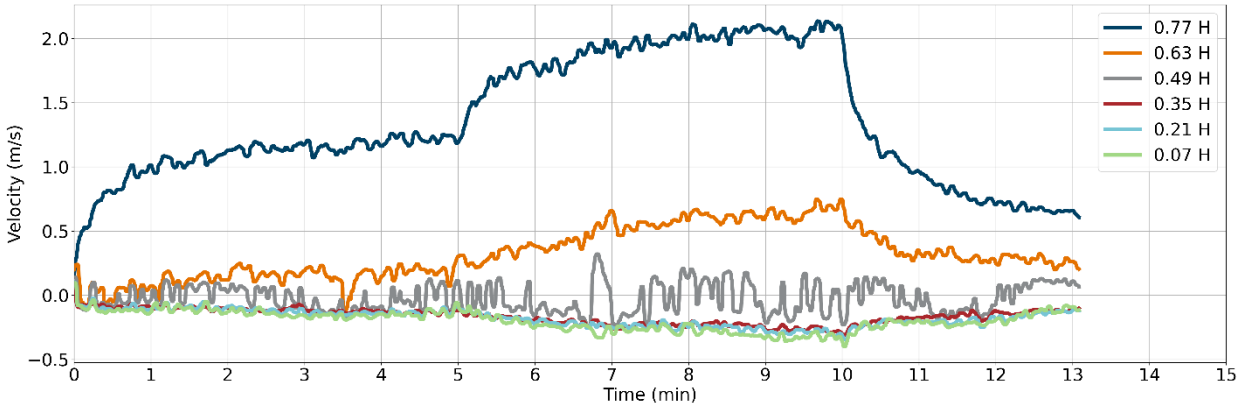

Figure F-82: Test 7-B gas velocities at the door

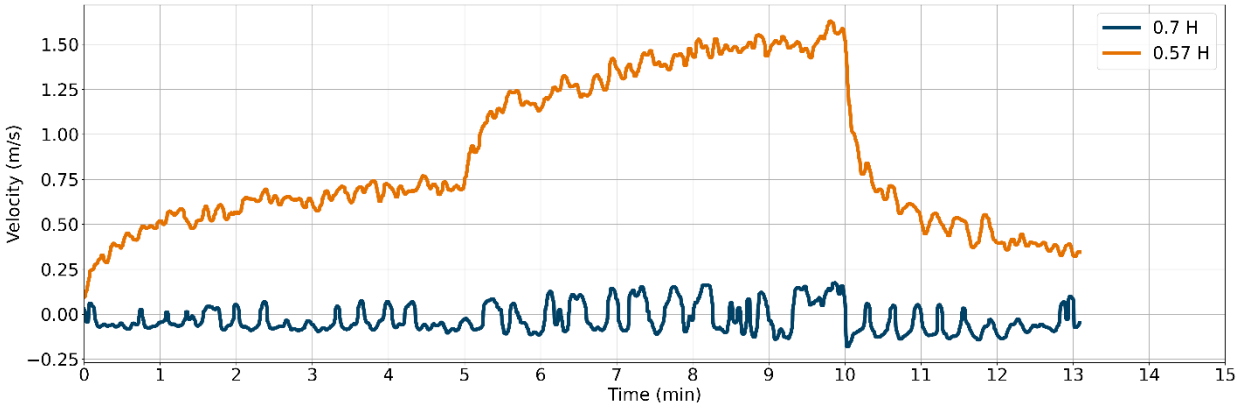

Figure F-83: Test 7-B gas velocities at the window

Heat Fluxes

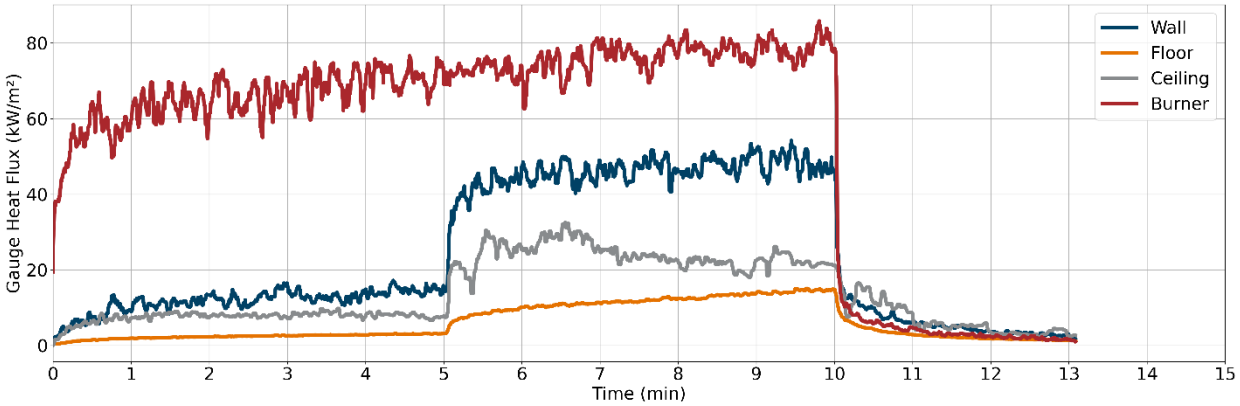

Figure F-84: Test 7-B heat fluxes

Optical Obscuration

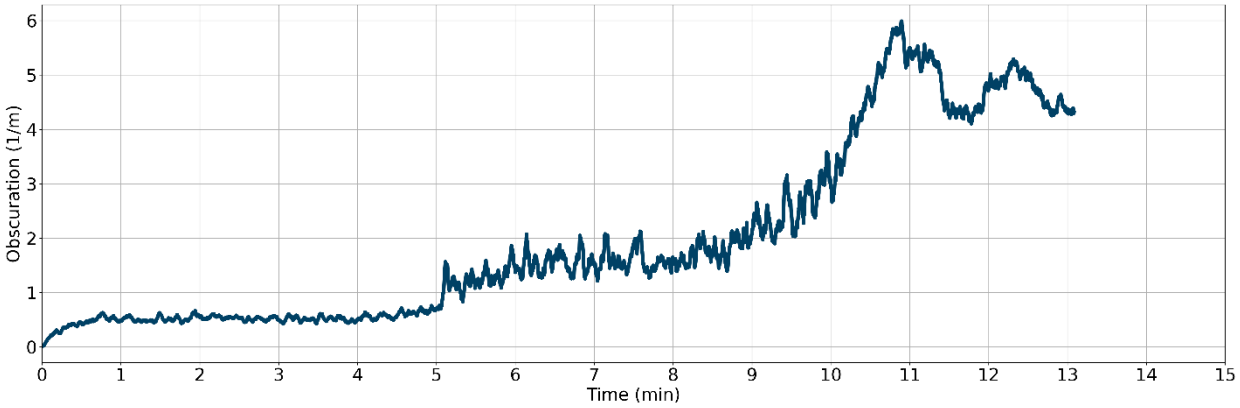

Figure F-85: Test 7-B optical obscuration in the exhaust duct

Test 8 Results (Half-Scale Liquid Fuel / JP-5 Configuration)

Heat Release Rate

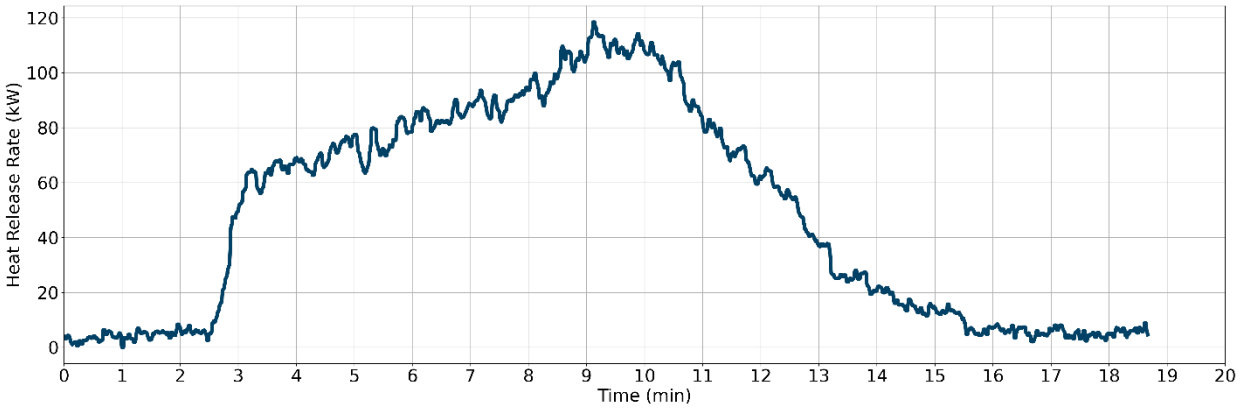

Figure F-86: Test 8 HRR

Gas Temperatures

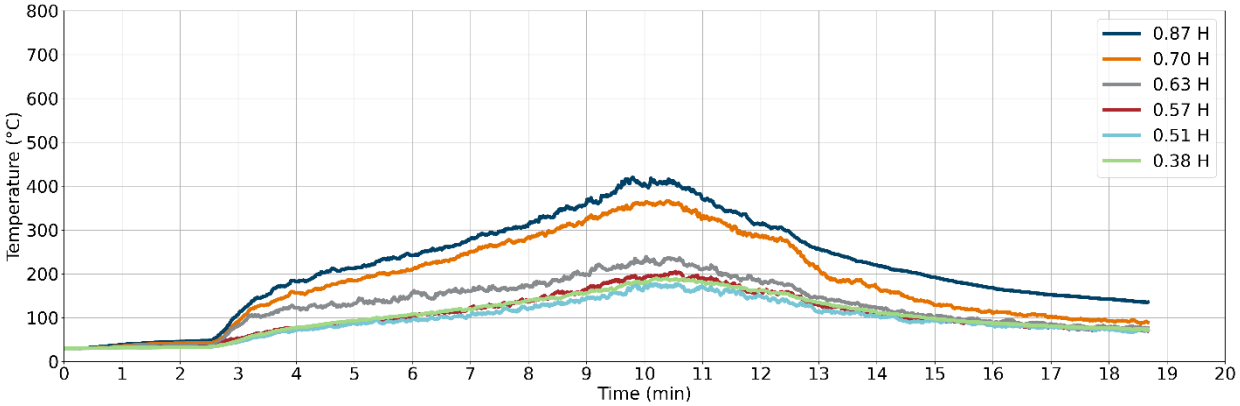

Figure F-87: Test 8 gas temperatures in the north-east corner

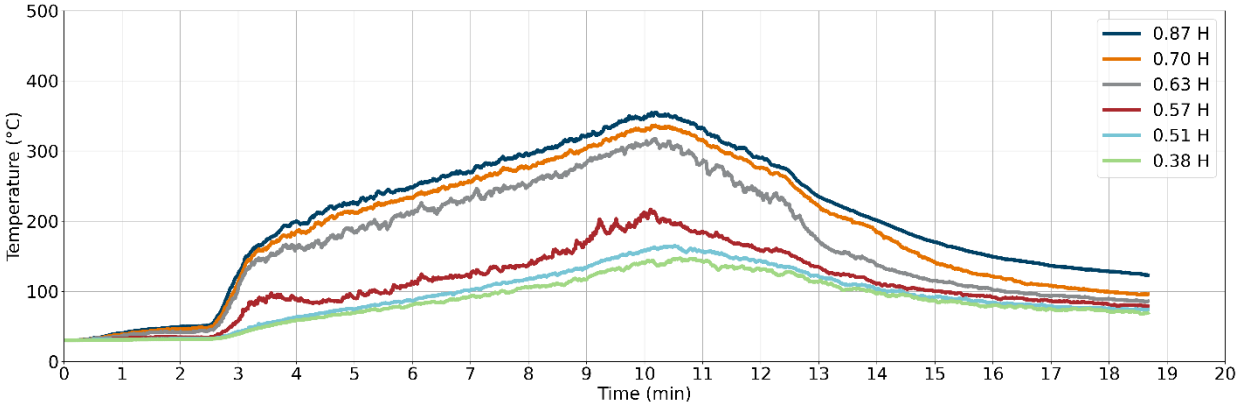

Figure F-88: Test 8 gas temperatures in the south-east corner

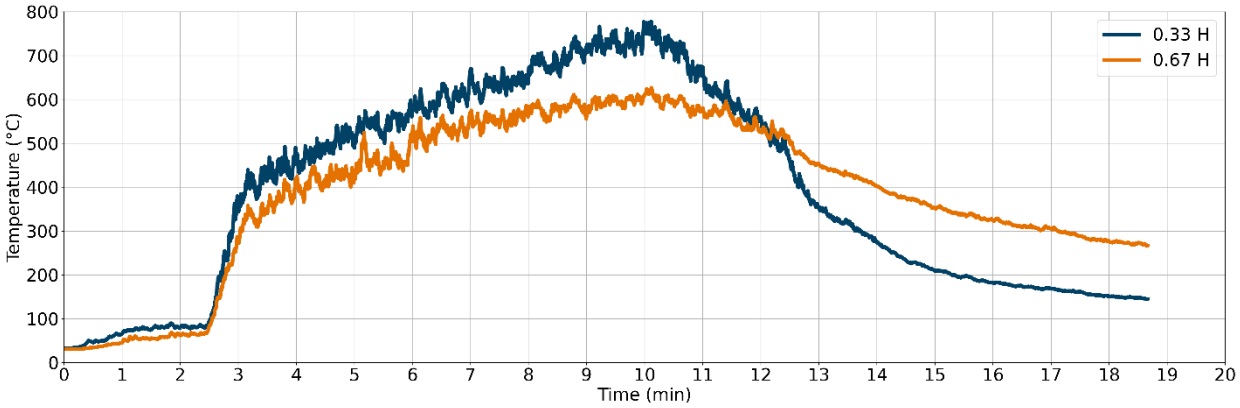

Figure F-89: Test 8 gas temperatures at the burner

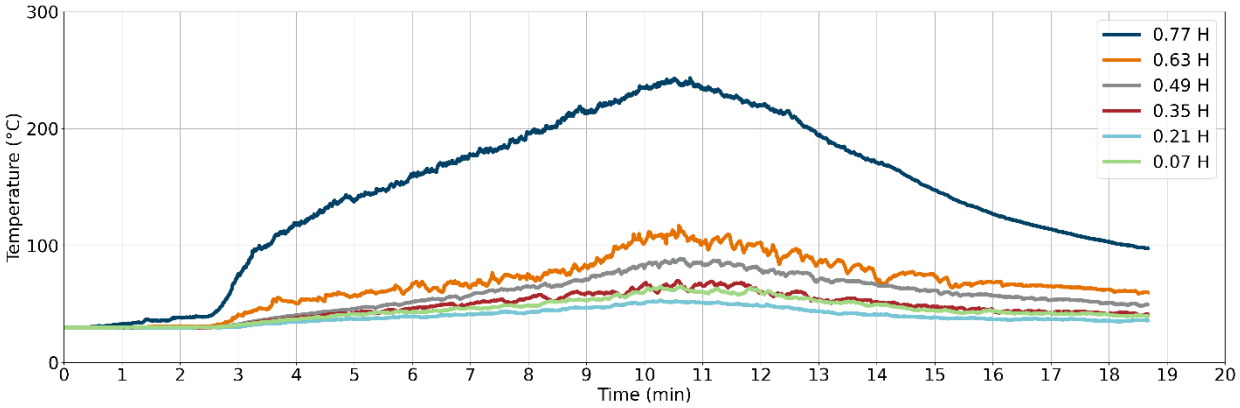

Figure F-90: Test 8 gas temperatures at the door

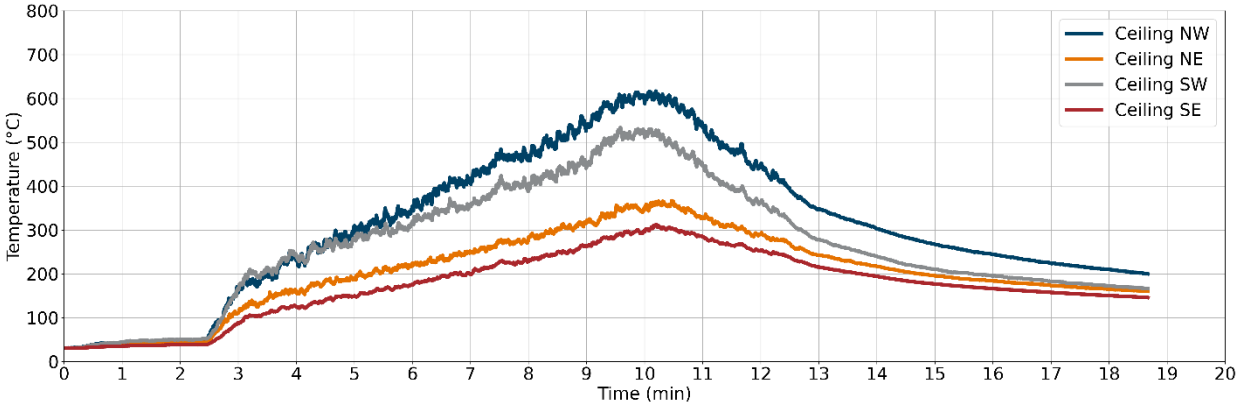

Figure F-91: Test 8 gas temperatures at ceiling

Gas Velocities

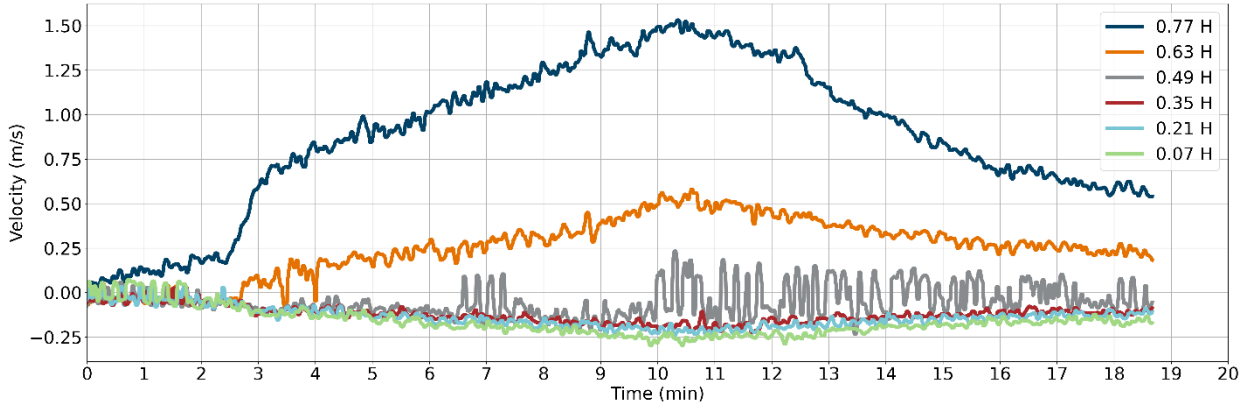

Figure F-92: Test 8 gas velocities at the door

Heat Fluxes

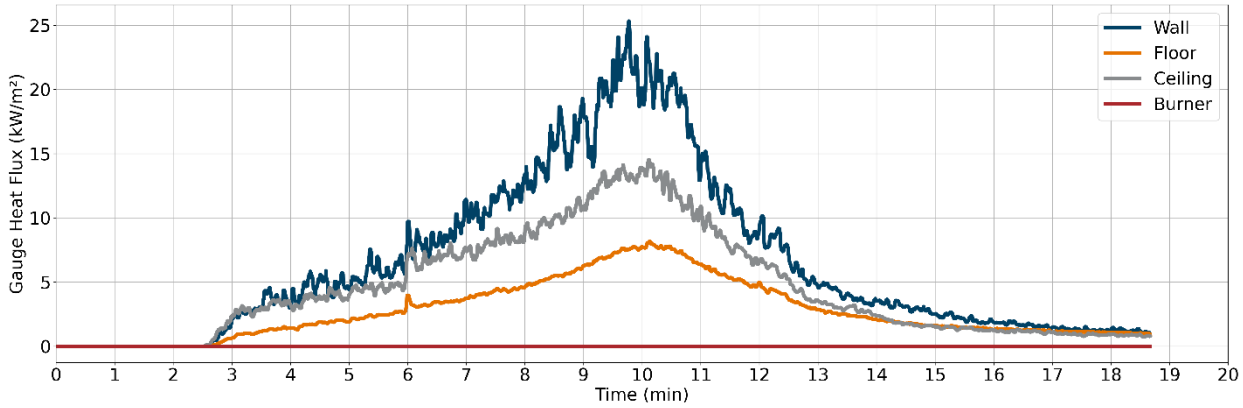

Figure F-93: Test 8 heat fluxes

Optical Obscuration

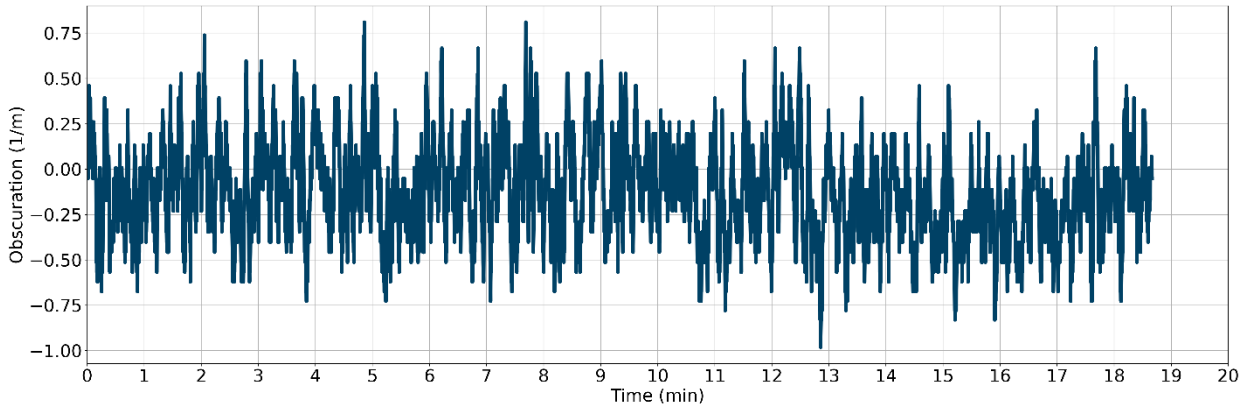

Figure F-94: Test 8 optical obscuration in the exhaust duct

Test 9 Results (Half-Scale Plywood Lining Configuration)

Heat Release Rate

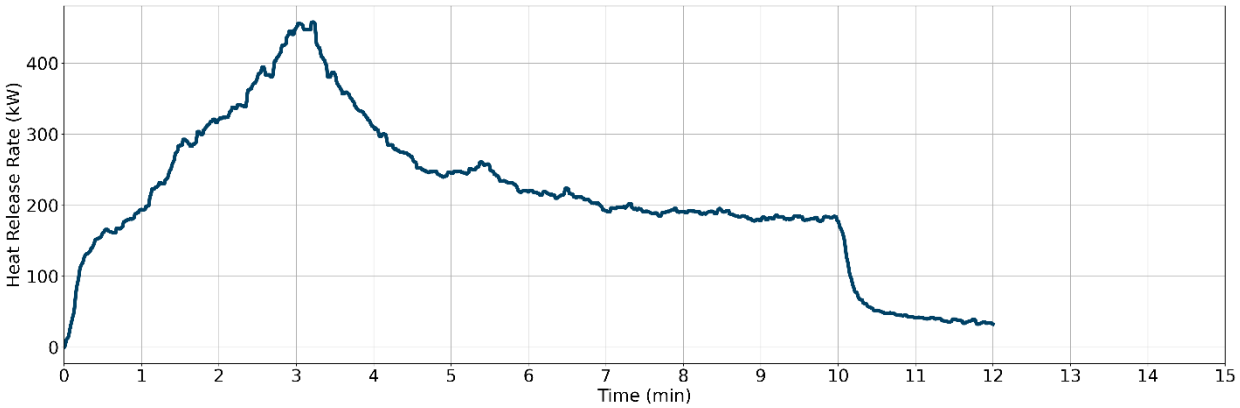

Figure F-95: Test 9 HRR

Gas Temperatures

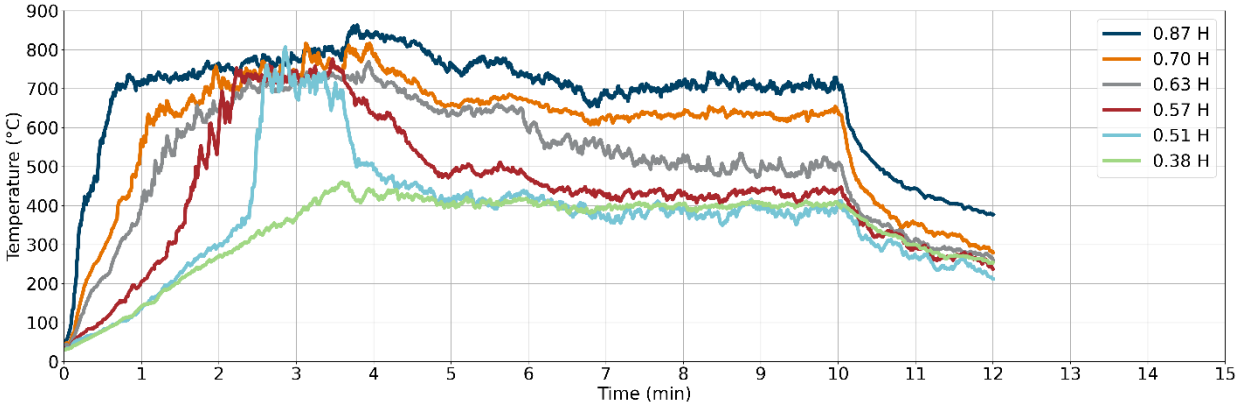

Figure F-96: Test 9 gas temperatures in the north-east corner

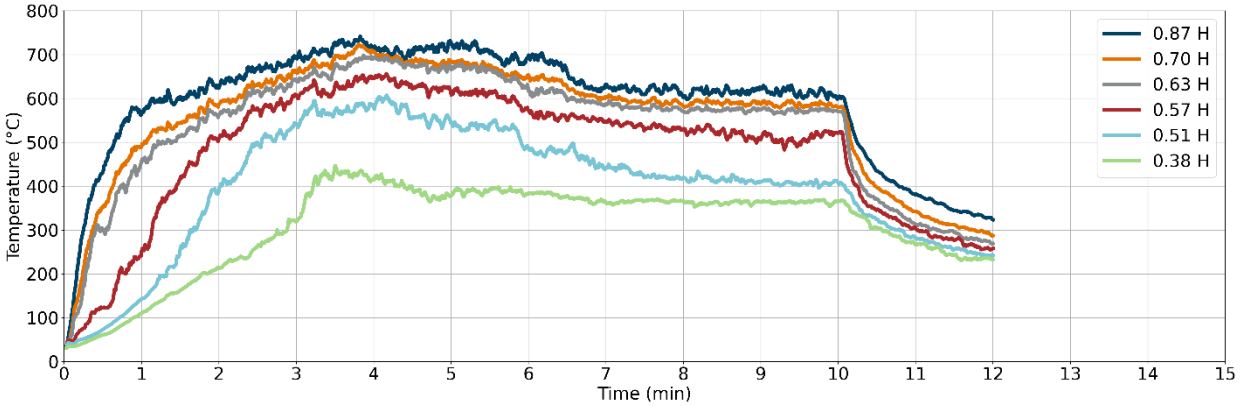

Figure F-97: Test 9 gas temperatures in the south-east corner

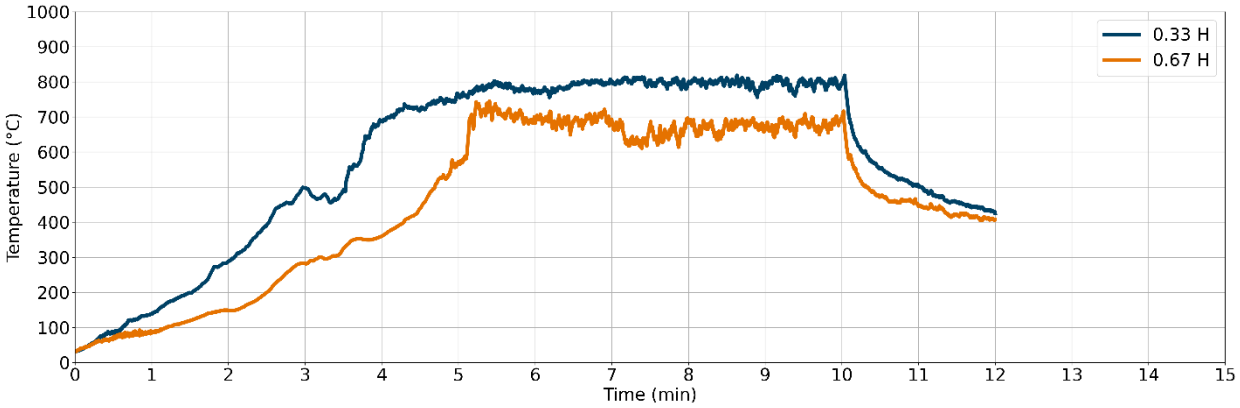

Figure F-98: Test 9 gas temperatures at the burner

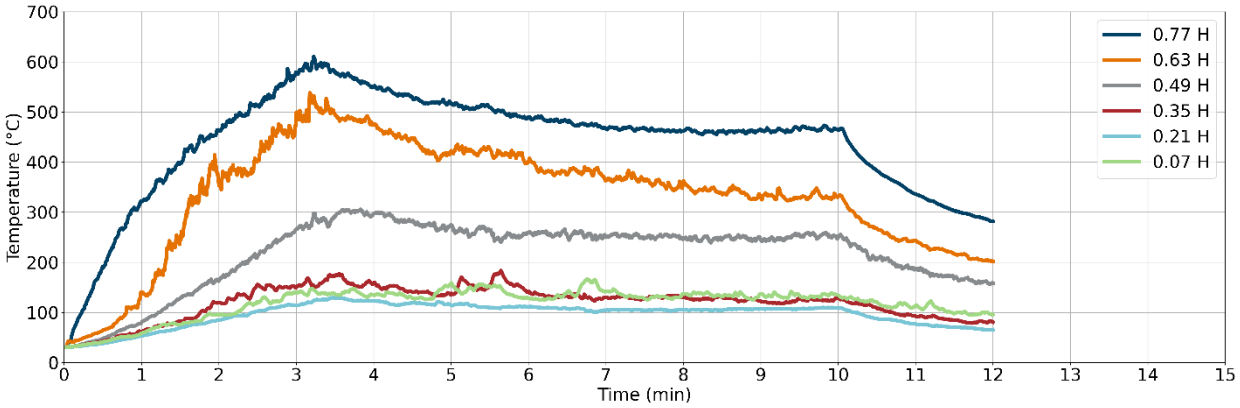

Figure F-99: Test 9 gas temperatures at the door

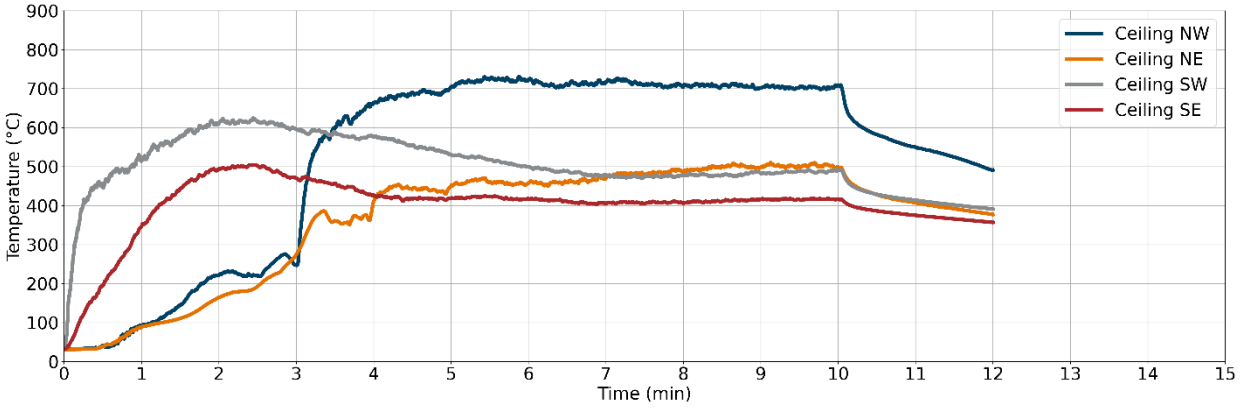

Figure F-100: Test 9 gas temperatures at ceiling

Gas Velocities

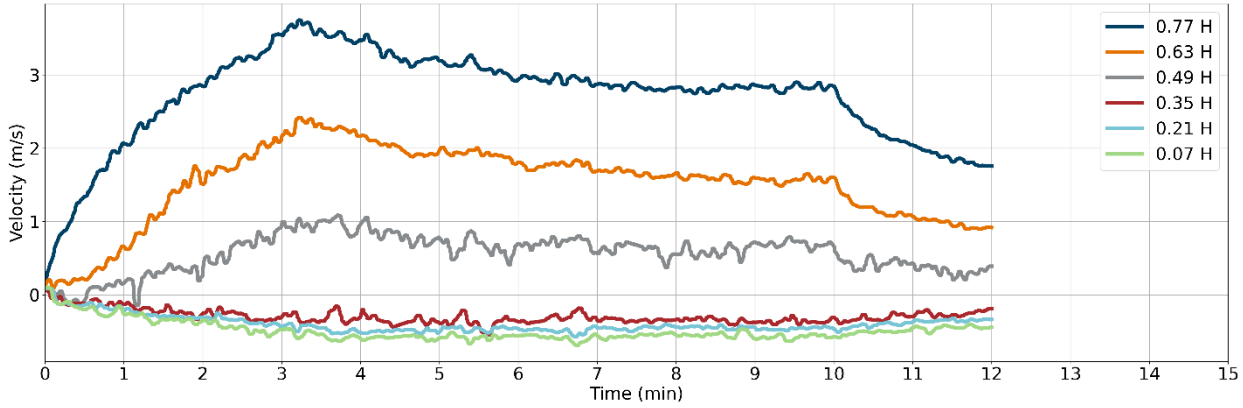

Figure F-101: Test 9 gas velocities at the door

Heat Fluxes

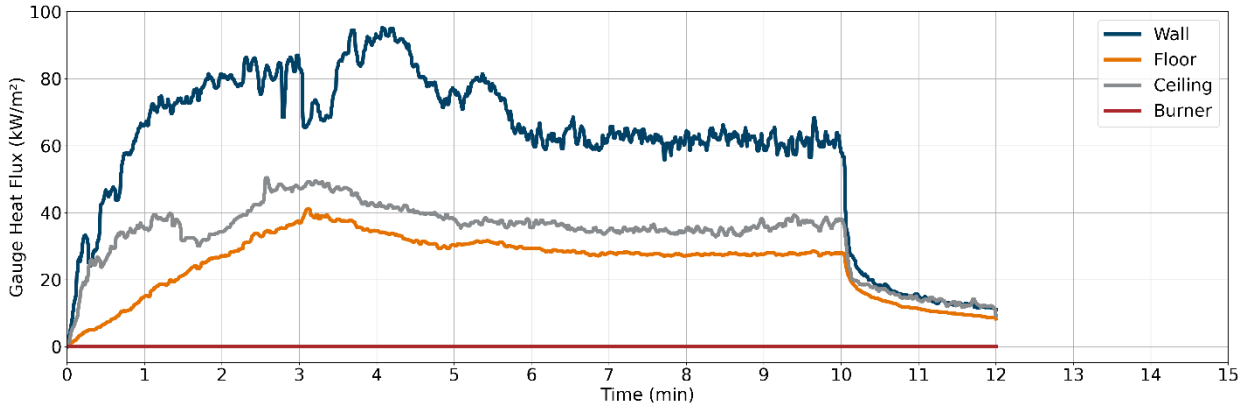

Figure F-102: Test 9 heat fluxes

Optical Obscuration

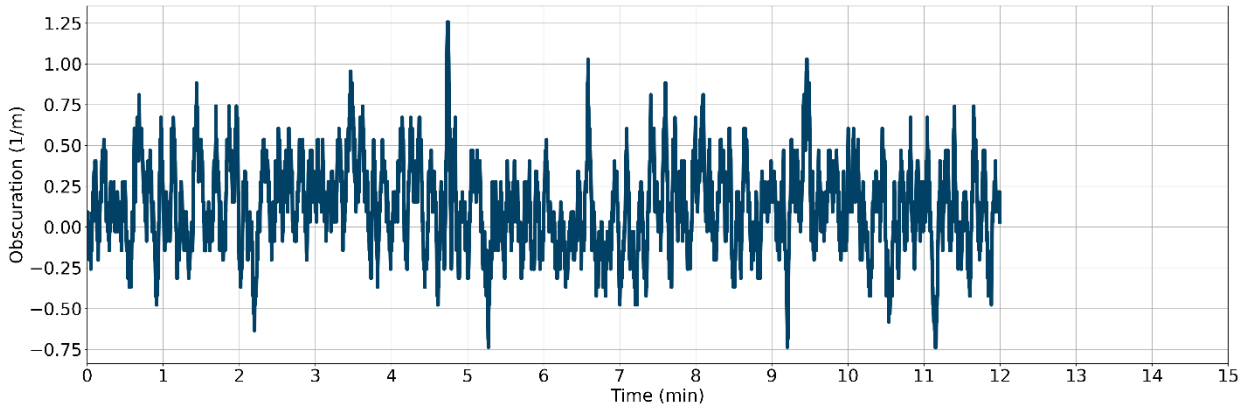

Figure F-103: Test 9 optical obscuration in the exhaust duct

Test 10 Results (Half-Scale FRP Lining Configuration)

Heat Release Rate

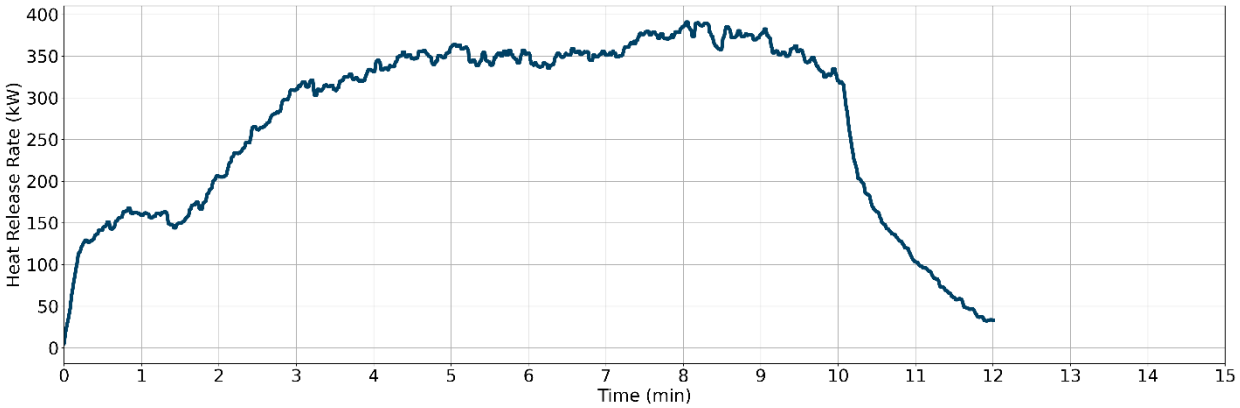

Figure F-104: Test 10 HRR

Gas Temperatures

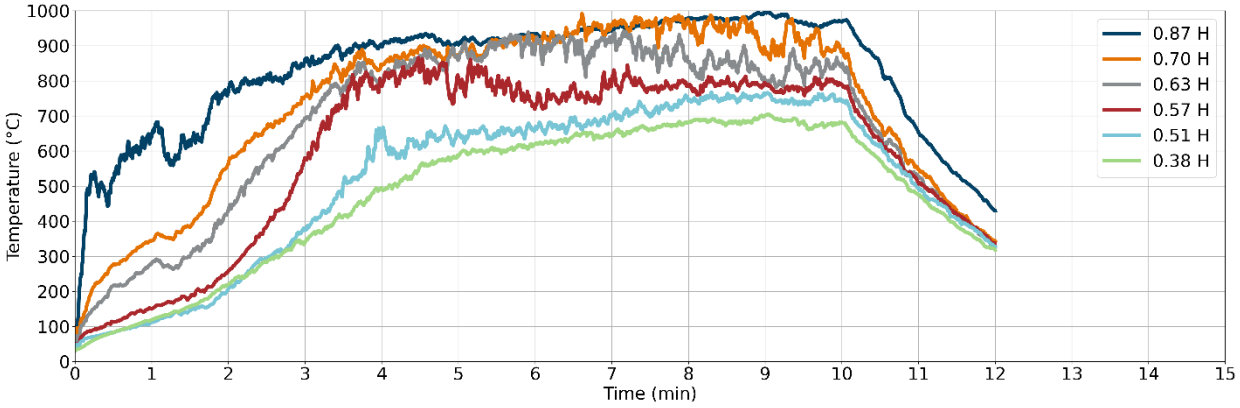

Figure F-105: Test 10 gas temperatures in the north-east corner

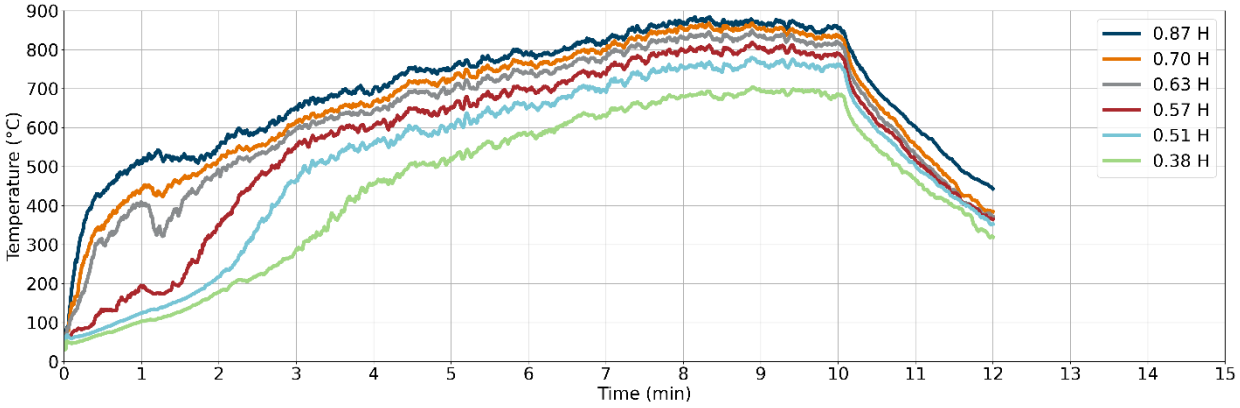

Figure F-106: Test 10 gas temperatures in the south-east corner

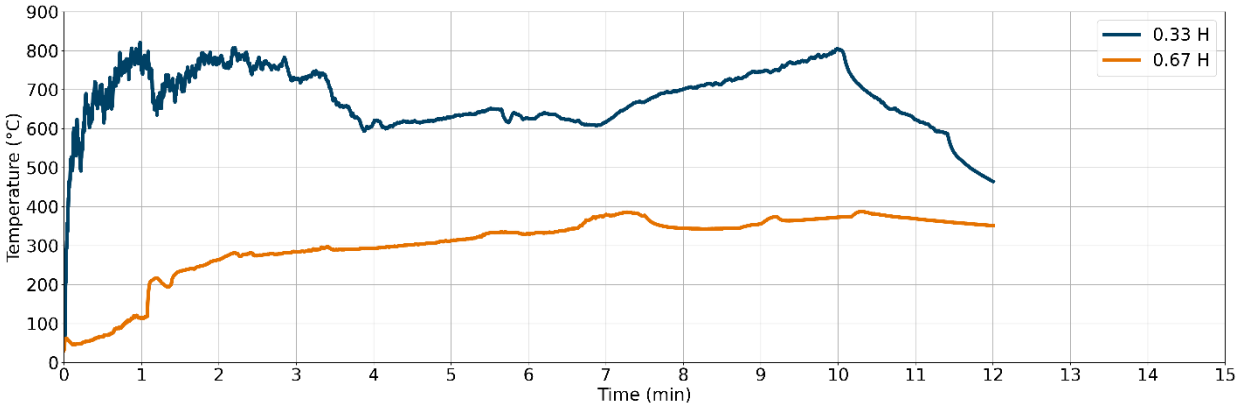

Figure F-107: Test 10 gas temperatures at the burner

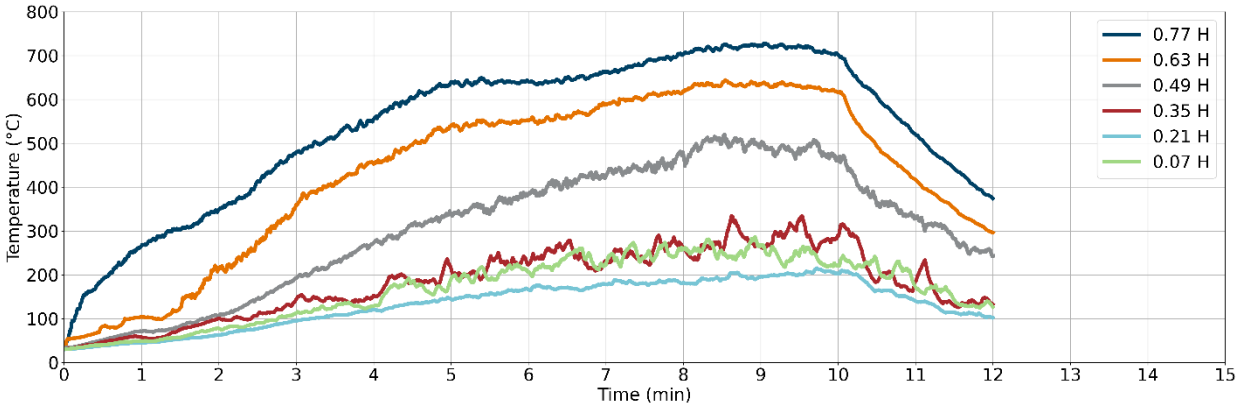

Figure F-108: Test 10 gas temperatures at the door

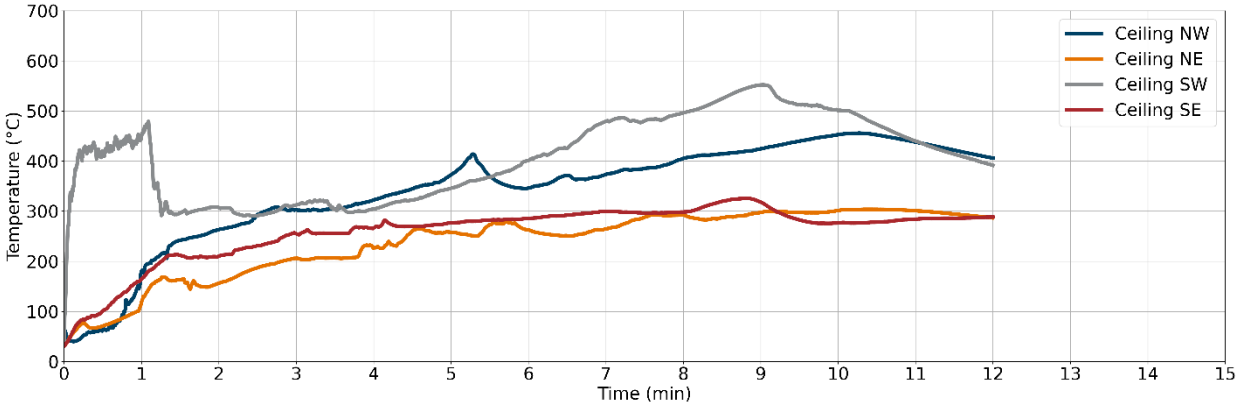

Figure F-109: Test 10 gas temperatures at ceiling

Gas Velocities

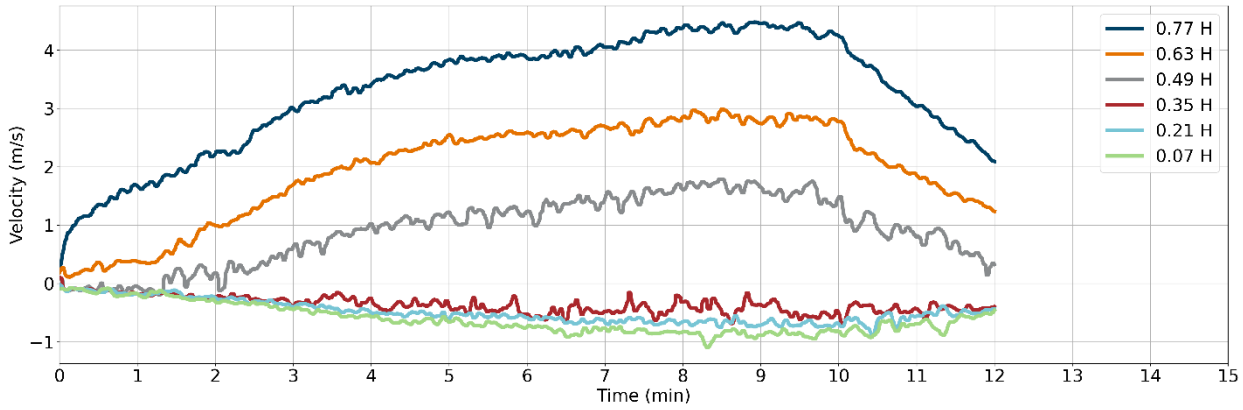

Figure F-110: Test 10 gas velocities at the door

Heat Fluxes

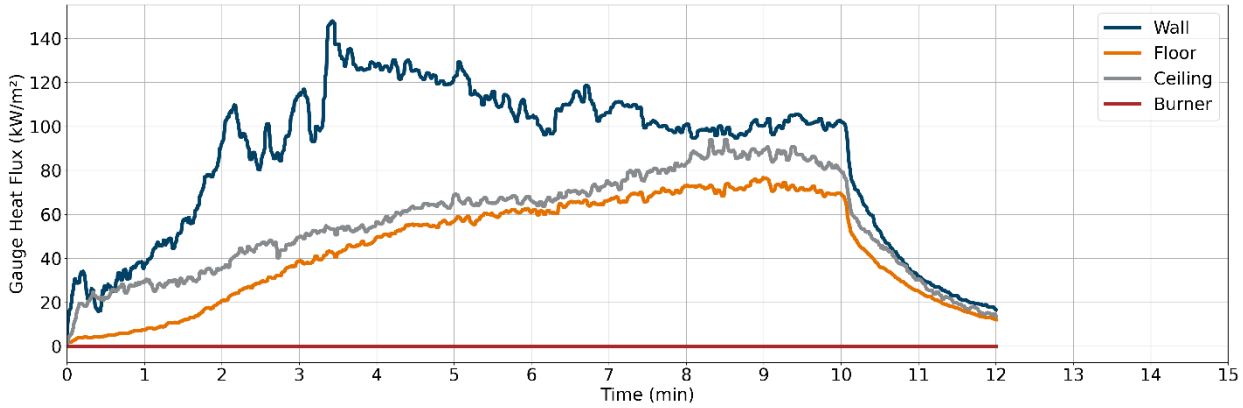

Figure F-111: Test 10 heat fluxes

Optical Obscuration

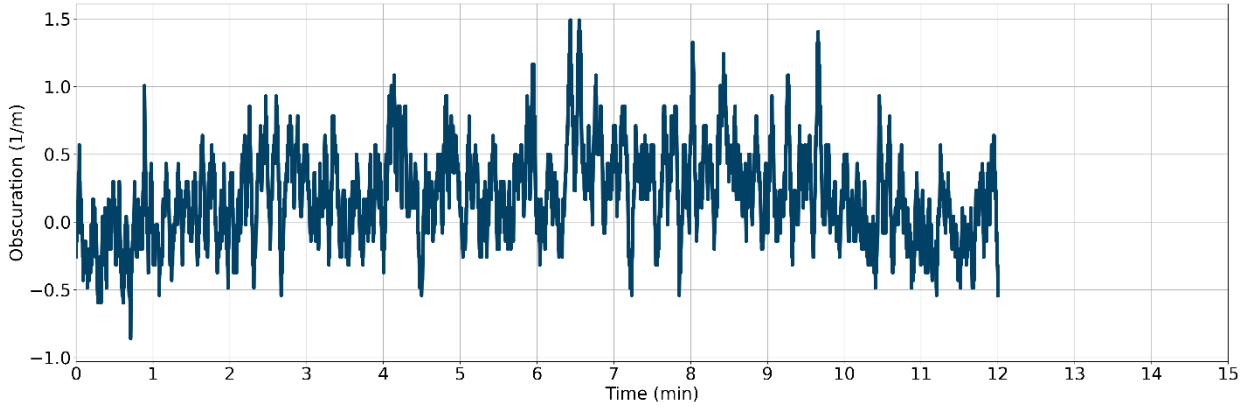

Figure F-112: Test 10 optical obscuration in the exhaust duct

Test 11 Results (Full-Scale Non-Combustible Door Configuration)

Heat Release Rate

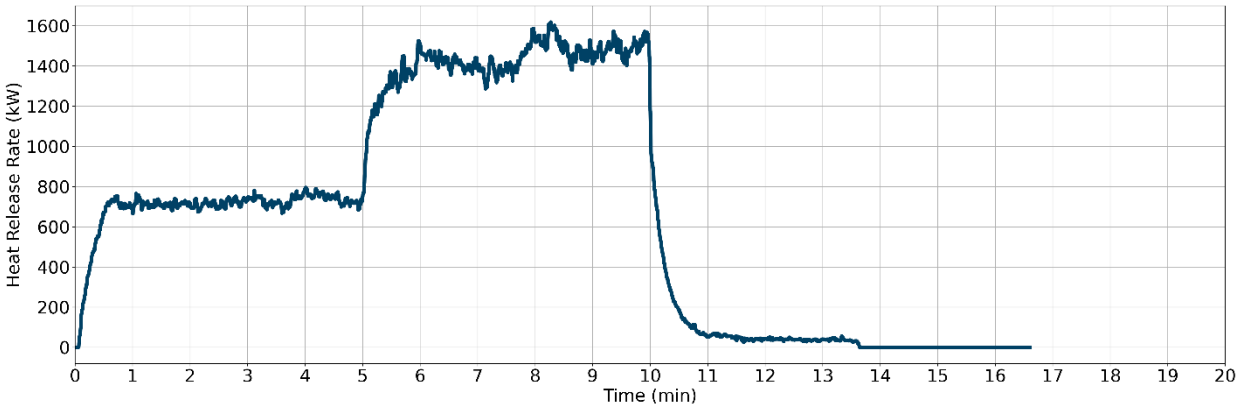

Figure F-113: Test 11 HRR

Gas Temperatures

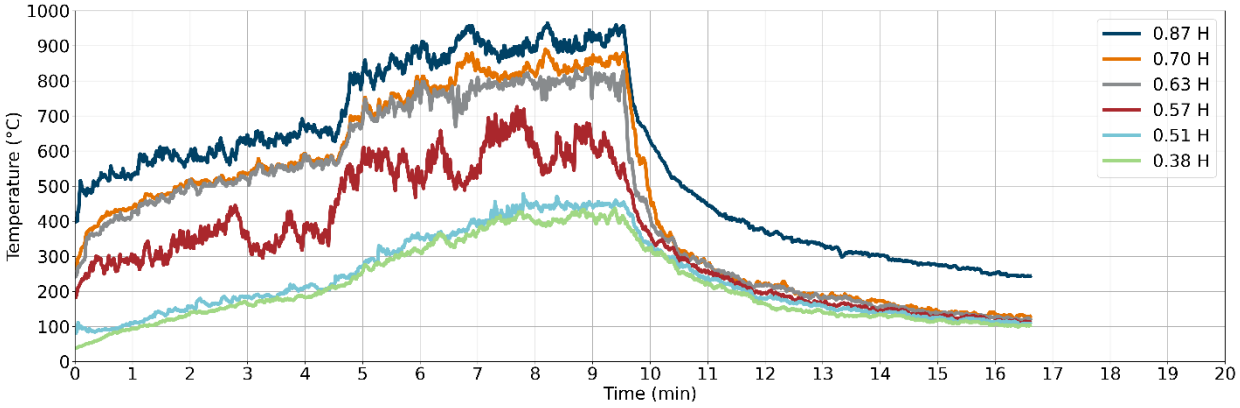

Figure F-114: Test 11 gas temperatures in the north-east corner

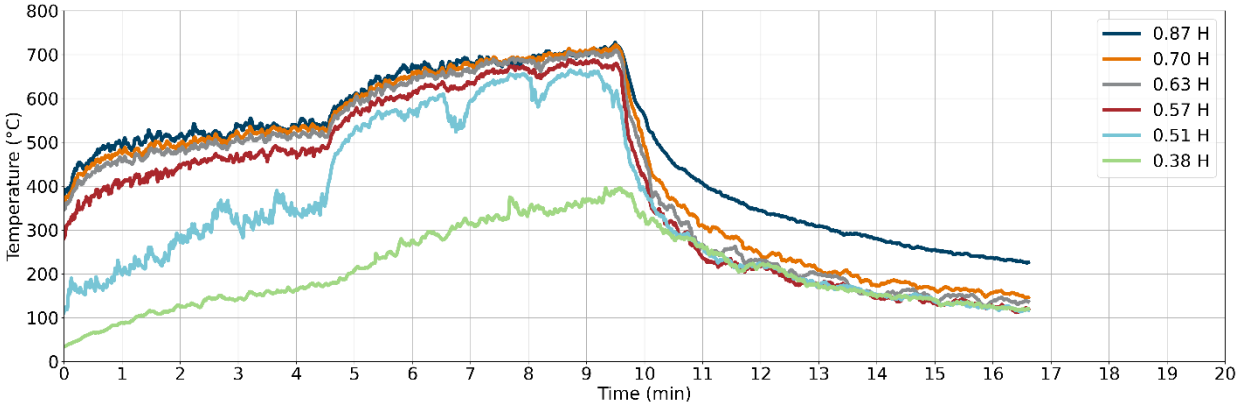

Figure F-115: Test 11 gas temperatures in the south-east corner

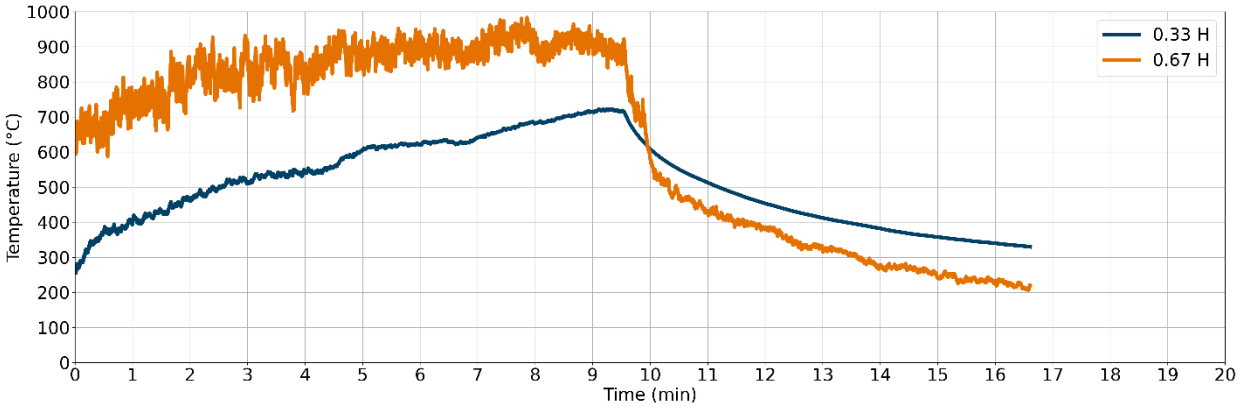

Figure F-116: Test 11 gas temperatures at the burner

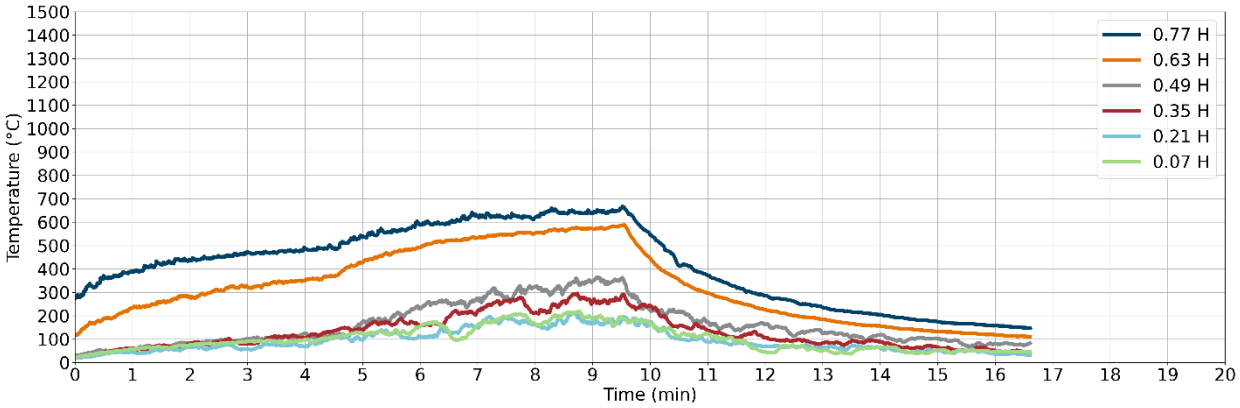

Figure F-117: Test 11 gas temperatures at the door

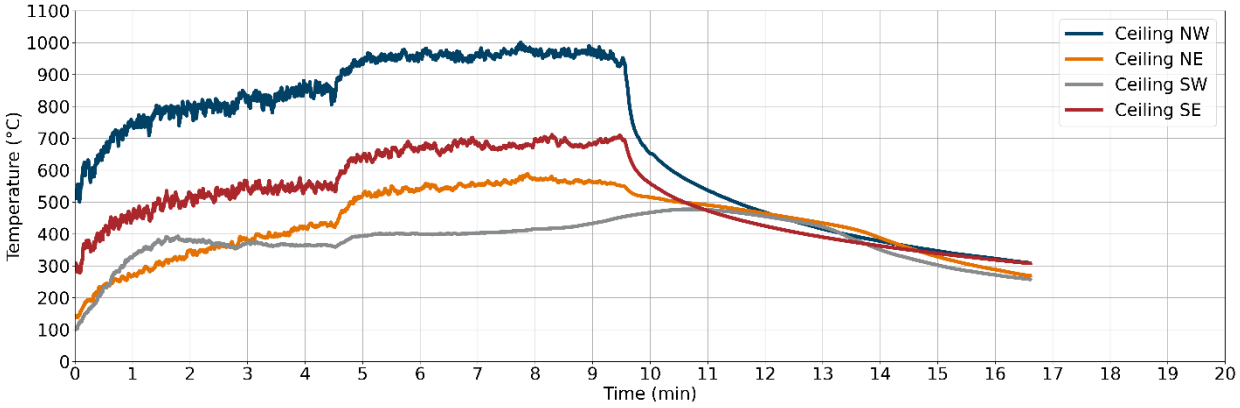

Figure F-118: Test 11 gas temperatures at ceiling

Gas Velocities

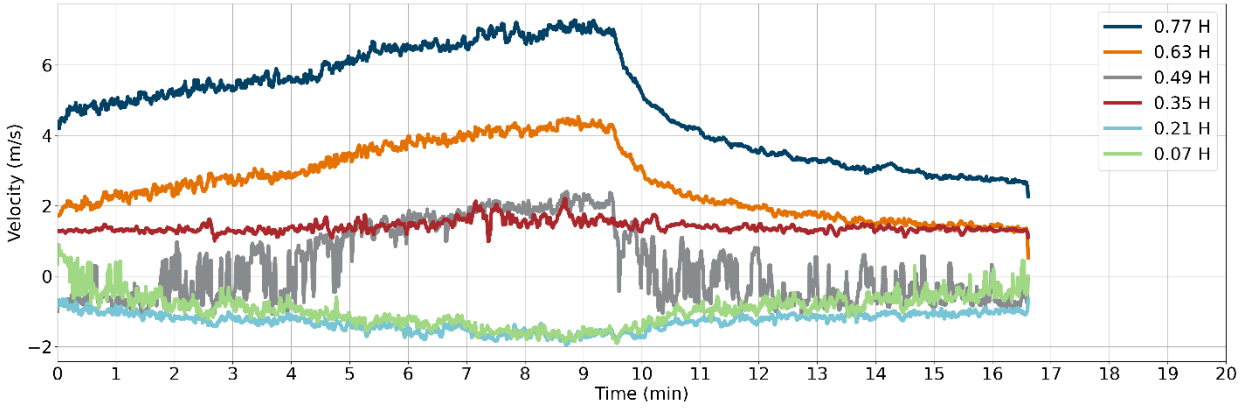

Figure F-119: Test 11 gas velocities at the door

Heat Fluxes

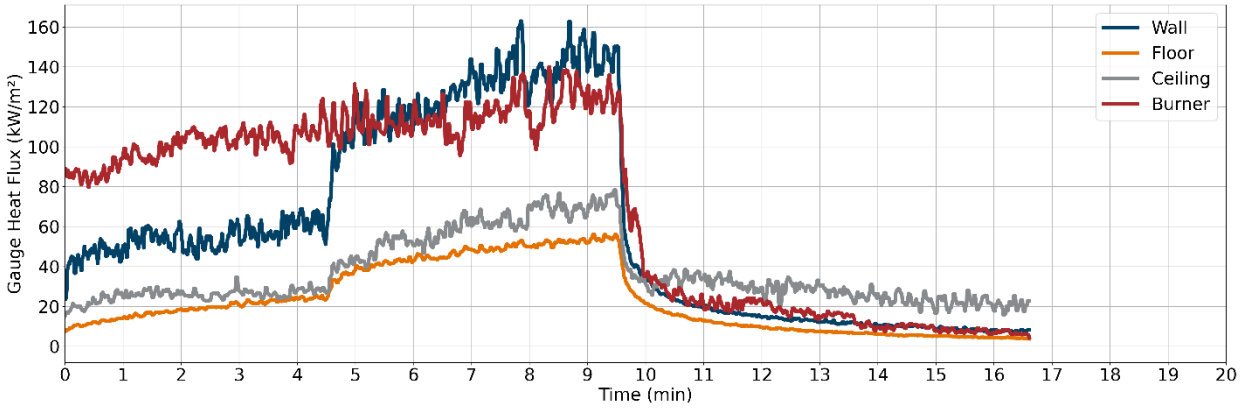

Figure F-120: Test 11 heat fluxes

Optical Obscuration

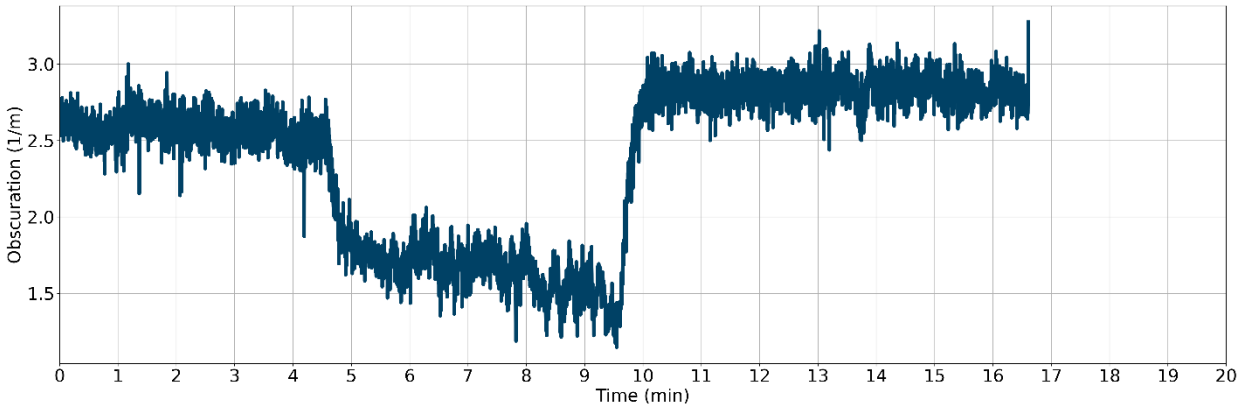

Figure F-121: Test 11 optical obscuration in the exhaust duct

Test 12-A Results (Full-Scale Non-Combustible Door-Window Configuration)

Heat Release Rate

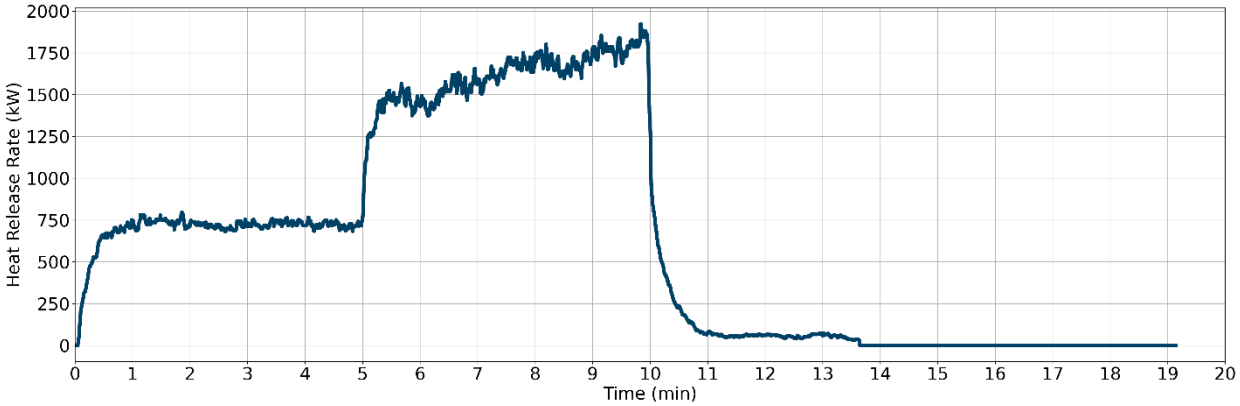

Figure F-122: Test 12-A HRR

Gas Temperatures

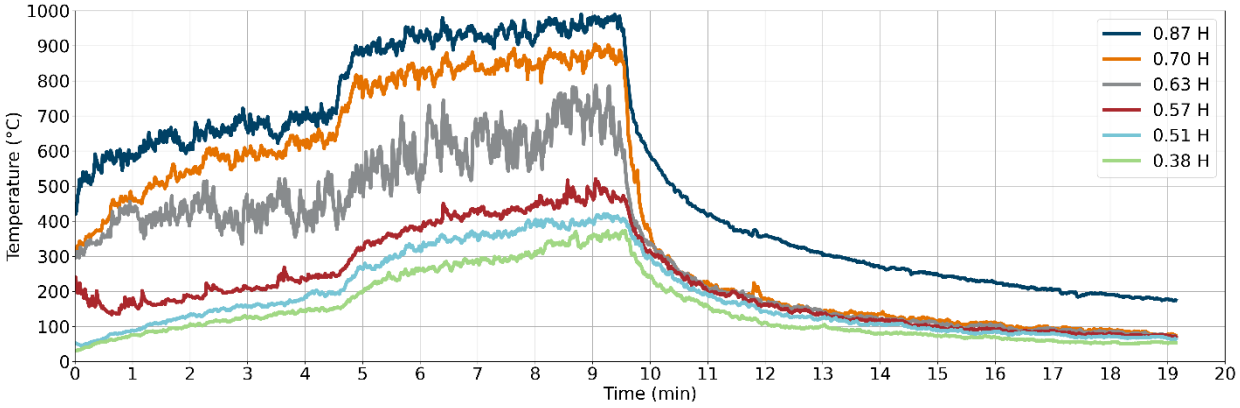

Figure F-123: Test 12-A gas temperatures in the north-east corner

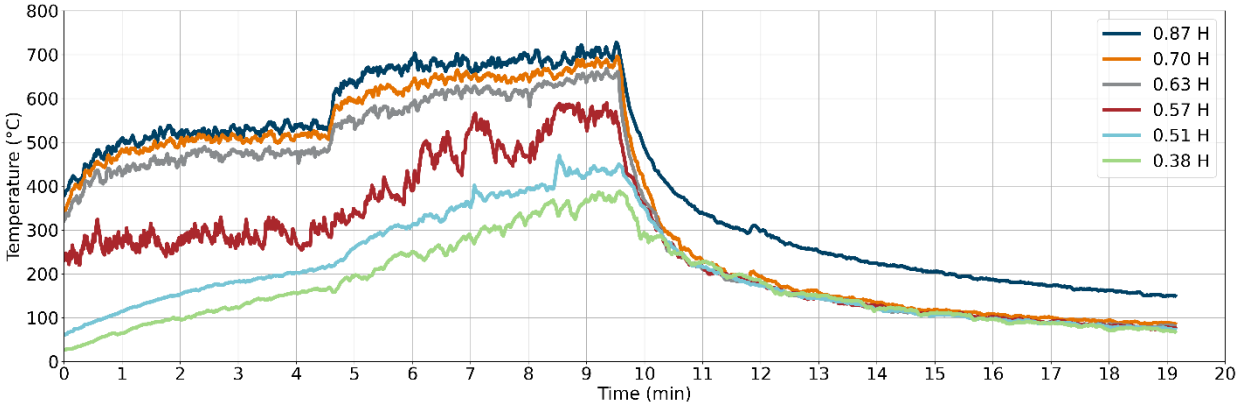

Figure F-124: Test 12-A gas temperatures in the south-east corner

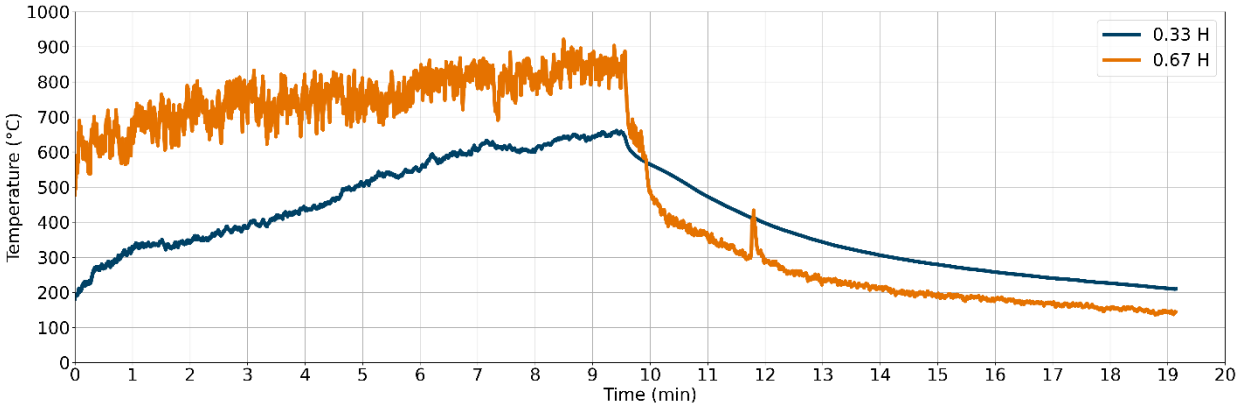

Figure F-125: Test 12-A gas temperatures at the burner

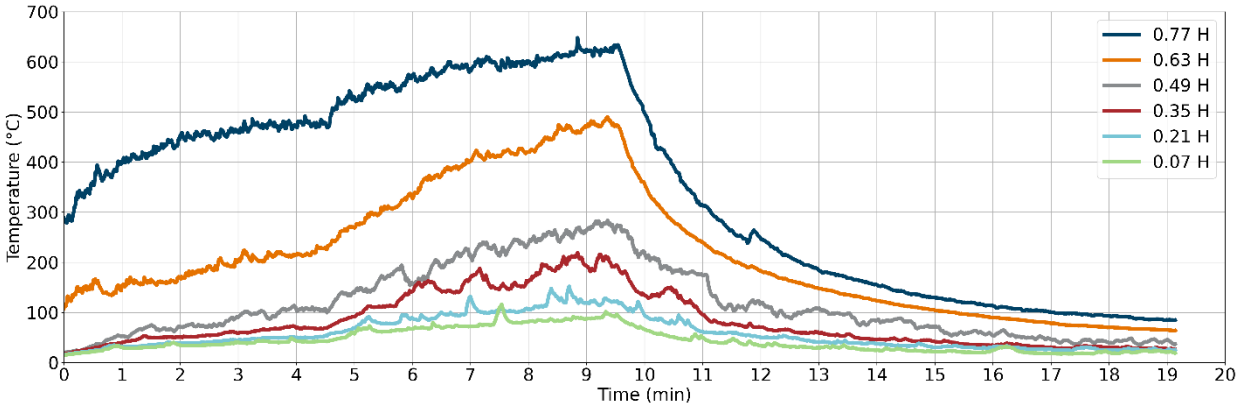

Figure F-126: Test 12-A gas temperatures at the door

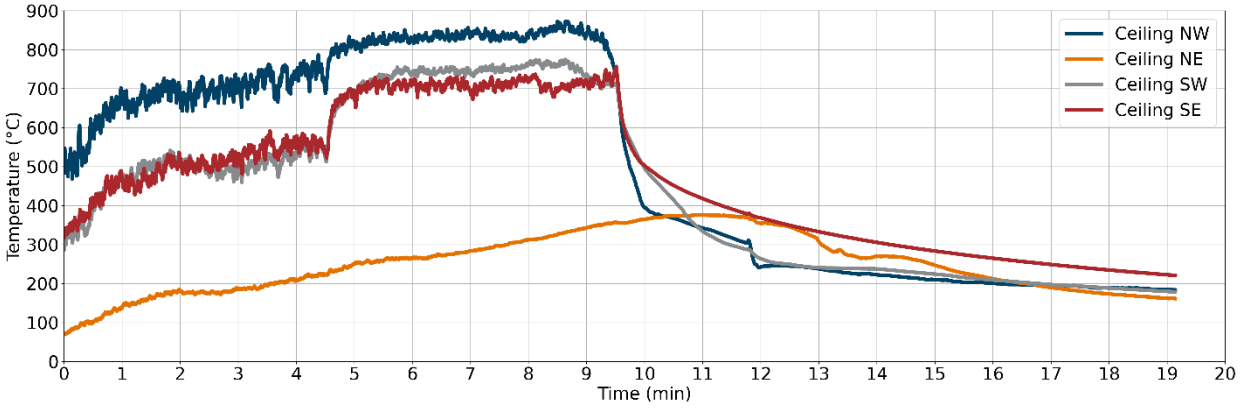

Figure F-127: Test 12-A gas temperatures at ceiling

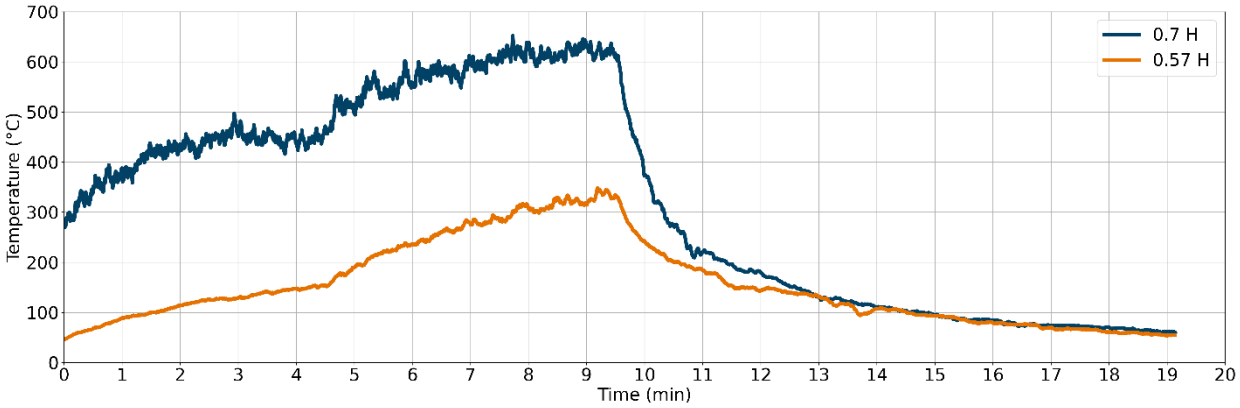

Figure F-128: Test 12-A gas temperatures at the window

Gas Velocities

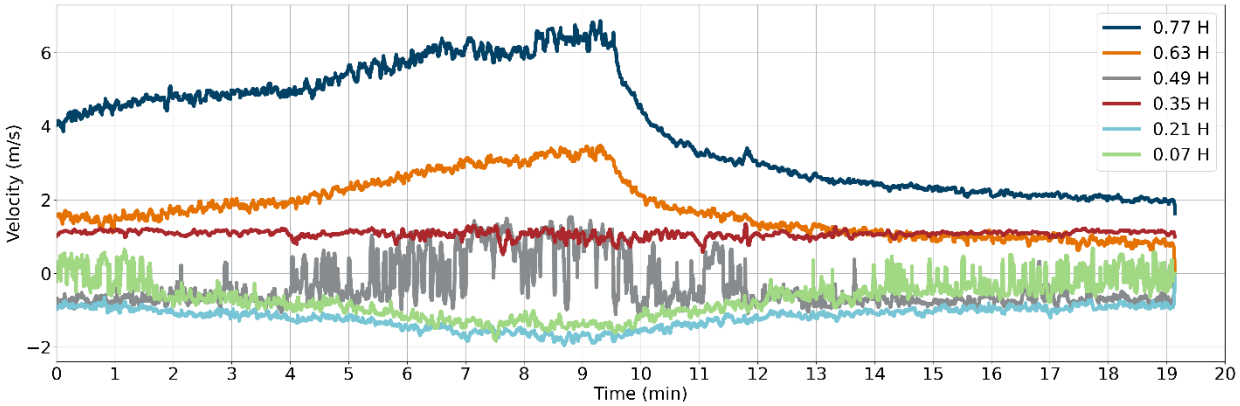

Figure F-129: Test 12-A gas velocities at the door

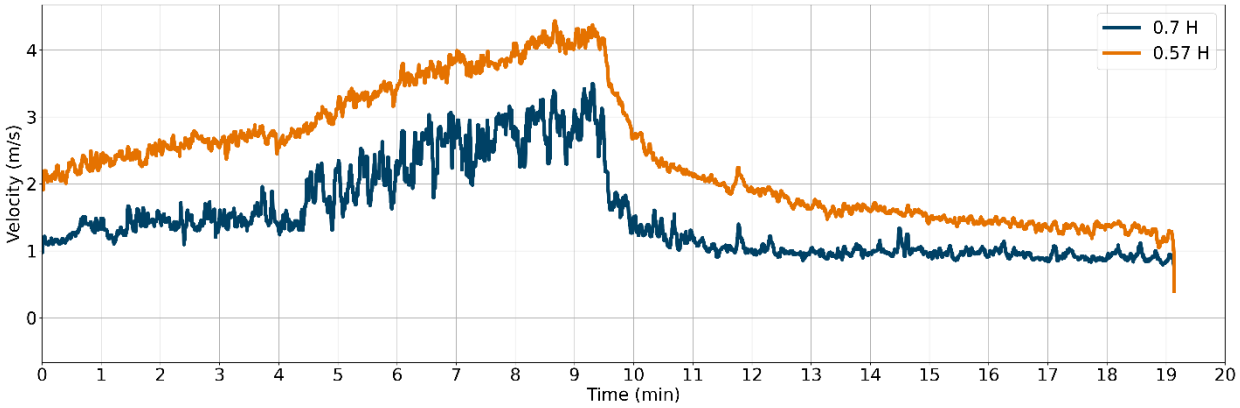

Figure F-130: Test 12-A gas velocities at the window

Heat Fluxes

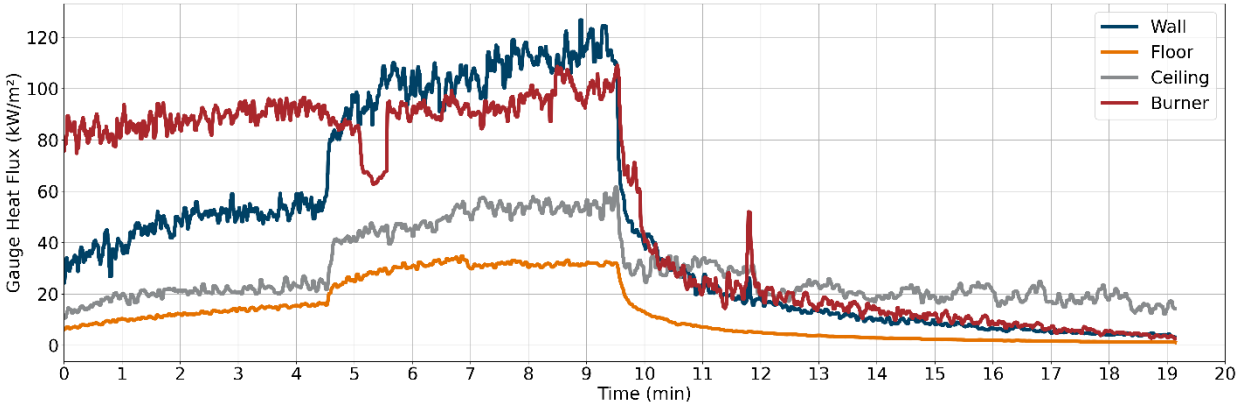

Figure F-131: Test 12-A heat fluxes

Optical Obscuration

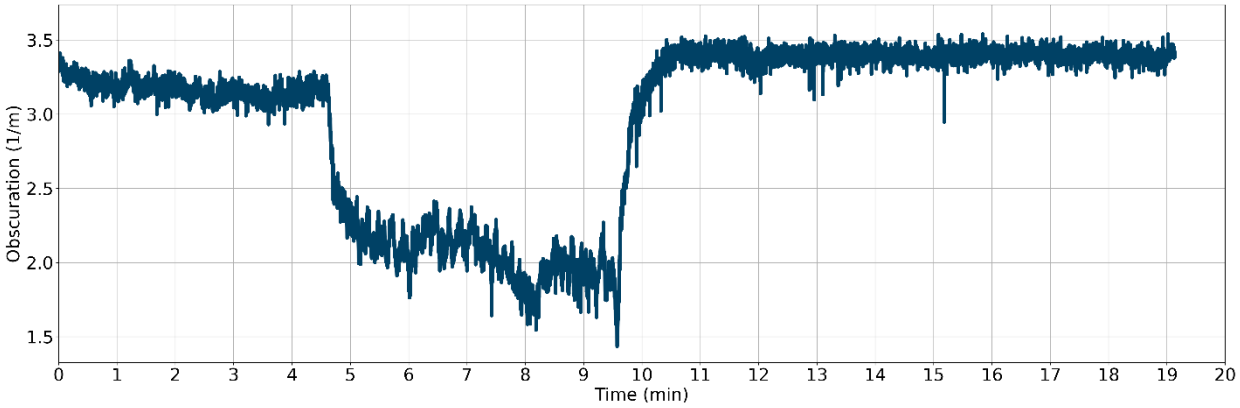

Figure F-132: Test 12-A optical obscuration in the exhaust duct

Test 12-B Results (Full-Scale Non-Combustible Door-Window Configuration)

Heat Release Rate

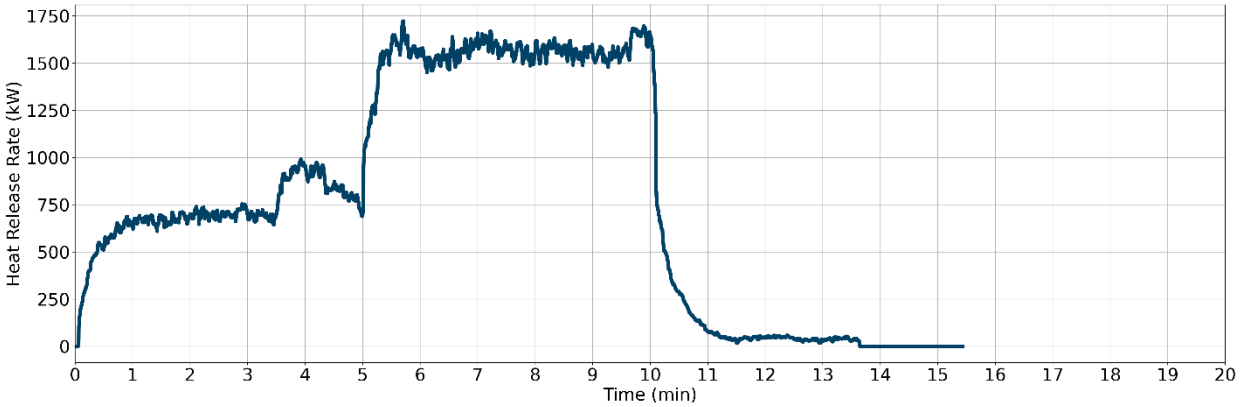

Figure F-133: Test 12-B HRR

Gas Temperatures

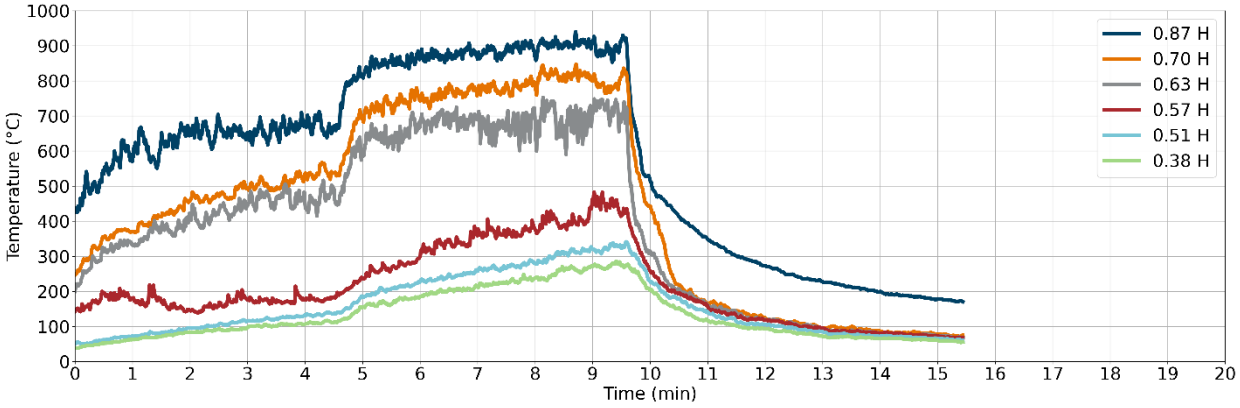

Figure F-134: Test 12-B gas temperatures in the north-east corner

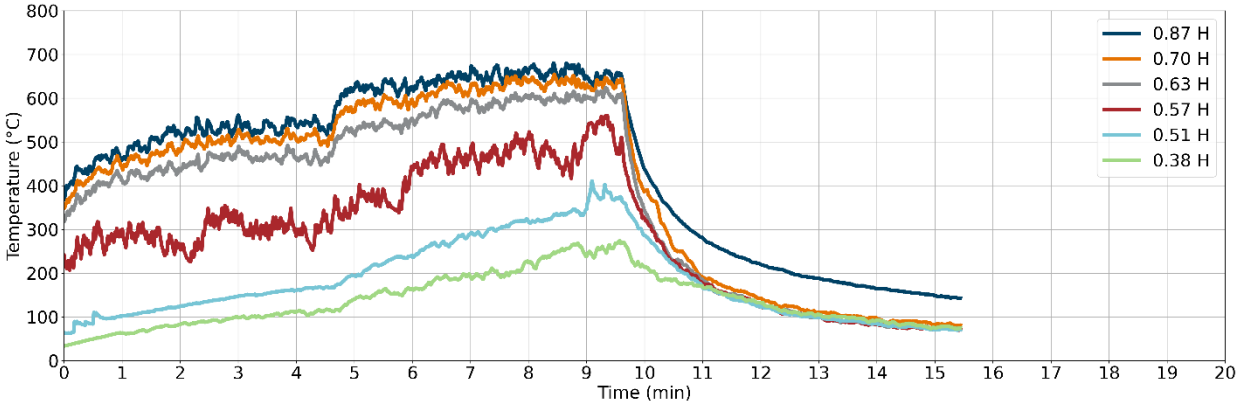

Figure F-135: Test 12-B gas temperatures in the south-east corner

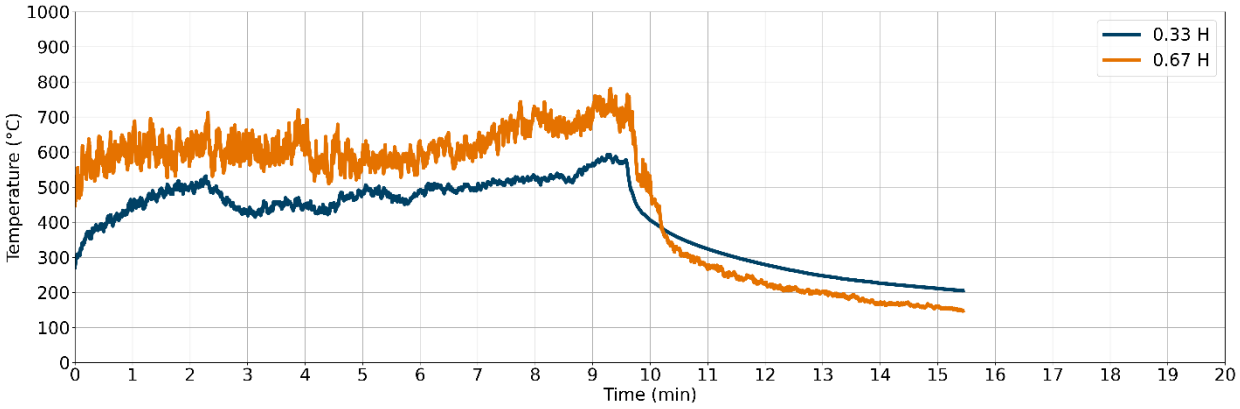

Figure F-136: Test 12-B gas temperatures at the burner

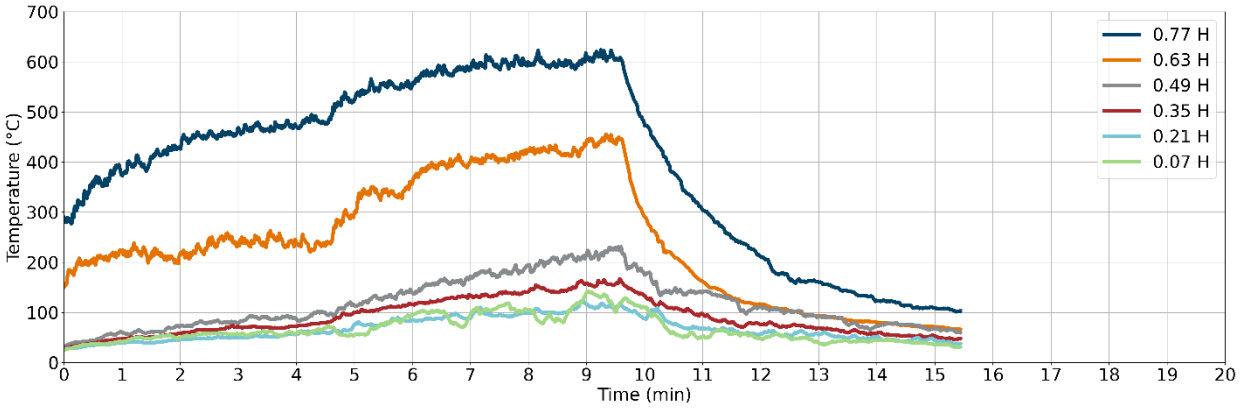

Figure F-137: Test 12-B gas temperatures at the door

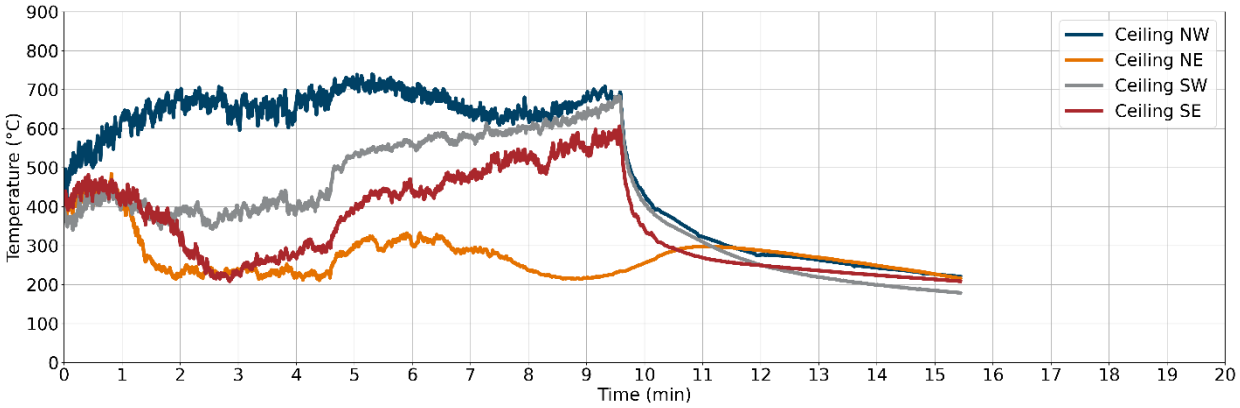

Figure F-138: Test 12-B gas temperatures at ceiling

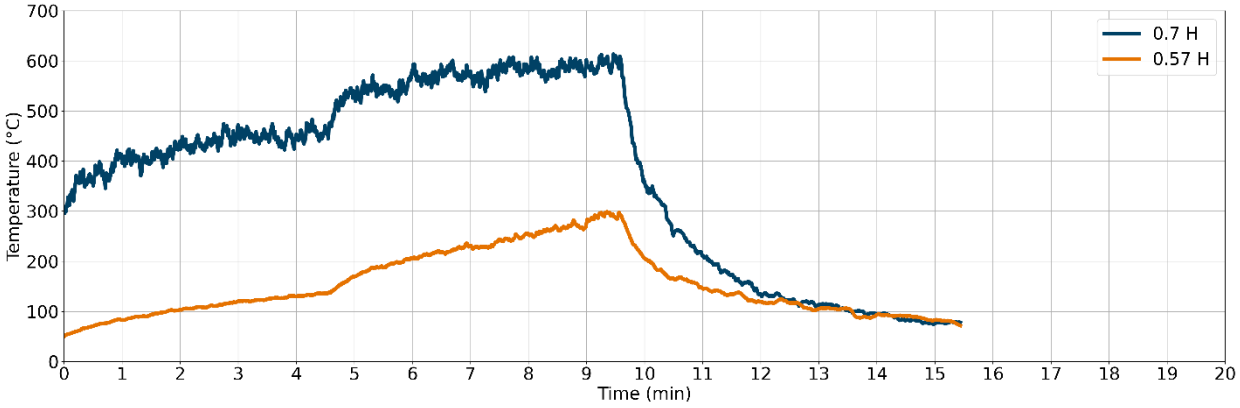

Figure F-139: Test 12-B gas temperatures at the window

Gas Velocities

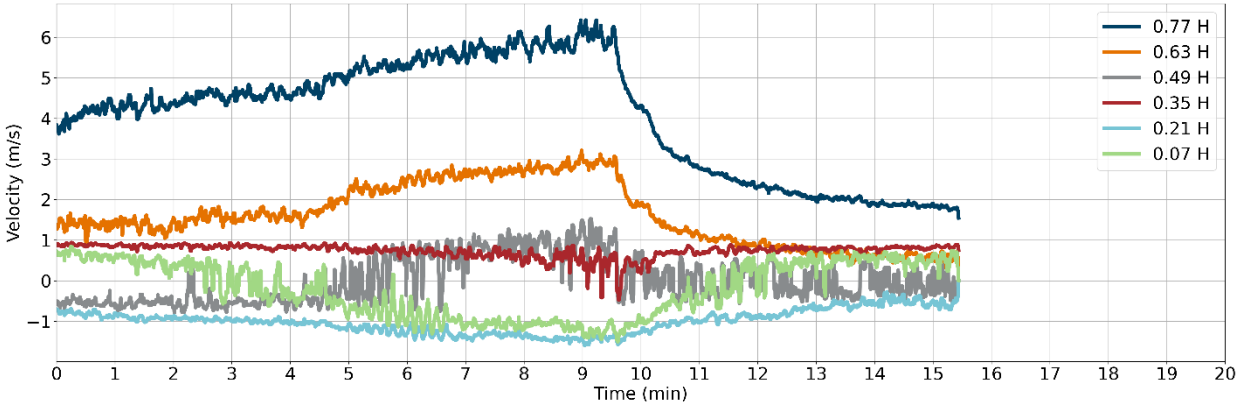

Figure F-140: Test 12-B gas velocities at the door

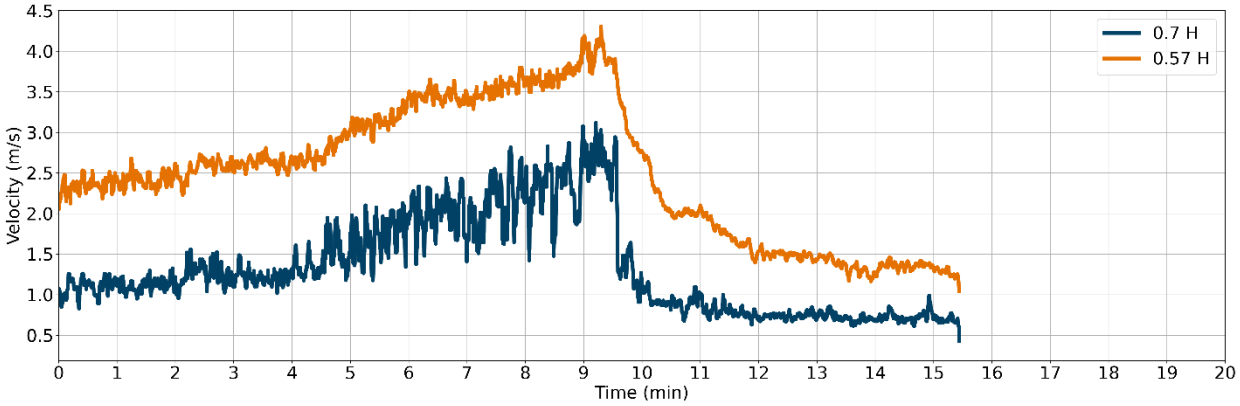

Figure F-141: Test 12-B gas velocities at the window

Heat Fluxes

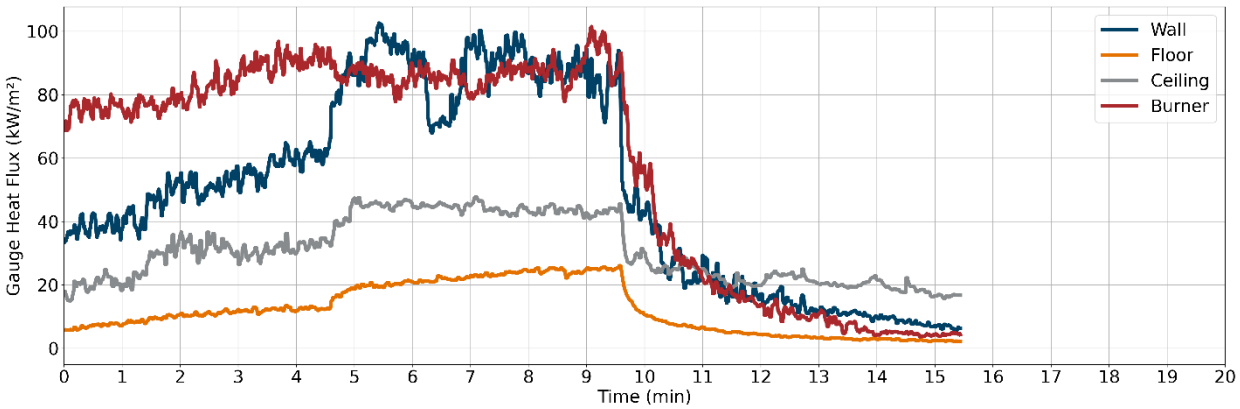

Figure F-142: Test 12-B heat fluxes

Optical Obscuration

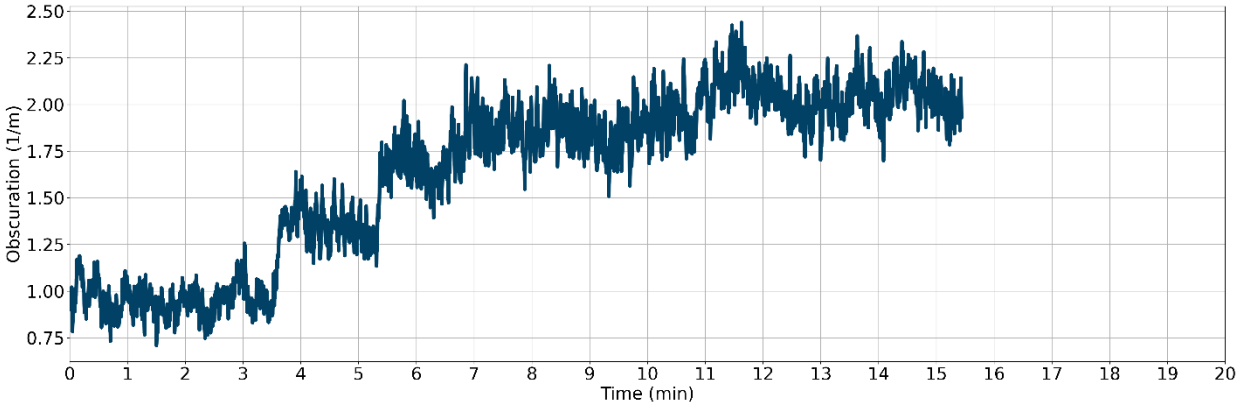

Figure F-143: Test 12-B optical obscuration in the exhaust duct

Test 13 Results (Full-Scale Liquid Fuel / JP-5 Configuration)

Test was not conducted during study.

Test 14 Results (Full-Scale Plywood Lining Configuration)

Heat Release Rate

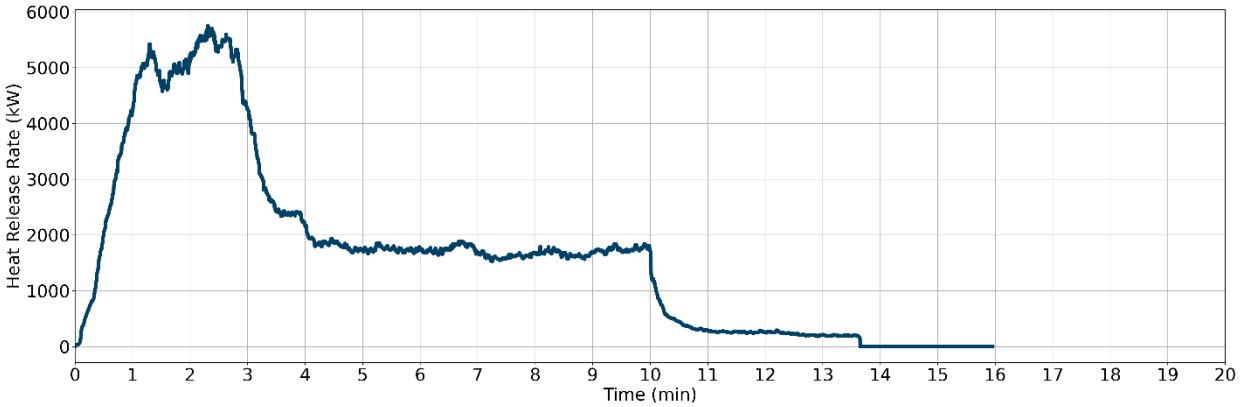

Figure F-144: Test 14 HRR

Gas Temperatures

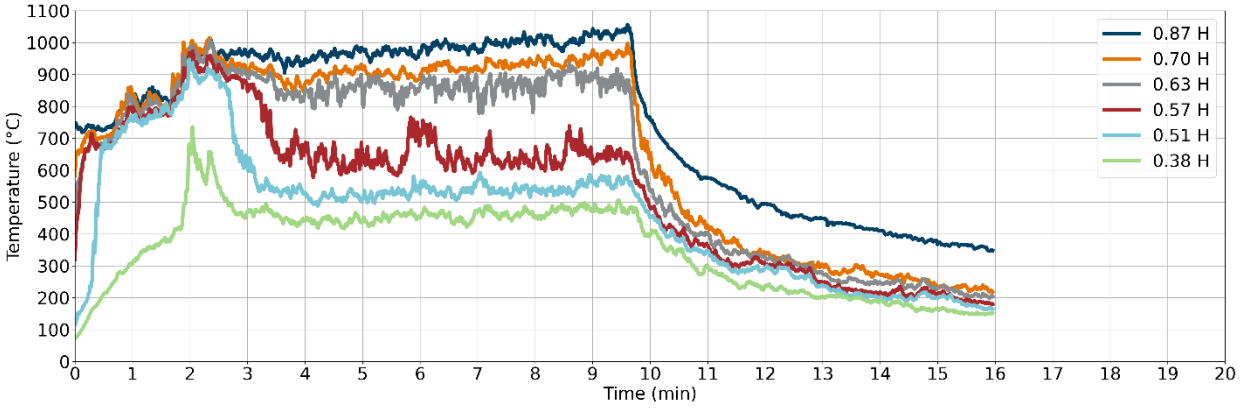

Figure F-145: Test 14 gas temperatures in the north-east corner

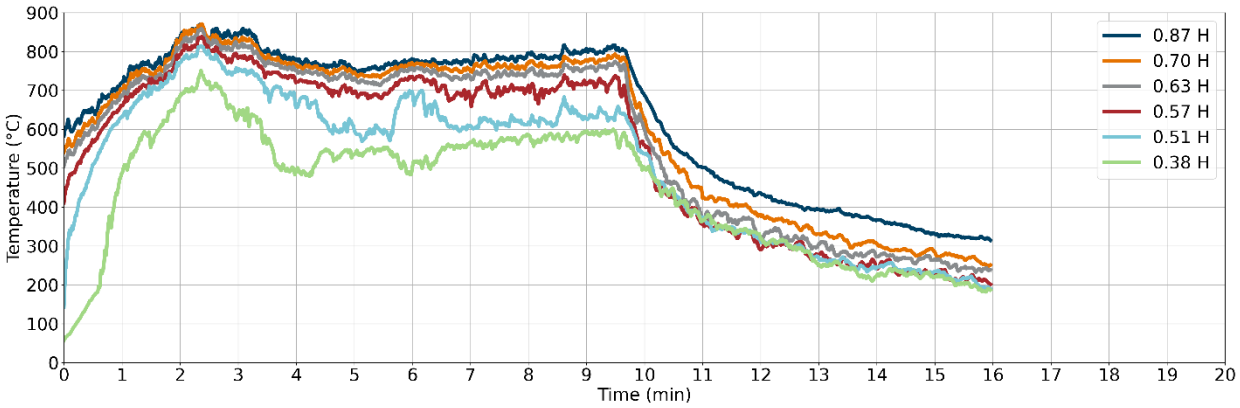

Figure F-146: Test 14 gas temperatures in the south-east corner

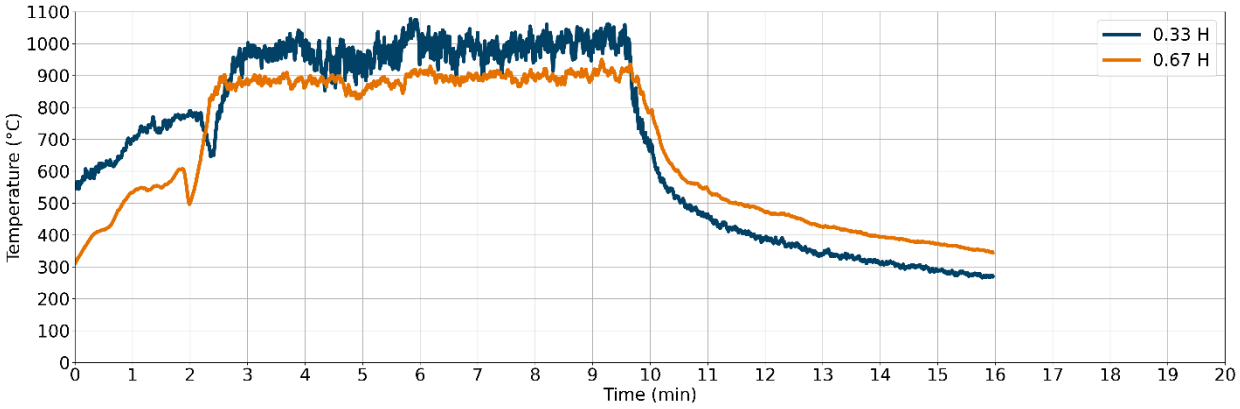

Figure F-147: Test 14 gas temperatures at the burner

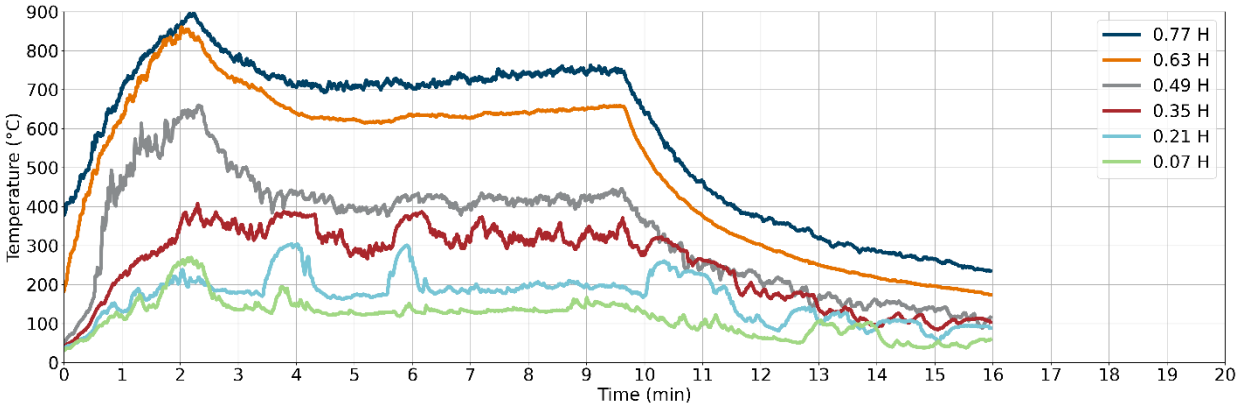

Figure F-148: Test 14 gas temperatures at the door

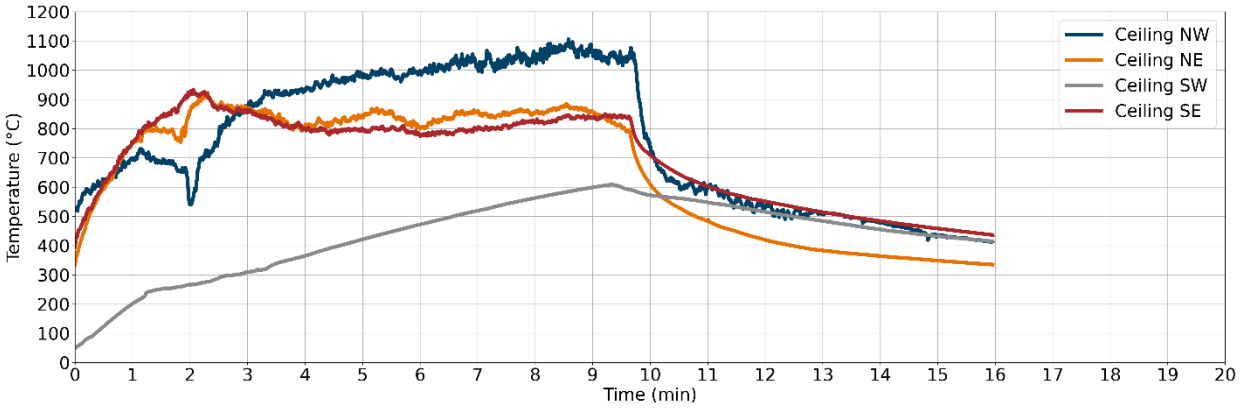

Figure F-149: Test 14 gas temperatures at ceiling

Gas Velocities

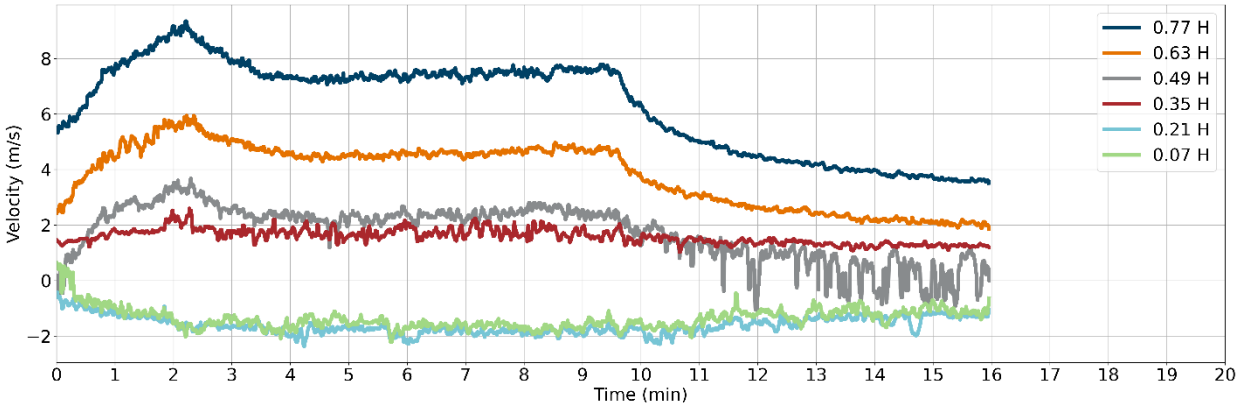

Figure F-150: Test 14 gas velocities at the door

Heat Fluxes

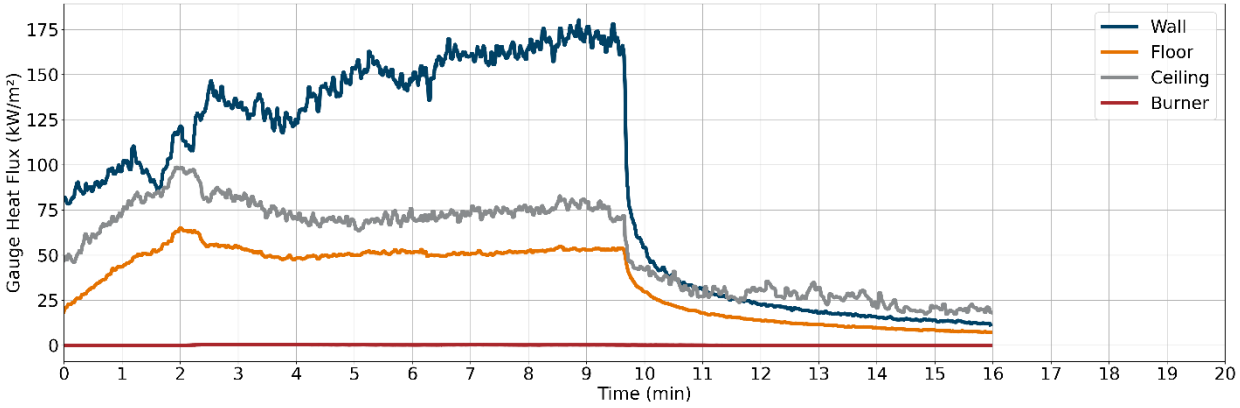

Figure F-151: Test 14 heat fluxes

Optical Obscuration

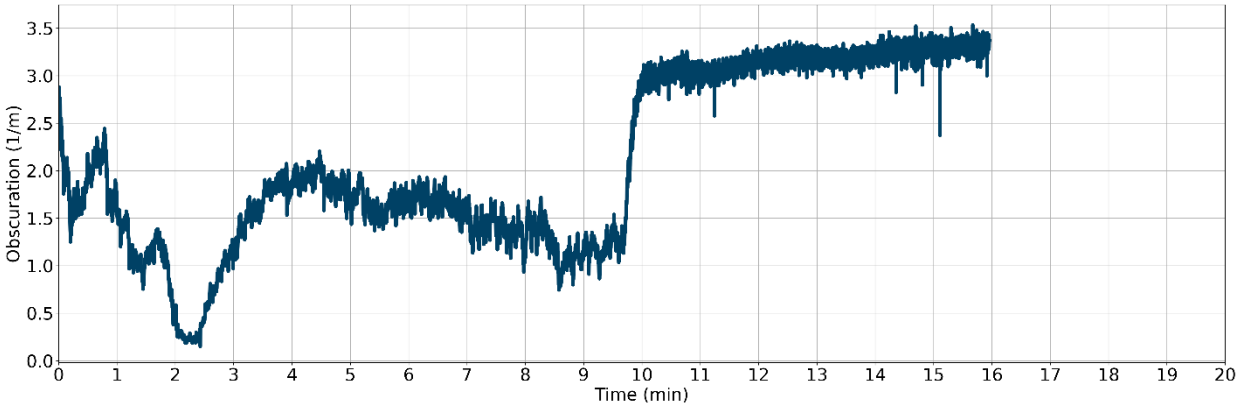

Figure F-152: Test 14 optical obscuration in the exhaust duct

Test 15 Results (Full-Scale FRP Lining Configuration)

Heat Release Rate

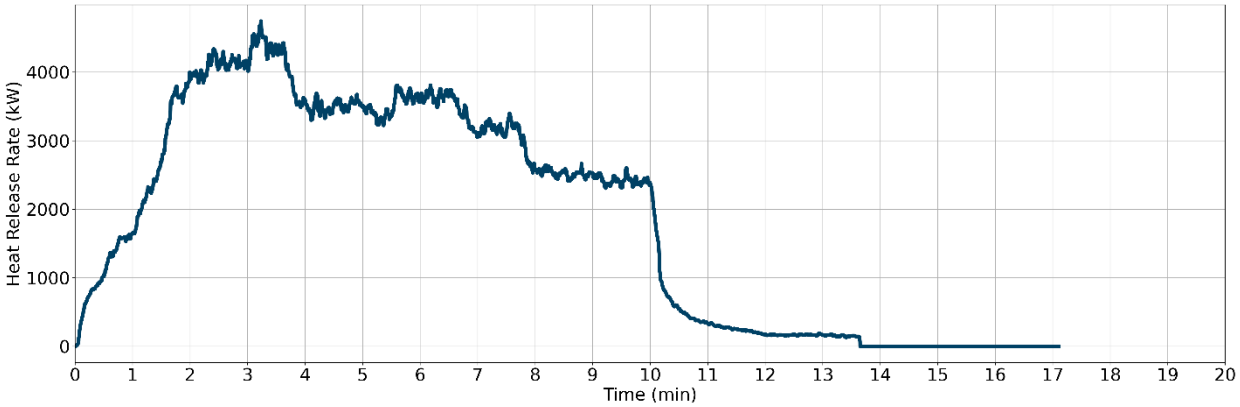

Figure F-153: Test 15 HRR

Gas Temperatures

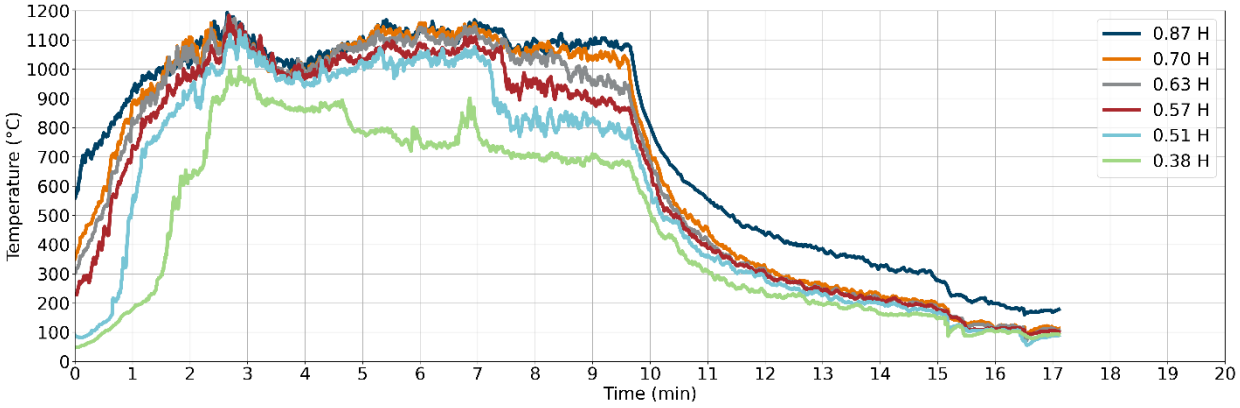

Figure F-154: Test 15 gas temperatures in the north-east corner

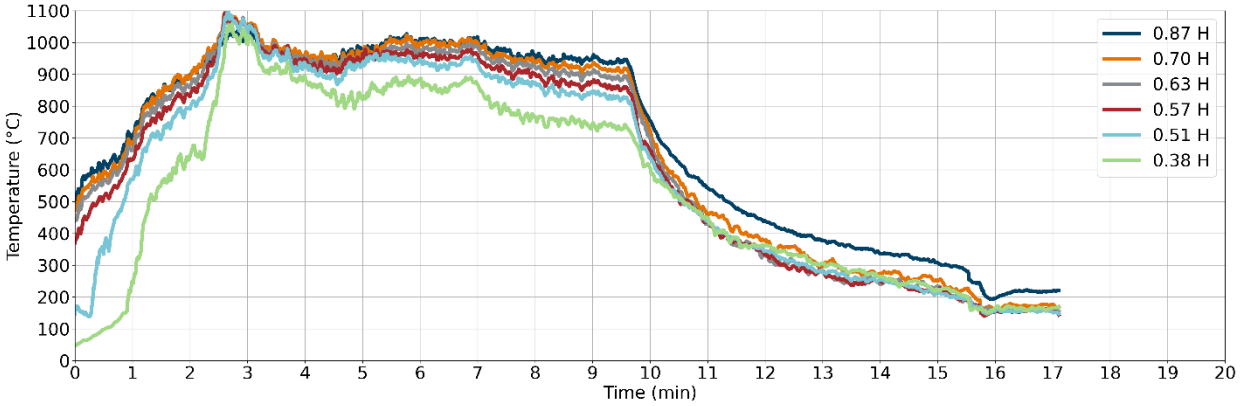

Figure F-155: Test 15 gas temperatures in the south-east corner

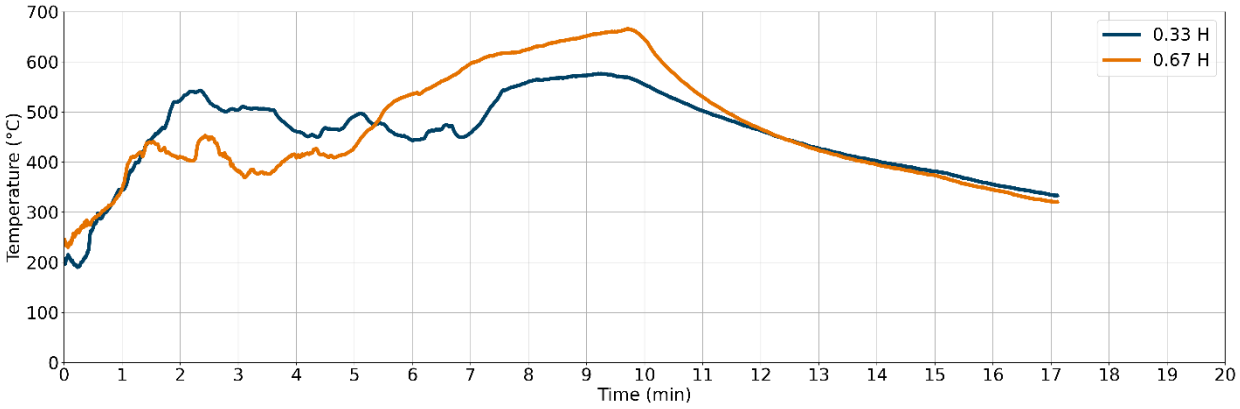

Figure F-156: Test 15 gas temperatures at the burner

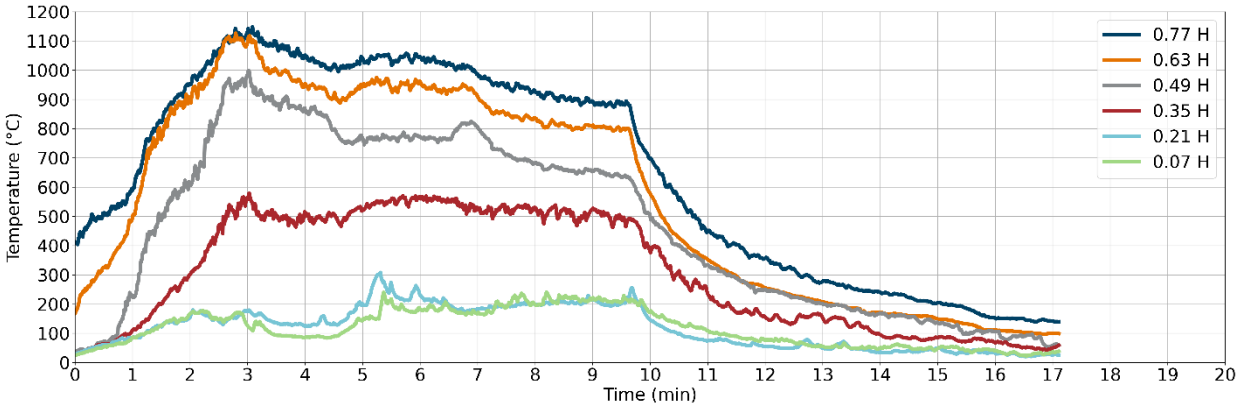

Figure F-157: Test 15 gas temperatures at the door

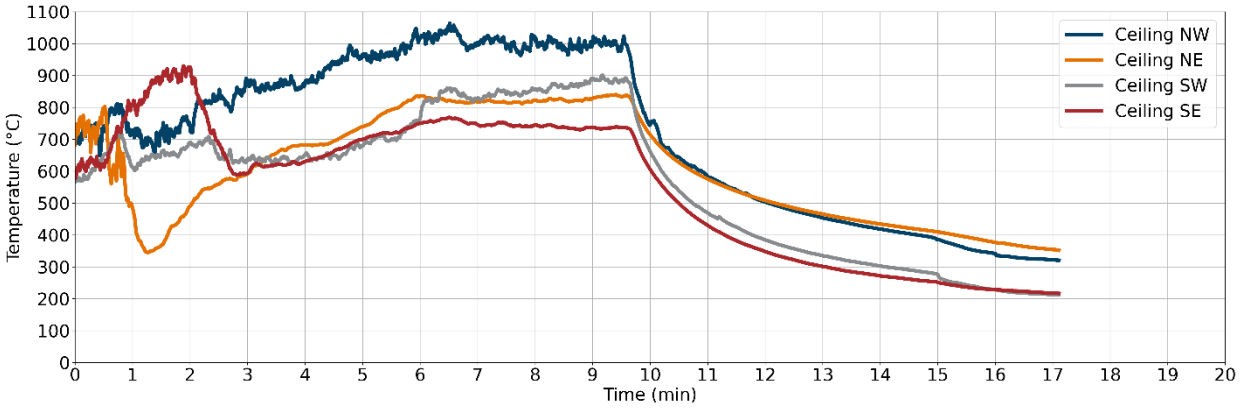

Figure F-158: Test 15 gas temperatures at ceiling

Gas Velocities

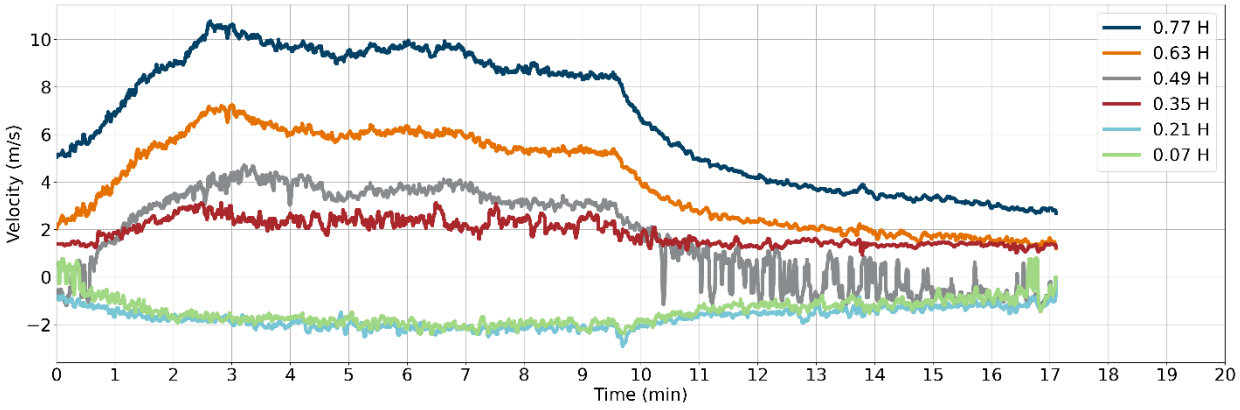

Figure F-159: Test 15 gas velocities at the door

Heat Fluxes

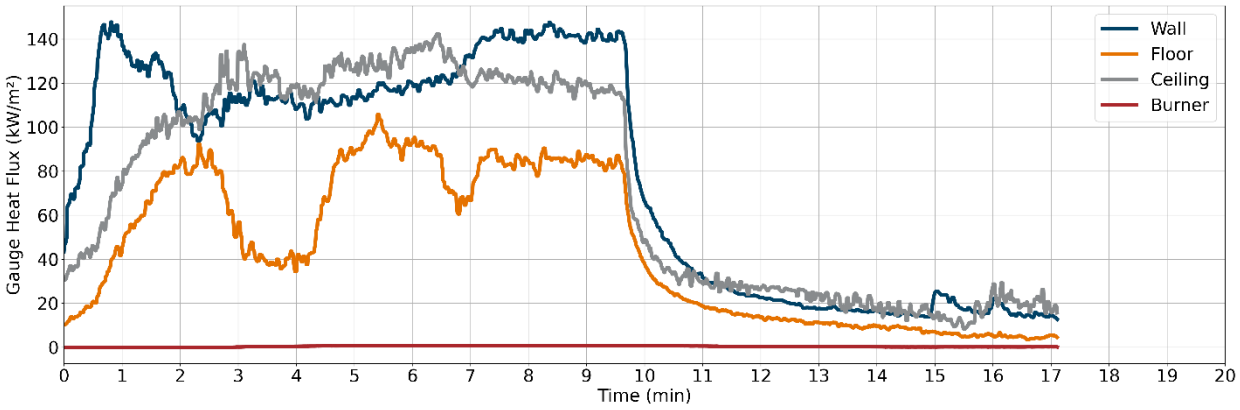

Figure F-160: Test 15 heat fluxes

Optical Obscuration

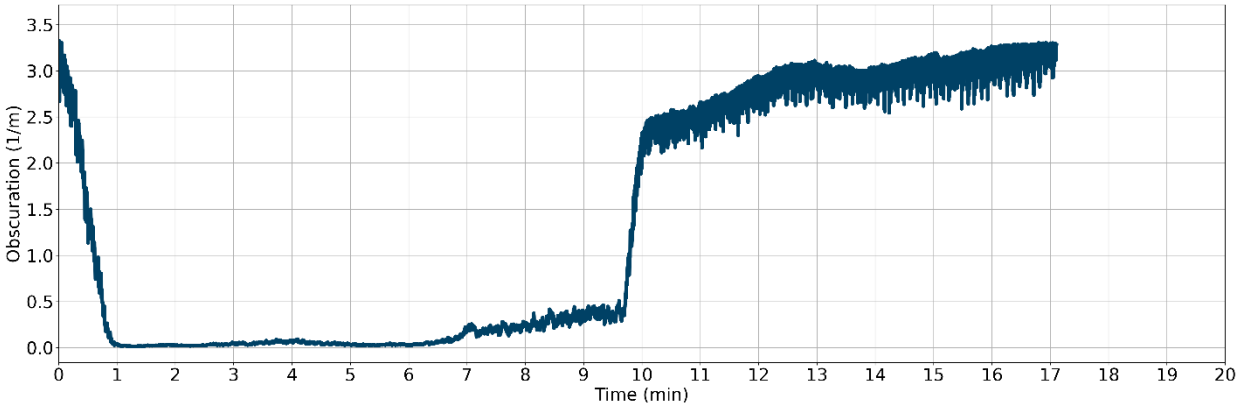

Figure F-161: Test 15 optical obscuration in the exhaust duct

Appendix G.
Test Series Measurement Summary

The compartment two-layer environment for the fixed HRR experiments is summarized in Table G-1, and the resulting heat fluxes are summarized in Table G-2. These tables can be used to directly compare experiment conditions with similar full-scale equivalent HRRs. The HRRs and total heat released in the variable HRR experiments are summarized in Table G-3.

Table G-1. Compartment two-layer environment for fixed HRR experiments

Test No.	Configuration	HRR (kW)	FSE HRR (kW)	NE T_U (°C)	NE T_L (°C)	NE z_i (m)	NE FSE z_i (m)	SE T_U (°C)	SE T_L (°C)	SE z_i (m)	SE FSE z_i (m)
1-A	1:4 NC door	20	320	328	102	0.38	1.51	268	63	0.34	1.37
		40	640	583	220	0.37	1.50	419	152	0.32	1.28
1-B	1:4 NC door	20	320	298	80	0.38	1.51	261	51	0.34	1.37
		40	640	570	178	0.37	1.49	412	123	0.32	1.30
2	1:4 NC window	20	320	280	110	0.39	1.55	264	76	0.34	1.36
		45	720	525	258	0.39	1.55	434	192	0.31	1.22
		50	800	606	361	0.39	1.56	505	288	0.30	1.19
6	1:2 NC door	80	320	290	98	0.74	1.49	269	72	0.67	1.34
		160	640	552	220	0.73	1.47	426	168	0.62	1.24
7-A	1:2 NC window	80	320	275	90	0.77	1.54	264	66	0.69	1.38
		180	720	586	214	0.76	1.52	441	160	0.65	1.31
		200	800	662	299	0.76	1.52	501	237	0.62	1.25
7-B	1:2 NC window	80	320	252	82	0.77	1.54	261	61	0.69	1.37
		180	720	574	190	0.77	1.53	438	139	0.65	1.29
11	1:1 NC door	720	720	526	151	1.28	1.28	467	141	1.09	1.09
		1430	1430	818	391	1.29	1.29	653	331	1.02	1.02
12-A	1:1 NC window	720	720	549	120	1.34	1.34	460	121	1.24	1.24
		1610	1610	806	315	1.30	1.30	621	312	1.20	1.20
12-B	1: NC window	720	720	524	95	1.36	1.36	455	95	1.24	1.24
		1610	1610	766	238	1.31	1.31	582	218	1.18	1.18

Table G-2. Compartment heat fluxes for fixed HRR experiments

Test No.	Configuration	HRR (kW)	FSE HRR (kW)	Wall GHF (kW/m^2)	Ceiling GHF (kW/m^2)	Floor GHF (kW/m^2)	Burner GHF (kW/m^2)
1-A	1:4 NC door	20	320	18.0	7.3	4.1	51.4
		40	640	46.4	19.3	13.5	57.4
1-B	1:4 NC door	20	320	18.4	7.2	2.8	51.5
		40	640	43.5	21.6	10.5	53.7
2	1:4 NC window	20	320	13.5	8.3	4.4	-
		45	720	46.2	26.7	16.6	-
		50	800	57.3	35.9	24.5	-
6	1:2 NC door	80	320	13.6	8.3	3.5	35.8
		160	640	47.5	23.7	13.8	81.2
7-A	1:2 NC window	80	320	13.7	8.1	3.0	63.5
		180	720	49.1	24.0	13.7	76.8
		200	800	59.1	26.2	20.5	82.0
7-B	1:2 NC window	80	320	12.6	8.1	2.4	65.7
		180	720	46.6	24.4	11.9	76.1
11	1:1 NC door	720	720	55.7	26.4	19.5	101.7
		1430	1430	134.2	63.0	49.0	117.9
12-A	1:1 NC window	720	720	59.4	21.2	12.8	88.9
		1610	1610	107.6	52.2	31.8	94.4
12-B	1: NC window	720	720	51.2	30.0	10.8	82.8
		1610	1610	87.2	44.1	23.2	85.9

Table G-3. Summary of variable HRR experiments

Test No.	Configuration	60s Avg Peak HRR (kW)	Test Avg HRR (kW)	Total HRR (MJ)	FSE 60s Avg Peak HRR (kW)	FSE Test Avg HRR (kW)	FSE Total Heat Released (MJ)
3	1:4 JP-5	52.1	24.3	9.7	833.6	388.2	155.3
4	1:4 Plywood	104.6	65.5	37.3	1,673.1	1,047.8	597.2
5	1:4 FRP	77.6	64.2	36.6	1,241.6	1,027.3	585.5
8	1:2 JP-5	110.4	65.5	46.6	441.7	261.9	186.4
9	1:2 Plywood	418.2	252.4	143.8	1,672.7	1,009.6	575.4
10	1:2 FRP	378.9	311.7	177.6	1,515.7	1,246.8	710.5
14	1:1 Plywood	5,364.8	2,630.1	1,347.2	5,364.8	2,630.1	1,347.2
15	1:1 FRP	4,305.1	3,201.4	1,776.4	4,305.1	3,201.4	1,776.4

Abbreviations and Acronyms

ACRONYMS	EXPLANATION
ASTM	American Society for Testing and Materials
BDVP	Bi-Directional Velocity Probe
CO2	Carbon Dioxide
CO	Carbon Monoxide
CBD	Chesapeake Bay Detachment
CFR	Code of Federal Regulations
CFD	Computational Fluid Dynamics
CMU	Concrete Masonry Unit
DAQ	Data Acquisition System
DPT	Differential Pressure Transducer
FFT	Fast Fourier Transform
FRA	Federal Railroad Administration
FRP	Fiber-Reinforced Plastic
FDS	Fire Dynamics Simulator
FSE	Full-Scale Equivalent
HRR	Heat Release Rate
HRRPUA	Heat Release Rate Per Unit Area
ISO	International Organization for Standardization
SI	International System of Units
JH	Jensen Hughes
LES	Large Eddy Simulation
MQH	McCaffrey, Quintiere, and Harkleroad
NFPA	National Fire Protection Agency
NIST	National Institute of Standards and Technology
NFPA	National Fire Protection Agency
N_2	Nitrogen
O_2	Oxygen
TC	Thermocouple
UL	Underwriters Laboratory

ACRONYMS	EXPLANATION
USC	United States Customary Units
USG	United States Gypsum Corporation